Dynamics and Statistical Mechanics of Keplerian Stellar Systems

Karamveer Kaur

Under the supervision of

Prof. S. Sridhar

Department of Astronomy & Astrophysics
Raman Research Institute, Bangalore.

This dissertation is submitted for the degree of
Doctor of Philosophy
to Jawaharlal Nehru University,
New Delhi.

March 2019

To my loving family . . .

Certificate

This is to certify that the dissertation entitled "Dynamics and Statistical Mechanics of Keplerian Stellar Systems" submitted by Karamveer Kaur for the award of the degree of Doctor of Philosophy to Jawaharlal Nehru University, is her original work. This has not been submitted or published for any other degree or qualification to any other university.

Prof. Ravi Subrahmanyan

Director

Prof. S. Sridhar

Thesis Supervisor

Raman Research Institute,

Bangalore 560 080

INDIA.

Declaration

I, Karamveer Kaur, hereby declare that the work presented in this thesis entitled "Dynamics and Statistical Mechanics of Keplerian Stellar Systems" is completely original. The thesis is composed independently by me at the Raman Research Institute under the supervision of Prof. S. Sridhar. I further declare that the subject matter presented in the thesis has not formed earlier the basis for the award of any degree, diploma, membership, associateship, fellowship or any other title of any university or institution. I have also run the thesis through *Turnitin* software.

Karamveer Kaur

Karamveer Kaur

Prof. S. Sridhar

Thesis Supervisor

Raman Research Institute,

Bangalore 560 080

INDIA.

Acknowledgements

Firstly I would like to acknowledge my Ph.D. supervisor Prof. S. Sridhar for guiding me all these years on the path of research. He always motivated me for learning new, taught me research methods, and introduced me to the fascinating field of dynamics. His originality of ideas and grand analytical methodology have always inspired me. It was always a fun working with him; every problem that we have worked on, has taught me so many things adding to my technical toolbox and scientific understanding. He has always been a firm support behind all of my professional achievements. Also, I feel very grateful to Prof. Jihad Touma of American University of Beirut for ever-stimulating discussions during his RRI visits. He has always been a support throughout the tough season of job applications, and offered very useful career advices. I also thank Dr. Mher Kazandjian of Leiden University for interesting Skype discussions regarding our project "waterbag instabilities". I am thankful to Prof. Tarun Deep Saini from IISc for numerous interesting discussions on the numerical part of my work, especially during my early Ph.D. years. A special thanks, for motivating me to use Mathematica which made my life so much easier!! I am grateful to Prof. Prasenjit Saha from University of Zurich for hosting me during my visit to the university. There I made my very first video on my work in his guidance!! I am also thankful to him for conveying about the 49$^{\text{th}}$ Saas-Fee course on Milky Way dynamics. I would thank him and Prof. Laurent Eyer (of the University of Geneva) for their help in getting financial support for this travel. I would like to thank Prof. Renu Malhotra from University of Arizona at Tucson for thorough discussions during her RRI visit. It was a great experience writing research proposal in her guidance for some postdoctoral fellowships. I also thank her for offering very useful career advices, and for introducing me to Prof. Jack Lissauer of NASA Ames research centre. I thank him for very useful exchange of ideas on "exo-planetary dyamics" over emails. I would thank Prof. Shiv Sethi for his support for some of the postdoctoral applications and most importantly, for helping all of us (students) in any time of need. I am thankful to Prof. Biman Nath and Prof. Yashodhan Hatwalne for their useful advices during my annual academic meetings. I would specially thank Prof. Yashodhan for very resourceful discussions about Mathematica coding. I want to thank – Prof. Ortwin Gerhard (MPE, Munich), Prof. Andreas Eckart (University of Koln), Prof. Nadine Neumayer (MPIA, Heidelberg), Prof. Bence Kocsis (Eotvos University, Budapest) and Prof. Carlo Nipoti (University of Bologna) – for hosting me during my Europe visits. I have indeed learnt a lot through discussions at these places.

Then I would acknowledge my friends at RRI, who made this whole journey so lively. I blessed to have some amazing buddies – Sreeja, Priyanka, Meera and Nafisa – who have kindly (hopefully happily :D) tolerated me all these years. Our outings at Thalassery and Fishing boat made me a big fan of Mallu food (especially fish). I thank Kartick for always being so caring and supportive. I would definitely miss daily socio-political discussions with Varun and Raj at lunch. I am thankful to Mangla ji, Yashodha ji and Ratna ji for cooking amazing breakfast for us; parantha, tea and newspaper always made a great yummy start for the day. In my last year of Ph.D., it was a cheerful and cozy feeling to have Gunjan, Manami and Shreya around at hostel. I would acknowledge SCM gang – Swami, Mari, Madhukar, Irla, Sushil and Sreeja – for their joyful aura during dinners at canteen. It was great to have around - Sanhita, Janakee, Aakash, Kavitha, Shruti, Jishnu, Saurabh, Saikat, Ranita, Aditi, Kshitija, Narendra, Anjan, Siddhartha, Hemanth and Naveen. I would like to acknowledge my seniors Mamta, Nishant, Chandreyi, Nazma, Lizo, Arpita, Sourabh and Gayathri, who used to rock Astro floor some years back. It used be great to have Ravi Ranjan around for many interesting discussions on topics ranging from research to politics. I am very happy to remember cheerful times with Mayuri and our swimming gang from Vyalikaval. It was great to have after-dinner walks with Bhargavi at hostel; I am thankful for her invitations for amazing food. I would definitely miss Saturday lunches with Sharadini at Fishing boat, and our discussions on socio-economic topics which taught me so many things. Special thanks to her for introducing me to different kinds of sea foods!! I would like to thank my B.Sc. and M.Sc. friends Kujji, Manji, Swati, Navpi, Aman and Sona for being always so close, inspite of physical distances.

I would acknowledge wonderful staffers of RRI in different sections – computers, library, administration and accounts. I am thankful towards institute authority for supporting my international travels, that helped me in communicating with fellow researchers in the field. Also, the hostel accommodation in the last year of Ph.D. was very crucial for focussing on work. I would like to especially acknowledge

Prof. Ravi Subrahmanyan, Mr. C.S.R. Murthy, Mr. Naresh, Mr. Suresh Varadarajan, Prof. Biswajit Paul, and Prof. Raghunathan for their support. I would also thank – Jacob, Krishna, Sridhar B., helpline staffers (computer section), Radha, Vidya, Shailaja and Savitha (admin.), and Manjunath & Manjunath, Nagaraj and Vani (from library) – for their ready assistance in any matter. I would acknowledge Harini and Vidya for being so caring, and helping us deal with all official/academic matters. I would thank Lakshmamma, Gangadhar anna, and (late) Hanumanthappa for their help in any matter of need. I would thank canteen staff for serving us healthy food daily. I would acknowledge flora and fauna of RRI, which fills ones heart with peace; I would definitely miss after-lunch walks through these beautiful greeny surroundings. I would thank gardeners and other staffers for taking care of it.

Most importantly, I would always be indebted to my parents, S. Rajinder Singh and Smt. Rajinder Kaur, for being so loving and supportive. They have always been my biggest strength in all endeavours of my life. I thank my brother S. Jagminder Singh and bhabhi Smt. Sukhwinder Kaur for being so caring and encouraging. I would like to thank my dada ji S. Jaswant Singh and dadi ji (late) Smt. Surjit Kaur for nurturing us with their love and care over the years. At last, I would acknowledge joyful aura of my nephews, Deep and Hem, and their stories of mischief – which keep us always on a lively track!!

Contents

Abstract

The nuclear star clusters (NSCs) orbiting massive blackholes (MBHs) at the centres of many galaxies are the densest known stellar systems, where the number density of stars can exceed those in globular clusters by a factor of 1000. The morphologies and kinematics of NSCs are varied (Seth et al., 2006), and questions concerning their dynamical evolution form the subject of this thesis. These are motivated by observations of the inner regions of the nearest two NSCs: the lopsided nuclear disc of M31 (Lauer et al., 1993), and the Milky Way NSC with its spheroid of old stars (Genzel et al., 2010) and a remnant disc of young stars (Yelda et al., 2014). The thesis explores the gravitational *dynamics* and *kinetics* of NSCs within the radius of influence of the MBH. The research presented is the first application of the general theory of secular dynamics and kinetics by Sridhar & Touma (2016a,b, 2017).

Secular dynamics and kinetics

We study NSCs consisting of $N_\star \gg 1$ stars, of total mass M, orbiting a MBH of mass $M_\bullet \gg M$. Hence the NSC is a *Keplerian* stellar system with the mass ratio $\varepsilon = M/M_\bullet \ll 1$ as the natural small parameter for studying dynamical problems. Since the gravitational force due to the Keplerian potential of the MBH dominates, stellar orbits can be thought of as Keplerian ellipses over the short orbital period, $T_{\rm kep}$. The orbital elements of these ellipses vary over the longer *secular* timescale, $T_{\rm sec} \sim T_{\rm kep}/\varepsilon$, due to other sources of gravity like cluster self-gravity, external tidal fields and general relativistic effects.

The long term, or secular, evolution of orbits can be followed by averaging the dynamics over the fast Keplerian orbital phase, a standard method in planetary dynamics deriving from Gauss. Secular dynamics conserves the semi-major axis of every Keplerian elliptical orbit. Each star can be thought of as a *Gaussian Ring*, which is a Keplerian ellipse of constant semi-major axis (with the stellar

mass distributed uniformly in time along the ellipse) whose other orbital elements deform over times $T_{\rm sec}$. Then secular dynamics, thermodynamics and kinetics are all about the study of mutual gravitational interactions between $N_\star \gg 1$ precessing and deforming Gaussian Rings.

Since the Keplerian energy of every orbit is conserved, the rings can only exchange angular momenta. According to Rauch & Tremaine (1996) mutual gravitational torquing can lead to a state of relaxation in the distribution of angular momentum over different orbits. They estimate that this *Resonant Relaxation* (RR) would occur over a timescale, $T_{\rm res} \sim N_\star T_{\rm sec}$. In contrast classical two-body relaxation (where there are energy exchanges as well) proceeds over the longer timescale $T_{\rm 2b} \sim T_{\rm res}/\varepsilon$, which can be greater than the Hubble time. Over timescales much shorter than $T_{\rm res}$, secular evolution is effectively *collisionless* and the NSC may be thought of as consisting of an infinite number of stars, each of infinitesimal mass, the whole having a fixed total mass M. Angular momentum exchange is mediated by the mean self-gravitational field of the NSC. As an example of the kind of dynamical questions that can be studied, within the theoretical framework of Sridhar & Touma, consider the following which is the subject of Part IA:

> Keplerian stellar discs orbiting a nuclear MBH are probably ubiquitous. The best studied cases are the Keplerian discs at the centre of the Milky Way and M31. The former has a disc of young stars that could have formed in a fragmenting, circular accretion disc around the MBH. Then we expect that the initial stellar orbits should have small eccentricities and the same sense of rotation (i.e. no counter-rotation) about the MBH. But Yelda et al. (2014) found that the mean eccentricity of the stellar orbits is $\bar{e} \simeq 0.27$. Is this largish value the result of secular instabilities?

The thesis consists of two parts, divided into collisionless and collisional secular dynamics.

Part I. Collisionless dynamics of stellar cusps and discs

A. *Secular Collisionless Instabilities of Keplerian Stellar Discs* (Chapter 2).

B. *Deformation of the Galactic Centre stellar cusp due to the gravity of a growing gas disc* (Chapter 3).

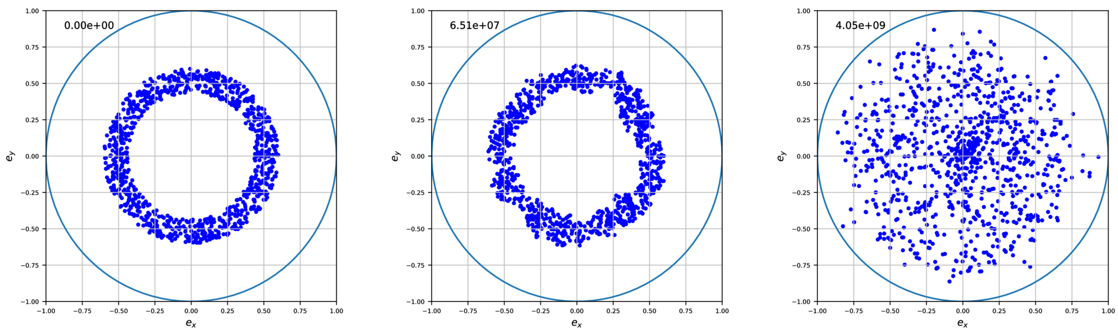

(a) $t = 0$ Gyr (b) $t \simeq 0.06$ Gyr (c) $t \simeq 4.05$ Gyr

Fig. 1 *Evolution of a waterbag band in eccentricity plane*: (a). The initial axisymmetric system with narrow range of eccentricities; (b). The linear collisionless regime of evolution with appearance of $m = 4$ unstable mode; (c). The collisionlessly relaxed nearly axisymmetric state with a wide spread in eccentricities. (Figure courtesy Mher Kazandjian)

Part II. Resonant Relaxation of Keplerian stellar discs

A. *Numerical exploration of the Fokker-Planck equation for an axisymmetric Keplerian disc* (Chapter 4)

B. *Inclusion of gravitational polarization in the Fokker-Planck equation* (Chapter 5).

Part I. Collisionless dynamics of stellar cusps and discs

A. Secular Instabilities of Keplerian Stellar Discs

Kaur K., Kazandjian M. V., Sridhar S., Touma J.R. 2018,

MNRAS(`https://doi.org/10.1093/mnras/sty403`)

We present idealized models of razor–thin, axisymmetric, Keplerian stellar discs around an MBH, and study non-axisymmetric secular instabilities in the absence of either counter-rotation or loss cones. This is done by combining analytical methods from Sridhar & Touma (2016a) with numerical simulations derived from Touma et al. (2009). The discs we consider are prograde monoenergetic waterbags, whose phase space distribution functions are constant for orbits within a range of eccentricities (e) and zero outside this range.

The linear normal modes of waterbags are composed of sinusoidal disturbances of the edges of distribution function in phase space. Waterbags which include circular orbits (*polarcaps*) have one stable linear normal mode for each azimuthal wavenumber m. The $m = 1$ mode always has positive pattern speed (in the same sense as the stars orbit the MBH) and, for polarcaps consisting of orbits with $e < 0.9428$, only the $m = 1$ mode has positive pattern speed. Waterbags excluding circular orbits (*bands*) have two linear normal modes for each m, which can be stable or unstable. We derive analytical expressions for the instability condition, pattern speeds, growth rates and normal mode structure. Both $m = 1$ and $m = 2$ modes are always stable, whereas modes with $m \geq 3$ can be unstable. Narrow bands are unstable to modes with a wide range in m.

Numerical simulations confirm linear theory and follow the non-linear evolution of instabilities. Long-time integration suggests that instabilities of different m grow, interact non-linearly and relax collisionlessly to a coarse-grained equilibrium with a wide range of eccentricities. These non-axisymmetric instabilities provide a pathway for transition from one axisymmetric state to another, accompanied by collisionless relaxation of eccentricities. The Figure 1 shows the evolution of a waterbag band undergoing $m = 4$ instability in the linear regime, and the final collisionlessly relaxed state.

B. Deformation of the Galactic Centre stellar cusp due to the gravity of a growing gas disc

Kaur K., Sridhar S. 2018, MNRAS (`https://doi.org/10.1093/mnras/sty612`)

The nuclear star cluster surrounding the massive black hole at the Galactic Centre consists of young and old stars, with most of the stellar mass in an extended, cuspy distribution of old stars. The compact cluster of young stars was probably born in situ in a massive accretion disc around the black hole (Levin & Beloborodov, 2003). We investigate the effect of the growing gravity of the disc on the orbits of the old stars, using an integrable model of the deformation of a spherical star cluster with anisotropic velocity dispersions.

A formula for the perturbed phase space distribution function is derived using linear theory, and new density and surface density profiles are computed. The cusp undergoes a spheroidal deformation with the flattening increasing strongly at smaller distances from the black hole. The Figure 2a showcases the density deformation (ρ_1) isocontours – ρ_1 is positive close to the equatorial plane of the disc (for $57.37^\circ < \theta < 122.63^\circ$) and negative otherwise. The Figure 2b shows the intrinsic axis ratio of density and surface density (as seen from different lines of sight) isocontours against the major axis; the axis ratio is nearly 0.8 at the distance of 0.15 pc from MBH. Stellar orbits are deformed such that they spend more time near the disc plane and this explains the resultant flattening of the cluster. Linear theory accounts only for orbits whose apsides circulate. The non-linear theory of adiabatic

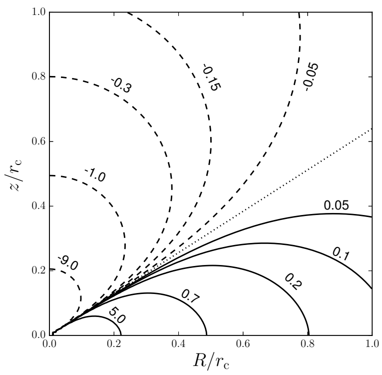

(a) Density Deformation (in units of $10^4 M_\odot/pc^3$)

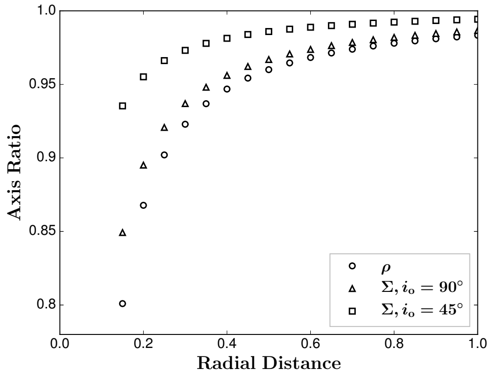

(b) Axis ratio of Density Isocontours

Fig. 2 *Deformation of Star Cluster*:(a). Density deformation (ρ_1)– Solid curves are for $\rho_1 > 0$, and dashed curves are for $\rho_1 < 0$; the dotted straight line at $\theta = 57.37°$ is for $\rho_1 = 0$. Here $r_c = 1$ pc. The structure of deformation implies flattened morphology for deformed cluster. (b). Axis ratios for density (ρ) and surface density (Σ) isocontours, for different line-of-sight inclinations i_0. The distance along the horizontal axis is in parsec.

capture into resonance is needed to understand orbits whose apsides librate. The mechanism is a generic dynamical process, and it may be common in galactic nuclei.

Part II. Resonant Relaxation of Keplerian stellar discs

A. Numerical exploration of the Fokker-Planck equation

Manuscript under preparation

We present a numerical code for the solution of the Fokker-Planck equation, derived by Sridhar & Touma (2017), for razor-thin, axisymmetric, monoenergetic Keplerian stellar discs. The resonant relaxation (RR) current density depends on the behaviour of the distribution function (DF), $f(\ell)$, in its entire domain, $\ell \in [-1, 1]$, where ℓ is the normalized angular momentum of a stellar orbit (as in Part IA). Hence the Fokker-Planck equation is a self-consistent, integral partial differential equation (pde). The RR current is driven by apsidal resonances; for the current at ℓ to be non-zero, there should exist ℓ' such that the corresponding apse precession rates (Ω), satisfy the resonant condition $\Omega(\ell') = \Omega(\ell)$. We employ a "conservative" scheme for discretization of the integral pde. The cumulative DF is interpolated with a cubic spline, providing a smooth continuation of the DF within the grid and ensuring the conservation of norm upto high precision. The apse precession rate for highly eccentricity rings is very small, and completely vanishes when $\ell = 0$. As a result there is in general a region in ℓ-space around $\ell = 0$ for which apsidal resonances do not occur, local currents vanish and hence the DF in the region remains frozen. Due to the presence of this non-resonant region and diffusion of angular momentum outside it, there is an accumulation of mass just near the boundary of the region. The end states turn out to be dynamically stable to non-axisymmetric modes. It is important to check the thermal stability of these states by numerical simulations, which will be pursued in future.

B. Inclusion of gravitational polarization in the Fokker-Planck equation

Manuscript under preparation

The above numerical study of RR of Keplerian axisymmetric discs is based on the Fokker-Planck equation derived by Sridhar & Touma (2017), where the effects of "gravitational polarization" were ignored. Here we derive the first-order polarization corrections to the RR current density. As earlier, it turns out that the polarization current is non-zero only in the presence of apsidal resonances, and hence the net current vanishes in the region of non-resonance. We also present a class of exact, stationary solutions of the Fokker-Planck equation that are not entropy maximizing DFs. Linear dynamical stability (which occurs on the secular timescale) of a subclass of DFs can be demonstrated analytically, and numerically for some other cases. It is not yet clear whether these DFs are also thermally stable (thermal instability occurs over the much longer RR timescale). Further progress requires comparison with numerical simulations and efforts to derive a Fokker-Planck equation for the RR evolution of non-axisymmetric discs.

List of Publications

- Secular instabilities of Keplerian stellar discs

  Karamveer Kaur, Mher V. Kazandjian, S. Sridhar, Jihad R. Touma

  Mon. Not. R. Astron. Soc., Volume 476, Issue 3, 21 May 2018, Pages 4104–4122, `https://doi.org/10.1093/mnras/sty403`

- Deformation of the Galactic Centre stellar cusp due to the gravity of a growing gas disc

  Karamveer Kaur, S. Sridhar

  Mon. Not. R. Astron. Soc., Volume 477, Issue 1, 11 June 2018, Pages 112–126, `https://doi.org/10.1093/mnras/sty612`

- Stalling of Globular Cluster Orbits in Dwarf Galaxies

  Karamveer Kaur, S. Sridhar

  The Astrophysical Journal, Volume 868, Number 2, 3 Dec 2018, Pages 134–152, `https://doi.org/10.3847/1538-4357/aaeacf`

- Manuscript on “Resonant Relaxation of Keplerian Stellar Discs” is in preparation.

List of Figures

List of Tables

Chapter 1

Introduction

Centres of galaxies host extreme astrophysical environments. Accumulation of mass in the deep gravitational potential wells at the galactic centres is thought to lead to the extreme conditions required for the growth of massive black holes (MBHs). MBHs accreting gas and stars are the central engines powering quasars and active galactic nuclei (AGNs) (Rees, 1984; Krolik, 1999). MBHs are also inferred in nearby galaxies by dynamical modelling of stellar kinematics (Kormendy & Richstone, 1995; Kormendy & Ho, 2013). The central MBHs have a wide range of masses $\sim 10^5 - 10^{10}\,M_\odot$. Orbiting the MBHs are densely-packed nuclear star clusters (NSCs), whose dynamics and kinetics is the subject of this thesis.

Characteristics of NSCs: NSCs have stellar densities $\sim 10^3$ times that of globular cluster cores (Böker et al., 2004), making them the most crowded stellar systems in the universe (Walcher et al., 2005; Misgeld & Hilker, 2011; Norris et al., 2014). Their half-light radii are typically of the order 3-5 pc, as revealed by *Hubble Space Telescope* (HST) observational studies (Böker et al., 2002; Georgiev & Böker, 2014). Their stellar masses span a wide range $\sim 10^6 - 10^8$ $M_\odot$(Norris et al., 2014). Owing to multiple episodes of star formation, these systems generally have diverse stellar populations corresponding to different generations of stars (Walcher et al., 2006; Rossa et al., 2006; Seth et al., 2006; Lyubenova et al., 2013). Their metallicities are in general higher than that of globular clusters, which consist of older populations of stars (Walcher et al., 2006; Rossa et al., 2006; Puzia & Sharina, 2008; Paudel et al., 2011). Interestingly, both the central MBHs and NSCs respect certain scaling relations with their host galaxies. These scaling relations are with regard to their masses (Scott & Graham, 2013; Georgiev et al., 2016) and stellar populations or colors (Turner et al., 2012). The relations suggest co-evolution of the combined central MBH - NSC with the host galaxy.

Formation of NSCs: NSCs likely retain a record of the accretion history of the central MBH. As gas falls towards the centre of galaxy, it might form a massive accretion disc about the MBH, which can undergo fragmentation in its outer cool regions forming stars (Levin & Beloborodov, 2003). The compact stellar disc of young stars at the Galactic Centre (see § 1.1.1), and inner compact disc (corresponding to P3; explained later in § 1.1.2) in M31 nucleus are two classic candidates for in situ star formation in NSCs. As a result, some distinct morphological characteristics arise, and the young blue stellar structures are observed to have compact flatter or more oblate geometries, compared to the redder and extended stellar spheroids composed of older generation of stars (Seth et al., 2006; Carson et al., 2015). Recurrent gas inflow and star formation events (Bekki et al., 2006; Bekki, 2007; Antonini et al., 2015) lead to multiple stellar populations. The studies of NSCs to reconstruct the complex star formation history, also help to probe the formation and growth of central MBH. Other competing mechanism of formation of these star clusters can be infalling star clusters (formed in the outer regions) due to dynamical friction, leading to their merger adding to the NSC (Tremaine et al., 1975; Capuzzo-Dolcetta, 1993; Capuzzo-Dolcetta & Miocchi, 2008a,b; Agarwal & Milosavljević, 2011; Antonini, 2013; Gnedin et al., 2014; Arca-Sedda & Capuzzo-Dolcetta, 2014). It is believed that both these scenarios can occur and contribute to the growth of NSCs (Hartmann et al., 2011; Neumayer et al., 2011; Turner et al., 2012; De Lorenzi et al., 2013; Feldmeier et al., 2014; den Brok et al., 2014; Antonini et al., 2015). Also, there is the hybrid scenario of infalling and merging of gas-rich clusters (Guillard et al., 2016).

Co-existence of MBHs and NSCs: The exploration of a sample of nearby galaxies by Neumayer & Walcher (2012) suggests that the massive galaxies with total stellar mass $\gtrsim 10^{12}$ $M_\odot$ have tendencies to host only MBH at their centres, while smaller galaxies with total stellar mass $\lesssim 10^{10}$ $M_\odot$ generally host only NSCs. The intermediate stellar mass range $10^{10} - 10^{12}$ $M_\odot$ galaxies tend to contain NSC with MBH at their centre. In this thesis, we focus on the stellar dynamics of an NSC within the radius of influence of its central MBH. Orbital structure, overall cluster morphology, gravitational instabilities, and collisional evolution resulting in orbital relaxation – form the main part of the subject-matter presented. The morphology controls the gas and stellar dynamics in the region and hence, the feeding of the central MBH. Relaxation effects due to "stellar collisions" are important to understand the mutual angular momentum exchanges, and can be the key to interpret the tidal disruption event (TDE) rates (Rauch & Tremaine, 1996; Rauch & Ingalls, 1996; Madigan et al., 2018; Wernke & Madigan, 2019) and stellar feeding of MBH (Bahcall & Wolf, 1976; Hopman & Alexander, 2006a,b). Many relativistic dynamical studies predict the event rates of stellar binary black hole (BBH) mergers and extreme-mass ratio inspirals (EMRIs), leading to gravitational wave emission detectable by aLIGO[1] and LISA[2] (Kupi et al., 2010; Merritt et al., 2011; Bar-Or & Alexander, 2016; Stone et al., 2017; Hamers et al., 2018).

Stellar Dynamics in the vicinity of an MBH: The earliest studies of stellar dynamics investigated feeding of stars to an MBH through two-body relaxation and proposed the formation of cuspy stellar density profile around the central MBH (Bahcall & Wolf, 1976; Cohn & Kulsrud, 1978). Young (1980) studied the collisionless formation of a stellar cusp due to the adiabatic growth of the MBH. Goodman & Binney (1984) explored changes in stellar orbital distribution as a result of the growth of the MBH. The studies by Gerhard & Binney (1985) demonstrated the destruction of box orbits in the inner parts of a triaxial galaxy hosting an MBH. The detailed photometric and kinematic observations of galaxy centres by state of the art telescopes (*Very Large Telescope* (VLT), *Keck Telescope*, HST) have resolved the region of influence of central MBH for some nearby galaxies (the Galaxy and M31). The double nucleus of M31 (Lauer et al., 1993) was explained as a lopsided eccentric disc of stars on aligned Keplerian orbits about a central MBH by Tremaine (1995). Rauch & Tremaine (1996) proposed the phenomenon of resonant relaxation driving the collisional evolution of stellar system surrounding MBH. These two pioneering works ushered an era of numerical studies on dynamics and statistical mechanics of stellar systems within the region of influence of an MBH. Sridhar & Touma (2016a,b) (henceforth ST16a,b) provided a theoretical framework for both the collisionless and collisional evolution of NSCs. This thesis consists of some of the first applications of ST16a,b.

In this chapter, we discuss the motivations and basic theoretical framework for the work presented in later chapters. In § 1.1, we describe some interesting features of the two nearest NSCs belonging to the Galaxy and M31. In § 1.2, the secular or long-term dynamics of a star cluster within the region of influence of central MBH, is introduced. § 1.3 and § 1.4 summarize the collisionless and collisional secular dynamics respectively, and the formalism of ST16a,b. The structure of the thesis is outlined in § 1.5.

1.1 Nearby Nuclear Star Clusters

The thesis investigates stellar dynamics of an NSC orbiting an MBH, in the region where gravitational potential of the MBH dominates. Unfortunately these compact

[1] Advanced Laser Interferometer Gravitational-Wave Observatory
[2] Laser Interferometer Space Antenna

regions are not yet resolved by even the present biggest telescopes for most of the galactic nuclei. Here, we discuss the characteristics of the two nearest NSCs for which the region of influence of MBH is well-resolved.

1.1.1 Milky Way NSC

The Galactic centre source Sgr A* is thought to be an MBH with mass of about 4×10^6 M$_\odot$. This is surrounded by an NSC of 2.5×10^7 M$_\odot$ with a half-light radius of about 4 pc, consisting of late-type (old, $>$ 1 Gyr) stars (Genzel et al., 2010; Schödel et al., 2014; Boehle et al., 2016; Gillessen et al., 2017). There also exists a less massive cluster of early-type (young, $<$ 10 Myr) stars within $\sim$ 0.5 pc (Buchholz et al., 2009; Do et al., 2009; Bartko et al., 2010; Fritz et al., 2016). Recent work has refined our knowledge of the distribution of the old stars (Gallego-Cano et al., 2018; Schödel et al., 2018). Within about 3 pc of the MBH the density profile of resolved faint stars and sub-giants and dwarfs (inferred from diffuse light) is cuspy, and well-described by a single power-law. But red clump and brighter giant stars have a similar cuspy profile only beyond a projected radius of about 0.3 pc, inside which they display a core-like surface density profile.

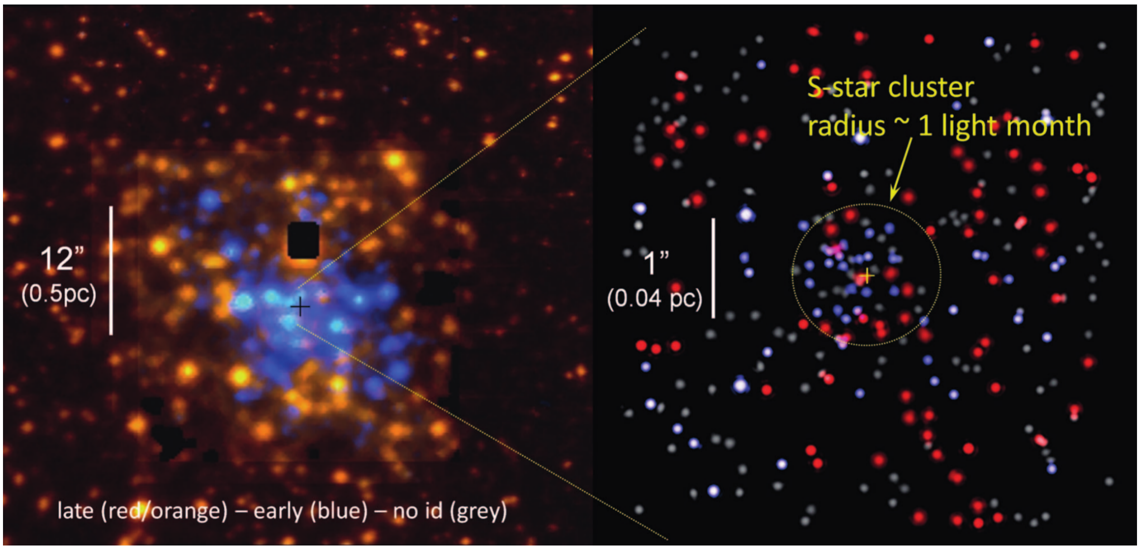

Fig. 1.1 *Galactic NSC:* Stellar distribution within [Left] $\sim$ 1 pc and [Right] $\sim$ 0.08 pc distance from MBH (denoted by a “+”). Early-type stars are shown in blue, while late-type stars are in red. The circle on the right encloses S-star cluster. [Figure from Genzel et al. (2010)]

There are about 200 young stars in a compact cluster of size $\lesssim$ 0.5 pc around the MBH, including WR stars, O, B type main sequence stars, giants and supergiants (Allen et al., 1990; Krabbe et al., 1991; Ghez et al., 2003; Paumard et al., 2006; Bartko et al., 2010; Do et al., 2013). Stellar orbits have a range of eccentricities, inclinations and orientations, with about 20% in a clockwise disc that extends between about $0.03 - 0.13$ pc, with mean eccentricity ~ 0.3 (Yelda et al., 2014). Outside ~ 0.13 pc, the orbital planes are much more scattered. It has been suggested that the young stars were probably born in situ in a starburst event in a massive, fragmenting accretion disc around the MBH (Levin & Beloborodov, 2003).

The distribution of O/WR stars of the young stellar disc has a sharp cut-off at ~ 0.03 pc ($\sim 1''$). But, the distribution of B-type stars continues further inside this radius, and is called the S-star cluster. There are nearly 40 stars within the central arcsecond, whose orbitals parameters have been determined, and employed to further constrain the MBH mass and its distance from the sun (Gillessen et al., 2017). Spectroscopic studies give the ages of the B-type stars to be within 6-400 Myr (Eisenhauer et al., 2005; Genzel et al., 2010). Their orbital structure has been constrained by various studies (Schödel et al., 2003; Eisenhauer et al., 2005; Ghez et al., 2005; Gillessen et al., 2009, 2017). The orbital planes are nearly isotropically distributed, and eccentricity distribution favours high eccentricity orbits. The timescales of two-body relaxation are too long in the region, and cannot explain this apparently relaxed orbital distribution of young stars. Many studies (Perets & Gualandris, 2010; Madigan et al., 2011; Antonini & Merritt, 2013; Hamers et al., 2014) have tried to understand the orbital distribution of S-stars as arising from the more efficient secular mechanism of resonant relaxation (Rauch & Tremaine, 1996), discussed in the § 1.2.

1.1.2 M31 NSC

Observations from balloon–borne telescope Stratoscope II (Light et al., 1974) first revealed the asymmetric nucleus of M31, with its off-centred peak brightness. Then HST photometric observations (V and I band) by Lauer et al. (1993) showed a double-nucleus with two distinct peaks in surface brightness images. The brighter peak P1 is ~ 2 pc away from the fainter one named P2, which nearly coincides with the centre of the host bulge. Ultraviolet excess detected in the vicinity of P2 suggested the presence of an MBH (Dressler & Richstone, 1988; Kormendy, 1988; King et al., 1995). Later, HST spectroscopy (Lauer et al., 1998) resolved a peak P3 shining in ultraviolet, embedded within the P2 region (on the side of P1 along the line joining P1 and P2). This compact feature was modelled as a compact rotating disc of young massive A-type stars about a central MBH of mass $\sim 1.4 \times 10^8$ $M_\odot$ (Bender et al., 2005).

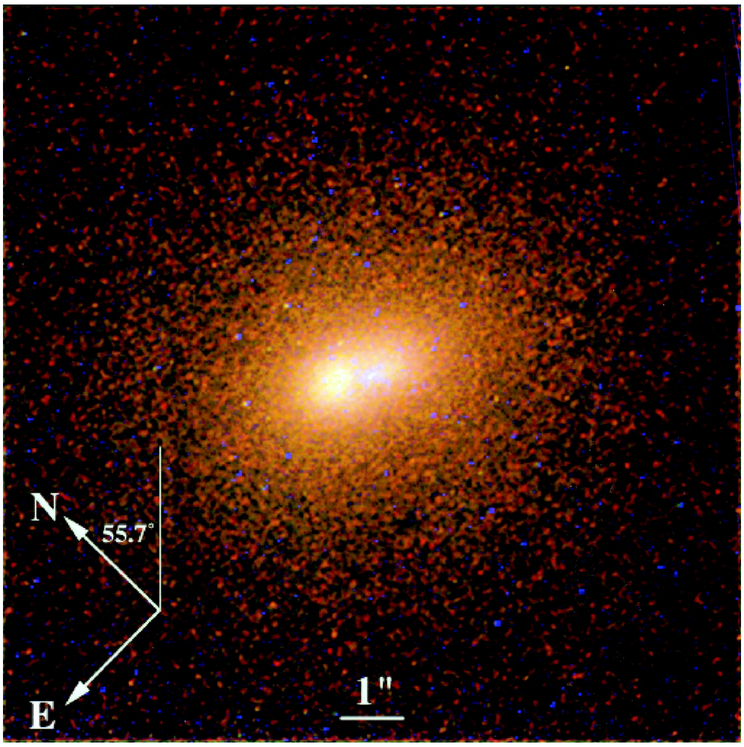

Fig. 1.2 *Triple nucleus of M31:* P1-P2 double nucleus made up of relatively old stars (mainly in V and I bands) is shown in orange; P3 composed of young stars appears as a central peak in U band shown in blue. The figure shows the central $11''.65 \times 11''.65$ square of the M31 nucleus. [Figure from Lauer et al. (1998)]

Tremaine (1995) interpreted the P1-P2 double nucleus as an eccentric disc of K-type stars (Lauer et al., 1993, 1998) moving on nearly Keplerian elliptical orbits whose apsides are closely aligned in direction. The stars orbiting Keplerian ellipses move slowly near their apoapses and hence, the bright off-centred peak P1 can be interpreted as the location of the apoapses of stellar orbits. The fainter P2 is probably close to the periapses of the elliptical orbits where the stellar velocities are highest. The spectroscopic studies of Bender et al. (2005) also lend further support to the eccentric disc model. The velocity dispersion peak lies in the P2 region (opposite to side of P1) indicative of the location of periapses. The rotation curve (Dressler & Richstone, 1988; Kormendy, 1988; Bacon et al., 1994; van der Marel et al., 1994; Bender et al., 2005) is nearly symmetric about P2, indicating the close-proximity of P2 to the dynamical centre of the nucleus.

The triple nucleus of M31 hosts two nested discs – (a). the inner circular disc corresponding to P3 lying within ~ 0.8 pc, (b). the outer lopsided disc corresponding to P1-P2 extending to roughly 8 pc. The discs are nearly coplanar and orbit the MBH in the same sense (Bender et al., 2005). A kinematic axisymmetric disc model of inner disc of young stars gave an MBH mass $\sim 1.4 \times 10^8$ $M_\odot$ (Bender et al., 2005). The discovery of the intriguing lopsided double nucleus P1-P2 by Lauer et al. (1993)

and the subsequent eccentric disc model of Tremaine (1995), initiated an era of stellar dynamical studies in the vicinity of MBH. Many extensions of the eccentric disc model were explored and lopsided dynamical equilibria were constructed (Statler, 1999; Bacon et al., 2001; Salow & Statler, 2001, 2004; Sambhus & Sridhar, 2002; Peiris & Tremaine, 2003; Brown & Magorrian, 2013). Kazandjian & Touma (2013) gave a model for self-consistent stellar dynamical origin of the double nucleus. They simulated linearly unstable counter-rotating stellar discs, and studied the growth and evolution of instabilities. After the initial growth of a lopsided $m = 1$ mode (where m is the azimuthal wavenumber), there is non-linear evolution saturating to a massive lopsided uniformly precessing disc, embedded in a triaxial star cluster. These models qualitatively resemble both photometric and kinematic features of the M31 nucleus. The authors proposed mergers of stellar nucleus with counter-rotating star clusters (infalling from outer regions due to dynamical friction) as a possible origin mechanism for the double nucleus.

Note that there exist some nearby galaxies which are observed to host lopsided nuclei (Lauer et al., 1996, 2005; Gültekin et al., 2011) similar to M31. Lauer et al. (2005) observed a sample of 65 early-type galaxies and $\sim 20\%$ of them, have observational features consistent with lopsided galactic nuclei.

1.2 Secular Dynamics of Keplerian Star Clusters

We consider an NSC of mass M orbiting an MBH of mass $M_\bullet \gg M$. The cluster consists of $N_\star \gg 1$ stars, whose dynamics is governed by the combined gravitational field of the MBH, other stars in the NSC and massive external perturbers (if present). Within the radius of influence $r_{\rm in}$ of the MBH (Binney & Tremaine, 2008), the Keplerian potential dominates, because the regions of interest are far outside the Schwarzschild radius $r_\bullet = 2GM_\bullet/c^2$, and hence general relativistic effects can be neglected. Hence, these systems can be termed as *Keplerian* star clusters within the spatial domain defined by $r_\bullet \ll r \leqslant r_{\rm in}$.

The orbits of the constituent stars of the Keplerian star cluster would be closed-orbit confocal Keplerian ellipses, if the weaker gravitational potential of the star cluster (and also other possible perturbers) is entirely neglected. As a result of the weak gravitational forces due to cluster's self-gravity and external perturbing masses (and possibly weak general relativistic effects), these Keplerian elliptical orbits deform and precess over timescales much longer than Keplerian orbital period. This long-term or slow dynamics of Keplerian elliptical orbits of the Keplerian star cluster is termed *secular dynamics*.

In order to eliminate the fast Keplerian motion, the dynamics is averaged over the fast Keplerian orbital phase. This method comes from Gauss in the field of planetary dynamics, and hence is called *Gauss averaging* (Murray & Dermott, 1999). This is mathematically implemented by averaging the system Hamiltonian over the fast Keplerian phase as discussed in § 1.2.3. The corresponding physical picture implies that a star (point mass) is spread over its Keplerian elliptical orbit such that resulting linear mass density is inversely proportional to the local Keplerian velocity. The resultant elliptical rings, called as *Gaussian Rings*, precess and deform over secular timescales that are longer than Kepler orbital times. A well known property of the secular dynamics is the conservation of the semi-major axes of Gaussian Rings, while they undergo secular precession and deformation. Gauss averaging leads to reduced dynamics, because one of variables (i.e. the fast Keplerian orbital phase) is averaged over and hence, disappears from the problem.

In the averaged dynamics, the system can be considered to be made up of $N_\star$ Gaussian Rings (instead of point mass stars). The mass ratio $\epsilon = M/M_\bullet \ll 1$ is the natural small parameter of the problem. The Keplerian orbital times $T_{\mathrm{Kep}} = 2\pi\sqrt{a^3/(GM_\bullet)}$ corresponding to a Gaussian Ring of semi-major axis a. In the *collisionless* limit of dynamics, the Ring precession due to the mean-gravitational potential of the cluster, occurs over long secular timescale $T_{\mathrm{sec}} \sim T_{\mathrm{Kep}}/\epsilon$ (Sridhar & Touma, 1999, 2016a). The *collisional* effects of granularity of the system and stochastic interactions among discrete Gaussian Rings become significant over still longer times. Rauch & Tremaine (1996) (hereafter called RT96) proposed the collisional mechanism of resonant relaxation (RR) which leads to the relaxation of the angular momentum distribution of the system over the RR timescale $T_{\mathrm{res}} \sim N_\star T_{\mathrm{sec}}$ (RT96, ST16b). These two limits of secular dynamics are discussed further in the § 1.3 and § 1.4.

Secular dynamics occurs in five-dimensional (three-dimensional) Ring phase space for Keplerian star cluster of general morphology (planar disc structure). The Ring space variables are discussed below along the lines of ST16a.

1.2.1 Ring Space Variables

Three-Dimensional System: Let $\boldsymbol{r}$ and $\boldsymbol{u}$ be the relative position and velocity of a star with respect to (wrt) the central MBH. Instead of the physical space variables $\{\boldsymbol{r}, \boldsymbol{u}\}$, the dynamics of Keplerian stellar system assumes its simplest form in the *Delaunay variables*, which are a set of action angle variables for the exact Keplerian potential. Since the Keplerian stellar system is a perturbed Kepler problem, it is

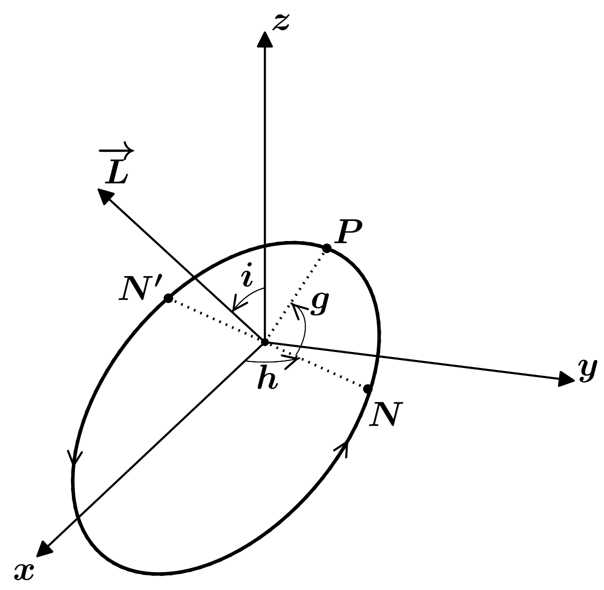

Fig. 1.3 *Orbital elements of a Gaussian Ring in three-dimensions:* The orbital motion of star is in anti-clockwise sense about the MBH located at the origin. N and N' are the ascending and descending nodes; P is periapse of the Ring.

more physically illuminating to use the Delaunay variables, which can be expressed simply in terms of the physical orbital elements $\{a,\, e,\, i,\, w,\, g,\, h\}$ of a star orbiting along a Gaussian Ring. Here a is the semi-major axis of the Ring, with e eccentricity, and i inclination of its orbital plane wrt the reference xy-plane. h is the longitude of ascending node wrt reference x-axis, and g is the argument of periapse wrt the ascending node. Here i and h fix the orbital plane of the Ring, while g measures the orientation of the Ring in the orbital plane itself. These orbital elements are shown in Figure 1.3. The mean anomaly $w = \Omega_{\rm kep}\, t_{\rm p}$ measures the fast Keplerian phase covered in the time $t_{\rm p}$ elapsed since periapse passage of the star (orbiting along the Ring), where $\Omega_{\rm kep} = \sqrt{GM_\bullet/a^3}$ is the Keplerian orbital frequency.

Below we give the *three-dimensional* Delaunay Variables explicitly in terms of these physical variables (Plummer, 1960; Murray & Dermott, 1999; Binney & Tremaine, 2008):

$$I = \sqrt{GM_\bullet a} \quad , \qquad w \tag{1.1a}$$
$$L = I\sqrt{1-e^2} \quad , \qquad g \tag{1.1b}$$
$$L_z = L\cos i \quad , \qquad h\,. \tag{1.1c}$$

On the left side $\{I,\, L,\, L_z\}$ are the actions and on the right side $\{w,\, g,\, h\}$ are their conjugate angles. I is a measure of the Keplerian energy of a Ring $E_{\rm Kep} =$

$-GM_\bullet/(2\,a) = -(GM_\bullet)^2/(2\,I^2)$, L is the magnitude of angular momentum and L_z is the z-component of angular momentum of the Ring. Since the fast Keplerian phase w is averaged over in secular dynamics, the Ring space is five-dimensional with the Ring variables $\mathcal{R} \equiv \{I, L, L_z, g, h\}$ for systems with general morphology. The motion of a Ring is confined to the four-dimensional subspace, I = constant. But this motion is governed by the gravitational attraction of Rings of different I.

Two-Dimensional System: A planar Keplerian stellar system is composed of Gaussian Rings lying in the xy-plane (say). It requires only four orbital elements $\{a,\ e,\ w,\ g\}$ to specify the full dynamical state of a star. Three of these elements a , e and w have the same physical meaning as in the three-dimensional case. But g now refers to the longitude of periapse wrt to the reference x-axis. These orbital elements are shown in Figure 1.4. The *two-dimensional* version of the Delaunay Variables (ST16a) is given as:

$$I = \sqrt{GM_\bullet a} \quad , \qquad w \tag{1.2a}$$

$$L = \sigma I \sqrt{1-e^2} \ , \qquad g \tag{1.2b}$$

where $\sigma = 1\,(-1)$ for anti-clockwise (clockwise) orbital motion of the star about the MBH. Here L is the angular momentum of a Ring which, unlike the three dimensional case, can be positive or negative. For planar discs, the Ring space is three-dimensional with the Ring variables $\mathcal{R} \equiv \{I, L, g\}$, and motion of a Ring is confined to the two-dimensional, I = constant, surface.

1.2.2 Transformation to Delaunay Variables

The first step of Gauss averaging is the representation of the physical space variables $\{\boldsymbol{r}, \boldsymbol{u}\}$ in terms of the Delaunay variables.

Three-Dimensional System: The position vector $\boldsymbol{r} = (x,\ y,\ z)$ can be expressed in terms of the orbital elements as (Plummer, 1960; Murray & Dermott, 1999; Sambhus & Sridhar, 2000):

$$\begin{pmatrix} x \\ y \\ z \end{pmatrix} = \begin{pmatrix} C_g C_h - C_i S_h S_g & -S_g C_h - C_i S_h C_g & S_i S_h \\ C_g S_h + C_i C_h S_g & -S_g S_h + C_i C_h C_g & -S_i C_h \\ S_i S_g & S_i C_g & C_i \end{pmatrix} \begin{pmatrix} a(C_\eta - e) \\ a\sqrt{1-e^2}\ S_\eta \\ 0 \end{pmatrix} \tag{1.3}$$

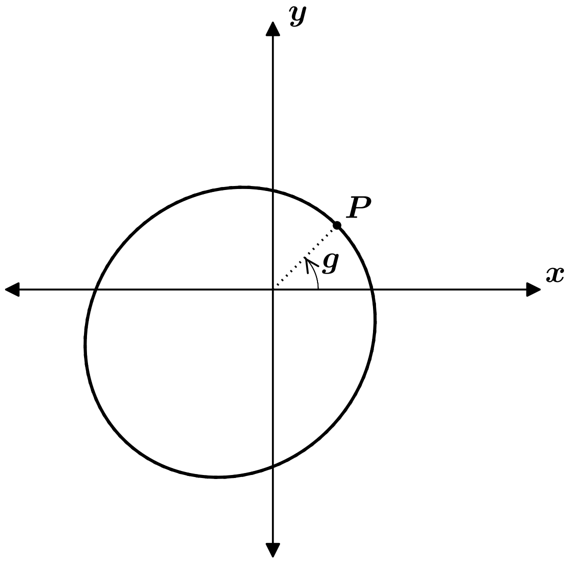

Fig. 1.4 *Orbital elements for a Gaussian Ring in two-dimensions:* P represents the periapse of Keplerian orbit of a star around the MBH (located at origin).

where $S \equiv$ sine and $C \equiv$ cosine of the angles given as subscripts. Here η is the eccentric anomaly and is related to the mean anomaly by $w = (\eta - e \sin \eta)$. The eccentricity $e = \sqrt{1 - L^2/I^2}$ and inclination $i = \cos^{-1}(L_z/L)$. The radial distance from the MBH is $r = \sqrt{x^2 + y^2 + z^2} = a(1 - e \cos \eta)$. The velocity vector $\boldsymbol{u}$ can be expressed in terms of Delaunay variables by using the definitions of the action variables:

$$I = \frac{GM_\bullet}{\sqrt{-2\,E_{\rm kep}}} = GM_\bullet \left[\frac{2\,GM_\bullet}{r} - u^2\right]^{-1/2} \tag{1.4a}$$

$$L = |\boldsymbol{r} \times \boldsymbol{u}| \tag{1.4b}$$

$$L_z = (\boldsymbol{r} \times \boldsymbol{u}) \cdot \hat{z} \quad . \tag{1.4c}$$

Two-Dimensional System: The position vector $\boldsymbol{r} = (x,\, y)$ for a planar system can be expressed as (ST16a):

$$x \;=\; a\,(C_\eta - e)\,C_g - \sigma\,a\,\sqrt{1-e^2}\,S_\eta\,S_g \tag{1.5a}$$

$$y \;=\; a\,(C_\eta - e)\,S_g + \sigma\,a\,\sqrt{1-e^2}\,S_\eta\,C_g \tag{1.5b}$$

where $\sigma = \mathrm{Sign}(L)$ and is positive (negative) for the anti-clockwise (clockwise) circulation of star along the Ring as defined earlier. Here g is the longitude of periapse measured from the reference x-axis in a counter-clockwise sense. The velocity vector $\boldsymbol{u}$ is again given by the definitions of two-dimensional Delaunay actions:

$$I = \frac{GM_{\bullet}}{\sqrt{-2\,E_{\mathrm{Kep}}}} = GM_{\bullet}\left[\frac{2\,GM_{\bullet}}{r} - u^2\right]^{-1/2} \tag{1.6a}$$

$$L = (\boldsymbol{r}\times\boldsymbol{u})\cdot\hat{z} \quad . \tag{1.6b}$$

After expressing the system Hamiltonian in terms of Delaunay variables using the suitable transformations given above, the averaging over the fast Keplerian phase w is done, as illustrated below for a test Ring.

1.2.3 Introducing Averaged Dynamics

Here we demonstrate the method of Gauss averaging for the dynamics of a test Gaussian Ring evolving under the gravity of a Keplerian stellar system of general morphology.

The Hamiltonian $H_{\mathrm{Re}}(\boldsymbol{r},\boldsymbol{u})$ for the corresponding test star in six-dimensional real phase space $\{\boldsymbol{r},\boldsymbol{u}\}$ is:

$$H_{\mathrm{Re}}(\boldsymbol{r},\boldsymbol{u}) = \frac{u^2}{2} - \frac{GM_{\bullet}}{r} + \Phi_{\mathrm{Re}}(\boldsymbol{r}) \tag{1.7}$$

where Φ_{Re} is the sum of the cluster potential and the tidal potential of a static massive external perturber. The first step is the canonical transformation to Delaunay variables. Using the equation (1.4), the first two terms reduce to the Kepler Energy $E_{\mathrm{Kep}} = -GM_{\bullet}/(2\,a) = -(GM_{\bullet})^2/(2\,I^2)$ which is a function of only the action I. The third term Φ_{Re} can be expressed as a function of all six Delaunay variables $\{I, L, L_z, w, g, h\}$ using the equation (1.3). Then we average the Hamiltonian wrt the fast orbital phase w giving the orbit-averaged Hamiltonian:

$$\begin{aligned} \overline{H}(\mathcal{R}) &= \oint \frac{\mathrm{d}w}{2\pi}\, H_{\mathrm{Re}} = -\frac{1}{2}\left(\frac{GM_{\bullet}}{I}\right)^2 + \overline{\Phi}(\mathcal{R}) \\ \text{where} \quad \overline{\Phi}(\mathcal{R}) &= \oint \frac{\mathrm{d}w}{2\pi}\, \Phi_{\mathrm{Re}}(\boldsymbol{r})\,. \end{aligned} \tag{1.8}$$

Since the averaged Hamiltonian $\overline{H}$ is independent of the fast angle w, the conjugate action I is conserved. Therefore, the first term representing the Keplerian energy is constant, and can be dropped from the Hamiltonian. Then the Hamiltonian reduces to $\overline{H} \equiv \overline{\Phi}$. Hence, the Gaussian Ring evolves under the orbit-averaged gravitational potential of the star cluster (and possible external perturbers). The Hamiltonian equations of motion for averaged/secular dynamics are:

$$I \;=\; \sqrt{GM_\bullet a} \;=\; \text{constant}\,, \tag{1.9a}$$

$$\frac{\mathrm{d}L}{\mathrm{d}t} \;=\; -\frac{\partial \overline{H}}{\partial g}\;, \qquad \frac{\mathrm{d}g}{\mathrm{d}t} \;=\; \frac{\partial \overline{H}}{\partial L}\,, \tag{1.9b}$$

$$\frac{\mathrm{d}L_z}{\mathrm{d}t} \;=\; -\frac{\partial \overline{H}}{\partial h}\;, \qquad \frac{\mathrm{d}h}{\mathrm{d}t} \;=\; \frac{\partial \overline{H}}{\partial L_z}\,. \tag{1.9c}$$

A Gaussian Ring precesses changing its orientation in space due to evolving variables $\{L_z, h, g\}$, and deforms due to evolving eccentricity $e = \sqrt{1 - L^2/I^2}$, while its semi-major axis a remains constant. Sridhar & Touma (1999) employed Gauss averaging for secular dynamics of Keplerian star clusters and explored the nature of the more ordered dynamics of stellar orbits within the radius of influence of the MBH. The problem acquires greater complexity when the collective self-gravitational response of the NSC is taken into account.

1.3 Secular Collisionless Dynamics

In the collisionless limit, the stellar system is approximated as a smooth mass distribution, composed of an infinite number of Gaussian Rings, each of infinitesimal mass, i.e. $N_\star \to \infty$ and $m_\star \to 0$, such that the total stellar mass $M = N_\star m_\star$ remains constant. The Rings precess and deform under the effect of the mean gravitational potential of the cluster arising from the smooth mass distribution. This collisionless behaviour appears as a continuous precession and deformation of Rings over the secular time $T_{\text{sec}} = T_{\text{Kep}}/\epsilon$; $\epsilon = M/M_\bullet$ being the small parameter as defined earlier in § 1.2.

The double nucleus of M31 discovered by Lauer et al. (1993) was interpreted by Tremaine (1995) as an eccentric disc of stars moving on aligned Keplerian orbital ellipses. The pioneering idea led to further detailed numerical modelling of M31 lopsided nucleus as an asymmetric Keplerian stellar disc in several later works described in § 1.1. Secular orbital dynamics, linear collisionless instabilities, non-linear collisionless evolution or violent relaxation, mode excitation by external masses were the main lines of enquiry over the next three decades.

1.3.1 Development of Secular Collisionless Dynamics

Orbital dynamics: Sridhar & Touma (1997a,b); Merritt & Valluri (1999) worked out stellar orbits for galactic-type potentials with a central MBH. Motivated by the lopsided nuclei of M31 and NGC 4486B, Sridhar & Touma (1999) studied a family of planar, non-axisymmetric potentials, and their orbital structure. They identified two orbital families – lenses with librating Gaussian Rings and loops with circulating Rings – for lopsided Keplerian discs. They also found a family of loop orbits which are lopsided in the sense of the disc potential. The work explicitly displayed the underlying ordering of dynamics in the region of influence of the MBH and emphasized the importance of the secular conservation of a. The orbital structure for three-dimensional Keplerian stellar systems with triaxial morphology were explored by Sambhus & Sridhar (2000), Poon & Merritt (2001) and Merritt & Vasiliev (2011). A family of centrophilic orbits was recognized, which could bring stars close to the MBH. Merritt (2013) provides a review for these studies. It also gives an account on general relativistic precession due to MBH in the post-Newtonian limit.

Collisionless equilibria and linear stability: The simplest dynamical modelling of NSCs deals with the construction of stable collisionless equilibria. The steady state distribution functions (DFs) satisfying the criterion of stability to small perturbations are constructed. The long-range nature of gravity complicates the analysis for even simple morphologies giving integro-differential equations. The stability studies are mainly confined to the two-dimensional Keplerian discs and spherical Keplerian star clusters.

Sridhar et al. (1999) studied the secular lopsided $m = 1$ mode of a dynamically cold Keplerian stellar disc, employing Laplace-Lagrange theory (Murray & Dermott, 1999) which is historically used mainly in planetary context. Lee & Goodman (1999) explored non-linear $m = 1$ single-armed stationary spiral density waves in Keplerian gaseous discs. They derived dispersion relation, angular momentum flux and propagation velocity in the tight-winding limit by employing variational methods. Tremaine (2001) recognized that the Laplace-Lagrange theory used by Sridhar et al. (1999) is valid only for discs with no orbit crossing. He formulated a generic approach to linear modes, and showed that stellar discs were stable to $m = 1$ lopsided modes in the Wentzel-Kramers-Brillouin (WKB) limit; an integral eigenvalue problem for a 'softened gravity' disc was also solved to determine linear secular modes. Jalali & Tremaine (2012) studied the linear perturbations of Keplerian discs, and solved the linearized collisionless Boltzmann equation (CBE) and Poisson's equation to find eigen-frequencies and shapes of modes. The $m = 1$ and $m = 2$ emerged as the two prominent secular modes. They illustrated the excitation of secular modes due to the fly-by of a massive perturber.

Touma (2002) derived the Laplace-Lagrange theory for softened gravity discs, and showed that a small fraction of counter-rotating stars is sufficient to make an axisymmetric Keplerian disc linearly unstable to $m = 1$ modes. He also proposed that the merger of a counter-rotating cluster with the NSC as a possible origin mechanism for M31 lopsided nucleus. The study also confirmed the stability of prograde systems in agreement with previous results. Sambhus & Sridhar (2002) showed that some fraction of stars should be on counter-rotating orbits to explain the observed properties of the M31 nucleus.

Tremaine (2005) investigated the secular stability of non-rotating spherical Keplerian star clusters and razor-thin axisymmetric discs. He found that DFs which are decreasing function of angular momentum magnitude are stable. For the DFs which are increasing function of angular momentum magnitude and have an empty loss cone, all spherical systems are only neutrally stable and razor-thin discs are generally unstable to lopsided $m = 1$ instability. These discs are non-rotating and have DFs which are even functions of the angular momentum, which means equal fractions of prograde and retrograde stars. The instability result was proved using the Goodman (1988) variational principle. Polyachenko et al. (2007) studied the monoenergetic (i.e. all Rings with equal semi-major axes) Keplerian star clusters composed of nearly radial orbits. The authors showed the existence of loss-cone instabilities given the retrograde apse precession (opposite to fast Keplerian orbital motion) of Rings in the system. Spherical systems, with DFs as non-monotonic functions of angular momentum, turned out to be unstable for spherical harmonics $l \geq 3$. Discs with a fraction of counter-rotating stars were found to be unstable to all azimuthal wave-numbers m. Sridhar & Saini (2010) investigated $m = 1$ secular instability for dynamically hot counter-rotating softened gravity discs. The linear modes were analyzed in the WKB limit, and precession frequencies and growth rates were explicitly computed. They constructed global modes for non-rotating discs, with equal fractions of counter-rotating stars. The study was generalized by Gulati et al. (2012), who studied global modes by solving the integral eigenvalue problem for these discs, and calculated precession frequencies and growth rates.

Non-linear evolution: Bacon et al. (2001) performed N-body simulations for long-lived and uniformly precessing $m = 1$ modes in a thin Keplerian stellar disc. They constructed collisionlessly relaxed end states, which resemble the observed lopsided surface density profile and asymmetric mean velocity profile for M31 nucleus. Jacobs & Sellwood (2001) also constructed long-lived non-linear $m = 1$ lopsided modes in annular stellar discs by numerical simulations. Touma et al. (2009) applied the algorithm proposed by Gauss to construct a numerical code for solving the secular evolution of a finite number of interacting Gaussian Rings by softened gravity. They demonstrated the growth of unstable $m = 1$ mode for counter-rotating Keplerian discs, followed by non-linear evolution to a uniformly precessing lopsided collisionless equilibrium. Touma & Sridhar (2012) used a two-population secular collisionless Boltzmann equation to study the non-linear evolution of the counter-rotating instability. They also explored the resultant uniformly precessing lopsided configurations for their stability properties. Kazandjian & Touma (2013) performed N-body simulations of counter-rotating axisymmetric thick discs, and demonstrated collisionless relaxation to a lopsided massive disc embedded in a less massive and diffuse triaxial cluster. The three-dimensional final state was found to be consistent with the observed kinematic features of the M31 double nucleus.

ST16a formulated a general theory of non-linear secular evolution, by orbit averaging the CBE over the fast Keplerian orbital phase using the method of multiple timescales (Bender & Orszag, 1978). The NSC is described by a DF in the (reduced) five-dimensional Ring phase space, and its evolution is described by a secular CBE which includes the orbit-averaged effects of self-gravitational cluster potential, an external gravitational potential and general relativistic effects due to MBH upto 1.5 post-Newtonian order. Linear perturbation theory was formulated to study the secular stability of Keplerian star clusters. They also constructed some simple collisionless dynamical equilibria by employing a secular version of Jean's Theorem and discussed their basic physical characteristics. They analyzed the linear secular stability of some simple DFs for spherical clusters and razor-thin axisymmetric discs. They found that the axisymmetric discs with DFs as monotonic function of angular momentum, are linearly stable to all secular modes.

The collisionless studies included in Part I of the thesis, employ the formulation given by ST16a, which is described below.

1.3.2 Secular Collisionless Theory

The Ring space for a general Keplerian stellar system is five-dimensional, with coordinates $\mathcal{R} \equiv \{I;\, L,\, L_z,\, g,\, h\}$. For a discussion on two-dimensional Keplerian stellar discs, refer to § 2.1 of Chapter 2. Here we discuss the general three-dimensional case.

For secular studies, it is natural to define a slow time variable $\tau = \epsilon \times$ time. For a given τ, the state of a Gaussian Ring is specified by the Ring variables $\mathcal{R}$. Each of the $N_\star \to \infty$ Rings of the system is represented as a point $\mathcal{R}$ in the five-dimensional Ring space. The mass distribution of Rings is described by a single-Ring probability DF $F(\mathcal{R},\, \tau) = F(I;\, L,\, L_z,\, g,\, h,\, \tau)$ which is normalized as:

$$\int \mathrm{d}\mathcal{R}\, F(\mathcal{R},\, \tau) = \int \mathrm{d}I\, \mathrm{d}L\, \mathrm{d}L_z\, \mathrm{d}g\, \mathrm{d}h\; F(I;\, L,\, L_z,\, g,\, h,\, \tau) = 1\ . \tag{1.10}$$

A Gaussian Ring $\mathcal{R}(\tau)$ evolves under the orbit-averaged secular Hamiltonian, $H(\mathcal{R},\, \tau) = \Phi(\mathcal{R},\, \tau) + \Phi_{\mathrm{ext}}(\mathcal{R},\, \tau)$. Here the Ring potential $\Phi(\mathcal{R},\, \tau)$ due to cluster is equal to the (scaled) orbit-averaged self-gravitational cluster potential. $\Phi_{\mathrm{ext}}(\mathcal{R},\, \tau)$ is the (scaled) orbit-averaged gravitational potential experienced by a Gaussian Ring due to an external massive perturber. The Ring potential $\Phi(\mathcal{R},\, \tau)$ is:

$$\Phi(\mathcal{R},\, \tau) = \int \mathrm{d}\mathcal{R}'\, \Psi(\mathcal{R},\, \mathcal{R}')\, F(\mathcal{R}',\, \tau) \tag{1.11}$$

where

$$\Psi(\mathcal{R},\, \mathcal{R}') \;=\; -GM_\bullet \oint\!\!\oint \frac{\mathrm{d}w}{2\pi}\, \frac{\mathrm{d}w'}{2\pi}\, \frac{1}{|\boldsymbol{r} - \boldsymbol{r}'|} \tag{1.12}$$

is the scaled interaction potential of two Gaussian Rings. It is straightforward to verify that $\Phi(\mathcal{R}, \tau)$ is equal to ϵ^{-1} times the orbit-averaged self-gravitational potential of the NSC.

Using equation (1.12) in (1.11), and upon slight manipulation, we have:

$$\Phi(\mathcal{R},\, \tau) = \frac{M_\bullet}{M} \oint \frac{\mathrm{d}w}{2\pi} \left(-G\,M \int \mathrm{d}\mathcal{R}'\, \frac{\mathrm{d}w'}{2\pi} \frac{F(\mathcal{R}',\, \tau)}{|\boldsymbol{r} - \boldsymbol{r}'|} \right) \tag{1.13}$$

Transformation from real space variables $\{\boldsymbol{r},\, \boldsymbol{u}\}$ to Delaunay variables is a canonical transformation, which respects the conservation of the phase space volumes and hence, $\mathrm{d}\boldsymbol{r}'\, \mathrm{d}\boldsymbol{u}' = \mathrm{d}\mathcal{R}'\, \mathrm{d}w'/2\pi$. Thus, the probability conservation during coordinate transformation implies, the real space DF $F_{\mathrm{Re}}(\boldsymbol{r}',\, \boldsymbol{u}',\, t) = F(\mathcal{R}',\, \tau)$; here t represents the real time. Upon transforming to real space variables, the expression within parenthesis "( )" in equation (1.13), equals the real space self-gravitational cluster potential $\Phi_{\mathrm{Re}}(\boldsymbol{r},\, t)$. Also, employing the definition of mass ratio ϵ, we have:

$$\Phi(\mathcal{R},\, \tau) = \frac{1}{\epsilon} \oint \frac{\mathrm{d}w}{2\pi} \Phi_{\mathrm{Re}}(\boldsymbol{r},\, t) = \frac{\overline{\Phi}}{\epsilon} \tag{1.14}$$

from equation (1.8). Similarly, $\Phi_{\mathrm{ext}}(\mathcal{R}, \tau)$ is the (scaled) orbit-averaged real space gravitational potential due to an external perturber.

Ring orbits $\mathcal{R}(\tau)$ are determined by the following Hamiltonian equations of motion:

$$I \;=\; \sqrt{GM_{\bullet}a} \;=\; \text{constant}\,, \tag{1.15a}$$

$$\frac{\mathrm{d}L}{\mathrm{d}\tau} \;=\; -\frac{\partial H}{\partial g} \quad , \qquad \frac{\mathrm{d}g}{\mathrm{d}\tau} \;=\; \frac{\partial H}{\partial L}\,, \tag{1.15b}$$

$$\frac{\mathrm{d}L_z}{\mathrm{d}\tau} \;=\; -\frac{\partial H}{\partial h} \quad , \qquad \frac{\mathrm{d}h}{\mathrm{d}\tau} \;=\; \frac{\partial H}{\partial L_z}\,. \tag{1.15c}$$

This represents a Hamiltonian flow in $\mathcal{R}$-space which is restricted to an I = constant four-surface, and carries the DF $F(\mathcal{R},\, \tau)$ with it. The evolution of the DF $F(\mathcal{R},\, \tau)$ is determined by the secular CBE:

$$\frac{\partial F}{\partial \tau} + [F, H] = 0 \quad , \quad [F, H] = \left(\frac{\partial F}{\partial g}\frac{\partial H}{\partial L} - \frac{\partial F}{\partial L}\frac{\partial H}{\partial g}\right) + \left(\frac{\partial F}{\partial h}\frac{\partial H}{\partial L_z} - \frac{\partial F}{\partial h}\frac{\partial H}{\partial L_z}\right) \tag{1.16}$$

where $[F, H]$ represents a four-dimensional Poisson Bracket wrt (L, g) and (L_z, h) action-angle pairs. Note that H has an integral dependence on F, as evident from the equation (1.11). Hence, the secular CBE is an initial value, integral partial differential equation (pde), which governs the collisionless evolution of the DF $F(\mathcal{R}, \tau)$ over the secular timescales T_{sec}.

A collisionless equilibrium has DF $F_0(\mathcal{R})$ for which $\partial F_0/\partial\tau = 0$ and hence $[F_0, H_0] = 0$. Here $H_0(\mathcal{R}) = \Phi_0(\mathcal{R}) + \Phi_{\mathrm{ext}}(\mathcal{R})$, with $\Phi_0(\mathcal{R})$ equal to the scaled self-gravitational cluster potential corresponding to the stationary DF $F_0(\mathcal{R})$. $\Phi_{\mathrm{ext}}(\mathcal{R})$ is a time-independent external gravitational potential. It is important to note that these collisionless equilibria are stationary only over timescales of order $\sim$ several T_{sec}, but undergo the collisional evolution as mutual interactions among finite number of constituent Gaussian Rings accumulate over longer collisional times $T_{\mathrm{res}} \sim N_{\star}\, T_{\mathrm{sec}}$.

The secular version of Jeans Theorem, derived in ST16a, implies that the stationary state DF $F_0(\mathcal{R})$ depends upon the phase space variables $\mathcal{R}$ only through the time-independent isolating integrals of motion of Hamiltonian $H_0(\mathcal{R})$, and any function of time-independent isolating integrals of $H_0(\mathcal{R})$ is a stationary solution of secular CBE. In secular dynamics, a general Keplerian stationary state always has at least two isolating integrals, I and $H_0(\mathcal{R})$. Equilibria respecting symmetries (spherical, axisymmetric) provide extra integrals of motion (L, L_z), so a richer variety of equilibria are allowed in secular dynamics, when compared with general stellar dynamics. ST16a constructed some simple collisionless equilibria with symmetric spatial geometries and discussed their physical characteristics.

Let us consider a system in collisionless equilibrium defined by the DF $F_0(\mathcal{R})$ and corresponding Hamiltonian $H_0(\mathcal{R}) = \Phi_0(\mathcal{R}) + \Phi_{\text{ext}}(\mathcal{R})$. Let $\Phi_{1,\text{ext}}(\mathcal{R},\, \tau)$ be a weak time-dependent external potential perturbing the system with $|\Phi_{1,\text{ext}}| \ll |H_0|$. The system responds by developing a small deformation $F_1(\mathcal{R},\, \tau)$, so the total DF $F(\mathcal{R},\, \tau) = F_0(\mathcal{R}) + F_1(\mathcal{R},\, \tau)$. The total self-gravitational potential is $\Phi(\mathcal{R},\, \tau) = \Phi_0(\mathcal{R}) + \Phi_1(\mathcal{R},\, \tau)$, where:

$$\Phi_1(\mathcal{R},\, \tau) = \int \mathrm{d}\mathcal{R}'\, \Psi(\mathcal{R},\, \mathcal{R}')\, F_1(\mathcal{R}',\, \tau)\,. \tag{1.17}$$

The Hamiltonian of the deformed system is $H(\mathcal{R},\, \tau) = H_0(\mathcal{R}) + \Phi_1(\mathcal{R},\, \tau) + \Phi_{1,\text{ext}}(\mathcal{R},\, \tau)$. The system evolves by secular CBE given in equation (1.16). Since the quantities F_1, Φ_1 and $\Phi_{1,\text{ext}}$ are small in magnitude, the linear treatment of problem reduces CBE to its linearized form,

$$\frac{\partial F_1}{\partial \tau} + [F_1,\, H_0] = [\Phi_1 + \Phi_{1,\text{ext}},\, F_0]\,. \tag{1.18}$$

The above linearized CBE (LCBE) is an integral pde for the integral dependence of Φ_1 on F_1, evident in the equation (1.17). If the external perturber is absent, i.e. $\Phi_{1,\text{ext}} = 0$, the LCBE determines the linear dynamical stability of F_0. The above equation reduces to a homogeneous integral pde and modal analysis leads to an integral eigenvalue equation. If the solution $F_1(\mathcal{R},\, \tau)$ grows in magnitude with time, the initial stationary state is unstable. The general analysis with $\Phi_{1,\text{ext}} \neq 0$ gives the linear response of the system to the perturber. In Chapter 2 and 3, the LCBE is used to study these dynamical aspects.

1.4 Secular Collisional Dynamics

The collisionless equilibria, described in the previous section, evolve over times much longer than T_{sec}, due to the granularity of mass distribution of real stellar systems with finite $N_\star \gg 1$. This collisional evolution occurs over much longer RR timescales $T_{\text{res}} \sim N_\star T_{\text{sec}}$.

Classical two-body relaxation (Chandrasekhar, 1942, 1943a,b; Binney & Tremaine, 2008) considers an infinite homogeneous sea of stars where the stars move on straight line orbits. This results in the diffusion of both energy and angular momentum. But for Keplerian star clusters, stellar velocities inside the region of influence of the MBH are large, so the coherence timescales for gravitational interactions among two stars are typically less than Keplerian orbital timescales $T_{\rm Kep}$. This makes the two-body relaxation timescales $T_{\rm 2b}$ much larger than it would be in the absence of the MBH; in many galactic nuclei $T_{\rm 2b}$ exceeds the Hubble time. RT96 proposed the more efficient mechanism of RR (mentioned in § 1.2) which leads to a stochastic exchange of angular momentum between pairs of stellar orbits, viewed as Gaussian Rings. Stars that have lost net angular momentum would be on more eccentric orbits, making them susceptible to close interactions with MBH. This can lead to direct stellar feeding of MBH, tidal disruption of stars, EMRIs of compact stellar remnants emitting low frequency gravitational waves (GWs) and a host of other interesting phenomena (Alexander, 2017).

Degeneracy of the pure Kepler problem forms the basis of RR. The radial and azimuthal orbital frequencies are equal leading to a closed elliptical orbit (fixed Gaussian Ring). Since the dynamics of a Keplerian star cluster can be thought of as a perturbed Kepler problem, the precession and deformation of Gaussian Rings occur over longer secular times $T_{\rm sec}$. Hence the coherence time for gravitational torquing between two Rings is of order $T_{\rm sec} \gg T_{\rm Kep}$. This extended period of interplay or coherence between Gaussian Rings makes RR more efficient than classical two-body relaxation. The two-body relaxation timescales $T_{\rm 2b}$ are order-of-magnitude greater than the RR timescales $T_{\rm res}$ with the approximate relation, $T_{\rm res} \sim \epsilon T_{\rm 2b}$, as shown by RT96.

RR being driven by secular gravitational interactions between discrete Gaussian Rings, does not lead to exchanges in Keplerian energies, because $I = \sqrt{GM_\bullet a}$ is an integral of motion in secular dynamics. Hence unlike classical two-body relaxation, there is no energy relaxation among stars by RR. RT96 demonstrated the enhanced rates of angular momentum relaxation both through order-of-magnitude estimates and simulations. They suggested that the inner regions of galactic nuclei might be relaxed in angular momentum, but not in energy. It is a bit complicated to describe the relaxation of angular momentum, being a vector quantity. They presented approximate analytical studies in the two extreme limits – *scalar RR* dealing with the diffusion of the magnitude of angular momentum (or eccentricities of Gaussian Rings), and *vector RR* dealing with the diffusion of direction of angular momentum (or orbital planes of Gaussian Rings). Scalar RR emerges as a consequence of apsidal resonances, while vector RR is due to nodal resonances among precessing Gaussian Rings. Nearly spherical Keplerian systems have stellar orbits with nodal precession much slower than even the slow apse precession. Hence, in this subset of systems, RT96 found that vector RR occurs on relatively shorter timescales $\sim N_\star^{-1/2} T_{\rm res}$.

1.4.1 Development of the theory of Resonant Relaxation

We review briefly the development of the theory of RR, following the pioneering work of RT96. RT96 did N-body simulations and N-wire/Ring simulations (with Gaussian Rings as constituents), and also constructed a random walk model for RR. Most of the later works dealt with numerical simulations, and analytical works employed stochastic models deriving their parameters from simulations.

Hopman & Alexander (2006a,b) investigated MBH feeding driven by RR, similar to earlier studies based on two-body relaxation (Bahcall & Wolf, 1976). They solved a Fokker-Planck equation for the distribution of energies, including an RR sink term based on the RT96 model. According to the authors, RR affects mainly the tightly bound orbits closer to the MBH, and dynamics of larger orbits are not much affected. They constrained the MBH feeding rate, and the event rates of EMRIs and TDEs. They applied their results to the Galactic S-star cluster, and the young and old populations of our Galaxy's NSC and found them consistent with observed stellar kinematics. Gürkan & Hopman (2007) employed the wire/Ring approximation of RT96 in simulations to compute RR torques among stars. They determined the RR timescales as a function of orbital eccentricities, and found that RR is more efficient for high eccentricity orbits, compared with near-circular Rings. Kupi et al. (2010) studied small scale N-body simulations to parameterize RR strength, and explored the effect of RR on event rates of EMRIs. They concluded an increase in event rate compared with that predicted on the basis of two-body relaxation alone.

Madigan et al. (2011) constructed an autoregressive moving average model for RR, calibrated by extensive N-body simulations. They applied this model to study RR by Monte Carlo simulations of a stellar cluster around an MBH. Their results showed a stellar cored distribution, attributed to tidal disruption of stars close to the MBH. Also, they studied the RR of stellar orbits originating from disruption of binaries, usually considered as possible formation channel for the S-star cluster. They found that the resultant eccentricities of resonantly relaxed stellar orbits are higher, compared with the observed orbits of S-star cluster.

Kocsis & Tremaine (2011) explored vector RR by constructing an analytical model based on Laplace–Lagrange theory. They studied vector RR of a stellar disc embedded in a spherical star cluster, paying attention to possible warping, with the aim of explaining the young stellar distribution within 0.5 pc of the Galactic MBH. Kocsis & Tremaine (2015) studied vector RR of a spherical star cluster by numerical simulations, wherein each star is replaced by an annulus of mass obtained by averaging over both orbital motion and apsidal precession. RR evolution is driven by interactions among these annuli, and was modelled as a random walk of orbit normals of annuli on a sphere. They found a high efficiency of vector RR for high eccentricity orbits, because the corresponding overlapping annuli exert stronger torques on each other.

Touma & Tremaine (2014) constructed Boltzmann-type maximum entropy equilibrium DFs for Keplerian stellar discs, composed of Gaussian Rings of equal semi-major axes. This is possible for the case of Keplerian star clusters in general for the existence of a compact phase space (unlike general self-gravitating stellar systems), due to conservation of semi-major axes in secular dynamics. They solved for microcanonical axisymmetric thermal equilibria and studied their dynamical and thermodynamic stability. Some of these equilibria are thermally unstable to non-axisymmetric lopsided modes, with the corresponding lopsided and uniformly precessing thermal states.

Merritt et al. (2011) performed relativistic N-body simulations (in post-Newtonian limit) of Keplerian stellar system around a Schwarzschild MBH. The dominant relativistic apsidal precession leads to quenching of RR in the inner regions of the cluster. This suppressed rate of capture of stars by MBH greatly reduces the event rate of the inspirals (EMRIs). There is a maximum possible eccentricity ("Schwarzschild Barrier") approachable by a resonantly relaxing Gaussian Ring corresponding to a fixed semi-major axis. The authors proposed dynamical mechanisms for stars to cross this barrier. EMRI formation is strongly inhibited due to the barrier, and resultant event rates are suppressed by factor of $\sim 10 - 100$ compared to non-relativistic studies.

Bar-Or & Alexander (2014) studied relativistic stellar dynamics of a Keplerian star cluster around a Schwarzschild MBH by constructing a statistical framework for RR where the background potential is described as a correlated Gaussian noise. They derived a Fokker–Planck equation, and confirmed the existence of Schwarzschild barrier. Bar-Or & Alexander (2016) investigated the relativistic dynamics of a Keplerian star cluster in a steady state by Monte-Carlo simulations, and evaluated the steady rate of loss of stars on direct plunge and inspiral orbits relevant to TDEs and EMRIs.

Hamers et al. (2014) performed post-Newtonian, restricted N-body simulations to study the stars close to (both inside and outside) the Schwarzschild barrier, in the context of the S-star cluster. They considered three types of relaxation - non-resonant (for high eccentricity orbits), resonant (for low eccentricity orbits) and anomalous. They evaluated diffusion coefficients for a Fokker-Planck equation and constructed the steady state distribution of angular momentum. Merritt (2015a) constructed an algorithm to solve a Fokker-Planck equation in energy-angular momentum space, which includes the diffusion coefficients for the different types of relaxation proposed by Hamers et al. (2014), and energy loss due to emission of GWs. Merritt (2015b,c) applied this method to calculate steady state solutions and associated steady rates for TDEs and EMRIs.

In contrast to the ad hoc statistical modelling of earlier works, ST16b gave an analytical framework for RR of Keplerian stellar systems, by using the kinetic theory of Gilbert (1968). Gilbert's theory takes into account gravitationally interacting real stellar orbits in a general star cluster potential. ST16b extended the Gilbert's kinetic equation to include an MBH potential, and then orbit averaged the extended kinetic equation over the fast Keplerian orbital phase, by the method of multiple scales. The RR kinetic equation, thus obtained corresponds to a Keplerian stellar system of generic morphology and orbital structure. Sridhar & Touma (2017) (hereafter ST17) applied the general theory of ST16b to study RR of an axisymmetric stellar disc.

Hamers et al. (2018) investigated the evolution of a stellar binary black hole (BBH) orbit taking into account Lidov-Kozai (LK) dynamics and vector RR (modelled by a statistical approach). The central MBH can excite eccentricity of mutual/inner orbit of the binary by the LK mechanism, trigging close encounters between the black holes potentially leading to GW emission detectable by aLIGO. This LK driven orbital excitation is effective only for high inclinations of binary orbit wrt its orbit around the MBH. The vector RR can excite the orbital inclination of the binary orbit, driving the binary into an "LK-effective" regime. They carried out Monte Carlo simulations to calculate the resultant increase in the rate of BBH mergers. They concluded that vector RR driven LK mechanism could be effective in elevating event rates only for MBHs of smaller masses ($M_\bullet \sim 10^4 \mathrm{M}_\odot$).

Bar-Or & Fouvry (2018) studied scalar RR as a diffusion process by modelling the cluster potential as random correlated noise. They evaluated the related diffusion coefficients of scalar RR, for a spherically symmetric system. Fouvry et al. (2018) studied RR evolution of razor-thin axisymmetric Keplerian stellar disc by solving a kinetic equation (equivalent to that derived by ST16b; for details see § 1.4.2). They studied mass segregation for multiple mass stellar populations in this framework. They recovered the "Schwarzschild barrier" resulting from high relativistic apse precession of Gaussian Rings.

Below we describe briefly the collisional theory of ST16b and discuss some of its physical properties.

1.4.2 Formalism for Secular Collisional Theory

ST16b constructed a first-principles theory of RR by building on the $O(1/N_\star)$ kinetic theory of Gilbert (1968). Gilbert's theory accounts for actual stellar orbits while considering gravitational interactions among stars in a general star cluster. Such an approach is essential for secular studies of Keplerian star clusters, because the orbits are far from being straight lines as assumed in the framework of the classical two-body relaxation. Gilbert's theory is an $1/N_\star$ expansion of the Bogoliubov–Born–Green–Kirkwood–Yvon (BBGKY) equations of physical kinetics or non-equilibrium statistical mechanics. The order unity terms correspond to collisionless theory (i.e. the CBE); while collisional terms appear at $O(1/N_\star)$. This also explains the approximate relation for the RR timescale $T_{\rm res} \sim N_\star T_{\rm sec}$.

ST16b first extended Gilbert's work to include the Kepler potential of an MBH. This was followed by the transformation to Delaunay variables, and averaging of the extended Gilbert's equations over the fast Keplerian orbital phase by using the method of multiple scales of ST16a. This resulted in a kinetic equation for the RR (or collisional) evolution of Keplerian star clusters over times $T_{\rm res}$. RR is a result of angular momentum exchange between the pairs of Rings that are in apsidal and nodal resonances. The formulation makes it clear that the separation between 'scalar' and 'vector' RR is, basically, an artificial one, and exists for only the special case of a spherically symmetric cluster. The resonantly relaxing system can be thought of as passing through the intervening collisionless (quasi)equilibria over times $T_{\rm res}$. The irreversible collisional evolution is driven by the two-Ring correlations which accumulate by direct and collective interactions of Gaussian Rings.

The kinetic equation (in BBGKY form) governing the RR evolution of a Keplerian stellar system, described by single-Ring DF $F(\mathcal{R},\tau)$, is given as:

$$\frac{\partial F}{\partial \tau} \;+\; \left[\, F \,,\, H - \frac{\Phi(\mathcal{R},\tau)}{N_\star} \right] \;=\; \mathcal{C}[F]\,, \tag{1.19}$$

where

$$\mathcal{C}[F] \;=\; \frac{1}{N_\star}\int \Big[\,\Psi(\mathcal{R},\mathcal{R}')\,,\; F^{(2)}_{\rm irr}(\mathcal{R},\mathcal{R}',\tau)\Big]\;{\rm d}\mathcal{R}' \tag{1.20}$$

is the 'collision integral' and $(1/N_\star)F^{(2)}_{\rm irr}$ is the irreducible part of the two–Ring correlation function. The correlation function can be expressed in terms of Ring wake function W as:

$$F^{(2)}_{\text{irr}}(\mathcal{R},\mathcal{R}',\tau) \;=\; W(\mathcal{R}\,|\,\mathcal{R}',\tau)\,F(\mathcal{R}',\tau) \;+\; W(\mathcal{R}'\,|\,\mathcal{R},\tau)\,F(\mathcal{R},\tau) \\ +\; \int W(\mathcal{R}\,|\,\mathcal{R}'',\tau)\,W(\mathcal{R}'\,|\,\mathcal{R}'',\tau)\,F(\mathcal{R}'',\tau)\,\mathrm{d}\mathcal{R}''\,, \qquad (1.21)$$

where wake function $W(\mathcal{R}\,|\,\mathcal{R}',\tau)$ describes the wake of Ring $\mathcal{R}'$ at the phase space location $\mathcal{R}$ at time τ. The correlation function is the sum of the wake of $\mathcal{R}'$ at $\mathcal{R}$ (1^{st} term); the wake of $\mathcal{R}$ at $\mathcal{R}'$ (2^{nd} term) and the product of the wake of $\mathcal{R}''$ at $\mathcal{R}$ and $\mathcal{R}'$, summed over all $\mathcal{R}''$ (3^{rd} term).

ST16b derived an equation for the wake function $W(\mathcal{R}\,|\mathcal{R}',\tau)$ by applying the *gedanken* experiment of Rostoker (1964) and Gilbert (1968) to the secular case. The approach focuses on evaluating the cumulative deformation due to the discrete Ring $\mathcal{R}'$ (at τ), taking into account its entire orbital history. $\mathcal{R}'(\tau')$ represents the orbit of the Ring $\mathcal{R}'$ (at τ) for $\tau' \le \tau$. The perturbation of the DF due to a single Ring can be treated in linear regime, and is expressed as:

$$F_1(\mathcal{R},\tau') \;=\; -\frac{F(\mathcal{R},\tau')}{N_\star} \;+\; \frac{\delta(\mathcal{R}-\mathcal{R}'(\tau'))}{N_\star} \;+\; \frac{W(\mathcal{R}\,|\,\mathcal{R}'(\tau'),\tau')}{N_\star}\,. \qquad (1.22)$$

The first term signifies the removal of one of the $N_\star$ Rings from smooth DF; the second term accounts for the insertion of this Ring in the orbit written as $\mathcal{R}'(\tau')$; the third term is the wake function which represents the response of the system to the previous two operations of Ring removal and insertion. The evolution of this linear perturbation can be studied by employing the LCBE of equation (1.18), giving the following pde for the wake function:

$$\frac{\partial W}{\partial \tau'} \;+\; [\,W(\mathcal{R}\,|\,\mathcal{R}'(\tau'),\tau')\,,\,H(\mathcal{R},\tau')\,] \;+\; [\,F(\mathcal{R},\tau')\,,\,\Phi^{\mathrm{w}}(\mathcal{R},\mathcal{R}'(\tau'),\tau')\,] \\ =\; [\,\Phi^{\mathrm{p}}(\mathcal{R},\mathcal{R}'(\tau'),\tau')\,,\,F(\mathcal{R},\tau')\,]\,, \qquad \text{for } \tau' \;\le\; \tau. \qquad (1.23)$$

Here Φ^{w} is the gravitational potential due to the wake:

$$\Phi^{\mathrm{w}}(\mathcal{R},\mathcal{R}',\tau') \;=\; \int W(\mathcal{R}''\,|\,\mathcal{R}',\tau')\,\Psi(\mathcal{R},\mathcal{R}'')\,\mathrm{d}\mathcal{R}''\,, \qquad \text{Ring wake potential} \qquad (1.24)$$

and takes into account the collective gravitational interactions (gravitational polarization) among the Rings $\mathcal{R}$ and $\mathcal{R}'$. This can be thought of as the gravitational potential due to the wake of the Ring $\mathcal{R}'$ at the phase space location $\mathcal{R}$.

$\Phi^{\rm p}$ is the difference between the 'bare' inter–Ring interaction potential Ψ and the mean–field potential Φ of equations (1.12) and (1.11):

$$\Phi^{\rm p}(\mathcal{R},\mathcal{R}',\tau') \;=\; \Psi(\mathcal{R},\mathcal{R}') \;-\; \Phi(\mathcal{R},\tau')\,, \qquad\qquad \text{Ring perturbing potential}\,. \quad (1.25)$$

The equation (1.23) should be solved with the 'adiabatic turn–on' initial condition, $W(\mathcal{R}\,|\,\mathcal{R}'(\tau'),\tau') \to 0$ as $\tau' \to -\infty$. The right side of the equation (1.23) represents the 'source term' for the wake, because if it were absent $W = 0$ would be a solution that is compatible with the initial condition.

For RR evolution, one needs to simultaneously solve the kinetic equation (1.19) and the wake equation (1.23). Using equation (1.21) for the correlation function, the RR kinetic equation (1.19) can be cast in the following form:

$$\frac{\partial F}{\partial \tau} \;+\; \left[F\,,\,H - \frac{\Phi(\mathcal{R},\tau)}{N_\star}\right] \;=\; \mathcal{C}^{\rm dis}[F] \;+\; \mathcal{C}^{\rm fluc}[F]\,, \qquad (1.26a)$$

$$\mathcal{C}^{\rm dis}[F] \;=\; \frac{1}{N_\star}\int [\,\Psi(\mathcal{R},\mathcal{R}')\,,\,F(\mathcal{R},\tau)W(\mathcal{R}'\,|\,\mathcal{R},\tau)\,]\;{\rm d}\mathcal{R}'\,, \qquad (1.26b)$$

$$\mathcal{C}^{\rm fluc}[F] \;=\; \frac{1}{N_\star}\int F(\mathcal{R}',\tau)\,[\,\Psi(\mathcal{R},\mathcal{R}') \;+\; \Phi^{\rm w}(\mathcal{R},\mathcal{R}',\tau)\,,\,W(\mathcal{R}\,|\,\mathcal{R}',\tau)\,]\,{\rm d}\mathcal{R}'\,. \quad (1.26c)$$

where the collision integral has been divided into a dissipation part $\mathcal{C}^{\rm dis}[F]$ and a fluctuation part $\mathcal{C}^{\rm fluc}[F]$. The $O(1)$ terms of the above kinetic equation correspond to the CBE of equation (1.16). The subtraction of $\Phi/N_\star$ in the Poisson Bracket implies that the gravity of only other $(N_\star - 1)$ Rings is responsible for the evolution of a Ring. The collisional terms appear only at the order $1/N_\star$ on the right side of the equation (1.26a). This implies that, generically, the long term collisional or RR evolution of the system occurs over times $T_{\rm res} \sim N_\star T_{\rm sec}$.

The theory is valid for Keplerian stellar systems of generic geometries and orbital structures. ST17 applied the general theory of ST16b to an axisymmetric stellar disc. The neglect of gravitational polarization and simple orbital structure due to axisymmetry allowed the explicit evaluation of collision integrals. They derived the kinetic Fokker-Planck equation governing evolution of the resonantly relaxing disc. They worked out the secular version of the H-Theorem for these systems, and showed that the Boltzmann entropy never decreases during RR evolution driven by the kinetic equation. They constructed extremum entropy states employing the method of Lagrange multipliers, resulting in Boltzmann type thermal equilibrium DFs.

In Chapter 4, we review the results of ST17 and simplify them further in the monoenergetic limit. We then present a numerical algorithm to solve for the RR evolution of a fully self-gravitating monoenergetic axisymmetric Keplerian disc. In Chapter 5, we extend the formulation of ST17 for an axisymmetric Keplerian disc to include gravitational polarization.

1.5 Structure of the Thesis

This thesis presents work on the secular dynamics of NSC in two parts.

Part I deals with the collisionless dynamics of stellar discs and cusps, and consists of Chapters 2 and 3. Linear secular instabilities and further non-linear evolution are demonstrated in Chapter 2, for a class of simple models (called *waterbags*) for an axisymmetric disc with Gaussian Rings of equal semi-major axes (monoenergetic case). We speculate on the implications for the young stellar disc at the Galactic centre. In Chapter 3, we calculate the linear deformation of an initially spherical Keplerian star cluster under the gravitational pull of an adiabatically growing massive gas disc. This is of relevance to the oblate spheroidal deformation of the NSC at the Galactic centre.

Part II is concerned with the collisional phenomenon of RR of axisymmetric discs, and consists of Chapters 4 and 5. In Chapter 4, we construct an algorithm "RR code" to solve the RR kinetic equation of ST17 for monoenergetic axisymmetric Keplerian stellar discs, and present the results for an initial DF. The Chapter 5 extends the formulation of RR of axisymmetric Keplerian discs by developing a framework to include the gravitational polarization in an iterative manner.

We conclude in Chapter 6 with a brief discussion of the way forward.

Part I

Collisionless Dynamics

Chapter 2

Secular Collisionless Instabilities of Keplerian Stellar Discs

NSCs of the Milky Way and M31 are the most closely observed and well-studied galactic nuclei. Each of them possesses a Keplerian stellar disc around an MBH. Since the black hole's gravity dominates the force on stars, Toomre $Q \gg 1$, so an axisymmetric Keplerian disc is expected to be linearly stable to axisymmetric perturbations on Keplerian orbital timescales T_{Kep}. Even when a disc is stable to all modes on these short timescales, it may be unstable to modes that grow over the much longer secular timescale T_{sec} of apse precession. Secular, canonical deformations of a flat, razor-thin axisymmetric Keplerian disc must necessarily be non-axisymmetric, so we will assume that the azimuthal wavenumber of the perturbations $m \neq 0$. So, axisymmetric Keplerian discs can host only non-axisymmetric secular instabilities; a good example is presented by the counter-rotating $m = 1$ instability, which may be applicable to the nuclear disc of M31 (Touma, 2002; Kazandjian & Touma, 2013). Stellar discs with DFs even in the angular momentum and empty loss cones (i.e. DF is zero at zero angular momentum) may be unstable to $m = 1$ modes (Tremaine, 2005). In § 1.3.1 of Chapter 1, we give a more complete account of previous studies related with the lopsided $m = 1$ secular mode. Monoenergetic discs (all Gaussian Rings with equal semi-major axes) dominated by nearly radial orbits could be prone to loss cone instabilities of all m, if there is some amount of counter-rotating stars (Polyachenko et al., 2007).

This gives rise to a natural question: can prograde, axisymmetric discs support secular instabilities, even when counter-rotation and loss-cone are absent? The answers available in the literature pertain to the stability of razor-thin discs. Tremaine (2001) proved that a Schwarzschild DF is stable to modes of all m in the tight-winding limit. This was generalized by ST16a who proved that a DF which is a strictly monotonic function of the angular momentum at fixed semi-major axis (i.e. at fixed Keplerian energy), is stable to modes of all m. However, these results are insufficient to address the general question, which could be relevant to the history of the clockwise disc of young stars at the centre of the Milky Way (also see § 1.1.1). If these stars formed in a fragmenting, circular gas disc around the MBH (Levin & Beloborodov, 2003), the initial stellar orbits should have small eccentricities and the same sense of rotation (i.e. no counter-rotation) about the MBH. But Yelda et al. (2014) found the mean eccentricity of the stellar orbits $\bar{e} \simeq 0.27$. Is this largish value of mean eccentricity the result of secular instabilities? In this chapter, we investigate this question by presenting the simplest models of stellar discs orbiting MBHs, whose secular instabilities can be studied explicitly. This is done by combining analytical methods from ST16a with numerical simulations derived from Touma et al. (2009). The work presented is based on the paper Kaur et al. (2018).

In § 2.1 we present the framework of secular collisionless dynamics of ST16a for Keplerian stellar discs. This is an extension of § 1.3.2 of Chapter 1, where the formalism for general three-dimensional systems is given. Using the stability result of ST16a as a guide, we motivate the search for DFs that are either non-monotonic or not strictly monotonic in the angular momentum. Then we specialize our analysis to monoenergetic discs in § 2.2. The phase space of a monoenergetic disc is the two-dimensional surface of a sphere (see Figure 2.1). Drawing on earlier work in plasma physics we introduce the simplest of prograde, axisymmetric DFs, which correspond to 'waterbags'. The phase space DF of a waterbag is constant for orbits whose eccentricities lie within a certain range, and zero outside this range. These are of two types of waterbags: *polarcaps*, which include circular orbits, and *bands*, which exclude circular orbits – see Figure 2.2. The linear stability analysis of these systems leads to normal modes which are composed of sinusoidal disturbances of the edges of DF in the phase space. For each $m \neq 0$, a polarcap has one stable normal mode, whereas a band has two normal modes that may be stable or unstable. In § 2.3 we present numerical simulations of an unstable and a stable band; these give an immediate picture, both in real space and phase space, of linear and non-linear evolution. The linear stability problem for a band is formulated and solved in § 2.4. Then § 2.5 explores instabilities further, drawing detailed comparisons between linear theory and numerical simulations, as well as following the long-time collisionless evolution of an unstable band. Conclusions are presented in § 2.6.

2.1 Secular Collisionless Dynamics of Keplerian Stellar Discs

Our model system is a razor-thin flat stellar disc of total mass M orbiting an MBH of mass $M_\bullet \gg M$. This is a Keplerian stellar disc with the mass ratio $\varepsilon = M/M_\bullet \ll 1$ being a small parameter. The disc is composed of $N_\star \gg 1$ number of stars, which are treated in the secular picture as Gaussian Rings precessing and deforming under the average self-gravitational potential over the secular times $T_{\rm sec} \sim T_{\rm Kep}/\epsilon \gg T_{\rm Kep}$. As detailed in Chapter 1, ST16a describes the average behaviour of dynamical quantities over times $T_{\rm sec}$, by systematically averaging over the fast Keplerian orbital phase. Hence the natural measure of time in secular theory is $\tau = \varepsilon \times$ time, the 'slow' time variable. The state of a Gaussian Ring at any time τ can be specified by giving its three-dimensional Ring variables, $\mathcal{R} = \{I, L, g\}$, where $I = \sqrt{GM_\bullet a} =$ constant which is a measure of the Keplerian energy, L is the specific angular momentum which is restricted to the range $-I \le L \le I$, and $0 \le g < 2\pi$ is the longitude of the periapse; see § 1.2.1 of Chapter 1. Ring space (or $\mathcal{R}$-space) is topologically equivalent to $\mathbb{R}^3$, with I the 'radial coordinate', $\arccos(L/I)$ the 'colatitude', and g the 'azimuthal angle'. A disc composed of $N_\star$ stars, each of mass $m_\star = M/N_\star$, is a collection of $N_\star$ points in $\mathcal{R}$-space. The simplest description of a stellar disc uses the single-Ring probability DF, $F(\mathcal{R},\tau) = F(I,L,g,\tau)$, which is normalized as,

$$\int \mathrm{d}\mathcal{R}\; F(\mathcal{R},\tau) \;=\; \int \mathrm{d}I\,\mathrm{d}L\,\mathrm{d}g\; F(I,L,g,\tau) \;=\; 1\,. \tag{2.1}$$

Over times much shorter than the resonant relaxation times, $T_{\rm res} \sim N_\star T_{\rm sec}$, the graininess of the Ring-Ring interactions has negligible effects and the stellar system can be thought of as collisionless. Formally, the collisionless limit corresponds to assuming that the system is composed of an infinite number of stars, each of infinitesimal mass, the whole having a mass M equal to the total stellar mass. Then each star is like a test-Ring, whose motion is governed by the secular Hamiltonian, $\Phi(I,L,g,\tau)$, which is equal to the (scaled) self-gravitational disc potential, given as:

$$\Phi(I,L,g,\tau) \;=\; \int \mathrm{d}I'\,\mathrm{d}L'\,\mathrm{d}g'\;\Psi(I,L,g,I',L',g')\,F(I',L',g',\tau)\,, \tag{2.2}$$

where

$$\Psi(I,L,g,I',L',g') \;=\; -GM_\bullet \oint\oint \frac{\mathrm{d}w}{2\pi}\,\frac{\mathrm{d}w'}{2\pi}\,\frac{1}{|\boldsymbol{r}-\boldsymbol{r}'|} \tag{2.3}$$

is the (scaled) interaction potential between two planar Gaussian Rings. Here $\boldsymbol{r} = (x,y)$ and $\boldsymbol{r}' = (x',y')$ are the position vectors of the two stars orbiting the respective Gaussian Rings, with respect to the MBH. The physical variables $(\boldsymbol{r}, \boldsymbol{r}')$ are transformed first to Delaunay variables using equation (1.5). Here w and w' are the mean anomalies of the stars representing the Keplerian orbital phase on their respective Gaussian Rings. Ring orbits are determined by the Hamiltonian equations of motion:

$$I \;=\; \sqrt{GM_{\bullet}a} \;=\; \text{constant}\,, \qquad \frac{\mathrm{d}L}{\mathrm{d}\tau} \;=\; -\,\frac{\partial \Phi}{\partial g}\,, \qquad \frac{\mathrm{d}g}{\mathrm{d}\tau} \;=\; \frac{\partial \Phi}{\partial L}\,. \tag{2.4}$$

This is a Hamiltonian flow in $\mathcal{R}$-space which is restricted to the $I =$ constant two-sphere. The flow carries with it the DF, whose evolution is governed by the secular CBE:

$$\frac{\partial F}{\partial \tau} \;+\; [F\,,\,\Phi]_{Lg} \;=\; 0\,, \qquad \text{where} \qquad [F\,,\,\Phi]_{Lg} \;=\; \frac{\partial F}{\partial g}\frac{\partial \Phi}{\partial L} \;-\; \frac{\partial F}{\partial L}\frac{\partial \Phi}{\partial g} \tag{2.5}$$

is the two-dimensional Poisson Bracket in (L, g)-space. Φ itself depends on F through the $\mathcal{R}'$-space integral of equation (2.2). Therefore equation (2.5), together with the secular Hamiltonian of equation (2.2), defines the self-consistent initial value problem of the secular time evolution of the DF, given an arbitrarily specified initial DF $F(I, L, g, 0)$. A general property of this time evolution is the following: since the I of any Ring is constant in time, the probability for a Ring to be in $(I,\, I + \mathrm{d}I)$ is a conserved quantity. In other words the probability distribution function in one-dimensional I-space, defined by

$$P(I) \;=\; \int dL\, dg\; F(I,\, L,\, g,\, \tau)\,, \tag{2.6}$$

is independent of τ, as can be verified directly using the CBE of equation (2.5).

2.1.1 Axisymmetric Equilibria and Linear Stability

Secular collisionless equilibria are DFs that are time-independent and self-consistent solutions of the CBE. They can be constructed using the secular Jeans theorem of ST16a, which states that F must be function of the isolating integrals of motion of the secular Hamiltonian, as stated earlier in § 1.3.2. An axisymmetric equilibrium DF is independent of g and can be written as $F = (2\pi)^{-1} F_0(I, L)$, because I and L are two isolating integrals of motion of the axisymmetric Hamiltonian, $\Phi_0(I, L)$. Equation (2.2) gives Φ_0 self-consistently in terms of F_0:

$$\Phi_0(I, L) \;=\; \int \mathrm{d}I'\, \mathrm{d}L'\, F_0(I', L') \oint \frac{\mathrm{d}g'}{2\pi}\, \Psi(I, L, g, I', L', g')\,. \tag{2.7}$$

Note that $\Psi(I, L, g, I', L', g')$ depends on the apses only in the combination $|g - g'|$, so the integral over g' is independent of g. The equations of motion (2.4) for a Ring become very simple in an axisymmetric disc:

$$I \;=\; \text{constant}\,, \qquad L \;=\; \text{constant}\,, \qquad \frac{\mathrm{d}g}{\mathrm{d}\tau} \;\equiv\; \Omega_0(I, L) \;=\; \frac{\partial \Phi_0}{\partial L}\,. \tag{2.8}$$

The semi-major axis and eccentricity of a Ring are constant, with the apsidal longitude precessing at the constant angular frequency $\Omega_0(I, L)$.

The time evolution of perturbations to an axisymmetric equilibrium DF can be studied by considering the total DF to be $F = (2\pi)^{-1}F_0(I, L) + F_1(I, L, g, \tau)$, where the perturbation F_1 contains no net mass:

$$\int \mathrm{d}I\,\mathrm{d}L\,\mathrm{d}g\;F_1(I, L, g, \tau) \;=\; 0\,. \tag{2.9}$$

If $\Phi_1(I, L, g, \tau)$ is the self-gravitational potential due to F_1, then the total Hamiltonian is $\Phi = \Phi_0(I, L) + \Phi_1(I, L, g, \tau)$. By substituting for F and Φ in the CBE (2.5), and using $[F_0\,, \Phi_0]_{Lg} = 0$, we can derive the equation governing the time evolution of F_1. For small perturbations $|F_1| \ll F_0$ this is the linearized CBE (LCBE):

$$\frac{\partial F_1}{\partial \tau} \;+\; \Omega_0 \frac{\partial F_1}{\partial g} \;=\; \frac{1}{2\pi}\frac{\partial F_0}{\partial L}\frac{\partial \Phi_1}{\partial g}\,, \tag{2.10a}$$

$$\Phi_1(I, L, g, \tau) \;=\; \int \mathrm{d}I'\,\mathrm{d}L'\,\mathrm{d}g'\;\Psi(I, L, g, I', L', g')\,F_1(I', L', g', \tau)\,. \tag{2.10b}$$

The LCBE is a linear (partial) integro-differential equation for F_1, and determines the linear stability of the axisymmetric DF, $F_0(I, L)$.

An axisymmetric perturbation $F_1(I, L, \tau)$ gives rise to a $\Phi_1(I, L, \tau)$ that is also independent of g. Then the LCBE (2.10) implies $\partial F_1/\partial\tau = 0$, whose physical solution is $F_1 = 0$, because an axisymmetric perturbation cannot change the angular momentum of a star. Hence it is only non-axisymmetric, or g-dependent, perturbations that are of interest in secular theory. Since τ and g appear in the LCBE only as $(\partial/\partial\tau)$ and $(\partial/\partial g)$ we can look for linear modes of the form $F_1 \propto \exp\left[\mathrm{i}(mg - \omega\tau)\right]$, where $m \neq 0$ is the azimuthal wavenumber. Using only the general symmetric properties of $\Psi(\mathcal{R}, \mathcal{R}')$, the following result was proved in ST16a for DFs that are strictly monotonic functions of L:

- Stationary, axisymmetric discs with DFs $F_0(I, L)$ are neutrally stable (i.e. ω is real) to secular perturbations of all m when $\partial F_0/\partial L$ is of the same sign (either positive or negative) everywhere in its domain of support, $-I \leq L \leq I$ and $I_{\min} \leq I \leq I_{\max}$.

As noted in ST16a these secularly stable DFs can have both prograde and retrograde populations of stars because $-I \leq L \leq I$. The discs have net rotation and include physically interesting cases, such as a secular analogue of the well-known Schwarzschild DF. To investigate secular instabilities, the above stability result motivates us to look at axisymmetric discs with DFs, $F_0(I, L)$, that are either non-monotonic or not strictly monotonic functions of L at fixed I.

One way to proceed would be to develop stability theory, using the symmetry properties of $\Psi(\mathcal{R}, \mathcal{R}')$, as ST16a did. But the present work deals with the more specific goal of constructing the simplest class of disc models that permits quantitative study of the onset and growth of linear non-axisymmetric instabilities. In order to do this one must be able to calculate physical quantities such as the apse precession frequency $\Omega_0(I, L)$, using equations (2.7) and (2.8). This requires using an explicit forms for Ψ, for a physically motivated model of a stellar disc.

2.2 Monoenergetic Discs

2.2.1 Collisionless Boltzmann equation

$\Psi(I, L, g, I', L', g')$ depends on the apses only in the combination $|g - g'|$, and can be developed in a Fourier series in $(g - g')$. When the spread in the semi-major axes of the disc stars is comparable to the mean disc radius, the Fourier coefficients are, in general, complicated functions of (I, L, I', L') – although for numerical calculations it is straightforward to calculate them on any grid in this four dimensional space. Analytical approximations are available if restrictions are placed on L and L', such as both the Rings being near-circular and well-separated (the 'Laplace–Lagrange' limit of planetary dynamics) or both Rings being very eccentric, corresponding to the 'spoke' limit of Polyachenko et al. (2007). But secular dynamics and statistical mechanics are really about the exchange of angular momentum of stars at fixed semi-major axes, so it seems preferable if we do not place such severe restrictions on L or L'. Let us consider discs with a small spread in semi-major axes; since this is equivalent to a small spread in Keplerian orbital energies, the disc may be called nearly monoenergetic. Having nearly the same semi-major axes, any two Rings either cross each other or come very close to each other, so $\Psi(\mathcal{R}, \mathcal{R}')$ can be large, even infinite, in magnitude. For nearly-circular Rings the dominant contribution was worked out by Borderies et al. (1983), and we use this below in the monoenergetic limit.

In a nearly monoenergetic disc most pairs of Rings intersect each other. It is useful to consider the strictly monoenergetic limit, $I = I_0 = \sqrt{GM_\bullet a_0}$, when every Ring intersects every other Ring. Since all Rings have the same semi-major axis a_0, they also have the same Keplerian orbital period, $T_{\rm Kep} = 2\pi(a_0^3/GM_\bullet)^{1/2}$. Hence it is convenient to use a dimensionless slow time variable, $t = \tau/T_{\rm Kep} = \text{time}/T_{\rm sec}$, to study the dynamics of monoenergetic discs. The state of a Ring at time t can be specified by giving its periapse, g, and the dimensionless specific angular momentum $\ell = L/I_0$. Since $-1 \leq \ell \leq 1$, the motion of any Ring is restricted to the unit sphere (Figure 2.1) on which $\ell = \cos(\text{colatitude})$ and $g =$ azimuthal angle are canonical coordinates. For a monoenergetic disc F takes the form:

$$F(I, L, g, \tau) \;=\; \frac{\delta(I - I_0)}{I_0}\, f(\ell, g, t)\,. \tag{2.11}$$

Then equation (2.1) implies the following normalization for f :

$$\int \mathrm{d}\ell\, \mathrm{d}g\;\, f(\ell, g, t) \;=\; 1\,. \tag{2.12}$$

Hence $f(\ell, g, t)$ is the (dimensionless) DF for monoenergetic discs on the (ℓ, g) phase space of Figure 2.1. The eccentricity of a Ring, $e = \sqrt{1 - \ell^2}$, is equal to the length of the projection of the corresponding position vector on the sphere's equatorial plane. The eccentricity vector (or Lenz vector) is defined as $\boldsymbol{e} = (e_x, e_y)$ with $e_x = e\cos g$ and $e_y = e\sin g$. We can think of (e_x, e_y, ℓ) as a right-handed Cartesian coordinate system, with the Ring phase space realized as the unit sphere, $e_x^2 + e_y^2 + \ell^2 = 1$.

The formula of Borderies et al. (1983) for the normalized Ring-Ring interaction potential, $\psi(\ell, \ell', g - g')$, takes the following attractive form given in Touma & Tremaine (2014):

$$\psi(\ell, \ell', g - g') \;=\; \left(\frac{GM_\bullet}{2\pi a_0}\right)^{-1} \Psi(I_0, I_0\ell, g, I_0, I_0\ell', g') \;=\; -8\,\log 2 \;+\; \log|\boldsymbol{e} - \boldsymbol{e}'|^2\,. \tag{2.13}$$

For a derivation, see Appendix A.1. This expression for ψ is, strictly speaking, valid only when $e, e' \ll 1$. But Touma & Tremaine (2014) have shown that this formula for ψ serves as a good approximation for all values of e and e', and used this fact to study axisymmetric and non-axisymmetric secular thermodynamic equilibria; they also provide an improved fitting formula but we do not use this. Henceforth in this chapter we take equation (2.13) as the basic 'law of interaction', between any two Rings in a monoenergetic disc. Using equation (2.11) in (2.2) we see that the mean-field self-gravitational potential, $\varphi(\ell, g, t) = \Phi(I_0, I_0\ell, g, \tau)$ is given in explicit

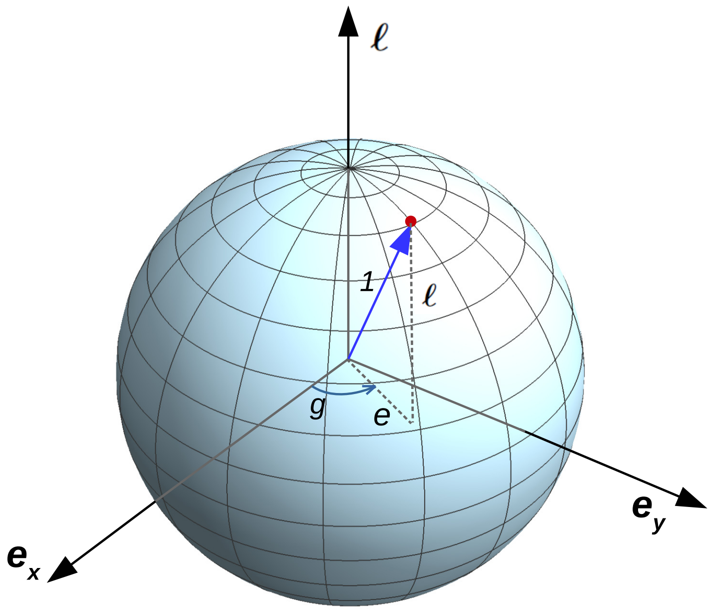

Fig. 2.1 *Phase space of a monoenergetic disc.* Each star in the disc is represented by point on the unit sphere (shown in red), with canonical coordinates (ℓ, g). The latitudes are lines of constant ℓ, and longitudes are lines of constant g. The projection of (ℓ, g) onto the equatorial plane gives the eccentricity vector $\boldsymbol{e} = (e_x, e_y)$.

form as:

$$
\begin{aligned}
\varphi(\ell, g, t) \;&=\; \frac{GM_\bullet}{2\pi a_0}\int \mathrm{d}\ell'\,\mathrm{d}g'\;\psi(\ell,\ell',g-g')f(\ell',g',t) \\
&=\; -\frac{4GM_\bullet}{\pi a_0}\log 2 \;+\; \frac{GM_\bullet}{2\pi a_0}\int \mathrm{d}\ell'\,\mathrm{d}g'\;\log\left|\boldsymbol{e}-\boldsymbol{e}'\right|^2 f(\ell',g',t)\,.
\end{aligned}
\tag{2.14}
$$

We have already cast the independent variables (ℓ, g, t) in dimensionless form. Equations (2.4), governing the dynamics of a Ring, can now be written in the following dimensionless form:

$$
\frac{\mathrm{d}\ell}{\mathrm{d}t} \;=\; -\frac{\partial H}{\partial g}\,, \qquad\qquad \frac{\mathrm{d}g}{\mathrm{d}t} \;=\; \frac{\partial H}{\partial \ell}\,, \tag{2.15}
$$

where

$$
\begin{aligned}
H(\ell, g, t) \;&=\; \frac{T_{\mathrm{Kep}}}{I_0}\,\varphi(\ell,g,t) \;=\; \left(\frac{GM_\bullet}{2\pi a_0}\right)^{-1}\varphi(\ell,g,t) \\
&=\; \int \mathrm{d}\ell'\,\mathrm{d}g'\;\log\left|\boldsymbol{e}-\boldsymbol{e}'\right|^2 f(\ell',g',t) \;+\; \text{constant}
\end{aligned}
\tag{2.16}
$$

is the dimensionless secular Hamiltonian.

These equations of motion imply the natural Poisson Bracket on the (ℓ, g) unit sphere:

$$[\, f \,,\, H \,] \;=\; \frac{\partial f}{\partial g}\frac{\partial H}{\partial \ell} \;-\; \frac{\partial f}{\partial \ell}\frac{\partial H}{\partial g}\,. \tag{2.17}$$

Substituting equation (2.11) in (2.5) we obtain the following CBE governing the self-consistent evolution of the DF:

$$\frac{\partial f}{\partial t} \;+\; [\, f \,,\, H \,] \;=\; 0\,. \tag{2.18}$$

Equations (2.15)–(2.18) provide a complete, dimensionless description of the secular collisionless dynamics of monoenergetic Keplerian discs.

2.2.2 Linear Stability of Axisymmetric Equilibria

In the study of axisymmetric equilibria and their linear, non-axisymmetric perturbations it is useful to have at hand the Fourier expansion of the Ring–Ring interaction potential, $\log |\boldsymbol{e} - \boldsymbol{e}'|^2$, that appears in the definition of the Hamiltonian in equation (2.16). From equation (C.2) of Touma & Tremaine (2014) we have,

$$\begin{aligned}\log |\boldsymbol{e} - \boldsymbol{e}'|^2 \;&=\; \log\left[e^2 - 2ee'\cos(g - g') + e'^2\,\right] \\ &=\; \log\left(e_>^2\right) \;-\; 2\sum_{m=1}^{\infty}\frac{1}{m}\left(\frac{e_<}{e_>}\right)^m \cos\left[m(g - g')\right],\end{aligned} \tag{2.19}$$

where $e_< = \min\,(e, e')$ and $e_> = \max\,(e, e')$.

Any DF of the form $f = (2\pi)^{-1} f_0(\ell)$, which is normalized as $\int_{-1}^{1} \mathrm{d}\ell\, f_0(\ell) = 1$, represents an axisymmetric equilibrium. Using equation (2.19) in (2.16), we have the corresponding axisymmetric Hamiltonian:

$$\begin{aligned}H_0(\ell) &= \int_{-1}^{1} \mathrm{d}\ell' \,\log\left(e_>^2\right)\, f_0(\ell') \qquad (2.20)\\ &= \int_0^{|\ell|} \mathrm{d}\ell' \log\left(1 - \ell'^2\right)\{f_0(\ell') + f_0(-\ell')\} + \log\left(1 - \ell^2\right)\int_{|\ell|}^{1} \mathrm{d}\ell'\,\{f_0(\ell') + f_0(-\ell')\}\,,\end{aligned}$$

where we have dropped a constant term. The apse precession frequency is given:

$$\Omega_0(\ell) \;=\; \frac{\mathrm{d}H_0}{\mathrm{d}\ell} \;=\; -\frac{2\,\ell}{1 - \ell^2}\int_{|\ell|}^{1} \mathrm{d}\ell'\;\{f_0(\ell') + f_0(-\ell')\}\,. \tag{2.21}$$

Some general properties of Ω_0 are: (i) Since the product $\ell.\Omega_0(\ell) \le 0$, the apse precession of a Ring is always opposite to the faster Keplerian orbital motion; (ii) As $\ell \to 0$ we have $\Omega_0(\ell) \to -2\ell$, so highly eccentric Rings precess very slowly; (iii) In the limit of circular Rings $\ell \to \pm 1$, and $\Omega_0(\ell) \to \mp \{f_0(1) + f_0(-1)\}$ goes to a finite limit.

When the axisymmetric equilibrium is perturbed the total DF is $f(\ell, g, t) = (2\pi)^{-1} f_0(\ell) + f_1(\ell, g, t)$, and the corresponding self-consistent Hamiltonian is $H_0(\ell) + H_1(\ell, g, t)$. Substituting these in the monoenergetic CBE (2.18) and linearizing, we obtain the LCBE governing the evolution of f_1 :

$$\frac{\partial f_1}{\partial t} + \Omega_0(\ell)\frac{\partial f_1}{\partial g} \;=\; \frac{1}{2\pi}\frac{\mathrm{d}f_0}{\mathrm{d}\ell}\frac{\partial H_1}{\partial g}\,, \tag{2.22a}$$

$$\text{where} \qquad H_1(\ell, g, t) \;=\; \int \mathrm{d}\ell'\,\mathrm{d}g'\;\log|\boldsymbol{e} - \boldsymbol{e}'|^2\, f_1(\ell', g', t)\,. \tag{2.22b}$$

We seek solutions of the form $f_1(\ell, g, t; m) = \mathrm{Re}\,\{f_{1m}(\ell)\exp\left[\mathrm{i}(mg - \omega_m t)\right]\}$ and $H_1(\ell, g, t) = \mathrm{Re}\,\{H_{1m}(\ell)\exp\left[\mathrm{i}(mg - \omega_m t)\right]\}$ where, without loss of generality, we take m to be a positive integer. Equation (2.22b) gives $H_{1m} = -2\pi/m\int_{-1}^{1}\mathrm{d}\ell'(e_</e_>)^m f_{1m}(\ell')$. Then the LCBE reduces to the following equation,

$$[\,\omega_m - m\Omega_0(\ell)\,]\; f_{1m}(\ell) \;=\; \frac{\mathrm{d}f_0}{\mathrm{d}\ell}\int_{-1}^{1}\mathrm{d}\ell'\left(\frac{e_<}{e_>}\right)^m f_{1m}(\ell')\,, \tag{2.23}$$

which is an integral eigenvalue problem, for the eigenvalues ω_m and corresponding eigenfunctions $f_{1m}(\ell)$. This equation is a special case of equation (75) of ST16a, which is valid for a general axisymmetric disc. Proceeding in a manner similar to ST16a, it is straightforward to prove the stability result: *all DFs $f_0(\ell)$ that are strictly monotonic functions of ℓ are linearly stable.* This raises again the question of the stability of DFs that are not strictly monotonic in ℓ. Since this question is now posed in the context of equation (2.23) – which is given in explicit form – we can proceed to explore it quantitatively. Among all the DFs that are not strictly monotonic functions of ℓ, the simplest are probably the 'waterbag' DFs which are discussed below.

2.2.3 Waterbags and the Linear Stability Problem

A monoenergetic waterbag is a region of the unit sphere phase space of Figure 2.1 within which the DF takes a constant positive value and is zero outside this region.[1] Time evolution that is governed by the CBE of equations (2.16)–(2.18) conserves both the area of the region as well as the value of the DF. Hence the dynamical problem reduces to following the evolution of the contour(s) bounding the region.

[1]The "waterbag" model was originally developed for the Vlasov equation by Berk et al. (1970).

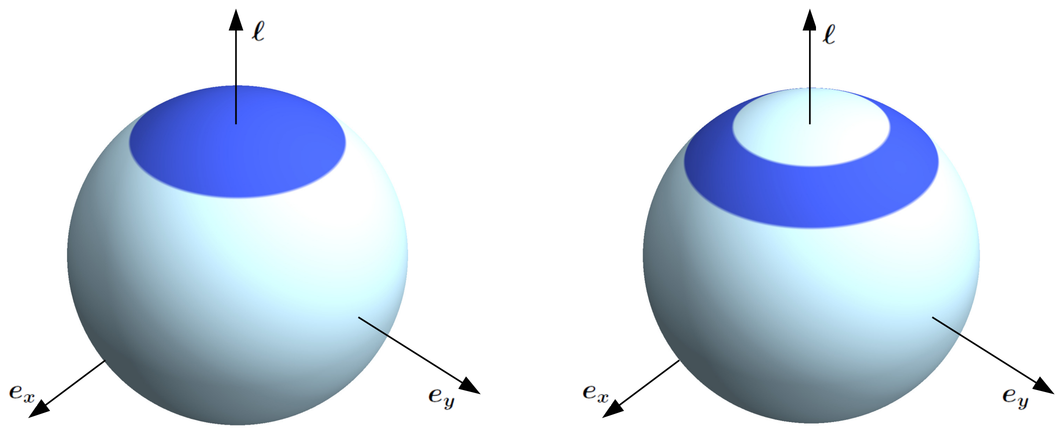

(a) Polarcap with $\ell_1 = 0.8$ and $\ell_2 = 1$ (b) Band with $\ell_1 = 0.7$ and $\ell_2 = 0.9$

Fig. 2.2 *Two types of prograde waterbags*

Analogous to the contour dynamics of fluid vortices on a sphere (Dritschel, 1988), the deformation of the contour(s) defining a waterbag stellar disc can be very complicated.

Axisymmetric equilibria

An axisymmetric monoenergetic waterbag has a DF, $f_0(\ell)$, that takes a constant positive value for $\ell \in [\ell_1, \ell_2]$, and is zero outside this interval. Since our primary interest in this chapter concerns the stability of discs in which stars orbit the MBH in the same sense, we assume that $0 \leq \ell_1 < \ell_2 \leq 1$. The normalized DF for such a 'prograde waterbag' is:

$$f_0(\ell) \;=\; \begin{cases} \dfrac{1}{\ell_2 - \ell_1} & \text{for} \quad \ell_1 \leq \ell \leq \ell_2\,, \\[2ex] \quad 0 & \text{otherwise.} \end{cases} \tag{2.24}$$

There are two different cases, corresponding to $\ell_2 = 1$ (Polarcap) and $\ell_2 < 1$ (Band) – see Figure 2.2. It can be seen that bands have DFs that are non-monotonic in ℓ, whereas polarcaps have DFs that are not strictly monotonic in ℓ. Hence the stability result, stated below equation (2.23), does not apply to either of these systems. But their stability properties can be determined completely, as we show below.

The waterbag DF describes a circular annular disc composed of stars with eccentricities $e = \sqrt{1 - \ell^2} \in [e_2, e_1]$, where $e_i = \sqrt{1 - \ell_i^2}$ for $i = 1, 2$. The inner and outer radii of the disc are $r_{\text{min}} = a_0(1 - e_1)$ and $r_{\text{max}} = a_0(1 + e_1)$ are determined by the most eccentric Rings in the disc. The surface density profile, $\Sigma_0(r)$, is obtained

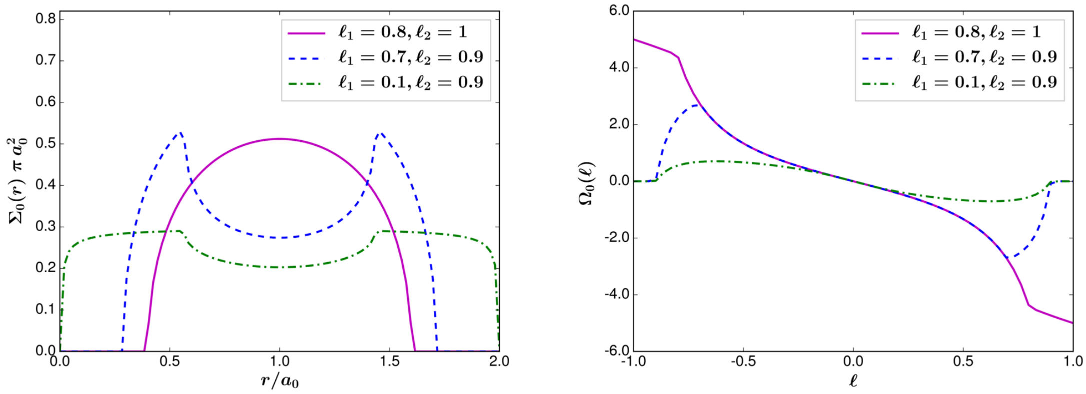

(a) Surface density (b) Apse precession rate

Fig. 2.3 *Physical features of waterbags*: Solid and dashed lines are for the polarcap and band of Figure 2.2, respectively. The broken dashed line is for a broad band, to be studied later.

by integrating $f_0(\ell)$ over the velocities, as is done in Appendix B. This gives

$$\Sigma_0(r) = \begin{cases} \dfrac{\sin^{-1}[\ell_2/\ell_0(r)] - \sin^{-1}[\ell_1/\ell_0(r)]}{2\pi^2 a_0^2(\ell_2-\ell_1)}\,, & |r-a_0| \le a_0 e_2 \\[2ex] \dfrac{\cos^{-1}[\ell_1/\ell_0(r)]}{2\pi^2 a_0^2(\ell_2-\ell_1)}\,, & a_0 e_2 < |r-a_0| \le a_0 e_1 \\[2ex] 0\,, & a_0 e_1 < |r-a_0| \end{cases} \tag{2.25}$$

where $\ell_0(r) = \sqrt{2r/a_0 - r^2/a_0^2}$. Surface density profiles are plotted in Figure 2.3a for the polarcap and band of Figure 2.2, and also a broad band ($\ell_1 = 0.1\,, \ell_2 = 0.9$), whose stability is studied later. We note that the $\Sigma_0(r)$ profiles of a polarcap and a band are very different: the former has a single maximum at the centre of the disc, whereas the latter has a characteristic double-horned shape.

The apse precession frequency $\Omega_0(\ell)$ can be determined by using equation (2.24) in (2.21). For a polarcap,

$$\Omega_0(\ell) = \begin{cases} -\dfrac{2\,\ell}{(1-\ell^2)}\,, & 0 \le |\ell| \le \ell_1 \\[2ex] -\dfrac{2\,\ell}{(1+|\ell|)(1-\ell_1)}\,, & \ell_1 < |\ell| \le 1\,, \end{cases} \tag{2.26}$$

and for a band,

$$\Omega_0(\ell) \;=\; \begin{cases} -\dfrac{2\,\ell}{(1-\ell^2)}\,, & 0 \le |\ell| \le \ell_1 \\[2ex] -\dfrac{2\,\ell}{(1-\ell^2)}\left(\dfrac{\ell_2-|\ell|}{\ell_2-\ell_1}\right), & \ell_1 < |\ell| \le \ell_2 \\[2ex] \qquad 0\,, & \ell_2 < |\ell| \le 1\,. \end{cases} \tag{2.27}$$

Even though the waterbag itself occupies only the interval $[\ell_1, \ell_2]$ we calculate $\Omega_0(\ell)$ for all $\ell \in [-1, 1]$, because it gives the apse precession frequency of any test-Ring that may be introduced into the system. Ω_0 is an antisymmetric function of ℓ, as can be seen in Figure 2.3b. For a polarcap Ω_0 is non zero when $\ell = \pm 1$, whereas for a band $\Omega_0(\ell)$ vanishes for all $|\ell| > \ell_2$.

Stability to non-axisymmetric modes

An arbitrary collisionless perturbation of a waterbag can be described as a deformation of its boundaries. From Figure 2.2 we see that a polarcap has just one boundary at $\ell = \ell_1$ whereas a band has two boundaries, at $\ell = \ell_1$ and $\ell = \ell_2$. Non-axisymmetric perturbations of the boundaries can be resolved as a Fourier series in the apsidal longitude g. Figure 2.4 shows a $m = 3$ deformation of the polarcap and band of Figure 2.2, where m is the azimuthal wavenumber of perturbation.

Polarcaps are linearly stable to all non-axisymmetric modes. In order to prove this we note that, for a polarcap, $\mathrm{d}f_0/\mathrm{d}\ell = (1-\ell_1)^{-1}\delta(\ell-\ell_1)$. Substituting this in the integral equation (2.23) we obtain:

$$[\,\omega_m - m\Omega_0(\ell)\,]\; f_{1m}(\ell) \;=\; \frac{\delta(\ell-\ell_1)}{1-\ell_1}\int_{-1}^{1}\mathrm{d}\ell' \left(\frac{e_<}{e_>}\right)^m f_{1m}(\ell')\,, \tag{2.28}$$

where $\Omega_0(\ell)$ is given by equation 2.26. The physical solution is $f_{1m}(\ell) = A_m\,\delta(\ell-\ell_1)$, where A_m is a complex amplitude. Using this in equation (2.28) we obtain the eigenvalue,

$$\omega_m \;=\; m\,\Omega_0(\ell_1) \;+\; \frac{1}{1-\ell_1}\,. \tag{2.29}$$

Since ω_m is real for all $m = 1, 2, \ldots$ and $0 \le \ell_1 < 1$, all normal modes are stable and purely oscillatory. For each m there is a normal mode with

$$f_1(\ell, g, t; m) \;=\; \mathrm{Re}\left\{A_m\delta(\ell-\ell_1)\,\exp\left[\mathrm{i}m(g-\lambda_{\mathrm{P}}t)\right]\right\}, \tag{2.30}$$

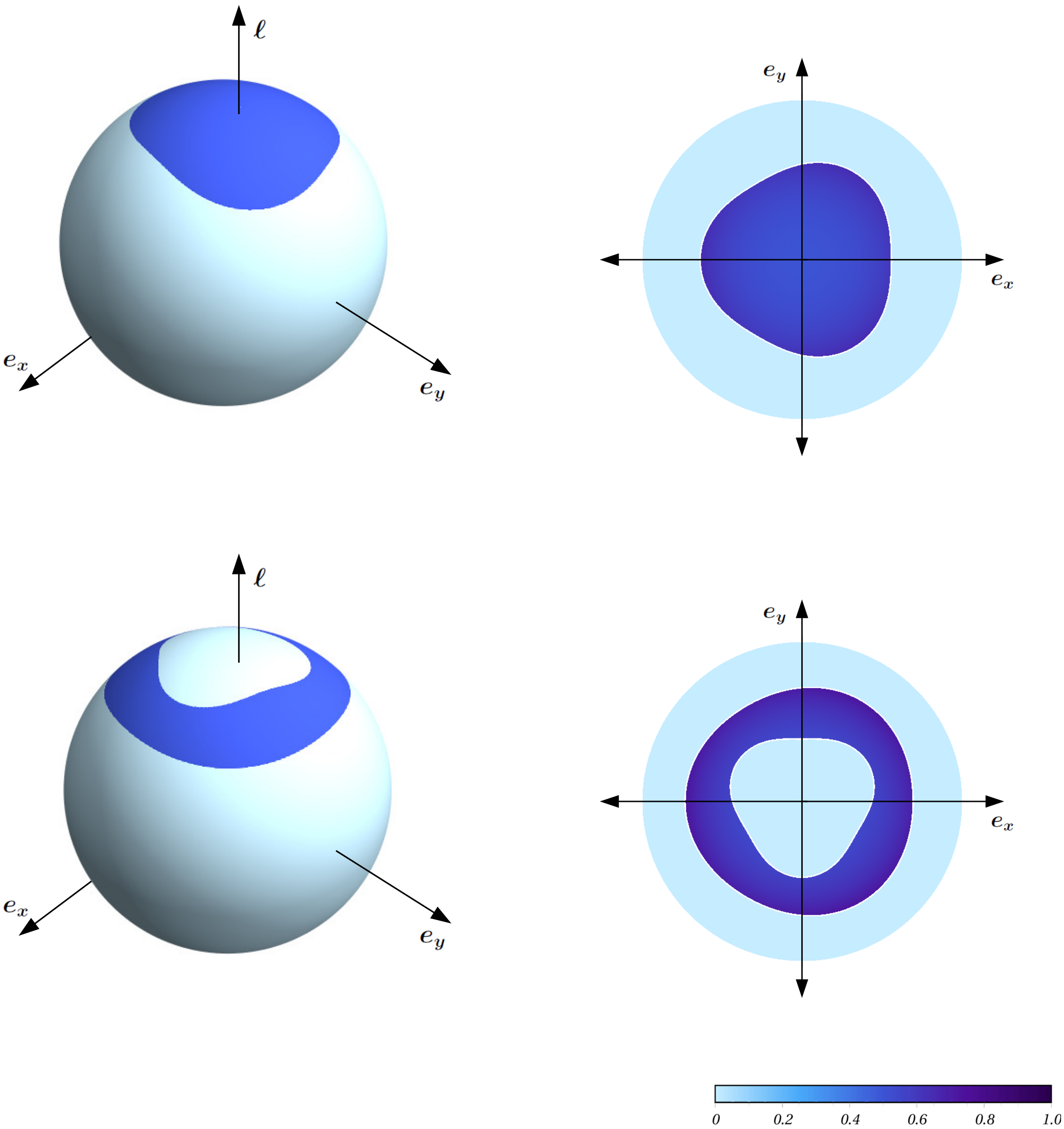

Fig. 2.4 $m = 3$ *normal mode for Polarcap and Band.* The panels on the left show the deformed polarcap (Upper panel) and band (Lower panel) DFs. The panels on the right are for the corresponding probability densities, $n(e_x, e_y) = \ell^{-1} \times DF$, in the (e_x, e_y) plane. Since the DF is constant within the deformed boundaries, $n \propto 1/\sqrt{1-e^2}$.

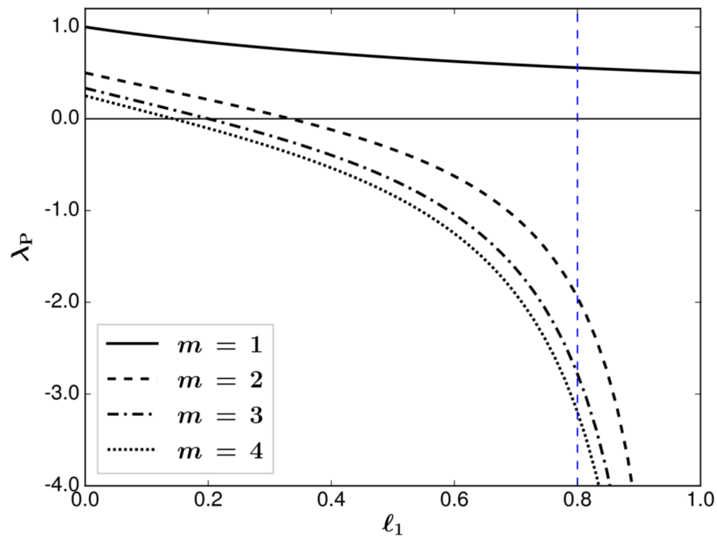

Fig. 2.5 *Mode precession frequency for Polarcaps.* The intersections of the vertical dashed line with the λ_P curves gives the spectrum of the normal modes of the polarcap of Figure 2.2. Only the $m = 1$ normal mode has positive precession for all values of ℓ_1.

where

$$\lambda_P(m, \ell_1) \;=\; \frac{\omega_m}{m} \;=\; -\frac{2\,\ell_1}{(1-\ell_1^2)} \;+\; \frac{1}{m(1-\ell_1)} \tag{2.31}$$

is the precession frequency of the m-lobed, sinusoidal deformation of the polarcap boundary. The first term on the right side is just the apse precession frequency in the unperturbed polarcap, and is negative. The second term comes from the self-gravity of the deformation, which is positive. The competition between these two terms results in the following interesting features of $\lambda_P(m, \ell_1)$, as can be seen in Figure 2.5:

- For a polarcap with given ℓ_1, λ_P is a decreasing function of m. This is because the self-gravity of the deformed edge is smaller for bigger m, due to mutual cancellation from its lobes and dips. In the limit $m \to \infty$ this vanishes altogether and $\lambda_P \to \Omega_0(\ell_1)$.

- The $m = 1$ mode always has prograde precession, with $\lambda_P = 1/(1 + \ell_1)$.

- Modes with $m = 2, 3, \ldots$ precess in a prograde sense for $0 \le \ell_1 < 1/(2m - 1)$, and in a retrograde sense for $1/(2m - 1) < \ell_1 \le 1$. λ_P vanishes when a polarcap is such that $\ell_1 = 1/(2m - 1)$ for some m; then it has a stationary time-independent deformation with m lobes.

- For $\ell_1 > 1/3$, only the $m = 1$ mode has positive pattern speed.

Bands have richer stability properties because, for each m, there are two normal modes (as shown in § 2.5). Each of these is composed of sinusoidal disturbances of the two edges – see the lower panels of Figure 2.4 for a representation of a $m = 3$ mode. For bands $\mathrm{d}f_0/\mathrm{d}\ell = \{\delta(\ell - \ell_1) - \delta(\ell - \ell_2)\}/\Delta\ell$, where $\Delta\ell = (\ell_2 - \ell_1)$. Substituting this in equation (2.23) we obtain the following integral equation:

$$[\,\omega_m - m\Omega_0(\ell)\,]\; f_{1m}(\ell) \;=\; \frac{\delta(\ell - \ell_1) - \delta(\ell - \ell_2)}{\Delta\ell} \int_{-1}^{1} \mathrm{d}\ell' \left(\frac{e_<}{e_>}\right)^m f_{1m}(\ell')\,, \tag{2.32}$$

where $\Omega_0(\ell)$ is given by equation (2.27). Hence the eigenfunctions are of the form:

$$f_{1m}(\ell) = A_{m1}\,\delta(\ell - \ell_1) + A_{m2}\,\delta(\ell - \ell_2). \tag{2.33}$$

where A_{m1} and A_{m2} are complex amplitudes. When equation (2.33) for $f_{1m}(\ell)$ is substituted in equation (2.32) the integral equation reduces to a 2×2 matrix eigenvalue problem. This is the simplest no-trivial linear stability problem in secular dynamics that can be studied analytically in detail – see § 2.4. Before doing this we present numerical simulations of an unstable band and a stable band, so the reader may have an immediate picture of the time evolution going beyond the linear evolution of small disturbances.

2.3 Numerical Exploration of Waterbag Stability

The N-Ring numerical simulations of waterbag bands were performed by Mher Kazandjian and Jihad Touma for a range of system parameters $(\ell_1,\, \ell_2)$. The full list is given in Table 2.1 of § 2.5. The last entry has $\ell_2 = 1$, so is a polarcap and not a band. It is included in the table as a limiting case of a class of broad bands. Here we discuss the stability of the two bands whose $\Sigma_0(r)$ and $\Omega_0(\ell)$ profiles feature in Figure 2.3: one is the band `waterbag_1_s0` with $(\ell_1 = 0.7,\, \ell_2 = 0.9)$, and the other is the broad band `waterbag_2_s0` with $(\ell_1 = 0.1,\, \ell_2 = 0.9)$.

We simulate a planar system of $N_\star$ Rings, each of which has the same semi-major axis a_0 and mass $m_\star$, orbiting a MBH of mass $M_\bullet$. The total disc mass $M = N_\star m_\star$ is chosen to be much smaller than $M_\bullet$, so $\varepsilon = M/M_\bullet \ll 1$ and the secular timescale, $T_{\rm sec} = \varepsilon^{-1} T_{\rm kep}$, is much longer than the Kepler orbital period. Each Ring can be thought of as a point on the unit sphere phase space of Figure 2.1, with coordinates $(\ell^i,\, g^i)$ for $i = 1, 2, \ldots, N$. The projection of the points onto the equatorial plane gives $N_\star$ eccentricity vectors, $\boldsymbol{e}^i = e^i(\cos g^i\,\hat{x} + \sin g^i\,\hat{y})$, where $e^i = \sqrt{1 - (\ell^i)^2}$ is the eccentricity. Then the normalized secular energy of the whole system is:

$$\mathcal{H} \;=\; \frac{1}{N_\star}\sum_{\substack{i,j\\ j>i}} \log\left|\boldsymbol{e}^i - \boldsymbol{e}^j\right|^2, \tag{2.34}$$

which serves as the N-Ring Hamiltonian for secular dynamics on the sphere:

$$\frac{\mathrm{d}g^i}{\mathrm{d}t} \;=\; \frac{\partial\mathcal{H}}{\partial\ell^i}\,, \qquad \frac{\mathrm{d}\ell^i}{\mathrm{d}t} \;=\; -\frac{\partial\mathcal{H}}{\partial g^i} \qquad\qquad (\text{for } i = 1, 2, \ldots, N_\star)\,, \tag{2.35}$$

where $t = \text{time}/T_{\text{sec}}$ is, as earlier, the dimensionless time variable. The Hamiltonian equations can be rewritten compactly as:

$$\frac{\mathrm{d}\boldsymbol{e}^i}{\mathrm{d}t} \;=\; \frac{2}{N_\star}\sum_{\substack{j=1\\ j\neq i}}^{N_\star} \frac{(\boldsymbol{e}^i - \boldsymbol{e}^j)\times\boldsymbol{\ell}^i}{|\boldsymbol{e}^i - \boldsymbol{e}^j|^2} \tag{2.36}$$

where $\boldsymbol{\ell}^i = \ell^i\,\hat{z}$. These vectorial equations are similar to those presented in Touma et al. (2009), with the difference that our interaction Hamiltonian is unsoftened and logarithmic. The equations were solved using a Bulirsch-Stoer integrator, with relative and absolute tolerances equal to 10^{-8}. Our fiducial system has the following parameters:

- The disc is composed of $N_\star = 1000$ Rings.
- Semi-major axis of each Ring is $a_0 = 1$ pc.
- Black hole mass $M_\bullet = 10^7\,\mathrm{M}_\odot$, giving a Kepler orbital period $T_{\text{Kep}} = 0.03$ Myr.
- Disc mass $M = 10^3\,\mathrm{M}_\odot$, so $\varepsilon = 10^{-4}$ and the secular timescale $T_{\text{sec}} = 0.3$ Gyr.

The typical relative errors for energy and angular momentum in the simulations of bands listed in Table 2.1 are $\sim 10^{-6}$.

The evolution of the two bands, `waterbag_1_s0` and `waterbag_2_s0`, is shown in Figure 2.6 and Figure 2.7, respectively. The upper two panels are for the surface mass density in the the xy-plane, and the lower two panels show the Rings represented as 1000 points on the (e_x, e_y) plane.[2] We begin with initial conditions corresponding to the two bands of Figure 2.3. The following overall features can be noticed:

- For `waterbag_1_s0` a non-axisymmetric $m = 3$ instability grows; it is seen very clearly around 0.3 Gyr and, by ~ 0.6 Gyr, there are distinct signs of nonlinear evolution.

[2]Since we are dealing with prograde discs, all the points have positive ℓ^i.

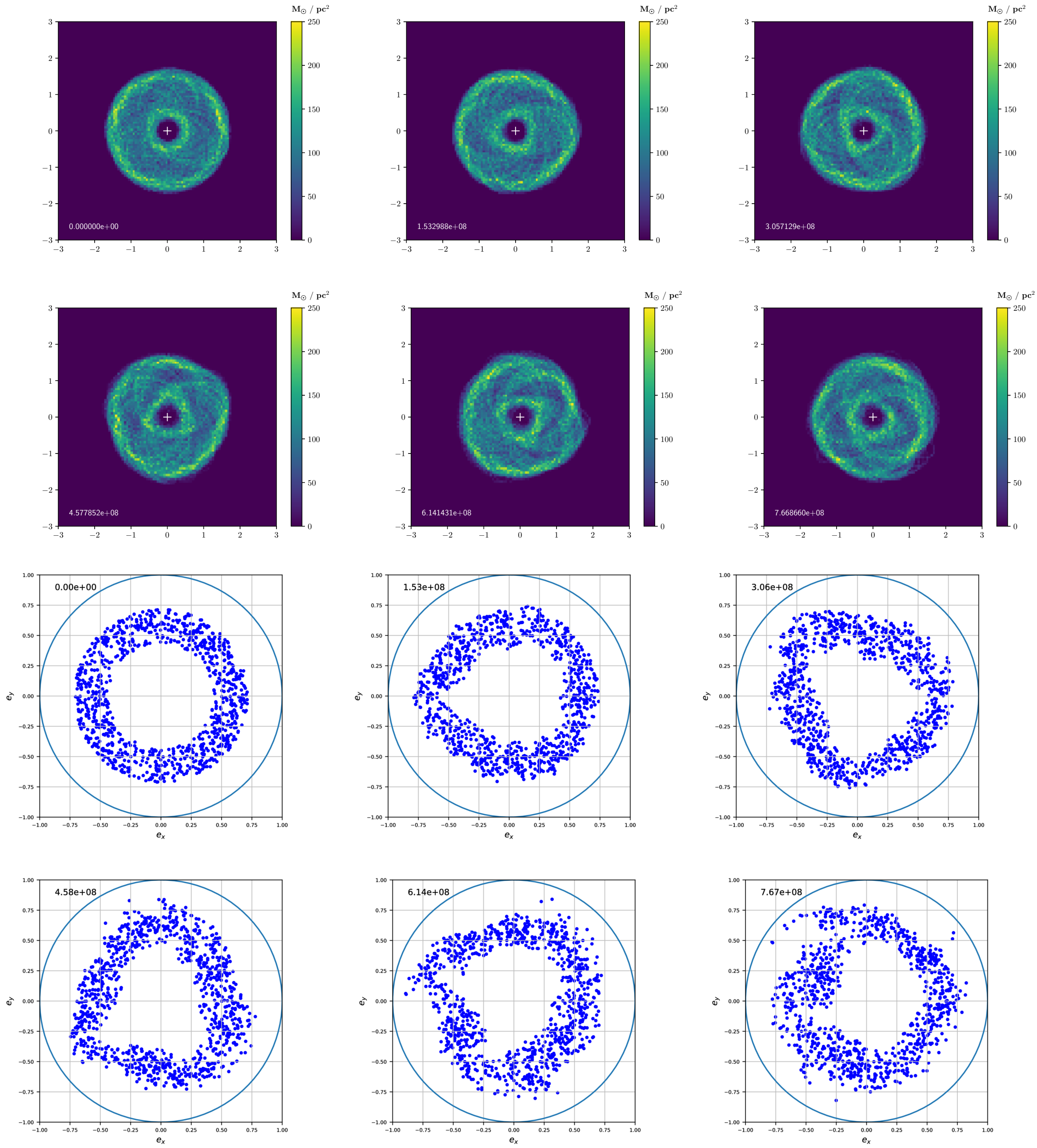

Fig. 2.6 *Evolution of the unstable band* `waterbag_1_s0`. Upper two rows show the surface density in real space (with distances measured in parsec), and the lower two rows show the distribution in the eccentricity plane at the same respective time. The $m = 3$ mode is clearly visible as three overdensity lumps in the surface density plots and as a triangular feature in the eccentricity plane. Note that the time (in years) is indicated inside the panels.

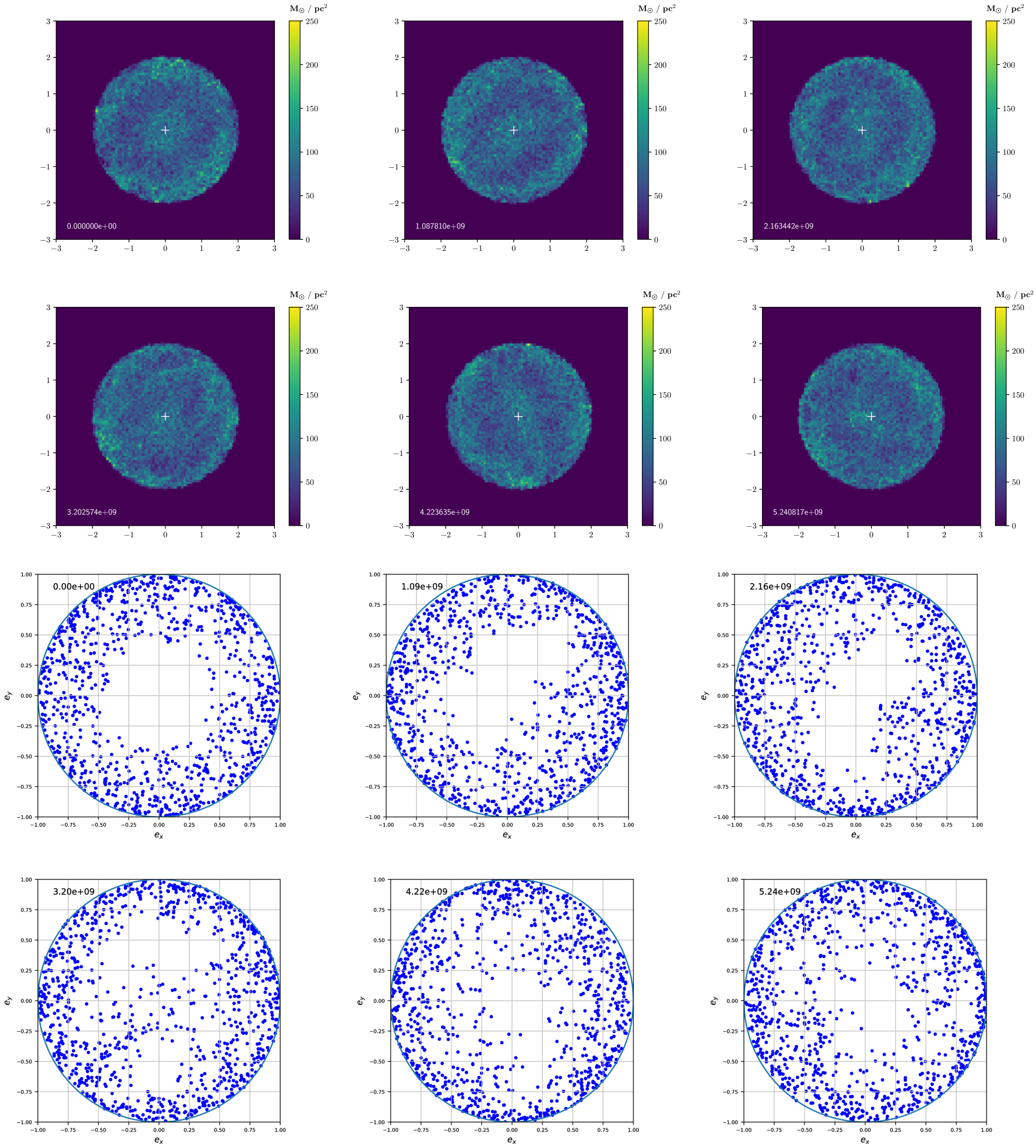

Fig. 2.7 *Evolution of the stable broad band* `waterbag_2_s0`. Upper two rows show the surface density in real space (with distances measured in parsec), and the lower two rows show the distribution in the eccentricity plane at the same respective time. Note that the time (in years) is indicated inside the panels.

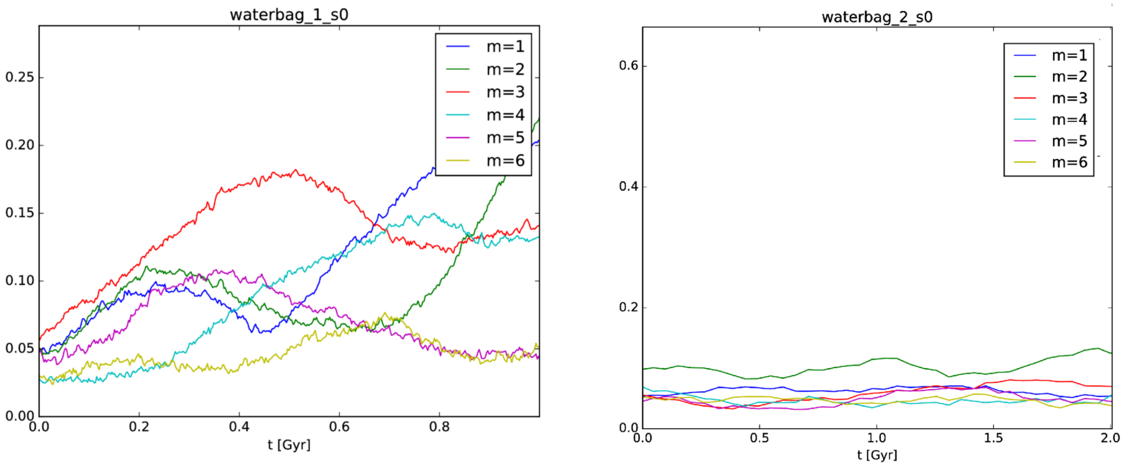

(a) `waterbag_1_s0` (b) `waterbag_2_s0`

Fig. 2.8 *Evolution of mode amplitudes* $a_m(t)$.

- In contrast the broad band `waterbag_2_s0` is seen to be stable over a timescale of 5 Gyr.

Dynamical behaviour can be characterized in more detail by looking at mode amplitudes, $a_m(t)$, which were evaluated by computing Fast Fourier Transforms over annuli of the projected mass density. These are plotted in Figure 2.8a for `waterbag_1_s0` and Figure 2.8b for `waterbag_2_s0`. The main features are:

- For `waterbag_1_s0` the initially unstable mode has $m = 3$, and this remains dominant until about 0.6 Gyr. Later there is growth of other modes, especially, $m = 1$ and $m = 2$.

- Modes of all m maintain a low amplitude for `waterbag_2_s0`. We note that sampling noise, which is unavoidable in the initial conditions, was such that a $m = 2$ mode had a greater initial amplitude than the other modes (see Figures 2.8b). The $m = 2$ mode is seen to be stable and precessing in Figure 2.7. Interactions of some stars with the $m = 2$ mode has, presumably, scattered them in phase space. Whereas a study of this mode-particle scattering is beyond the scope of present work, simulations with a larger number of particles will help clarify the nature of this process.

In the next section we present a detailed account of the linear stability of bands. We will also discuss how linear theory accounts for the behaviour of `waterbag_1_s0` and `waterbag_2_s0`.

2.4 Linear Stability of Bands

A normal mode of a band has the form $f_1(\ell, g, t; m) = \mathrm{Re}\,\{f_{1m}(\ell)\exp[\mathrm{i}(mg - \omega_m t)]\}$, where ω_m is a complex eigenfrequency. Since a normal mode is composed of sinusoidal disturbances of the two edges of the phase space DF, the corresponding eigenfunction is of the form, $f_{1m}(\ell) = A_{m1}\,\delta(\ell - \ell_1) + A_{m2}\,\delta(\ell - \ell_2)$, where A_{m1} and A_{m2} are complex amplitudes – see equation (2.33). When this is substituted in the integral equation (2.32), it reduces to the following 2×2 matrix eigenvalue problem:

$$\begin{pmatrix} \dfrac{1}{\Delta\ell} + m\,\Omega_0(\ell_1) & \dfrac{1}{\Delta\ell}\left(\dfrac{e_2}{e_1}\right)^m \\[2ex] -\dfrac{1}{\Delta\ell}\left(\dfrac{e_2}{e_1}\right)^m & -\dfrac{1}{\Delta\ell} + m\,\Omega_0(\ell_2) \end{pmatrix} \begin{pmatrix} A_{m1} \\[2ex] A_{m2} \end{pmatrix} = \omega_m \begin{pmatrix} A_{m1} \\[2ex] A_{m2} \end{pmatrix}. \tag{2.37}$$

Here $\Delta\ell = (\ell_2 - \ell_1)$, and equation (2.27) gives $\Omega_0(\ell_1) \equiv \Omega_1 = -2\ell_1/(1 - \ell_1^2)$ and $\Omega_0(\ell_2) = 0$. The solutions for the eigenfrequency and the ratio of edge disturbance amplitudes are,

$$\omega_m^{\pm} = \frac{m\Omega_1}{2} \pm \frac{1}{\Delta\ell}\sqrt{\left[1 + \frac{m\,\Delta\ell\,\Omega_1}{2}\right]^2 - \left(\frac{e_2}{e_1}\right)^{2m}}\,, \tag{2.38a}$$

$$\left(\frac{A_{m2}}{A_{m1}}\right)^{\pm} = -\left[1 + \frac{m\,\Delta\ell\,\Omega_1}{2}\right]\left(\frac{e_1}{e_2}\right)^m \pm \sqrt{\left[1 + \frac{m\,\Delta\ell\,\Omega_1}{2}\right]^2\left(\frac{e_1}{e_2}\right)^{2m} - 1}\,. \tag{2.38b}$$

A number of properties of linear modes follow:

- For each $m = 1, 2, \ldots$ there are two normal modes denoted by '$\pm$'. Each normal mode is made up of two edge disturbances corresponding to the DF boundaries $\ell = \ell_1$ and $\ell = \ell_2$.
- The eigenfrequencies, $\omega_m^{\pm}$, are either real or complex conjugates of each other. If they are both real then both the normal modes are stable with pattern speed $\lambda_{\mathrm{P}}^{\pm} = \omega_m^{\pm}/m$. When the eigenfrequencies are complex conjugates, then one normal mode grows exponentially (an instability) and the other decays exponentially, with both modes having the same pattern precession frequency.
- From equation (2.38a) we see that the condition for instability is:

$$\left(\frac{1 - \ell_2^2}{1 - \ell_1^2}\right)^{m/2} > \left|\,1 - \frac{m\,(\ell_2 - \ell_1)\,\ell_1}{1 - \ell_1^2}\,\right|. \tag{2.39}$$

- It can be verified that the above inequality cannot be satisfied for any $0 \le \ell_1 < \ell_2 < 1$, when $m = 1, 2$. So all bands have stable $m = 1$ and $m = 2$ modes, and only modes with $m = 3, 4, \ldots$ can be unstable.

- The unstable band `waterbag_1_s0` has $\ell_1 = 0.7$ and $\ell_2 = 0.9$. The stable broad band `waterbag_2_s0` has $\ell_1 = 0.1$ and $\ell_2 = 0.9$. Using these values of (ℓ_1, ℓ_2) in equation (2.39) it can be verified that (i) `waterbag_1_s0` has precisely two unstable modes, for $m = 3$ and $m = 4$; (ii) For `waterbag_2_s0` modes of all m are stable. This is in agreement with the numerical simulations discussed in § 2.3.

- The inequality condition (2.39) defines a region of instability in the (ℓ_1, ℓ_2) parameter plane, for each value of m. These are displayed in Figure 2.9 for $m = 3, 4, 5, 6$. As m increases the crescent-like region of instability expands.

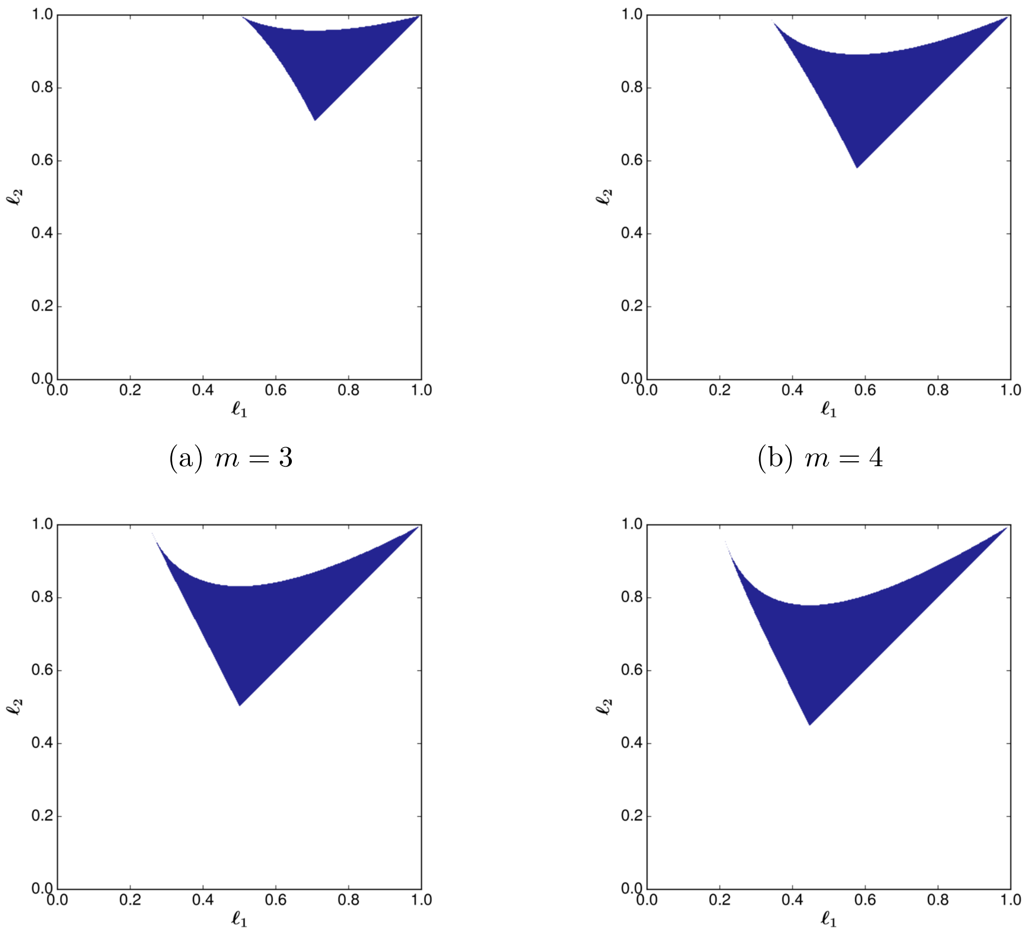

(a) $m = 3$ (b) $m = 4$

(c) $m = 5$ (d) $m = 6$

Fig. 2.9 *Instability region in* (ℓ_1, ℓ_2) *plane for* $m = 3, 4, 5, 6$.

2.4.1 Structure of Normal Modes

Stable modes: When inequality (2.39) is not satisfied the two normal mode eigenfrequencies $\omega_m^{\pm}$, given by equation (2.38a), are both real with pattern speeds $\lambda_{\mathrm{P}}^{\pm} = \omega_m^{\pm}/m$. The DF of the normal modes is:

$$f_1^{\pm}(\ell, g, t; m) = \mathrm{Re}\Big\{A_{m1}^{\pm} \exp\left[\mathrm{i}m(g - \lambda_{\mathrm{P}}^{\pm} t)\right] \delta(\ell - \ell_1) + A_{m2}^{\pm} \exp\left[\mathrm{i}m(g - \lambda_{\mathrm{P}}^{\pm} t)\right] \delta(\ell - \ell_2)\Big\}. \tag{2.40}$$

The four complex amplitudes, $A_{m1}^{\pm}$ and $A_{m2}^{\pm}$, are related by equation (2.38b), which implies that $(A_{m2}/A_{m1})^{\pm}$ are real whenever $\omega_m^{\pm}$ are real. When the ratio is positive/negative, the normal mode is an in-phase/out-of-phase combination of the two sinusoidal edge disturbances. Moreover the product $(A_{m2}/A_{m1})^{+}\,(A_{m2}/A_{m1})^{-} = 1$, which implies (i) If the '+' mode is an in-phase (or out-of-phase) combination of the two edge disturbances so is the '−' mode, and vice versa; (ii) If disturbance at one of the edges makes a dominant contribution to the '+' mode, then the other edge disturbance makes a dominant contribution to the '−' mode. To summarize, a stable '±' mode is either an in-phase or out-of-phase superposition of the edge disturbances, with generally unequal amplitudes. The pattern speeds, $\lambda_{\mathrm{P}}^{\pm}$, of the '±' modes are generally unequal.

Unstable modes: When inequality (2.39) is satisfied the two normal mode eigenfrequencies $\omega_m^{\pm}$ given by equation (2.38a), are complex conjugates of each other. We write $\omega_m^{\pm} = m\lambda_{\mathrm{P}} \pm \mathrm{i}\,\omega_{\mathrm{I}}$, where λ_{P} is the pattern speed and $\omega_{\mathrm{I}} > 0$ can be thought as the growth rate of the '+' mode, or as the damping rate of the '−' mode; we will refer to ω_{I} as the growth rate. Equation (2.38a) gives:

$$\lambda_{\mathrm{P}} \;=\; \frac{\Omega_1}{2} = -\frac{\ell_1}{1-\ell_1^2} \tag{2.41a}$$

$$\omega_{\mathrm{I}} \;=\; \sqrt{\frac{1}{\Delta\ell^2}\left(\frac{1-\ell_2^2}{1-\ell_1^2}\right)^{m} - \left(\frac{1}{\Delta\ell} - \frac{m\,\ell_1}{1-\ell_1^2}\right)^{2}}\,. \tag{2.41b}$$

The pattern speed is negative and depends only on ℓ_1. On the other hand the growth rate depends on all of (ℓ_1, ℓ_2, m).

Equations (2.38a) and (2.38b) imply that whenever $\omega_m^{\pm}$ are complex conjugates, $(A_{m2}/A_{m1})^{\pm}$ are also complex conjugates. Moreover the magnitude of the amplitude ratio, $|(A_{m2}/A_{m1})^{\pm}| = 1$, so we can write $(A_{m2}/A_{m1})^{\pm} = \exp\left[\pm\mathrm{i}\,m\,\theta_m\right]$, where

$$\theta_m = \frac{1}{m}\,\cos^{-1}\left[\left(\frac{1-\ell_1^2}{1-\ell_2^2}\right)^{m/2}\left(\frac{m\,\ell_1\,\Delta\ell}{1-\ell_1^2} - 1\right)\right], \tag{2.42}$$

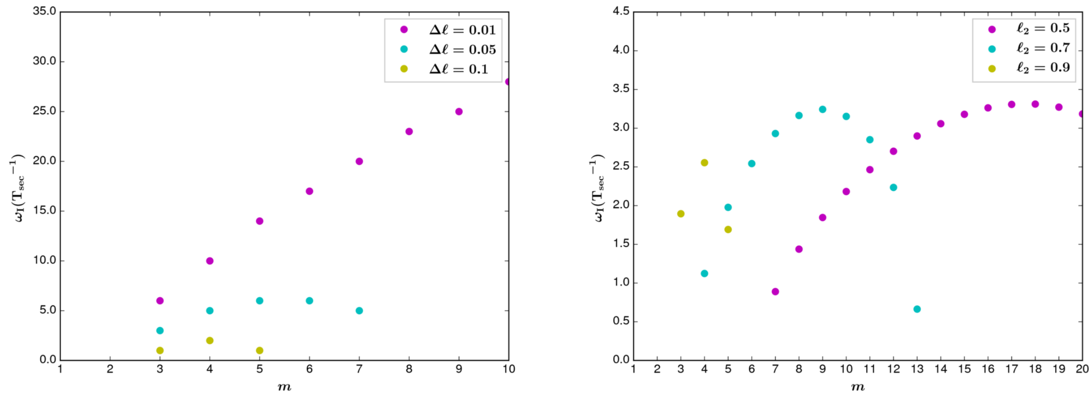

(a) $\ell_2 = 0.9$ (b) $\Delta\ell = 0.1$

Fig. 2.10 Growth rate ω_{I} variation with m: a). Left panel corresponds to waterbags with fixed $\ell_2 = 0.9$ b). Right panel for waterbags of fixed thickness $\Delta\ell = 0.1$

is the relative phase shift between the two edge disturbances composing a normal mode. Then the DF of the growing and damping normal modes of a given m is given by the following superposition of the two edge disturbances:

$$
\begin{aligned}
f_1^{\pm}(\ell, g, t; m) \;=\; & \exp\left[\pm\omega_{\mathrm{I}}\, t\right] \mathrm{Re}\Big\{ A_m^{\pm} \exp\left[\mathrm{i}m(g - \lambda_{\mathrm{P}} t)\right] \delta(\ell - \ell_1) \\
& + A_m^{\pm} \exp\left[\mathrm{i}m(g \pm \theta_m - \lambda_{\mathrm{P}} t)\right] \delta(\ell - \ell_2) \Big\}, \qquad (2.43)
\end{aligned}
$$

where $A_m^{\pm}$ is a complex amplitude that is common to both edge disturbances. In contrast to a stable mode, an unstable '$\pm$' mode is a superposition of the edge disturbances with a relative phase shift but equal amplitudes, and a pattern speed $\lambda_{\mathrm{P}} = \Omega_1/2$ which is the same for both '$\pm$' modes.

In order to get an idea of the dependence of the growth rate as a function of the parameters, (ℓ_1, ℓ_2, m) we plot in Figure 2.10 the growth rate as a function of m for different values of $\Delta\ell$ and ℓ_2. For fixed $\ell_2 = 0.9$ and three different values of $\Delta\ell$, we see that bands with smaller $\Delta\ell$ are unstable over a larger range of m, with higher maximum growth rates occurring at larger m. For fixed $\Delta\ell = 0.1$ and three different values of ℓ_2, the maximum growth rates are similar but occur at smaller m for larger ℓ_2.

We note that `waterbag_1_s0` has unstable modes for $m = 3, 4$ with the $m = 3$ mode having the higher growth rate, $\omega_{\mathrm{I}} \sim 0.72\, {T_{\mathrm{sec}}}^{-1} \simeq 2.4\,\mathrm{Gyr}^{-1}$; this is consistent with the initial growth of the $m = 3$ mode in Figure 2.6 and 2.8a. In the next section we present a more detailed comparison of numerical experiments with linear theory.

2.5 Evolution of Instabilities

Kazandjian and Touma ran a suite of numerical simulations of waterbag bands, with parameters listed in the Table 2.1. The primary goal is to put the linear theory of the previous section to stringent tests, and is explored through the upper (Set I) and lower (Set II) groups shown in Table 2.1:

- **Set I** consists of five cases, of which two – the unstable band `waterbag_1_s0` and the stable band `waterbag_2_s0` – have already been discussed.
- **Set II** is a detailed test of the linear theory prediction of the transition from instability to stability of a band with fixed $\ell_1 = 0.8$, as ℓ_2 is varied over a range of values.

System Name	ℓ_1	ℓ_2	T_{end}	Stable ?
waterbag_1_s0	0.7	0.9	2.5	no
waterbag_2_s0	0.1	0.9	9.4	yes
waterbag_3_s0	0.8	0.9	10.0	no
waterbag_4_s0	0.85	0.9	6.17	no
waterbag_5_s0	0.7	0.97	8.79	yes
waterbag_ℓ1_0.8_ℓ2_0.81	0.8	0.81	1.8	no
waterbag_ℓ1_0.8_ℓ2_0.82	0.8	0.82	10.0	no
waterbag_ℓ1_0.8_ℓ2_0.83	0.8	0.83	12.5	no
waterbag_ℓ1_0.8_ℓ2_0.84	0.8	0.84	13.3	no
waterbag_ℓ1_0.8_ℓ2_0.85	0.8	0.85	1.65	no
waterbag_ℓ1_0.8_ℓ2_0.86	0.8	0.86	34.2	no
waterbag_ℓ1_0.8_ℓ2_0.87	0.8	0.87	0.28	no
waterbag_ℓ1_0.8_ℓ2_0.88	0.8	0.88	5.9	no
waterbag_ℓ1_0.8_ℓ2_0.89	0.8	0.89	5.9	no
waterbag_ℓ1_0.8_ℓ2_0.90	0.8	0.90	41.2	no
waterbag_ℓ1_0.8_ℓ2_0.91	0.8	0.91	20.0	no
waterbag_ℓ1_0.8_ℓ2_0.92	0.8	0.92	10.8	no
waterbag_ℓ1_0.8_ℓ2_0.93	0.8	0.93	6.4	no
waterbag_ℓ1_0.8_ℓ2_0.94	0.8	0.94	44.0	no
waterbag_ℓ1_0.8_ℓ2_0.95	0.8	0.95	38.7	no
waterbag_ℓ1_0.8_ℓ2_0.96	0.8	0.96	18.4	no
waterbag_ℓ1_0.8_ℓ2_0.97	0.8	0.97	5.1	no
waterbag_ℓ1_0.8_ℓ2_0.98	0.8	0.98	211	yes
waterbag_ℓ1_0.8_ℓ2_0.99	0.8	0.99	16.3	yes
waterbag_ℓ1_0.8_ℓ2_1.00	0.8	1.00	19.0	yes

Table 2.1 *List of all the numerical simulations.* The upper five cases correspond to Set I and the lower ones to Set II. The total duration of each simulation, T_{end}, is given in units of Gyr; it is of order a few secular times and differs from case to case.

2.5.1 Set I

Of the five cases in Set I, `waterbag_1_s0` and `waterbag_2_s0` have been discussed earlier. `waterbag_5_s0` is stable according to linear theory, and the simulation results confirmed this, showing stable evolution similar to `waterbag_2_s0`. We now consider two new unstable bands, `waterbag_3_s0` and `waterbag_4_s0`. In Table 2.2 we list the predictions of linear theory for these two bands, including also `waterbag_1_s0` whose instability was discussed earlier. For each band all its unstable modes are identified, and the growth rate and pattern speed of the most unstable mode (m_0) are computed using equations (2.41b) and (2.41a).

Simulations of `waterbag_3_s0`: From Figure 2.11 we see that a $m = 4$ pattern emerges by $\sim$ 0.06 Gyr, which is in agreement with linear theory. Non-linear interactions, mainly with the unstable $m = 5$ mode, lead to distortions of the pattern. This can be seen clearly in Figure 2.13a which plots the mode amplitudes a_m versus time: the $m = 4$ mode has the maximum amplitude until $\sim$ 0.2 Gyr, after which the $m = 5$ mode begins to dominate.

Simulations of `waterbag_4_s0`: From Figure 2.12 we see that a $m = 6$ pattern emerges by $\sim$ 0.03 Gyr, which is in agreement with linear theory. Non-linear interactions with other unstable modes lead to distortions of the pattern. This can be seen clearly in Figure 2.13b which plots the mode amplitudes a_m versus time: the $m = 6$ mode dominates until $\sim$ 0.2 Gyr, after which there seems to be non-linear interactions among many modes.

Table 2.3 shows the general agreement between linear theory and simulations.

		Fastest growing mode		
System name	Unstable m	m_0	$\omega_{\mathrm{I,max}}(\mathrm{Gyr}^{-1})$	$\lambda_{\mathrm{P}0}(\mathrm{rad\ Gyr}^{-1})$
`waterbag_1_s0`	3,4	3	2.4	-4.57
`waterbag_3_s0`	3,4,5	4	8.5	-7.41
`waterbag_4_s0`	3 - 7	6	20.6	-10.21

Table 2.2 *Theoretical predictions for the unstable bands of Set I.*

	Fastest growing mode		
System name	m_0 (Theory)	m_0 (Simulations)	Agreement
`waterbag_1_s0`	3	3	yes
`waterbag_3_s0`	4	4	yes*
`waterbag_4_s0`	6	6	yes*

Table 2.3 *Comparison between linear theory and simulations for the unstable bands of Set I.* * There is good agreement for `waterbag_3_s0` for $t < 0.2$ Gyr, and for `waterbag_4_s0` for $0.05 < t < 0.15$ Gyr.

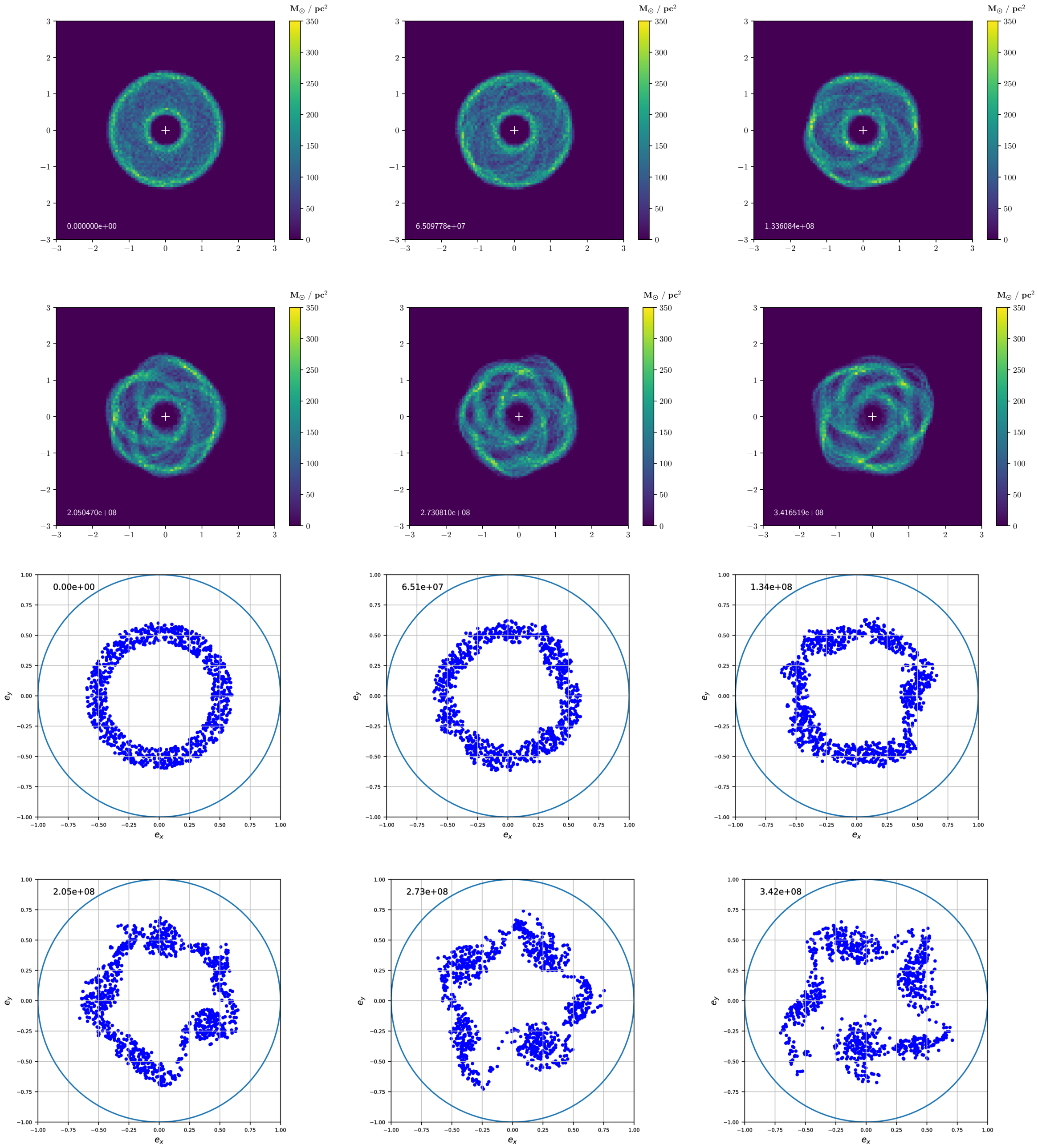

Fig. 2.11 *Similar to Fig. 2.6, but for* `waterbag_3_s0`. An $m = 4$ pattern emerges by ~ 0.06 Gyr.

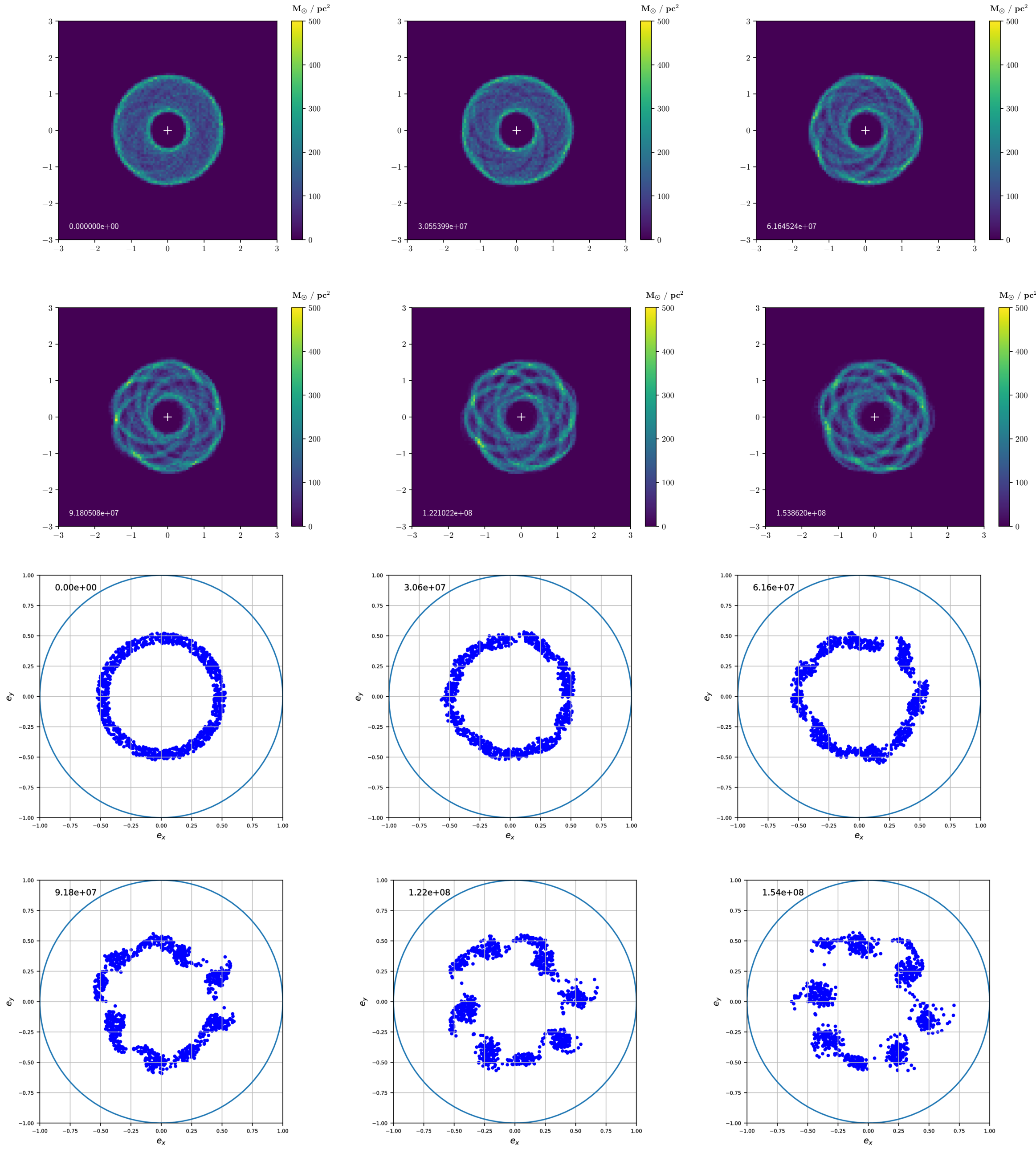

Fig. 2.12 *Similar to Fig. 2.6, but for* `waterbag_4_s0`. An $m = 6$ pattern emerges by ~ 0.03 Gyr.

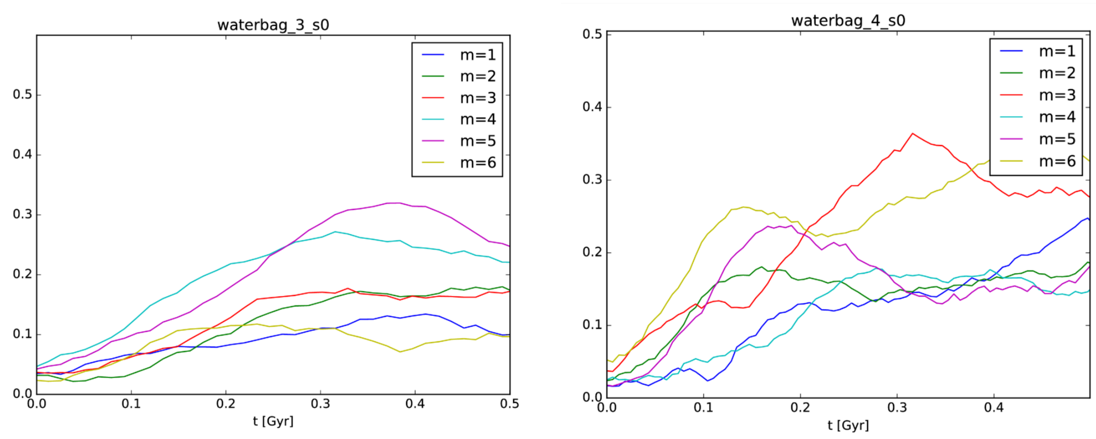

(a) `waterbag_3_s0` (b) `waterbag_4_s0`

Fig. 2.13 *Evolution of mode amplitudes* a_m. (a) `waterbag_3_s0`, (b) `waterbag_4_s0`.

2.5.2 Set II

The narrowest band in Table 2.1 is `waterbag_ℓ1_0.8_ℓ2_0.81`, with $\Delta\ell = 0.01$. According to linear theory this band is unstable to a wide range of modes with $m = 3 - 57$, with $m = 36$ having the fastest growth rate. Figure 2.14 shows the evolution of this narrow band, whose initial evolution shows an instability dominated by $m \sim 36$ mode, in agreement with linear theory.

Linear theory also predicts a transition from instability to stability when the lower boundary is held fixed at $\ell_1 = 0.8$ and the band is made broader by increasing ℓ_2. This transition occurs at $\ell_2 = \ell_{\rm crit} \simeq 0.963$: bands with $\ell_2 < \ell_{\rm crit}$ are unstable to various modes whereas broader bands with $\ell_{\rm crit} < \ell_2 < 1$ are stable for all m. In order to test this precise prediction, we ran a total of 20 simulations increasing ℓ_2 in steps of 0.01, from 0.81 to 1, and looked for signs of instabilities. From the last column of Table 2.1 we see that the simulations confirm linear theory, with the small difference that the transition seems to happen when ℓ_2 crosses 0.97, instead of the predicted value of 0.963.

2.5.3 Collisionless Relaxation

Here we discuss the long-term evolution of an unstable band, that goes well beyond the applicability of linear theory. The point of interest is in the collisionless relaxation to a state with a wide spread in eccentricities.

As instabilities unfold and non-linear interactions between modes dominate, what can we expect of evolution over long times? We have earlier in this section followed the short-time evolution of the unstable band `waterbag_3_s0`, with its initial growth

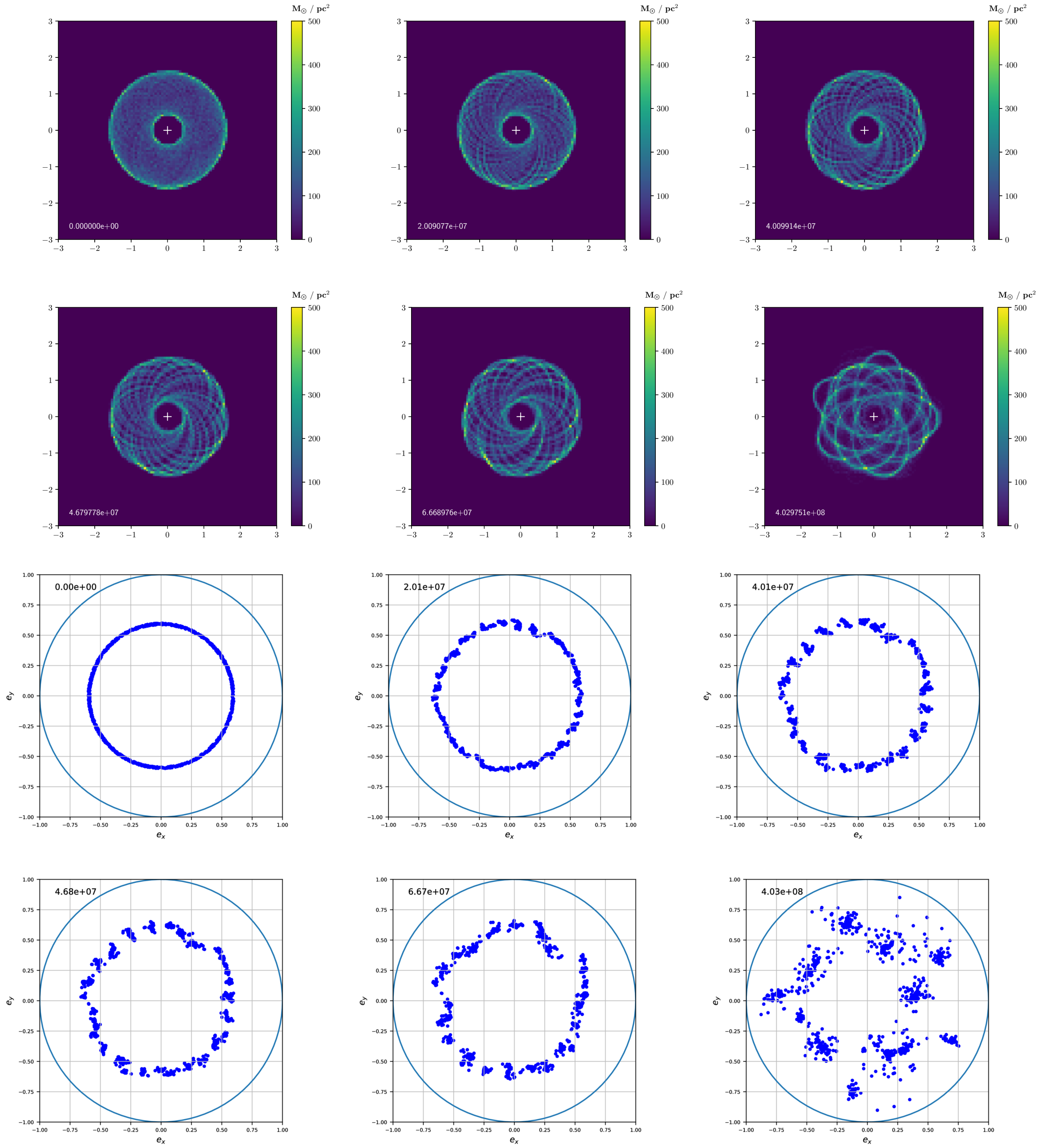

Fig. 2.14 *Similar to Fig. 2.6, but for* `waterbag_ℓ1_0.8_ℓ2_0.81`. A high m pattern emerges by ~ 0.02 Gyr.

of a dominant $m = 4$ mode over ~ 0.06 Gyr, followed by the rise of a $m = 5$ mode around ~ 0.2 Gyr lasting until at least ~ 0.34 Gyr. What happens after this? Here we follow the evolution for ~ 4 Gyr.

Figure 2.15 shows both the initial and final states of `waterbag_3_s0`. When compared with the intermediate states of Figure 2.11, the final state appears more axisymmetric. The final state also has a wider range of eccentricities than the initial state. It consists of a nearly circular high density ring, surrounded by a lower-density halo of particles with a wide range of eccentricities. The strong non-axisymmetric instabilities that plagued the initial state seem to have saturated, leaving behind a relaxed, coarse-grained state that is approximately axisymmetric and steady in time. The secular precessional timescale for the initial state is $T_{\rm sec} \sim 0.8$ Gyr, so the total duration of the run, 4 Gyr is about $5\,T_{\rm sec}$. This is too short a duration for a collisional process like resonant relaxation to be effective. Hence what we have witnessed must be collisionless relaxation, where non-axisymmetric instabilities provide the pathway for transition from one axisymmetric state to another.

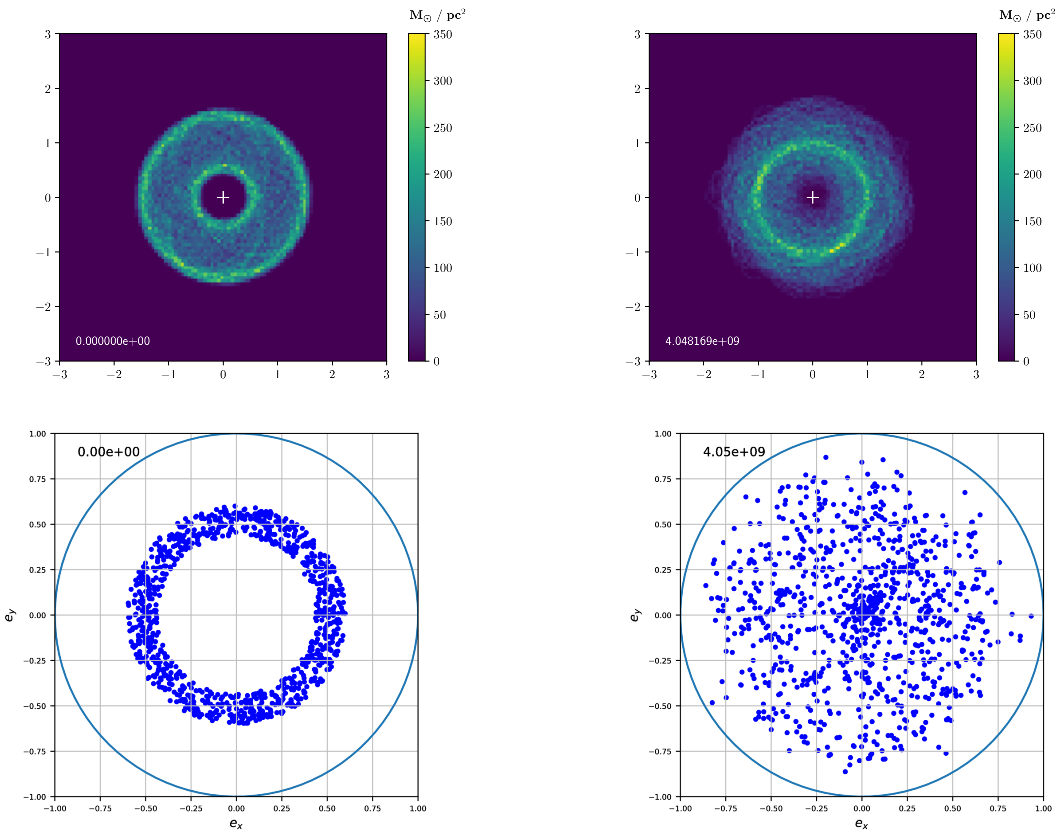

(a) Initial state (b) Relaxed state at 4.05 Gyr

Fig. 2.15 *Collisionless relaxation of* `waterbag_3_s0`.

2.6 Conclusions

Mono-energetic waterbags are the simplest models of low mass stellar discs around an MBH. We studied, analytically and numerically, the stability of initial states that are prograde and axisymmetric. These waterbags have a DF, $f_0(\ell)$, which is constant when $0 \leq \ell_1 \leq \ell \leq \ell_2 \leq 1$, and zero when ℓ is outside this range. There are two types of waterbags, polarcaps with $\ell_2 = 1$ and bands with $\ell_2 < 1$. The linear stability problem can be solved simply: for each m the growth rates of instabilities, pattern speeds of stable and unstable modes and the complete normal mode structure have been determined explicitly as functions of (ℓ_1, ℓ_2), the waterbag parameters.

- Polarcaps have one stable normal mode for each m, with the noteworthy feature that the $m = 1$ mode always has positive pattern speed. For a polarcap consisting of orbits with eccentricities $e < 0.94$, only the $m = 1$ mode has a positive pattern speed.
- Bands have two normal modes for each m, and can be either stable or unstable. Very narrow bands (with $\ell_1 \simeq \ell_2$) are unstable to modes with a wide range in m, whereas broad bands approaching a polarcap (with $\ell_2 \simeq 1$) are stable.

The evolution of instabilities was also explored through numerical simulations, which can span both linear and non-linear regimes. A variety of numerical experiments were performed which demonstrated good agreement with linear theory. Long-time integration showed the growth of instabilities of different m that interacted with each other non-linearly, then saturated and later relaxed collisionlessly into a quasi-steady state, with a wider range of eccentric orbits than the initial state. This suggests secular non-axisymmetric instabilities could provide pathways for stars to exchange angular momentum via the mean self-gravitational field, and spread out in eccentricities.

It is straightforward to extend our study to include external gravitational sources (such as nuclear density cusps or distant perturbers) and general relativity, as described in ST16a. But one clearly needs to go well beyond our simple models in order to study real systems, like the disc of young stars at the Galactic centre. We need to consider more general DFs and include orbits with a range of semi-major axes and inclinations. But self-gravitational dynamics poses difficult problems and secular dynamics is still in its infancy, so we need to build the tools step by step; describing the collisionless relaxation of even an unstable band remains a challenge for dynamists.

Chapter 3

Galactic Centre Stellar Cusp Deformation due to a Gas Disc

The Galactic centre (GC) NSC is an extended distribution of old stars of mass $\sim 2.5 \times 10^7$ $M_\odot$ with a half-light radius of about 4 pc (Genzel et al., 2010). The first high angular resolution observations seemed to imply that the old stars were distributed in a density cusp (Genzel et al., 2003; Schödel et al., 2007). But when the contamination of light from the young stars was accounted for, the old giant population appeared to have a core-like, rather than a cuspy, surface density profile (Buchholz et al., 2009; Do et al., 2009; Bartko et al., 2010; Fritz et al., 2016). Recent work by Gallego-Cano et al. (2018); Schödel et al. (2018) has refined our knowledge of the distribution of the old stars. Resolved faint stars (from deep star counts) and sub-giants and dwarfs (inferred from diffuse light) have a cuspy density profile, which is well-described by a single power-law within ~ 3 pc of central MBH. But the density profile of red clump and brighter giant stars rises toward the centre in a cuspy manner, but becomes core-like within about 0.3 pc. Some of these features of the GC NSC were discussed in § 1.1.1.

The compact young stellar distribution within 0.5 pc is believed to have formed in situ in a massive accretion disc around the MBH (Levin & Beloborodov, 2003). If this is the case then the young star cluster has evolved dynamically since its birth in the accretion disc. Repeated passages of the red clump and brighter giant stars through the dense inner parts of the accretion disc could have robbed them of their envelopes, rendering the innermost stars invisible; this would explain the difference between the core-like profiles of the old giants and the cuspy profiles of old stars lacking extended envelopes (Amaro-Seoane & Chen, 2014). In contrast the accretion disc's gravitational field will deflect the orbits of all old stars in the same manner.

What is the gravitational response of an old stellar cusp to the accumulation of gas in an accretion disc around the MBH?

In this chapter we address this question by constructing a simple model of the process within the radius of influence of the MBH, $r_{\rm infl} \simeq 2\,{\rm pc}$. The work presented is based on the paper Kaur & Sridhar (2018). The problem is stated in § 3.1 for a non-rotating, spherical stellar cusp with anisotropic velocity dispersions, which experiences gravitational perturbations due to a growing gas disc; we argue that disc growth is slow compared to typical apse precession periods of cusp orbits. In § 3.2 we cast the dynamical problem in terms of the secular theory of ST16a, which is its natural setting. In § 3.3 we derive a formula for the linear perturbation to the phase space DF: the magnitude of the perturbation is largest for orbits that are highly inclined with respect to the disc plane; it is positive when the angle between the lines of apsides and nodes is less than 45° and negative otherwise. This is explained in terms of the secular, adiabatic dynamics of individual orbits in the combined gravitational potentials of the cusp and disc. Linear theory accounts only for orbits whose apsides circulate. The non-linear theory of adiabatic capture into resonance is needed to understand orbits whose apsides librate. In § 3.4 we use the formula for the DF to compute the oblate spheroidal deformation of the three dimensional density profile of the cusp, as well as the surface density profiles for different viewing angles. We conclude in § 3.5 with a discussion of linear stability, extensions to rotating and axisymmetric cusps, and that the process studied in this paper may be common in galactic nuclei.

3.1 Statement of the problem

We are interested in describing stellar dynamics within 1 pc of a MBH of mass $M_\bullet = 4\times10^6\ {\rm M}_\odot$. Let $\boldsymbol{r}$ and $\boldsymbol{u}$ be the position vector and velocity of a star, relative to the MBH. Since this region is well inside $r_{\rm infl} \simeq 2\,{\rm pc}$, the dominant gravitational force on a star is the Newtonian $1/r^2$ attraction of the MBH. Hence the shortest timescale associated with a stellar orbit of semi-major axis a is its Kepler orbital period, $T_{\rm Kep}(a) \simeq 4.7\times10^4\, a_{\rm pc}^{3/2}$ yr where $a_{\rm pc} = (a/1\ {\rm pc})$.

3.1.1 The unperturbed stellar cusp

This is assumed to be spherically symmetric about the MBH, with a density profile

$$\rho_{\rm c}(r) \;=\; \frac{(3-\gamma)M_{\rm c}}{4\pi {r_{\rm c}}^3}\left(\frac{r_{\rm c}}{r}\right)^{\gamma}\,. \tag{3.1}$$

For the GC cusp $\gamma = 1.23 \pm 0.05$, and $M_{\rm c} = 10^6\ {\rm M}_\odot$ is the stellar mass within a radius $r_{\rm c} = 1$ pc of the MBH (Gallego-Cano et al., 2018; Schödel et al., 2018). The gravitational potential due to the cusp ($\gamma \neq 2$) is

$$\varphi_{\rm c}(r) \;=\; \frac{GM_{\rm c}}{(2-\gamma)r_{\rm c}} \left(\frac{r}{r_{\rm c}}\right)^{2-\gamma} , \tag{3.2}$$

where a constant additive term has been dropped. The cusp's spherically symmetric gravitational field will make the apsides of Kepler orbits precess in a retrograde sense in their respective orbital planes. The typical apse precession period is $T^{\rm c}_{\rm pr}(a) \sim (M_\bullet/M_{\rm ca})\, T_{\rm Kep}(a)$, where $M_{\rm ca} = M_{\rm c}\, a_{\rm pc}^{(3-\gamma)}$ is the mass in cusp stars inside a sphere of radius a. Then $T^{\rm c}_{\rm pr}(a) \sim 1.8 \times 10^5\, a_{\rm pc}^{(\gamma-3/2)}$ yr. Within a parsec the apse precession period is always longer than the Kepler orbital period. We assume that the distribution of these precessing orbits is such that, at every point in space, the mean velocity vanishes but the velocity distribution is anisotropic. This anisotropy is characterized by the parameter $\beta(r) = 1 - \left(\sigma_\theta^2 + \sigma_\phi^2\right)/2\sigma_r^2$, where the σ's are velocity dispersions along the three principal directions of a polar coordinate system centred on the MBH. When $\beta(r)$ is negative(positive) the velocity distribution is tangentially(radially) biased.

The cusp is described by a probability DF, $f_{\rm c}(\boldsymbol{r},\boldsymbol{u})$, in the six dimensional phase space, $\{\boldsymbol{r},\boldsymbol{u}\}$. For a non-rotating system with anisotropic velocity dispersion, the Jeans theorem implies that the unperturbed DF is a function of the energy per unit mass, $E = u^2/2 - GM_\bullet/r + \varphi_{\rm c}(r)$, and the magnitude of the angular momentum per unit mass $L = |\boldsymbol{r}\times\boldsymbol{u}|$ (Binney & Tremaine, 2008). Let us consider the double power-law DF,

$$f_{\rm c}(\boldsymbol{r},\boldsymbol{u}) \;=\; \begin{cases} \dfrac{A}{2\pi}\,(-E)^m\, L^n\,, & E \,<\, 0 \\[2ex] \quad 0\,, & E \,>\, 0\,, \end{cases} \tag{3.3}$$

which is composed entirely of bound orbits; $m > 0$ for the DF to be continuous at $E = 0$. For $r \leq 1$ pc the Kepler potential of the MBH dominates the cluster potential, so $E \simeq E_{\rm k} = u^2/2 - GM_\bullet/r =$ Kepler energy is a good approximation. Henceforth we will consider the DF of equation (3.3) to be a function of $E_{\rm k}$ and L. The reason we begin with a two–integral (anisotropic) DF, $f_c = F(E_k, L)$, rather than an isotropic DF, $F(E_{\rm k})$, is the following. We have to deal with the response of a Keplerian stellar system over timescales that are much longer than Kepler orbital periods. The Kepler energy, $E_{\rm k}$, is a secular invariant for processes that vary on (secular) times scales of the order of the apse precession periods, or longer. So a DF of the form, $F(E_{\rm k})$, would remain unchanged when perturbed by secularly varying gravitational potentials. Therefore we need to begin with at least a two–integral DF, in order to study non–trivial secular response.

There is one relation among the three parameters (A, m, n) due to the normalization of the DF, $\int f_{\rm c}\, {\rm d}\boldsymbol{r}\, {\rm d}\boldsymbol{u} = 1$. The density is obtained by integrating the DF over velocity space: $\rho_{\rm c}(r) = M_{\rm c} \int f_{\rm c}\, {\rm d}\boldsymbol{u}$, which is straightforward to do in the standard manner (Binney & Tremaine, 2008). Comparing with equation (3.1) gives two more relations between (A, m, n) and $(r_{\rm c}, \gamma)$. It is convenient to choose the independent parameters as $(r_{\rm c}, m, n)$ and write:

$$\begin{aligned} A &= \frac{3-\gamma}{4\pi\, 2^{\frac{n+1}{2}}\, B_{\left(\frac{n}{2}+1,\frac{1}{2}\right)}\, B_{\left(m+1,\frac{n+3}{2}\right)}\, {r_{\rm c}}^{3-\gamma}\, (GM_{\bullet})^{\gamma+n}}\,, \\ \gamma &= \frac{2m-n+3}{2}\,, \end{aligned} \tag{3.4}$$

where $B_{(p,q)}$ is the Beta function. It is also straightforward to calculate the velocity anisotropy, $\beta = -n/2$, which is now constant. We note that for the density to be finite, $n > -2$ (or $\beta < 1$), which puts an upper limit on how radially biased the double power-law DF of equation (3.3) can be.

3.1.2 The perturbing gas disc

Levin & Beloborodov (2003) proposed that the young stars at the GC were formed in situ, in a massive accretion disc around the MBH. As gas accumulated in the accretion disc it became gravitationally unstable in efficiently cooling regions with Toomre $Q \lesssim 1$, and fragmented into massive stars (Nayakshin, 2006; Levin, 2007). A thin gas disc that is supported by external irradiation prior to fragmentation can have a steep surface density, $\Sigma_{\rm d}(R) \propto R^{-3/2}$ according to Levin (2007). This is consistent with the steep surface density profile of the clockwise disc of young stars that lies within about 0.13 pc of the MBH (Paumard et al., 2006; Lu et al., 2009; Bartko et al., 2009; Yelda et al., 2014). We assume that the mass of the progenitor gas disc grew in time from some small value to a maximum value, just before the birth of the young stars. We need to choose a mass model representing an axisymmetric, thin accretion disc with surface density profile, $\Sigma_{\rm d}(R) \propto R^{-3/2}$. The gravitational potential of this mass model should be of a simple form, to enable explicit computation of the secular perturbation it exerts on the orbits of the old cusp stars. We found the following two-component model to be a suitable three dimensional density distribution:

$$\rho_{\rm d}(r,\theta,t) \;=\; \frac{2}{11\,\pi}\frac{M_{\rm d}(t)}{r_{\rm d}^3}\left(\frac{r_{\rm d}}{r}\right)^{5/2}\left[\delta\Big(\theta-\frac{\pi}{2}\Big) \;+\; \frac{9}{16}(1-|\cos\theta|)^2\right]\,, \tag{3.5}$$

where $M_{\rm d}(t)$ is the mass inside a sphere of radius $r_{\rm d} = 1$ pc at time t. The disc consists of two components: within a sphere of radius r, about 73% of its mass is in a razor-thin component confined to the equatorial plane; about 27% is in an extended but flattened corona. It is straightforward to verify that the gravitational potential due to $\rho_{\rm d}(r, \theta, t)$ is:

$$\varphi_{\rm d}(r,\theta,t) \;=\; -\frac{8}{11}\frac{G\,M_{\rm d}(t)}{r_{\rm d}}\left(\frac{r_{\rm d}}{r}\right)^{1/2}\left[\frac{9\,(33\,+\,\cos^2\theta)}{100}\;-\;\frac{|\cos\theta|}{2}\right]. \qquad (3.6)$$

We are interested in determining the perturbation caused by the time-dependent disc potential of equation (3.6) to the DF of equation (3.3). In order to do this we assume that $M_{\rm d}(t)$ grows monotonically on a timescale, $T_{\rm grow}$, to its maximum value, $M_{\rm dm}$, just before the birth of the young stars. We now estimate $M_{\rm dm}$ and $T_{\rm grow}$:

Disc mass: A circumnuclear disc (CND), composed of molecular clouds, orbits the MBH at distances $\sim 1.5 - 5$ pc (Gatley et al., 1986; Guesten et al., 1987; Yusef-Zadeh et al., 2001). The CND is presumably a remnant of the outer parts of the gas disc. If we assume that the total mass — but not the necessarily its distribution — in the annulus has not changed much over the last Myr, then we can estimate $M_{\rm dm}$ as follows. Since $\Sigma_{\rm d}(R) \propto R^{-3/2}$, the gas mass within R is $\propto R^{1/2}$, so we set $M_{\rm dm}\left(\sqrt{5} - \sqrt{1.5}\right) = M_{\rm CND}$. Estimates of $M_{\rm CND}$ range from 10^4 M$_\odot$ (Etxaluze et al., 2011; Requena-Torres et al., 2012) to 10^6 M$_\odot$ (Christopher et al., 2005). Adopting a mid-value, $M_{\rm CND} \sim 10^5$ M$_\odot$, we infer that $M_{\rm dm} \sim 10^5$ M$_\odot$, which is similar to the value suggested by Nayakshin & Cuadra (2005).

Growth time: $T_{\rm grow}$ depends on the agency that removes angular momentum from the gas flow at a radius of about a parsec. If it is accretion disc 'α-viscosity' then $T_{\rm grow} \sim T_{\rm Kep}(1\text{ pc})/(\alpha\xi^2)$, where $\alpha \sim 0.3$ for gravitationally induced turbulence (Gammie, 2001) and $\xi \lesssim 0.1$ is the half-opening-angle of the thin disc; this gives $T_{\rm grow} \gtrsim 1.5 \times 10^7$ yr. If angular momentum is lost through non-axisymmetric gravitational perturbations then $T_{\rm grow} \sim T_{\rm Kep}(1\text{ pc})/\delta_\varphi$ is the flow timescale, where δ_φ is the fractional non-axisymmetry in the gravitational potential at a radius of a parsec. Even for the pronounced $m = 1$ asymmetry of the nuclear disc of M31, $\delta_\varphi \sim 10^{-3} - 10^{-2}$ (Chang et al., 2007). Hence we expect, in either case, that $T_{\rm grow} \gtrsim 10^7$ yr for the GC accretion disc.

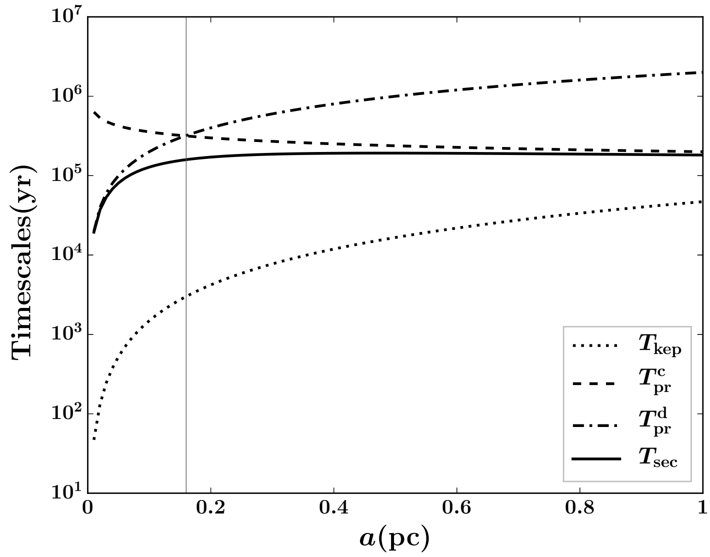

Fig. 3.1 *Timescales in the problem, as functions of the semi-major axis*: The thin vertical line corresponds to $a = 0.16$ pc for which $T^{\rm c}_{\rm pr} = T^{\rm d}_{\rm pr}$.

3.1.3 Adiabatic nature of the perturbation

The perturbation due to the disc contributes to both apsidal and nodal precession. We can estimate the perturbation by imagining gas of total mass, $M_{\rm dm} = 10^5$ M$_\odot$, to be distributed spherically symmetric with density profile $\propto r^{-5/2}$, instead of being highly flattened as given by equation (3.5). Such a spherically symmetric approximation to the perturbation does not cause nodal precession but contributes to retrograde apse precession over times, $T^{\rm d}_{\rm pr}(a) \sim (M_\bullet/M_{\rm da})\, T_{\rm Kep}(a)$, where $M_{\rm da} = 10^5\, a^{1/2}_{\rm pc}$ M$_\odot$ is the disc mass inside a sphere of radius a. Then $T^{\rm d}_{\rm pr}(a) \sim 2 \times 10^6\, a_{\rm pc}$ yr is an increasing function of a. This should be compared with the retrograde apse precession period due to the cusp stars, $T^{\rm c}_{\rm pr}(a) \sim 2 \times 10^5\, a^{-1/4}_{\rm pc}$ yr (for a fiducial value of $\gamma = 5/4$), which is a decreasing function of a. Since the apse precession due to gas and stars are both retrograde, the net precession frequency is the sum of the individual frequencies. The corresponding precession period then provides the natural timescale for secular dynamics, $T_{\rm sec}(a) = T^{\rm c}_{\rm pr}(a)\, T^{\rm d}_{\rm pr}(a)/\left[T^{\rm c}_{\rm pr}(a) + T^{\rm d}_{\rm pr}(a)\right]$. These different timescales, together with the short Kepler orbital period, $T_{\rm Kep}(a)$, are plotted in Figure 3.1. As can be seen, the net precession period, $T_{\rm sec}(a)$, is dominated by the disc mass for $a < 0.16$ pc and by the cusp mass for $a > 0.16$ pc. This precession period attains its maximum value of about 2×10^5 yr within 1 pc, which is much shorter than the estimate of $T_{\rm grow} \gtrsim 10^7$ yr, the growth time of the disc. Hence the perturbation may be assumed to be adiabatic.[1]

[1]Our estimates of apse precession periods accounted only for the sizes of stellar orbits (i.e. semi-major axes a), but not for orbital eccentricities. Highly eccentric orbits precess very slowly

3.2 Secular collisionless dynamics

We have three well-separated timescales in the problem. These are the short Kepler orbital period, $T_{\rm Kep}(a) \simeq 4.7\times 10^4\, a_{\rm pc}^{3/2}$ yr; the long timescale of disc growth, $T_{\rm grow} \gtrsim 10^7$ yr; and the intermediate secular time scale, $T_{\rm sec}(a) \lesssim 2\times 10^5$ yr: we always have $T_{\rm Kep}(a) \ll T_{\rm sec}(a) \ll T_{\rm grow}$ for $a \leq 1$ pc. In order to study the evolution of the cusp DF over times greater than $T_{\rm sec}(a)$, we can average the orbit of every star over the rapidly varying Kepler orbital phase. The appropriate framework to do this is the secular theory of collisionless evolution (ST16a), which is described in § 1.3.

3.2.1 The cusp-disc system

We are now in a position to formulate our problem in terms of the above description of secular collisionless dynamics.

The unperturbed cusp: The secular DF for the spherical unperturbed cusp is

$$F_0(I,L) \;=\; 2\pi\, f_{\rm c}(E_{\rm k},L) \;=\; \frac{A\,(GM_\bullet)^{2\,m}\,L^n}{2^m\,I^{2\,m}}\,, \tag{3.7}$$

where we have used equation (3.3). The corresponding (scaled) orbit-averaged potential, $\Phi_{\rm c}(I,L)$, is related to F_0 through equation (1.11)-(1.12), but we do not need to use this; it is easier to orbit-average equation (3.2). Then we get $\Phi_{\rm c}(I,L) = (M_\bullet/M_{\rm c})\oint \varphi_{\rm c}(r)\,{\rm d}w/2\pi$, is proportional to a hypergeometric function, but the following approximate expression will suffice for our purposes:[2]

$$\Phi_{\rm c}(I,L) \;=\; \frac{GM_\bullet}{(2-\gamma)\,r_{\rm c}}\left(\frac{a}{r_{\rm c}}\right)^{2-\gamma}(1+\alpha_\gamma\,e^2)\,, \qquad \text{where} \quad \alpha_\gamma \;=\; \frac{2^{3-\gamma}\,\Gamma(\frac{7}{2}-\gamma)}{\sqrt{\pi}\,\Gamma(4-\gamma)} \;-\;1\,. \tag{3.8}$$

This formula is exact for $\gamma=1$, and a good approximation for our fiducial value, $\gamma = 5/4$. $\Phi_{\rm c}(I,L)$ acts as the Hamiltonian for secular dynamics so the apse precession frequency, ${\rm d}g/{\rm d}\tau = \Omega_{\rm c}(I,L)$, is:

$$\Omega_{\rm c}(I,L) \;=\; \frac{\partial\Phi_{\rm c}}{\partial L} \;=\; -\,\frac{2\,\alpha_\gamma}{2-\gamma}\,\Omega_{\rm kep}(r_{\rm c})\,\frac{I^{3-2\,\gamma}}{(GM_\bullet\,r_{\rm c})^{\frac{3}{2}-\gamma}}\,\frac{L}{I}\,, \tag{3.9}$$

where $\Omega_{\rm kep}(r_{\rm c}) = (GM_\bullet/r_c^3)^{1/2}$ is the Kepler frequency for an orbit of semi–major axis $r_{\rm c}$. Since $\Omega_{\rm c} \propto -a^{(3/2-\gamma)}\sqrt{1-e^2}$, the (retrograde) apse precession is fastest for

– see equation (3.9) – and the adiabatic approximation is not valid for these; this is discussed in § 3.3.2.

[2] Both the exact expression and the approximation are given in equations (4.81) and (4.82) of Merritt (2013).

near-circular orbits and and slowest for highly eccentric orbits. Moreover for $\gamma < 3/2$, which is of interest to us, orbits of smaller a precess slower.

Orbit-averaged disc perturbation: $\Phi_\mathrm{d}(I, L, L_z, g, \tau) = (M_\bullet/M_\mathrm{c})\oint \varphi_\mathrm{d}(r, \theta, t)\mathrm{d}w/2\pi$ can be written in terms of Elliptic integrals for the potential of equation (3.6), as given in Appendix C. The following approximation, which is convenient for calculations, has a maximum fractional error $\lesssim 2\%$:

$$\begin{aligned}\Phi_\mathrm{d} \;=\; & \frac{16\,GM_\bullet}{11\pi\, r_\mathrm{c}}\mu(\tau)\sqrt{\frac{r_\mathrm{d}}{a}}\Bigg[-\frac{9}{100}\sqrt{1+e}\;\mathcal{E}(k)\left(33+\frac{\sin^2 i}{2}\right)+ \\ & \frac{\sin i}{2}\left(1+a_0e^2+b_0e^4+c_0e^6\right)-\left(\frac{\lambda}{2}\sin i-\frac{9}{100}\sin^2 i\right)\left(a_te^2+b_te^4+c_te^6\right)\cos 2g\Bigg]\,,\end{aligned} \tag{3.10}$$

where $k = \sqrt{2e/(1+e)}$, $\mathcal{E}(k)$ is the complete elliptic integral of second kind defined in equation (C.3), and $a_0 = -0.0742572$, $b_0 = 0.0417887$, $c_0 = -0.0672152$, $\lambda = 0.848835$, $a_t = 0.495367$, $b_t = -0.492259$, $c_t = 0.703998$. Here $\mu(\tau) = [M_\mathrm{d}(\tau)r_\mathrm{c}/M_\mathrm{c}r_\mathrm{d}]$ is a time-dependent small parameter characterizing the strength of the disc perturbation relative to the cusp: $\mu(\tau) \to 0$ as $\tau \to -\infty$ and μ takes its largest value of 0.1 when $M_\mathrm{d} = 10^5\ \mathrm{M}_\odot$.

Secular evolution of the cusp DF: The spherical cusp DF of equation (3.7) responds to the time-dependent, axisymmetric disc potential of equation (3.10). The DF of the axisymmetrically deforming cusp must be independent of the nodal longitude h, and takes the general form, $F(I, L, L_z, g, \tau)$. Let $\Phi(I, L, L_z, g, \tau)$ be the (scaled) self-gravitational potential, which is related to F through equation (1.11). The secular Hamiltonian is,

$$H(I, L, L_z, g, \tau) \;=\; \Phi(I, L, L_z, g, \tau) \;+\; \Phi_\mathrm{d}(I, L, L_z, g, \tau)\,. \tag{3.11}$$

Since both F and H are independent of h, the CBE of equation (1.16) simplifies to,

$$\frac{\partial F}{\partial \tau} \;+\; \frac{\partial H}{\partial L}\frac{\partial F}{\partial g} \;-\; \frac{\partial H}{\partial g}\frac{\partial F}{\partial L} \;=\; 0\,. \tag{3.12}$$

Both $I = \sqrt{GM_\bullet a}$ and $L_z = I\sqrt{1-e^2}\,\cos i$ are secular integrals of motion, even though H is time-dependent. If H were time-independent, it is itself a third integral of motion; in contrast to un-averaged stellar dynamics, all time-independent, axisymmetric secular dynamics is integrable (Sridhar & Touma, 1999). Then the secular Jeans theorem (ST16a) implies that a steady state F must be function of (I, L_z, H). We need to solve the problem for an adiabatically varying H.

3.3 Adiabatic response of the stellar cusp

The time-dependence of H is due to disc growth over times, $T_{\rm grow} \gtrsim 10^7$ yr, that are much longer than $T_{\rm sec} \lesssim 2 \times 10^5$ yr. In this case H is not conserved, but the principle of adiabatic invariance can be used to calculate a new action, $J = \oint L(H, I, L_z, g, \tau)\, \mathrm{d}g/2\pi$, that is conserved for orbits that are far from a separatrix, and undergoes a probabilistic change which can be calculated for orbits encountering a separatrix (Goldreich & Peale, 1966; Henrard, 1982); the corresponding evolution of the DF was worked out in Sridhar & Touma (1996) – see § 3.3.2 for a more detailed discussion of these points. The non-linear, axisymmetric, adiabatic response is an integrable and solvable problem. We derive an explicit formula for the linear response of the DF, due to the growing disc potential while neglecting the change in the cusp potential, as discussed below. This is used in the next section to calculate the density deformation. Then we study orbital structure: this provides a physical interpretation of the linear deformation, clarifies the limits of linear theory and sets the stage for the non-linear theory of adiabatic deformation.

3.3.1 Linear adiabatic response

The unperturbed cusp has DF $F_0(I, L)$ and Hamiltonian $H_0 = \Phi_{\rm c}(I, L)$. As the disc grows the cusp DF is $F = F_0(I, L) + F_1(I, L, L_z, g, \tau)$, with the corresponding new Hamiltonian $H = H_0 + H_1$ where $H_1 = \Phi_{\rm d}(I, L, L_z, g, \tau) + \Phi_1(I, L, L_z, g, \tau)$. Here Φ_1 is the (scaled) self-gravitational potential due to F_1, and related to it through the Poisson integral of equation (1.11):

$$\Phi_1(I, L, L_z, g, \tau) \;=\; \int F_1(I, L, L_z, g, \tau)\, \Psi(\mathcal{R}, \mathcal{R}')\, \mathrm{d}\mathcal{R}' \,. \tag{3.13}$$

From the discussion of timescales in § 3.1.3, we expect that disc perturbation is small for $a \gtrsim 0.2$ pc. Substituting for F and H in the CBE of equation (3.12), and keeping only terms linear in the small quantities, $\{F_1, \Phi_{\rm d}, \Phi_1\}$, we obtain the linearized collisionless Boltzmann equation (LCBE) governing the evolution of F_1 :

$$\frac{\partial F_1}{\partial \tau} \;+\; \Omega_{\rm c}(I, L)\, \frac{\partial F_1}{\partial g} \;\;=\;\; \frac{\partial F_0}{\partial L}\frac{\partial}{\partial g}\left\{\Phi_{\rm d} + \Phi_1\right\} . \tag{3.14}$$

The price to be paid for linearization is that we will not be able to describe capture into resonance (which is discussed later in § 3.3.2).

Since Φ_1 is given as an integral over F_1, the LCBE is a linear integro-differential equation for the unknown F_1. Calculating even this linear response requires substantial numerical computations. For a first cut at the problem we proceed by dropping Φ_1 (the likely effect of this would be to underestimate the response of the cusp). Then the right side of equation (3.14), $(\partial\Phi_\mathrm{d}/\partial g)$, represents only the known driving due to the disc, and the LCBE reduces to a linear partial differential equation. Further simplification occurs because of the adiabaticity of the problem, which was established in § 3.1.3: the first term on the left side, $(\partial F_1/\partial\tau)$, is smaller than the second term, $\Omega_\mathrm{c}(\partial F_1/\partial g)$, by a factor $(T^\mathrm{c}_\mathrm{pr}/T_\mathrm{grow}) \sim 2\times 10^{-2}$. Hence, dropping $\partial F_1/\partial\tau$, we can integrate over g to find F_1. [3] The physical solution cannot have a g-independent part because such a deformation is not allowed through collisionless, secular Hamiltonian deformations in phase space. Therefore

$$F_1(I, L, L_z, g, \tau) \;=\; \frac{1}{\Omega_\mathrm{c}(I, L)}\frac{\partial F_0}{\partial L}\left[\,\Phi_\mathrm{d} \;-\; \langle\Phi_\mathrm{d}\rangle_g\,\right], \qquad (3.15)$$

where $\langle\Phi_\mathrm{d}\rangle_g = \oint \Phi_\mathrm{d}\,\mathrm{d}g/2\pi$. Using the purely g-dependent part on the right side of equation (3.10), together with equations (3.9) and (3.7), we obtain the following explicit expression:

$$F_1 \;=\; \frac{D(\tau)}{(GM_\bullet r_\mathrm{c})^{3/2}}\,\frac{r_\mathrm{c}}{a}\,(1-e^2)^{\left(\frac{n}{2}-1\right)}\left(a_t e^2 + b_t e^4 + c_t e^6\right)\left(\frac{\lambda}{2}\sin i - \frac{9}{100}\sin^2 i\right)\cos 2g\,,$$

$$\text{where}\qquad D(\tau) \;=\; \frac{4n\,(2-\gamma)(3-\gamma)}{11\pi^2\,\alpha_\gamma\,2^{(\gamma+n)}\,B_{\left(\frac{n}{2}+1,\frac{1}{2}\right)}\,B_{\left(m+1,\frac{n+3}{2}\right)}}\sqrt{\frac{r_\mathrm{d}}{r_\mathrm{c}}}\;\mu(\tau)\,. \qquad (3.16)$$

The secular linear deformation has been written in terms of physical variables, instead of Delaunay variables, so we can read-off its general properties:

1. $F_1 \propto a^{-1}$ is independent of the cusp power-law index because γ cancels out in the ratio, $\Omega_\mathrm{c}^{-1}\,(\partial F_0/\partial L)$, in equation (3.15). The magnitude of F_1 increases with decreasing a because the perturbing gas density rises steeply at small radii. Linear theory requires that $|F_1| \ll |F_0| \propto a^{3/2-\gamma}$, so applies at small a only when $\gamma > 5/2$. For the shallow cusp we consider, $\gamma \approx 5/4$, equation (3.16) would not correctly represent the perturbation at small a.

[3] Since $|\Omega_\mathrm{c}| \propto a^{(3/2-\gamma)}\sqrt{1-e^2}$ decreases as a decreases (for $\gamma < 3/2$), and e increases, this assumption is not valid for small and/or highly eccentric orbits. But we need to account for non-linear effects long before we face this limitation of the adiabatic approximation in the linear theory itself. This is discussed later in this section.

2. The magnitude of F_1 is an increasing function of the inclination, i, because F_1 is proportional to the g-dependent part of the disc potential, whose effect increases with inclination.

3. For $n \leq 2$, the magnitude of F_1 is an increasing function of the eccentricity, e. For $n > 2$ orbits with intermediate values of e contribute the most, because the unperturbed cusp has very tangentially biased velocity dispersions.

4. Since $F_1 \propto \cos 2g$ it is positive/negative for orbits whose angles between their lines of apses and nodes is lesser/greater than $45°$. F_1 is positive and maximum for $g = (0°, 180°)$, and negative and minimum for $g = (90°, 270°)$.

Of the four properties the first three pertain to the magnitude of F_1. The fourth item alone determines the sign of F_1, and hence the flattening of the cusp. In order to understand this physically it is necessary to work out the broad characteristics of the individual orbits making up the stellar system. This also enables an appreciation of what is involved in calculating non-linear, adiabatic response.

3.3.2 Orbital structure and non-linear theory

The Hamiltonian governing orbital structure is $H(I, L, L_z, g, \tau) = \Phi_{\rm c} + \Phi_{\rm d}$. Using equations (3.8) and (3.10) we have:

$$H = \frac{GM_\bullet}{r_{\rm c}}\left[\frac{1}{(2-\gamma)}\left(\frac{a}{r_{\rm c}}\right)^{2-\gamma}(1+\alpha_\gamma e^2) + \frac{16\mu(\tau)}{11\,\pi}\sqrt{\frac{r_{\rm d}}{a}}\left\{\frac{-9}{100}\sqrt{1+e}\,\mathcal{E}\,(k)\left(33+\frac{\sin^2 i}{2}\right)\right.\right.$$
$$\left.\left.+\frac{\sin i}{2}\left(1+a_0e^2+b_0e^4+c_0e^6\right) - \left(\frac{\lambda}{2}\sin i - \frac{9}{100}\sin^2 i\right)(a_te^2+b_te^4+c_te^6)\cos 2g\right\}\right]. \tag{3.17}$$

As we discussed at the end of § 3.2, this time-dependent Hamiltonian always has two integrals of motion, $I = \sqrt{GM_\bullet a}$ and $L_z = I\sqrt{1-e^2}\,\cos i$. Therefore the eccentricity and inclination execute coupled oscillations: when e increases i decreases, while $a =$ constant. In order to say more about orbits we need some information on the time-dependence of H, which arises through the parameter $\mu(\tau)$.

'Time-frozen' Hamiltonian: Were $\mu(\tau) =$ constant, H would be time-independent, and is itself the third integral of motion. Orbital dynamics can be visualized by first fixing some values of (I, L_z), and drawing isocontours of H in the (L, g) phase plane, for $L \geq |L_z|$. For $\mu = 0$ we have $H = \Phi_{\rm c}(I, L)$, so the isocontours are just $L =$ constant horizontal lines. For $\mu \neq 0$ the isocontours have a more complicated

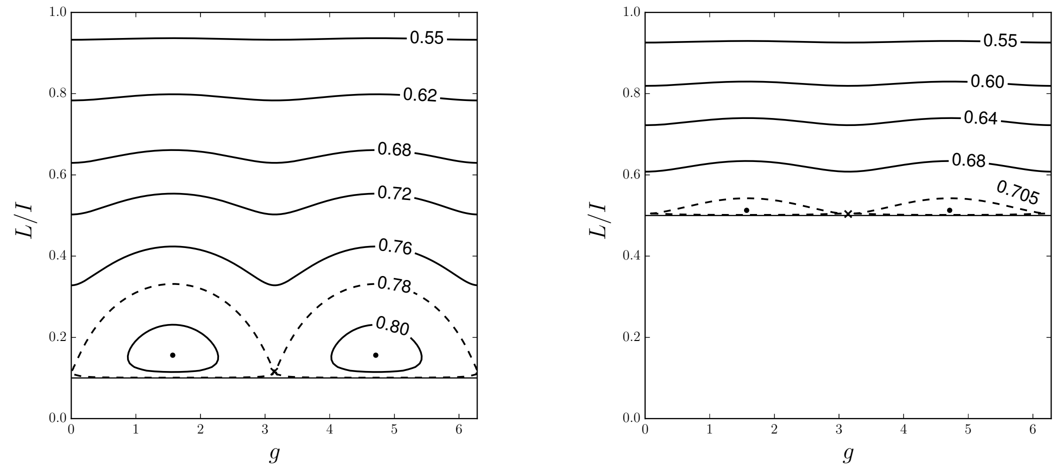

(a) $L_z/I = 0.1$ (b) $L_z/I = 0.5$

Fig. 3.2 *Isocontours of $H(I, L, L_z, g)$ in the (L, g) phase plane*, in units of $GM_\bullet/r_{\rm c}$, for $\mu = 0.1$ and a $= 0.5$ pc. The exact expressions for $\Phi_{\rm c}$, given in equation (4.81) of Merritt (2013), and $\Phi_{\rm d}$, given in equation (C.13), have been used.

topology: these are displayed in Figure 3.2 for $\mu = 0.1$ (its maximal value), $a = 0.5$ pc and two different values of L_z. The orbital structure shares the following generic features of secular dynamics in time-independent, axisymmetric potentials around a MBH (Sambhus & Sridhar, 2000; Merritt, 2013):

Circulating orbits, for which g advances by 2π over one period. These can be thought of as perturbations of the $L =$ constant orbits of the $\mu = 0$ case, exhibiting periodic oscillations of both L and g. The perturbations need not necessarily be small, but they are small enough so that the basic topology of the orbit remains unchanged.

Librating orbits, for which g librates periodically about $g = (\pi/2, 3\pi/2)$. These populate two 'islands' parented by two elliptic fixed point orbits (marked by the dots), which correspond to Kepler ellipses of fixed (a, e, i, g) whose nodes precess at a steady rate.

Two Separatrix orbits (dashed lines) that meet at the hyperbolic fixed points at $g = (0, \pi)$. These partition the phase plane into circulating and librating orbits. The period of a separatrix orbit is infinite, as apse precession slows down terminally near the fixed points.

Adiabatically varying Hamiltonian: When $\mu(\tau)$ varies slowly with time, H is no longer an integral of motion. At early times $\mu \to 0$ so $H \to \Phi_{\rm c}(I, L)$, which is just the unperturbed cusp. All orbits circulate at constant L, corresponding to

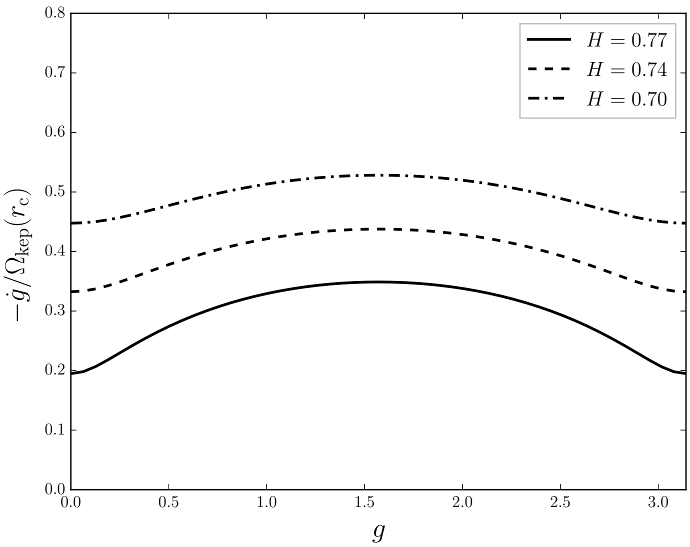

Fig. 3.3 *Apse precession rates for three circulating orbits* in the phase plane of Figure 3.2a, for $H = 0.70,\ 0.74,\ 0.77$.

retrograde apse precession at the constant rate $\Omega_{\rm c}(I, L)$ of equation (3.9). As $\mu(\tau)$ increases two islands appear around the elliptic fixed points, together with their separatrices. As $\mu(\tau)$ increases the separatrices expand and the islands grow until their areas attain a maximum when $\mu = 0.1$. There are two cases to consider:

(1) *Adiabatic invariance and linear theory*: For circulating orbits that do not ever encounter the growing separatrices, $\mu(\tau)$ may be considered to be slowly varying. Then $J = \oint L(H, I, L_z, g, \tau)\, {\rm d}g/2\pi$ is an adiabatic invariant, so we have three secular integrals of motion, (I, L_z, J). The secular Jeans theorem implies that the full, non-linear DF is of the form $F(I, L_z, J)$. The linear response calculation of § 3.3.1 is a particular case, valid for those circulating orbits that remain close to an unperturbed $L =$ constant orbit. In this case $F = F_0(I, L) + F_1(I, L, L_z, g, \tau)$, where F_0 and F_1 are given in equations (3.7) and (3.16). We can now understand the general form of F_1, by following individual circulating orbits.

From Figure 3.2 and the conservation of $L_z = L\cos i$, we see that both L and i take their smallest values at $g = (0°, 180°)$, and their largest values at $g = (90°, 270°)$. Figure 3.3 shows the (retrograde) apse precession rate, $\dot{g} = \partial H/\partial L$, as a function of g, for three circulating orbits taken from the left panel of Figure 3.2. Apse precession is slowest at $g = (0°, 180°)$, and fastest at $g = (90°, 270°)$. Since the orbit spends the most time where it precesses slowest, we expect a positive perturbation to the DF near $g = (0°, 180°)$, when the orbit also attains its maximum eccentricity and minimum inclination. Precisely the opposite behaviour obtains near $g = (90°, 270°)$. All of these contribute to an over-density in the perturbation close to the disc plane, and an under-density away from the disc plane, thereby flattening the cusp. Indeed the density deformation ρ_1, shown in Figure 3.4a, has this expected form.

(2) *Adiabatic capture and non-linear theory*: When a circulating orbit encounters one of the growing separatrices, it will be captured into the respective island and become a librating orbit. We now discuss the generic situation, which includes cases when one or both separatrices shrink.

Adiabatic invariance is broken in the vicinity of a time-dependent separatrix, both on the librating and circulating sides. This is because the orbital periods are formally infinite on the separatrices, and there is a band of actions around the separatrices for which the orbital periods are longer than the time of variation of the self-consistent Hamiltonian. This band, which includes the unstable fixed points, is very narrow in the adiabatic limit. But for orbits within it, the movement of the separatrices is not slow, and the dynamics within the band is chaotic because the orbit–separatrix encounter is very sensitive to the phase of the encounter. The behaviour of the orbit has been described in probabilistic terms in the planetary dynamics literature (Goldreich & Peale, 1966; Henrard, 1982); i.e. in terms of the probabilities of capture into, or escape from the islands of libration. Sridhar & Touma (1996) reconsidered this general problem in terms of the collisionless behaviour of a distribution of particles, and showed that the capture/escape probabilities can be calculated, without doing the detailed non-linear dynamics of the encounter of an orbit with a separatrix. We note their main results, and discuss it in the context of our problem:

- Let f be the fine-grained DF of the particles that obeys the CBE, whose Hamiltonian (which could be self-consistent or not) allows for a resonant island bounded by separatrices, which distort over timescales much longer than generic orbital periods (by generic we mean orbits that do not lie in the narrow band discussed above). Even if f was a smooth function to begin with, the chaotic orbit-separatrix encounter discussed above results in the post-encounter DF acquiring extremely fine-grained structure within the narrow band around the separatrix.

- We begin by noting that, at any given time, the band around the separatrices is very narrow. Then the fine-grained structure is essentially reflected in a rapid dependence of f as a function of the instantaneous angle variable. Hence it seems natural to introduce a coarse-grained DF, $\bar{f}$, which equals f averaged over the instantaneous angle variable.

- By using the conservation of the total mass in the coarse-grained DF, $\bar{f}$, Sridhar & Touma (1996) derived the evolution of $\bar{f}$ in phase space at any given time: (i) Away from the separatrices $\bar{f}$ retains its adiabatic invariant form, for both circulating and librating orbits; (ii) In the immediate vicinity of the separatrices, $\bar{f}$ undergoes changes, as listed in Table 1 of their paper. These rules are consistent with the classical expressions for capture probabilities, derived in planetary dynamics.

- The rules governing the changes in $\bar{f}$ near the separatrices are such that all entropy (or $\mathcal{H}$) functions associated with it grow in time (in contrast all entropy functions computed with respect to the fine-grained DF, f, are conserved during collisionless evolution). Hence the coarse-grained evolution is both mixing and irreversible, which should not be surprising because the nonlinear dynamics within the band around the separatrices is chaotic.

In the context of the cusp-disc problem studied in this chapter, the islands grow monotonically from vanishingly small sizes in the distant past. Hence every librating orbit was once a circulating orbit that was captured by the growing separatrices. Since the DF inside the islands is built up over time by capturing circulating orbits, the DF for the librating orbits depends on the entire time evolution of the system, in contrast to the case discussed above when J was conserved. The secular adiabatic evolution of an axisymmetric system — even when the self-gravity of the perturbation is included — is an integrable problem. So the full non-linear problem, with application of the rules from Sridhar & Touma (1996), can be computed in a definite manner, but this is beyond the scope of work presented here.

3.4 Spheroidal flattening of the cusp

Here we compute the deformation of the three dimensional density, and the surface density as seen from different viewing angles. The density perturbation can be calculated by integrating F_1 of equation (3.16) over velocity space. This can be carried through analytically (see Appendix D), and the result is:

$$\rho_1(r,\theta,\tau) \;=\; \frac{M_{\rm c}}{2\pi}\int F_1(I,L,L_z,g,\tau)\,{\rm d}\boldsymbol{u} \;=\; \frac{3-\gamma}{4\pi}\,C_{n,\gamma}(\tau)\,\frac{M_{\rm c}}{{r_{\rm c}}^3}\left(\frac{r_{\rm c}}{r}\right)^{\frac{5}{2}}\Theta(\theta)\,, \quad (3.18)$$

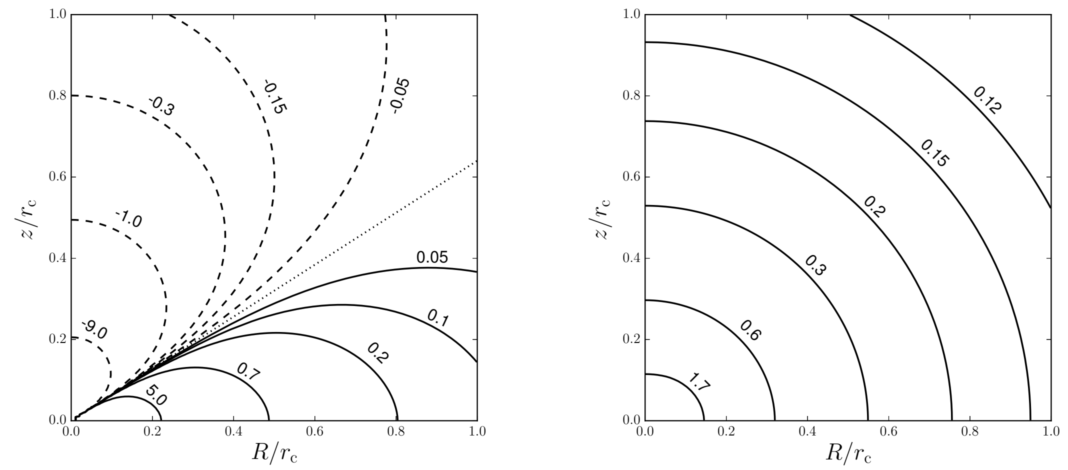

(a) Density perturbation, ρ_1 ($10^{-2}\, M_\mathrm{c}/{r_\mathrm{c}}^3$) (b) Total density, ρ ($M_\mathrm{c}/{r_\mathrm{c}}^3$)

Fig. 3.4 *Cusp deformation*: Isocontours of three dimensional densities, for $\gamma = 5/4$ and $n = 1/2$. [Left Panel] Solid curves are for $\rho_1 > 0$, and dashed curves are for $\rho_1 < 0$; the dotted straight line at $\theta = 57.37°$ is for $\rho_1 = 0$. [Right Panel] Isocontours of the total density, ρ, showing an oblate spheroidal deformation.

$$\text{where} \qquad \Theta(\theta) \;=\; \frac{\lambda}{2\pi}\left[\mathcal{E}(\sin\theta) \;-\; 2\cos^2\theta\,\mathcal{K}(\sin\theta)\right] \;-\; \frac{9}{400}(1 \;-\; 3\cos^2\theta)\,;$$

$$C_{n,\gamma}(\tau) \;=\; \frac{16n\,(2-\gamma)\,\mathcal{B}(n,\gamma)}{11\pi\, 2^{\left(\gamma-\frac{1}{2}\right)}\,\alpha_\gamma}\sqrt{\frac{r_\mathrm{d}}{r_\mathrm{c}}}\,\mu(\tau)\,. \tag{3.19}$$

Here $\mathcal{B}(n,\gamma)$ is a function of the indices, (n,γ), of the unperturbed spherical cusp, as given in equation (D.13). It should be noted that the dependence of ρ_1 on r and θ is independent of (n,γ).

This expression for ρ_1 is valid only when the F_1 of equation (3.16) is a reasonable approximation. This would be true for many of the circulating orbits of Figure 3.2 but not for the librating orbits that are trapped in the islands, as discussed in the previous section. For any (I, L_z) the librating orbits occur for the lowest values of L, so linear theory cannot be expected to work well when the unperturbed cusp has radially anisotropic velocity dispersions. But the GC cusp is probably tangentially anisotropic, with $\beta \approx -1/4$ for $r < 2$ pc (Feldmeier-Krause et al., 2017), so we can expect the linear theory result of equation (3.18) to be a useful first approximation.

Figure 3.4a shows the isocontours of ρ_1 in the (R,z) meridional plane, for $\gamma = 5/4$ and $n = -2\beta = 1/2$, for which $\mathcal{B}(1/2, 5/4) = 2.41$. The density perturbation $\propto r^{-5/2}$ rises steeply with decreasing r, similar to the density of the perturbing disc, ρ_d. It is positive close to the equatorial plane of the disc (for $57.37° < \theta < 122.63°$) and negative otherwise, a property that is independent of the cusp parameters (n,γ).

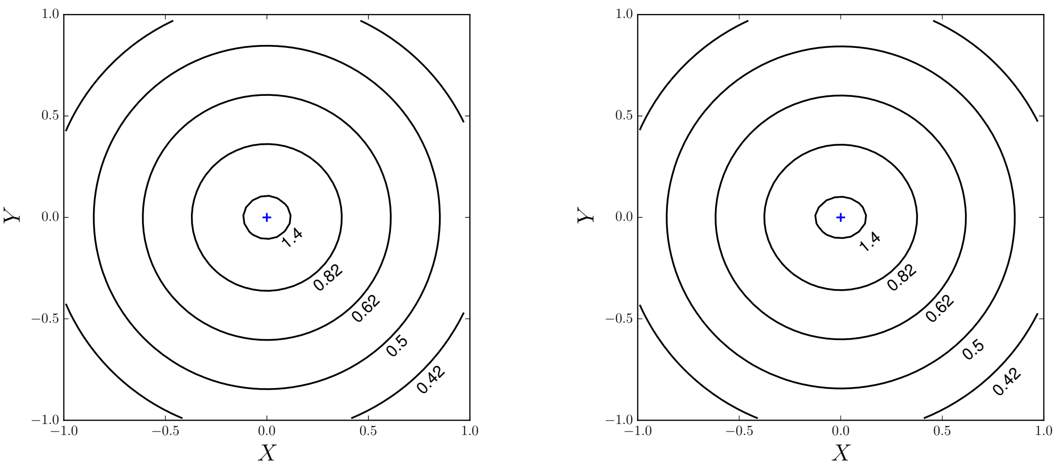

(a) $i_\mathrm{o} = 45°$ (b) $i_\mathrm{o} = 90°$

Fig. 3.5 *Surface density profile*, $\Sigma(X, Y)$ in units of $M_\mathrm{c}/{r_\mathrm{c}}^2$, for two different viewing angles. Distances are measured in units of r_c.

This behaviour is consistent with what we expected from the orbital dynamics discussed in the previous section. Figure 3.4b plots the isocontours of the total density, $\rho(r, \theta) = \rho_\mathrm{c} + \rho_1$. These reveal an oblate spheroidal deformation of the spherical cusp. The flattening increases steeply with decreasing r, with the axis ratio ~ 0.8 at ~ 0.15 pc — see Figure 3.6. We also computed $\Sigma(X, Y)$, the surface density profile of the deformed cusp, by integrating $\rho(r, \theta)$ along different lines of sight upto a distance of 3 pc from the MBH, because this corresponds to the break-radius of the cusp (Gallego-Cano et al., 2018). Figure 3.5 shows the isocontours of Σ on the sky plane for $i_\mathrm{o} = 45°$ and $i_\mathrm{o} = 90°$, where i_o is the angle between the line of sight and the disc normal. The flattening increases steeply with decreasing r, similar to the density profile; the edge-on view ($i_\mathrm{o} = 90°$) shows maximal flattening, as can be seen from Figure 3.6.

3.5 Discussion and Conclusions

We have presented a simple model of the deformation of a spherical stellar cusp (with anisotropic velocity dispersion) around a MBH, due to the growing gravity of a massive, axisymmetric accretion disc, for parameter values appropriate for the GC NSC. The mechanism is generic and may be common in galactic nuclei.

We argued that the disc grows over times that are much longer than the typical apse precession period of cusp stars within a parsec of the MBH. The dynamical problem is difficult to solve in general stellar dynamics. But within $r_\mathrm{infl} \simeq 2\,\mathrm{pc}$,

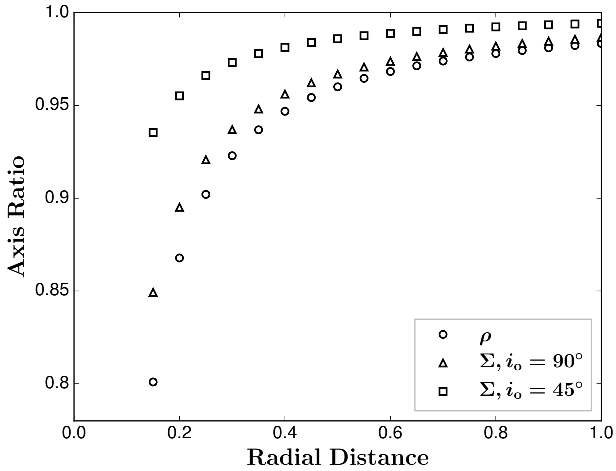

Fig. 3.6 Axis-ratio of the isocontours of total density, ρ, and surface density Σ, versus the major axis (in units of r_c) of the isocontours.

the dominant gravitational force on a star is the Newtonian $1/r^2$ attraction of the MBH, and the semi-major axis of every star is an additional conserved quantity for evolution over several apse precession periods (Sridhar & Touma, 1999). We used the secular theory of ST16a to construct an integrable model of the adiabatic deformation of the cusp DF. Although the non-linear, self-consistent problem is integrable, the full solution requires a lot of numerical computations. In order to get an idea of the nature of the deformation, we used linear secular theory to obtain an analytical expression for the DF perturbation due to the 'bare' effect of the disc. We explored orbital structure, which enables us to not only understand the physical properties of the linear deformation, but also to bound the limits of linear theory and discuss non-linear effects. The circulating orbits of linear theory are such that stars tend to spend more time near the equatorial plane of the disc, when their orbital eccentricity is maximal; this takes them closer to the inner, dense parts of the gas disc, an effect that could enhance the stripping of the envelopes of red giants (Amaro-Seoane & Chen, 2014).

Orbital structure also reveals the limits of linear theory, which does not apply to orbits whose apsides librate around 90° or 270°. For any given I and L_z, these orbits occupy regions of the highest eccentricities. Their DF depends on the entire orbital history — in contrast to the orbits of linear theory which respect adiabatic invariance — and requires computations based on the non-linear theory of adiabatic capture into resonance. For an initially tangentially anisotropic velocity dispersion, which seems to be the case for the GC NSC on scales < 2 pc from the MBH (Feldmeier-Krause et al., 2017), the relative number of eccentric orbits is small. Hence linear theory should do well as a first approximation for semi-major axes in the range $0.16 - 1$ pc.

Secular stability is an important issue, which we now review in the light of earlier results for the linear dynamical stability of non-rotating spherical DFs, $F_0(I, L)$. For the lopsided $l = 1$ linear mode Tremaine (2005) showed that DFs with $(\partial F_0/\partial L) < 0$ are secularly stable, whereas DFs with $(\partial F_0/\partial L) > 0$ are either stable or neutrally stable when $F_0 = 0$ at $L = 0$ (i.e. an empty loss-cone). The latter applies to the tangentially anisotropic case, $n = 1/2$, we have considered in this paper. Polyachenko et al. (2007) considered mono-energetic DFs, $F_0(I, L) = \delta(I - I_0)f(L)$, dominated by nearly radial orbits. They found linear secular instabilities for $l \geq 3$ when $f(L)$ is a non–monotonic function of L. Relaxing the restriction to nearly radial orbits, Polyachenko et al. (2008) concluded that the non-monotonicity of the DF as a function of L is the main requirement for this (empty) loss-cone instability to $l \geq 3$ modes. The cusp DFs of equation (3.7) are monotonic functions of L for $n \neq 0$, and may be expected to be stable in this sense; when $n = 0$, the DF is a function only of I and cannot be changed by any secular process because I is a secularly conserved quantity. So we are somewhat assured that the unperturbed cusp is likely to be linearly stable. But this does not imply that an axisymmetric deformation, forced by a disc of small (but not infinitesimal) mass, is necessarily stable; it could runaway in an axisymmetric manner, or be vulnerable to the growth of non-axisymmetric modes. To investigate this aspect, we need to first include the effect of the self-gravity of the perturbation on its own evolution, and then explore the problem through N-body simulations.

The density perturbation corresponding to the linear deformation results in an oblate spheroidal deformation of the formerly spherical cusp. The flattening increases steeply with decreasing distance from the MBH; the intrinsic axis ratio ~ 0.8 at ~ 0.15 pc. Surface density profiles for different viewing angles were presented. The appearance will depend on the assumed plane of the gas disc, and one could consider this for the GC NSC. The planes of the young stellar disc close to the MBH, and the CND farther away, have a high mutual inclination (Paumard et al., 2006). It is possible that the young stars were formed nearly coplanar with the CND and underwent dynamical evolution, also being perturbed by the CND (Šubr et al., 2009). The ionizing radiation from the hot young stars also seems to have pushed gas out from beyond 0.5 pc, and this would tend to decrease the spheroidal deformation we calculated at these distances. But a distinct possibility is that the accretion disc itself was warped.

The gravitational perturbation of a warped gas disc would cause a non-axisymmetric deformation of the spherical cusp, so our calculation needs to be extended to account for this. We considered an unperturbed spherical stellar cusp with anisotropic velocity dispersion, because we wanted to begin with the simplest generic case.[4] Chatzopoulos et al. (2015) constructed a self-consistent, flattened and rotating DF, $f(E, L_z)$, for the GC old stellar cusp. For $r < r_{\rm infl}$, this implies an unperturbed secular DF of the form, $F_0(I, L_z)$. Such a DF is immune to all secular axisymmetric perturbations, because I and L_z are conserved quantities for every stellar orbit. However, $F_0(I, L_z)$, would respond to the non-axisymmetric perturbation of a warped gas disc, because the L_z of every orbit would then evolve with time, even though I remains constant. The deformed cusp would then not be axisymmetric, a feature explored recently through triaxial modelling of the GC NSC (Feldmeier-Krause et al., 2017).

[4]An isotropic secular DF, $F_0(I)$, cannot undergo any secular change, either through collisionless perturbations or through resonant relaxation, because I is a secular invariant.

Part II

Resonant Relaxation

Chapter 4

Resonant Relaxation of Keplerian Stellar Discs

Secular collisionless dynamics of a Keplerian stellar system is driven by the mean gravitational potential of the (approximated) smooth mass distribution. Inherent graininess due to the finite $N_\star$ number of stars in a real stellar system, leads to its collisional evolution over longer timescales. RT96 proposed the efficient mechanism of resonant relaxation (RR) driving angular momentum relaxation of these systems over RR timescales $T_{\text{res}} \sim N_\star T_{\text{sec}}$. RR could be important for astronomical events associated with stellar dynamics in the region of influence of an MBH, like tidal disruption of stars (Rauch & Ingalls, 1996; Madigan et al., 2018), capture of stellar mass compact objects by the MBH leading to extreme mass ratio inspirals (EMRIs) (Merritt et al., 2011; Bar-Or & Alexander, 2016), and stellar feeding of the MBH (Hopman & Alexander, 2006a,b). In § 1.4.1, we discussed the development of RR theory. Due to ubiquity of nuclear stellar discs, M31 and Milky Way being the most well-studied examples, we investigate the RR of a planar Keplerian stellar system in Part II of the thesis.

ST16b presented a kinetic theory of RR for Keplerian stellar systems of general geometry, which is summarized in § 1.4.2. ST17 derived in explicit form the RR kinetic equation for razor-thin axisymmetric discs, in the absence of gravitational polarization. Being a planar study, this only involves scalar RR driven by apsidal resonances among the constituent Rings. They worked out the wake of a Gaussian Ring in terms of angular momentum exchanged with the rest of the Rings of the system. The resulting RR kinetic equation is a Fokker-Planck equation, whose functional form explicitly shows that only Rings in apsidal resonances contribute to the RR current. They also derived some statistical properties of the system and showed that Boltzmann entropy never decreases during RR evolution. Thermal equilibria are the maximum entropy states with DFs of Boltzmann form.

In this chapter, we apply the results of ST17 to study the explicit RR evolution of an axisymmetric Keplerian disc, consisting of Gaussian Rings of equal semi-major axes (monoenergetic limit). This is done by constructing a numerical algorithm, called "RR code", to solve the RR kinetic equation. We present the RR kinetic equation for an axisymmetric Keplerian disc from ST17 in § 4.1. Then in § 4.1.1, we specialize to a monoenergetic axisymmetric disc and derive a reduced form of the RR kinetic equation. We choose the log-interaction potential of equation (A.14) for gravitational interactions among the constituent Gaussian Rings of the system (as in Chapter 2), and give explicit expressions for different physical quantities, like the apse precession rate Ω and the interaction kernel K which are introduced in the same section. We discuss some interesting properties of RR probability current density J, which is driven by apsidal resonances among the Rings. In § 4.1.2, we show that the apsidal resonances among the Rings of the same angular momentum do not contribute to the RR current. This gives rise to a region in phase space, corresponding to high eccentricity Rings, for which there exist no resonances (see Figure 4.1b). Then in § 4.1.3, we present conserved quantities, such as the total mass, angular momentum and energy of the monoenergetic disc in their normalized forms. In § 4.1.4, we present the Boltzmann entropy (from ST17) for the monoenergetic case. In § 4.1.5, we find the stationary states for the RR kinetic equation for which corresponding currents vanish, and compare them with the thermal equilibria deduced from ST17. In § 4.2, we present the algorithm (RR code) used to solve the RR kinetic equation (4.11). The details of the method for locating the resonance points in angular momentum space are given in § 4.2.2. We present the results of the RR code for an example DF in § 4.3. We conclude in § 4.4.

4.1 Formalism

A razor–thin axisymmetric disc of mass M composed of $N_\star \gg 1$ number of Gaussian Rings is considered in xy–plane. The centre of the disc coincides with an MBH of mass $M_\bullet \gg M$ such that the mass ratio $\epsilon = M/M_\bullet \ll 1$ is a small parameter of the problem. A planar Gaussian Ring is characterized by three-dimensional Ring space variables $\{I,\, L,\, g\}$ (see § 1.2.1). $I = \sqrt{GM_\bullet a}$ relates to its semi-major axis a. $L = \sigma I\sqrt{1-e^2}$ is its angular momentum per unit mass with $\sigma = +1(-1)$ for anticlockwise (clockwise) sense of orbital motion of the star around the MBH (e being the eccentricity of the Ring). Here g is the longitude of periapse measured wrt x-axis. $\tau = \epsilon\times$time is the slow time variable, convenient for studying the secular dynamics of the system. For the limit $N_\star \gg 1$, a dynamical state of the axisymmetric planar system can be represented by a one-Ring distribution function (DF) $\widetilde{f}(I, L, \tau)/(2\pi)$ in Ring phase space. From the normalization property of equation (2.1), $\int \mathrm{d}I\mathrm{d}L\, \widetilde{f}(I, L, \tau) = 1$. Note that this normalization is valid at all times, because the MBH is not considered a sink of stars.

The interaction potential $\Psi(I, L, g, I', L', g')$ between two planar Gaussian Rings $\{I,\ L,\ g\}$ and $\{I',\ L',\ g'\}$ is given by equation (2.3). Due to spatial isotropy, the dependence of Ψ on g and g' occurs as $|g - g'|$. It is useful to consider the Fourier series of Ψ:

$$\Psi(I, L, g, I', L', g') = \sum_{m=-\infty}^{+\infty} \widetilde{C}_m(I, L, I', L') \exp\left[\mathrm{i}m(g - g')\right] \tag{4.1}$$

where $\widetilde{C}_m$'s denote the Fourier coefficients. Detailed symmetry properties of the two–Ring interaction potential Ψ and its Fourier coefficients $\widetilde{C}_m$'s are discussed in § 6.2 of ST16a. Employing the above Fourier series for Ψ in equation (2.2), the mean self-gravitational potential $\widetilde{\Phi}(I, L, \tau)$ of the disc is given as:

$$\widetilde{\Phi}(I, L, \tau) = \int \mathrm{d}I'\mathrm{d}L'\, \widetilde{C}_0(I, L, I', L')\widetilde{f}(I', L', \tau)\,. \tag{4.2}$$

For an isolated non-relativistic disc, $\widetilde{\Phi}$ is also the Hamiltonian of the secular dynamical problem. Orbits of Gaussian Rings in an axisymmetric collisionless equilibrium are already described by the equation (2.8) of § 2.1.1. The orbits are uniformly precessing Gaussian Rings with the apse precession rate $\widetilde{\Omega}(I, L, \tau) = \dot{g} = \partial\widetilde{\Phi}/\partial L$. The time–dependence of $\widetilde{\Omega}(I, L, \tau)$ is over the long-term RR timescale T_{res} and hence, on the shorter collisionless timescales T_{sec}, $\widetilde{\Omega}$ can be considered to be stationary. For axisymmetry, eccentricities of the precessing Rings are conserved, and hence the collisionless orbits are rigidly and uniformly precessing Gaussian Rings.

On the longer RR timescales T_{res}, discrete interactions among the Rings become important, and the system evolves by RR. ST17 derived the following RR kinetic equation for axisymmetric Keplerian discs giving the RR evolution of the probability DF $\widetilde{f}(I, L, \tau)$:

$$\frac{\partial \widetilde{f}}{\partial \tau} + \frac{\partial \widetilde{J}}{\partial L} = 0\,, \tag{4.3}$$

where $\widetilde{J}(I, L, \tau)$ is the probability density current in (I, L)–plane. $\widetilde{J}(I, L, \tau)$ gives the flow of Gaussian Rings in L direction; I is a conserved quantity in secular dynamics.

The current $\widetilde{J}$ is given explicitly as:

$$\widetilde{J} = \frac{1}{N_\star} \int \mathrm{d}I' \, \mathrm{d}L' \, \delta(\widetilde{\Omega}' - \widetilde{\Omega}) \widetilde{K}(I, L, I', L') \left\{ \widetilde{f} \frac{\partial \widetilde{f}'}{\partial L'} - \widetilde{f}' \frac{\partial \widetilde{f}}{\partial L} \right\} \tag{4.4}$$

where $\widetilde{f} \equiv \widetilde{f}(I, L, \tau)$, $\widetilde{f}' \equiv \widetilde{f}(I', L', \tau)$ and the apse precession rates $\widetilde{\Omega} \equiv \widetilde{\Omega}(I, L, \tau)$ and $\widetilde{\Omega}' \equiv \widetilde{\Omega}(I', L', \tau)$. The above kinetic equation corresponds to equations (53)–(54) of ST17. The interaction kernel $\widetilde{K}(I, L, I', L')$ measures the strength of interaction between the Rings $(I,\ L)$ and $(I',\ L')$, and is given as:

$$\widetilde{K}(I, L, I', L') = 2\pi \sum_{m=1}^{\infty} m \, \widetilde{C}_m(I, L, I', L')^2 \, . \tag{4.5}$$

It is evident from the equation (4.4) that the $\delta(\widetilde{\Omega}' - \widetilde{\Omega}) \widetilde{K}(I, L, I', L')$ forms the part of the integrand which is symmetric under the interchange of two Rings $(I, L) \longleftrightarrow (I', L')$; while the factor in "$\{\ldots\}$" forms an anti-symmetric part. The δ-function implies that the current at the location (I, L) is non-zero if and only if there exists some other point (I', L') satisfying the resonance condition $\widetilde{\Omega}(I', L', \tau) = \widetilde{\Omega}(I, L, \tau)$. In other words, the current at the point $(I,\ L)$ is contributed only by the Rings whose apsides are precessing at the same rate. This explicitly shows that scalar RR is driven by apsidal resonances.

Since the DF $\widetilde{f}(I, L, \tau)$ depends upon the phase space variables I and L (and not on g), which remain conserved over the collisionless timescales T_{sec} for an axisymmetric Keplerian disc, $\widetilde{f}(I, L, \tau)$ corresponds to a (quasi)collisionless equilibrium by the secular Jeans Theorem (Binney & Tremaine (2008), ST16a). The kinetic equation (4.3) describes the evolution of the system through a sequence of quasi-stationary states (collisionless equilibria) $\widetilde{f}$ over timescales T_{res}, given that the $\widetilde{f}$ forms a stable dynamical equilibrium. If the system reaches some unstable state, the instability will grow and saturate over the shorter secular timescales T_{sec}, and again the long term RR evolution would take over.

For further details on physical kinetics of an axisymmetric Keplerian stellar disc, refer to the § 5.2 of ST17. Now we descend to the special case of a monoenergetic axisymmetric disc for the rest of this chapter.

4.1.1 Reduction to a Monoenergetic Axisymmetric Disc

In a monoenergetic disc, all the $N_\star$ Rings have equal semi-major axes a_0, and hence $I = I_0 = \sqrt{GM_\bullet a_0}$. It is convenient to deal with the dimensionless variables – the normalized angular momentum $\ell = L/I_0 = \pm\sqrt{1-e^2} \in [-1,1]$ and normalized slow time $t = \Omega_{\rm kep}\tau/(2\pi N_\star) = {\rm time}/T_{\rm res}$. We define the probability DF $f(\ell,t)$ in ℓ-space which is related to $\widetilde{f}(I,L,\tau)$ as:

$$\widetilde{f}(I,L,\tau) = \frac{f(\ell,t)\delta(I-I_0)}{I}\,. \tag{4.6}$$

Using the above expression in the normalization equation for $\widetilde{f}$, we get $\int_{-1}^{1}{\rm d}\ell\, f(\ell,t) = 1$. Now, we define the normalized two-Ring interaction potential $\psi(\ell,\ell',g-g')$ and the corresponding Fourier coefficients $C_m(\ell,\ell')$, that are related to their general counterparts as:

$$\Psi = \frac{GM_\bullet}{2\pi a_0}\psi; \quad \widetilde{C}_0 = \frac{GM_\bullet}{2\pi a_0}C_0 \quad \text{and} \qquad \widetilde{C}_m = \frac{GM_\bullet}{2\pi a_0}C_m\,. \tag{4.7}$$

Using the above relations in the expression for $\widetilde{\Phi}$ in the equation (4.2), the normalized mean potential $\Phi(\ell,t)$ is given as:

$$\widetilde{\Phi} = \frac{GM_\bullet}{2\pi a_0}\Phi\,; \qquad \Phi(\ell,t) = \int {\rm d}\ell'\, f(\ell',t)C_0(\ell,\ell')\,. \tag{4.8}$$

Using the above expression in the definition of $\widetilde{\Omega} = \partial\widetilde{\Phi}/\partial L$, we define the normalized apse precession rate $\Omega(\ell,t)$ as:

$$\Omega(\ell,t) = \frac{2\pi\widetilde{\Omega}(I,L,\tau)}{\Omega_{\rm Kep}}; \quad \text{and hence} \quad \Omega = \frac{\partial\Phi}{\partial\ell} \tag{4.9}$$

where $\Omega_{\rm Kep}$ is the common Keplerian orbital frequency for all Rings with semi-major axis a_0. Likewise, we use the normalized Fourier coefficients of equation (4.7) in equation (4.5) and define the normalized interaction kernel $K(\ell,\ell')$ as:

$$\widetilde{K}(I,L,I',L') = \left(\frac{GM_\bullet}{2\pi a_0}\right)^2 K(\ell,\ell')\,; \text{ and hence } K(\ell,\ell') = 2\pi\sum_{m=1}^{\infty} m\,C_m(\ell,\ell')^2\,. \tag{4.10}$$

Using the equations (4.6), (4.9) and (4.10) in the equations (4.3)–(4.4), we get the following form of RR kinetic equation for the monoenergetic axisymmetric disc:

$$\frac{\partial f}{\partial t} + \frac{\partial J}{\partial \ell} = 0 \tag{4.11a}$$

where probability density current $J(\ell,t)$ in ℓ–space is given as:

$$J(\ell,t) = \int_{-1}^{1}{\rm d}\ell'\,\delta(\Omega-\Omega')K(\ell,\ell')\left\{f\frac{\partial f'}{\partial\ell'} - f'\frac{\partial f}{\partial\ell}\right\}\,. \tag{4.11b}$$

Here $f \equiv f(\ell, t)$, $f' \equiv f(\ell', t)$, $\Omega \equiv \Omega(\ell, t)$ and $\Omega' \equiv \Omega(\ell', t)$. From expression (4.10), it is evident that $K(\ell, \ell') \to 0$ if either/both of the Rings are circular i.e. ℓ or/and $\ell' \to \pm 1$. This implies that circular Rings do not contribute to the current in the entire domain of $\ell \in [-1, 1]$ even if they satisfy the resonance condition. Also, the currents at the boundaries $J(\ell = \pm 1, t) = 0$ throughout the evolution of the system. This can be physically understood as a circular Ring has an axisymmetric geometry and hence, cannot exert a net torque on a confocal and coplanar Gaussian Ring. The reverse argument is also true – other Rings cannot exert torque on circular Rings due to the same symmetry.

Interaction Potential: In order to proceed further to study the evolution of an initial DF $f_{\text{in}}(\ell)$ by the RR kinetic equation (4.11), we need to consider some explicit form of the two-Ring interaction potential $\psi(\ell, \ell', g - g')$ and evaluate its Fourier coefficients $C_m(\ell, \ell')$'s.

We choose the two-Ring log interaction potential (Borderies et al., 1983; Touma & Tremaine, 2014), derived in Appendix A.1,

$$\psi \;=\; -8 \log 2 \;+\; \log |\boldsymbol{e} - \boldsymbol{e}'|^2 \tag{4.12}$$

where $\boldsymbol{e} \equiv e(\cos g, \, \sin g)$ and $\boldsymbol{e}' \equiv e'(\cos g', \, \sin g')$ correspond to the eccentricity vectors of the Gaussian Rings under consideration. We have already employed the log potential for investigating the stability properties of axisymmetric monoenergetic discs in Chapter 2. The corresponding Fourier coefficients are given as in equation (A.16):

$$C_0(\ell, \ell') = -8 \log 2 + \log e_>^2 \;\; ; \qquad C_m(\ell, \ell') = -\frac{1}{|m|} \left(\frac{e_<}{e_>} \right)^{|m|} \tag{4.13}$$

where $e_< = \min(e, e')$ and $e_> = \max(e, e')$; $e = \sqrt{1 - \ell^2}$ and $e' = \sqrt{1 - \ell'^2}$ are eccentricities of the Rings. Using C_0 from the above equation in the definition of Ω given in equation (4.8)-(4.9), the apse precession frequency $\Omega(\ell, t)$ attains the following explicit form:

$$\Omega(\ell, t) = \frac{-2\ell}{1 - \ell^2} \left[1 - \int_{-|\ell|}^{|\ell|} \mathrm{d}\ell' \; f(\ell', t) \right] \tag{4.14}$$

as already expressed in the equation (2.21). For the limiting case of circular Rings as $\ell \to \pm 1$, $\Omega(\pm 1, t) \to \mp \{ f(1, t) + f(-1, t) \}$ and hence, the circular Rings have a finite apse precession rate given the non-zero value of $f(\pm 1)$ for a generic DF. We discussed a few properties of $\Omega(\ell, t)$ below the equation (2.21) ($\Omega \equiv \Omega_0$ in the context of the collisionless studies of Chapter 2).

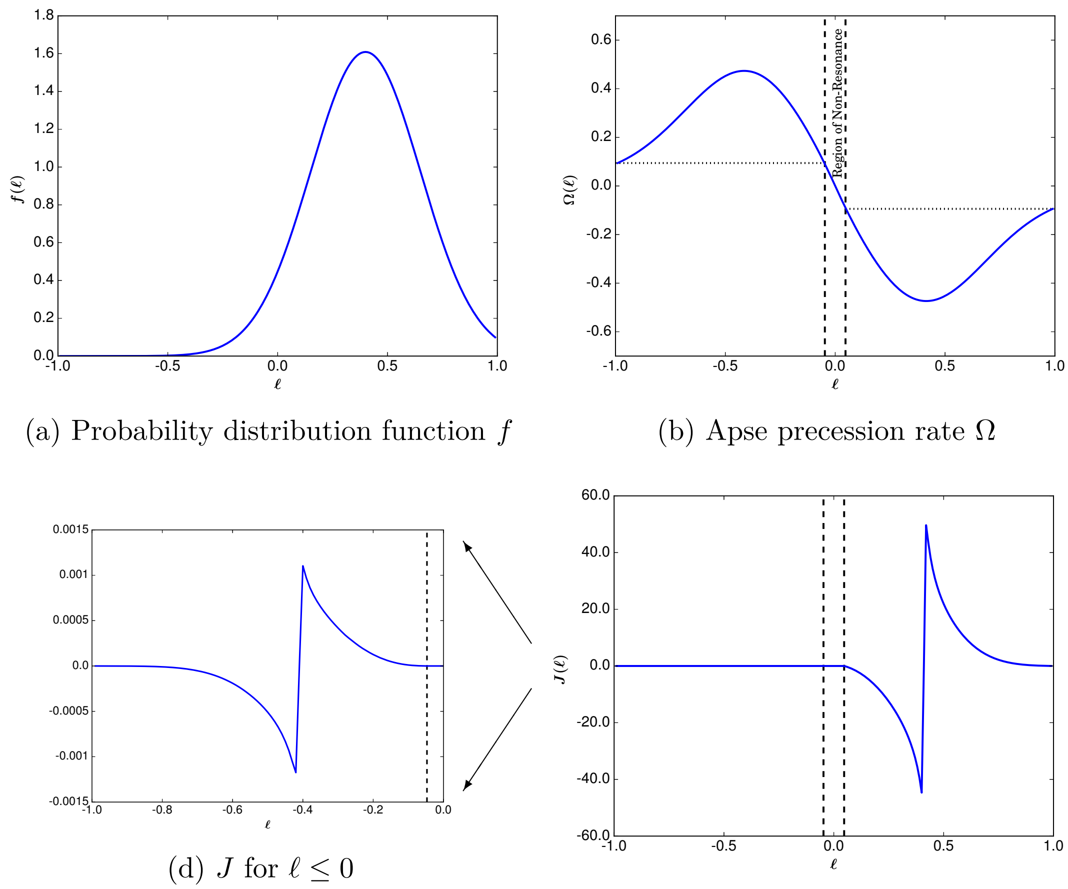

(a) Probability distribution function f

(b) Apse precession rate Ω

(d) J for $\ell \leq 0$

(c) Probability density current J

Fig. 4.1 A typical initial (a) Gaussian DF $f(\ell, t = 0)$, with its (b) apse precession $\Omega(\ell, t = 0)$ (in the units of ${T_{\text{sec}}}^{-1}$) and (c) current $J(\ell, t = 0)$ profiles. (d) The negative half of ℓ space is zoomed on, to observe the small magnitude currents and delineate the region of non-resonance. Later we study the evolution of this DF in § 4.3.

The interaction kernel for the log-potential is evaluated in Appendix A.2.1 leading to the final form of equation (A.17), and is given as:

$$K(\ell, \ell') = -2\pi \log \left[1 - \left(\frac{e_<}{e_>} \right)^2 \right] \tag{4.15}$$

where $e_<$ and $e_>$ have the same definitions as earlier. It is clear from the above expression that the kernel K vanishes if one/both of the Rings are circular. The above expression also implies the singularity of the interaction kernel as $\ell' \to \ell$. To avoid these singularities in the numerical calculations of RR code, we use the softened log potential of equation (A.18) and the corresponding softened interaction kernel of equation (A.25). We will discuss these singularities in more detail in § 4.1.2.

The δ-function in the current J-integral of equation (4.11b), implies that the current $J(\ell, t)$ gets contributions from those Rings ℓ' whose apse precession satisfies the resonance condition $\Omega(\ell', t) = \Omega(\ell, t)$. This leads to the following form for the current:

$$J(\ell, t) = {\sum_j}' \frac{K(\ell, \ell_{\mathrm{r}j})}{\left|\dfrac{\partial \Omega}{\partial \ell}\right|_{\ell_{\mathrm{r}j}}} \left\{ f \frac{\partial f_{\mathrm{r}j}}{\partial \ell_{\mathrm{r}j}} - f_{\mathrm{r}j} \frac{\partial f}{\partial \ell} \right\} \tag{4.16}$$

where $\ell_{\mathrm{r}j}$ are the resonant points of ℓ satisfying the condition $\Omega(\ell_{\mathrm{r}j}, t) = \Omega(\ell, t)$. Here $f_{\mathrm{r}j} \equiv f(\ell_{\mathrm{r}j}, t)$. The prime over the summation (Σ') indicates that $\ell_{\mathrm{r}j} \neq \ell$ and hence, the *self contribution* from ℓ does not add to the current $J(\ell, t)$; this is demonstrated in § 4.1.2. Hence, the current $J(\ell, t)$ vanishes if there is not any resonant point for ℓ.

In Figure 4.1, we present the precession rate $\Omega(\ell, t = 0)$ and current $J(\ell, t = 0)$ profiles for a typical Gaussian DF, given in equation (4.52). As seen from the Ω–profile (Figure 4.1b) there is a *region of non-resonance* around $\ell = 0$ within which there are no resonant pair of points; this is enclosed within dashed vertical lines. Such a region exists due to extremely slow precession rates of high e Rings, with $\Omega(\ell = 0, t) = 0$, which prevent them from having resonances since $\Omega(\pm 1, t)$ is finite or non-zero in general (for finite $f(\pm 1, t)$). Hence, the currents in this region vanish (see Figure 4.1c) and the DF $f(\ell, t = 0)$ remains *frozen* in this region at an initial time $t = 0$. In § 4.3, this DF is evolved by the RR code and the resulting profiles are shown in the Figure 4.2. For this particular choice of initial DF, the region of non-resonance expands in ℓ-space with time as DF evolves; see Figure 4.2b.

4.1.2 Self-Contribution to RR Current

Here we demonstrate that the self-resonant contribution from a generic point ℓ to its current $J(\ell, t)$ vanishes. This fact is incorporated in the equation (4.16) where the resonances $\ell_{\mathrm{r}j}$'s contributing to the current $J(\ell, t)$ satisfy $\ell_{\mathrm{r}j} \neq \ell$. Without loss of generality, we consider only the positive half of ℓ-space ($\ell > 0$) for discussion in this section, because the anti-symmetric property of $\Omega(\ell, t)$ (along with $\ell\,\Omega(\ell) < 0$) ensures that resonances lie in the same half-space, and the resonance pairs would be just inverted in sign for negative half-space. The apses of all the Rings corresponding to ℓ (but generally with different g's) precess at the same rate $\Omega(\ell, t)$ and hence the resonance criterion is satisfied. This suggests that in principle there should be a contribution from the term $\ell_{\mathrm{r}j} = \ell$. From equation (4.16), we can write the self-resonant term of the current explicitly as:

$$J_{\mathrm{sr}}(\ell, t) = \operatorname*{Lim}_{\ell' \to \ell} \frac{K(\ell, \ell')}{\left|\dfrac{\partial \Omega}{\partial \ell}\right|_{\ell'}} \left\{ f \frac{\partial f'}{\partial \ell'} - f' \frac{\partial f}{\partial \ell} \right\} . \tag{4.17}$$

It is evident from the above equation that the antisymmetric term in the parenthesis "{ }" vanishes as $\ell' \to \ell$, and the equation (4.15) implies that the interaction kernel $K(\ell, \ell') \to +\infty$ in this limit. We need to determine whether their product is zero, finite or infinite. So, to evaluate $J_{\rm sr}$, we substitute $\ell' = \ell + \Delta\ell$ where $\Delta\ell \to 0$. The kernel can be simplified as:

$$K(\ell,\ell') = \begin{cases} -2\pi\left(\log\left[\ell^2 - \ell'^2\right] - \log\left[1-\ell'^2\right]\right) \; ; & \ell > \ell' \\ -2\pi\left(\log\left[\ell'^2 - \ell^2\right] - \log\left[1-\ell^2\right]\right) \; ; & \ell < \ell' \end{cases} \tag{4.18}$$

which further reduces in the intended limit, upto the leading order in small parameter $\Delta\ell$, as:

$$\begin{aligned} \operatorname*{Lim}_{\Delta\ell\to 0} K(\ell,\ell+\Delta\ell) &= \begin{cases} -2\pi\left(\log\left[-2\ell\Delta\ell\right] - \log\left[1-\ell^2\right]\right) \; , & \Delta\ell < 0 \\ -2\pi\left(\log\left[2\ell\Delta\ell\right] - \log\left[1-\ell^2\right]\right) \; , & \Delta\ell > 0 \end{cases} \\ &= -2\pi\left(\log\left[\frac{2\ell}{1-\ell^2}\right] + \log|\Delta\ell|\right) \end{aligned} \tag{4.19}$$

and hence diverges logarithmically. The antisymmetric term in the limit becomes:

$$\operatorname*{Lim}_{\Delta\ell\to 0}\left\{ f\frac{\partial f'}{\partial \ell'} - f'\frac{\partial f}{\partial \ell}\right\}_{\ell'=\ell+\Delta\ell} = \left\{ f\frac{\partial^2 f}{\partial \ell^2} - \left(\frac{\partial f}{\partial \ell}\right)^2\right\}\Delta\ell \,. \tag{4.20}$$

Hence the limiting expression for self-contribution $J_{\rm sr}$ for generic points, which do not correspond to the extrema of Ω-profile (i.e. $\partial\Omega/\partial\ell \neq 0$), takes the following form and vanishes as $\Delta\ell \to 0$,

$$J_{\rm sr}(\ell,t) = -2\pi\left|\frac{\partial\Omega}{\partial\ell}\right|^{-1}\left\{ f\frac{\partial^2 f}{\partial \ell^2} - \left(\frac{\partial f}{\partial \ell}\right)^2\right\}\operatorname*{Lim}_{\Delta\ell\to 0}\Delta\ell\,\log|\Delta\ell| \to 0\,. \tag{4.21}$$

Now we investigate the case of an extremum point ℓ_0 in the Ω-profile for which $(\partial\Omega/\partial\ell)_{\ell_0} = 0$. For this case, we have:

$$\left(\frac{\partial\Omega}{\partial\ell}\right)_{\ell'=\ell_0+\Delta\ell} = \frac{\partial^2\Omega_0}{\partial\ell_0^2}\Delta\ell \tag{4.22}$$

upto the leading order in the small parameter $\Delta\ell$ where $\Omega_0 \equiv \Omega(\ell_0)$. Using the above expression in the equation (4.21), we have the following form of the self-resonant contribution to current:

$$J_{\rm sr}(\ell_0,t) = -2\pi\left|\frac{\partial^2\Omega_0}{\partial\ell_0^2}\right|^{-1}\left\{ f_0\frac{\partial^2 f_0}{\partial \ell_0^2} - \left(\frac{\partial f_0}{\partial \ell_0}\right)^2\right\}\operatorname*{Lim}_{\Delta\ell\to 0}\operatorname{sign}(\Delta\ell)\log|\Delta\ell| \tag{4.23}$$

with the required limit, $\mathrm{sign}(\Delta\ell)\log|\Delta\ell| \to \mp\infty$ as $\Delta\ell \to 0^{\pm}$. Here $f_0 \equiv f(\ell_0)$. But, the final limit is the average of left and right limits and hence the resonant contribution $J_{\rm sr}(\ell_0, t)$ vanishes. As a result the self contribution to current is zero for extremum point ℓ_0 as well. It is worth noting that the cause of the apparent directional divergence is the logarithmic singularity of the interaction kernel $K(\ell, \ell')$ of log potential as $\ell' \to \ell$. In order to control such steep features in $J(\ell, t)$ in the vicinity of extremum point/s ℓ_0, we employ the softened interaction kernel $K_{\rm S}(\ell, \ell')$ of equation (A.25) in the RR code.

4.1.3 Conserved Quantities

Since the MBH is not considered a sink of stars in the present study, the disc mass M remains conserved as the DF $f(\ell, t)$ evolves by the RR kinetic equation (4.11). Equivalently, considering the normalization property of DF $f(\ell, t)$, the norm $\mathscr{N}$ of the system is conserved as:

$$\mathscr{N} = \int \mathrm{d}\ell f(\ell, t) = 1\,. \tag{4.24}$$

As there are no external forces acting on the system, total energy $\mathcal{E}$ and total angular momentum $\mathcal{L}$ of the system are also conserved. The conservation of these quantities – M, $\mathcal{L}$ and $\mathcal{E}$ – can be deduced from the RR kinetic equation in a straightforward manner; see § 6.1 of ST17 for an axisymmetric disc. We reduce the expressions to the monoenergetic case by using equation (4.6) and (4.7). The total angular momentum $\mathcal{L}$ of the system is:

$$\mathcal{L} = MI_0 \int_{-1}^{1} \mathrm{d}\ell\; \ell f(\ell, t) = M\sqrt{GM_{\bullet}a_0}\int_{-1}^{1} \mathrm{d}\ell\; \ell f(\ell, t) \tag{4.25}$$

where MI_0 is the maximum possible angular momentum corresponding to the case of a disc composed of only circular prograde orbits. We express the normalized total angular momentum $\mathscr{L} = \mathcal{L}/(MI_0) \leq 1$ as:

$$\mathscr{L} = \int_{-1}^{1} \mathrm{d}\ell\; \ell f(\ell, t)\,. \tag{4.26}$$

The total energy $\mathcal{E}$ of the disc is given explicitly as:

$$\mathcal{E} = ME_{\rm K}(a_0) + \frac{1}{2}\int \mathrm{d}\ell\,\mathrm{d}\ell'\,\frac{\mathrm{d}g}{2\pi}\,\frac{\mathrm{d}g'}{2\pi}\,\frac{GM^2 f(\ell, t) f(\ell', t)}{2\pi a_0}\psi(\ell, \ell', g - g') \tag{4.27}$$

where the first term corresponds to the total Keplerian energy of the disc, with $E_{\rm K}(a_0) = -GM_{\bullet}/(2a_0)$ being the Keplerian energy of a Gaussian Ring of semi-major axis a_0. Since the semi-major axes of all the Rings in the system are conserved in secular dynamics, this part of $\mathcal{E}$ is evidently also conserved. The second term corresponds to the self-gravitational energy of the disc. The "1/2" corrects, in the usual manner, for the double counting of the gravitational potential of all the pairs of Rings in the system. The normalized two-Ring interaction potential ψ is given by equation (4.12). It is straightforward to solve the integrals over g and g' using the Fourier series expansion of equation (A.15), and the total energy becomes:

$$\mathcal{E} = ME_{\mathrm{K}}(a_0) + \frac{1}{2}\frac{GM^2}{2\pi a_0}\int \mathrm{d}\ell\,\mathrm{d}\ell'\, C_0(\ell,\ell')f(\ell,t)f(\ell',t)\,. \tag{4.28}$$

We define the normalized self-gravitational energy $\mathscr{E}$ of the disc in units of GM^2/a_0, as:

$$\mathscr{E} = \frac{1}{4\pi}\int \mathrm{d}\ell\,\mathrm{d}\ell' C_0(\ell,\ell')f(\ell,t)f(\ell',t)\,. \tag{4.29}$$

Using equation (4.13) for the Fourier coefficient C_0 we have:

$$\mathscr{E} = -\frac{2}{\pi}\log 2 + \frac{1}{4\pi}\int \mathrm{d}\ell\,\mathrm{d}\ell'\ \log e_>^2\ f(\ell,t)f(\ell',t)\,. \tag{4.30}$$

We find that the RR code respects the conservation of the quantities $\{\mathscr{N},\mathscr{L},\mathscr{E}\}$ to a good precision, as detailed in § 4.3.

4.1.4 Boltzmann Entropy

ST17 demonstrated that the Boltzmann entropy of an axisymmetric Keplerian disc is a non-decreasing function of time, as the system evolves according to the RR kinetic equation (4.3)-(4.4). This result also applies to the special case of a monoenergetic axisymmetric disc, which is the subject of the present study. The Boltzmann entropy S for a monoenergetic axisymmetric Keplerian disc is defined as:

$$S = -\int_{-1}^{1}\mathrm{d}\ell\, f(\ell)\log\left[f(\ell)\right]. \tag{4.31}$$

In § 4.3, we find that the entropy indeed remains a non-decreasing function of time during the RR code runs. The code evolves the system towards the higher entropy states with a gradual saturation towards the end; see Figure 4.4d.

4.1.5 Stationary States

Here we construct a class of stationary state solutions of the RR kinetic equation (4.11). The corresponding current $J(\ell)$ of equation (4.11b) should vanish at all the points $\ell \in [-1, 1]$. The antisymmetric factor in the current integral can be rewritten as follows:

$$\left\{ f \frac{\partial f'}{\partial \ell'} - f' \frac{\partial f}{\partial \ell} \right\} = f f' \left\{ \frac{1}{f'} \frac{\partial f'}{\partial \ell'} - \frac{1}{f} \frac{\partial f}{\partial \ell} \right\} . \tag{4.32}$$

For functions which have $f^{-1}\partial f/\partial \ell$ equal to a single-valued function of Ω (say $\eta[\Omega]$), the right side of the above expression becomes $f f' \{\eta[\Omega'] - \eta[\Omega]\}$. Hence the co-occurrence of $\delta(\Omega' - \Omega)$ and anti-symmetric factor $\{\eta[\Omega'] - \eta[\Omega]\}$ in the current integral makes the current vanish at every point in ℓ-space. Therefore, DFs $f_{\mathrm{s}}(\ell)$ that satisfy the property,

$$\frac{1}{f_{\mathrm{s}}(\ell)} \frac{\mathrm{d} f_{\mathrm{s}}(\ell)}{\mathrm{d}\ell} = \eta[\Omega_{\mathrm{s}}(\ell)] \tag{4.33}$$

are stationary states of the RR kinetic equation. Here $\Omega_{\mathrm{s}}(\ell)$ is the apse precession rate corresponding to the DF $f_{\mathrm{s}}(\ell)$, given by equation (4.14). The above equation can be integrated over ℓ to get the following form for these stationary states:

$$f_{\mathrm{s}}(\ell) = A \, \exp\left[\int_{-1}^{\ell} \eta[\Omega_{\mathrm{s}}(\ell)] \, \mathrm{d}\ell \right] \tag{4.34}$$

where A is the constant of integration, chosen by using normalization property of the DF. These DFs can be the possible end states for RR evolution of the discs, only if they are dynamically and thermally stable. For these states, $f_{\mathrm{s}}^{-1} \mathrm{d} f_{\mathrm{s}}/\mathrm{d}\ell = \eta[\Omega_{\mathrm{s}}]$ is a single-valued functional of Ω_{s}.

It is straightforward to see that the thermal equilibrium state is a special case of these stationary states. The Boltzmann-form of the thermal equilibrium DF for axisymmetric discs is derived by ST17, and is given in equation (81) of the same paper. Reduction to the monoenergetic case can be done by using equations (4.6) and (4.8), which gives the following form of the thermal equilibrium DF $f_{\mathrm{th}}(\ell)$:

$$f_{\mathrm{th}}(\ell) = A \exp\left[-\beta \Phi_{\mathrm{th}}(\ell) + \gamma \ell \right] \tag{4.35}$$

where A, β and γ are real constants, fixed by the total mass (i.e. normalization of equation 4.24), energy and angular momentum of the disc. $\Phi_{\mathrm{th}}(\ell)$ is the mean self-gravitational potential of the disc given by equation (4.8). Differentiating the above equation, we have the following property satisfied by these equilibria:

$$\frac{1}{f_{\rm th}(\ell)}\frac{\mathrm{d}f_{\rm th}(\ell)}{\mathrm{d}\ell} = \eta_{\rm th}[\Omega_{\rm th}(\ell)] = -\beta\,\Omega_{\rm th}(\ell) + \gamma\,. \tag{4.36}$$

The above equation upon comparison with the equation (4.33), establishes that the thermal equilibria $f_{\rm th}(\ell)$ are a sub-class of the stationary state DFs $f_{\rm s}(\ell)$ with $\eta[\Omega]$ being a linear polynomial in Ω.

The thermal equilibrium is an entropy-extremum by construction; but it is not clear whether or not the stationary states also correspond to extrema. It is of interest to see whether the end-states from RR evolution of an initial DF by the RR kinetic equation (4.11), actually correspond to the thermal equilibria or not. It is intriguing to find that the RR code evolves the example initial DF of the equation (4.52) to an end-state corresponding to the stationary states of the type $f_{\rm s}$, with the functional $\eta[\Omega_{\rm s}]$ being a non-linear function. Hence, this end-state is not a thermal equilibrium; see § 4.3.1 for details.

4.2 RR Code Algorithm

In this section, we describe the RR code algorithm in detail. The ℓ-space is divided into N intervals with $N+1$ number of uniformly spaced grid points ℓ_i with $i = 0, 1, 2, ..., N$. Here, $\ell_0 = -1$ and $\ell_N = 1$. The bin–areas $A_i \equiv \int_{\ell_i}^{\ell_{i+1}} \mathrm{d}\ell\, f(\ell)$ with $i = 0, 1, 2, ..., N-1$, which are direct measures of the DF, are updated in the RR code at each time-step. The RR kinetic equation (4.11) is integrated over ℓ in an interval $[\ell_i,\ell_{i+1}]$ giving the following equation:

$$\frac{\partial A_i}{\partial t} = J_i - J_{i+1} \tag{4.37}$$

where $J_i = J(\ell_i, t)$ denotes the current at the grid-point ℓ_i. We now discretize the above equation by choosing the forward stepping in time employing Forward Euler method:

$$\frac{A_i^{(k+1)} - A_i^{(k)}}{\Delta t} = J_i - J_{i+1}\,. \tag{4.38}$$

This is the time-stepping equation to obtain the bin-areas $A_i^{(k+1)}$ at time t_{k+1} from $A_i^{(k)}$ at the previous time $t_k = t_{k+1} - \Delta t$. Here the currents on the right side of the above equation are evaluated at time t_k; hence $J_i \equiv J_i^{(k)}$ and $J_{i+1} \equiv J_{i+1}^{(k)}$. The conservative scheme ensures the exact conservation of the total norm $\mathcal{N} = \sum_{i=0}^{N} A_i$ at each time-step.

From equation (4.16), the current J_i on the grid points is explicitly given as:

$$J_i = {\sum_j}' \frac{K(\ell_i, \ell_{\mathrm{r}j})}{\left|\dfrac{\partial\Omega}{\partial\ell}\right|_{\ell_{\mathrm{r}j}}} \left\{ f_i \frac{\partial f_{\mathrm{r}j}}{\partial\ell_{\mathrm{r}j}} - f_{\mathrm{r}j}\frac{\partial f_i}{\partial\ell_i} \right\} \tag{4.39}$$

where the points $\ell_{\mathrm{r}j} \neq \ell_i$ satisfy the resonant condition $\Omega(\ell_{\mathrm{r}j}) = \Omega(\ell_i)$, and also $f_i \equiv f(\ell_i)$. As evident from the equation (4.38), only the bin-areas $A_i^{(k)}$ are inherited from the previous time in the code. Hence to evaluate J_i at time t_k, we devise a methodology to model the DF with a smooth function $f^{(k)}(\ell)$ from the given bin-area array $A_i^{(k)}$ as explained below. Note that the function $f^{(k)}(\ell)$ (not merely the DF values f_i on the grid) is required to evaluate the quantities at resonant points $\ell_{\mathrm{r}j}$ which generally lie in-between the grid points. The model to evaluate $f^{(k)}(\ell)$ employs the notion of cumulative DF $F(\ell, t) = \int_{-1}^{\ell} \mathrm{d}\ell' \, f(\ell', t)$ and comprises the following steps.

- The grid values of the cumulative DF $F_i^{(k)} \equiv F(\ell_i, t_k)$ at time t_k are directly calculated from bin-areas as $F_i^{(k)} = \sum_{j=0}^{i-1} A_j^{(k)}$ for $i = 1, 2..., N$ with $F_0^{(k)} = 0$. Note that $F_N^{(k)} = 1$ from the normalization of DF.

- A cubic spline interpolation of the array $F_i^{(k)}$, with $i = 0, 1..., N$ is done to have the continuous model cumulative DF $F^{(k)}(\ell)$. The function $f^{(k)}(\ell)$ is got from the relation $f^{(k)}(\ell) = \mathrm{d}F^{(k)}/\mathrm{d}\ell$ and is a piece-wise quadratic polynomial with continuous slope (while the double derivative of $f^{(k)}(\ell)$ on a grid point is discontinuous in general).

- The cubic spline interpolation requires the two more boundary conditions – the values of $F'(-1) = f(-1) \equiv f_0^{(k)}$ and $F'(1) = f(1) \equiv f_N^{(k)}$. These are derived from the direct discretization of the RR kinetic equation (4.11) around $\ell = \ell_{0,N} = \pm 1$ employing the Forward Euler method as:

$$\frac{f_0^{(k)} - f_0^{(k-1)}}{\Delta t} = -\left.\frac{\partial J}{\partial \ell}\right|_{\ell=-1} \equiv -J_0' \tag{4.40a}$$

$$\frac{f_N^{(k)} - f_N^{(k-1)}}{\Delta t} = -\left.\frac{\partial J}{\partial \ell}\right|_{\ell=+1} \equiv -J_N' \,. \tag{4.40b}$$

 To obtain the current derivatives at $\ell = \pm 1$, we compute the current at the points $\ell_+ = (\ell_{N-1}+1)/2$ and $\ell_- = (\ell_1 - 1)/2$ which bisect the edge grid interval. Referring to the corresponding currents as J_+ and J_-, the derivatives are got from the direct discretization $-J_+/(1-\ell_+)$ and $J_-/(\ell_- + 1)$. The bisection is repeated on (ℓ_+,1) and (-1,ℓ_-), followed by the computation of the current derivatives using the new bisecting points for discretization as done earlier. These steps are iterated till the derivatives converge upto 0.1%, with 20 being the maximum number of trials.

The equations (4.40) along with (4.38) are employed at each time-step in the RR code to evolve the bin-areas A_i and the edge-values of DF f_0 and f_N. The above methodology to obtain the model function $f^{(k)}(\ell)$ by spline fit of the cumulative DF array F_i, conserves the norm $\mathcal{N}$. For the calculation of the currents, the method provides the required quantities f, $\partial f/\partial\ell$ and $\partial\Omega/\partial\ell$, which turn out to be continuous in ℓ-space.

We now describe the schematics of the code. The initial DF $f_{\rm in}(\ell)$ is chosen and its bin-areas A_i are evaluated leading to the cumulative DF array F_i. The cubic spline fitting of F_i is done, given the derivatives of F at the grid end points i.e. $f_{\rm in}(-1)$ and $f_{\rm in}(+1)$. The resultant array of spline coefficients and hence, the model function $f^{(k)}(\ell)$ is fed to the time loop, which comprises of the following sequence of steps.

- Given the continuous function $f^{(k)}(\ell)$ from the previous time-step, it is straightforward to evaluate the Ω profile from the equation (4.14). Then the extremum points of the Ω profile are identified, as explained in § 4.2.2. Let $\ell_0^{(m)}$ be the location of the extrema, and the corresponding value of precession rate be $\Omega_0^{(m)}$ on the $\ell > 0$ half of the ℓ-space; $m = 1, ..., m_s$, where m_s is the number of extremum points in the half-space. Since the Ω profile is monotonic between the two neighbouring extremum points, there are $(m_s + 1)$ number of slots/regions in the half-space where the Ω profile is monotonic.

- Resonance points for each grid point ℓ_i on the positive half-space ($\ell > 0$) are evaluated. For each ℓ_i, there can be at maximum m_s resonant points each possibly lying in a monotonic slot not containing ℓ_i. Also, note that each monotonic slot can have at the maximum only one resonant point for a given ℓ_i. The detailed steps involved are provided in § 4.2.2. Due to the anti-symmetry of the Ω profile (see equation 4.14), inverting the signs of the resonant points gives the resonant set of points in the negative half of the ℓ-space.

- The currents J_i are evaluated at all the grid points ℓ_i using equation (4.39). The interpolated continuous function $f^{(k)}(\ell)$ and the corresponding $\Omega(\ell)$ profile are employed to evaluate the required quantities f, $\partial f/\partial\ell$ and $\partial\Omega/\partial\ell$ at the resonant points.

- The currents J_i are then used in equation (4.38) to advance the bin areas A_i in time. Current derivatives are evaluated at the end points $\ell = \pm 1$ as explained earlier, to evolve the DF values at the end points, f_0 and f_N, using equation (4.40).

- The updated bin areas are finally used to evaluate the new cumulative DF array F_i that is cubic spline interpolated using the updated values of f_0 and f_N as boundary conditions.

The updated coefficient array got from the spline interpolation (and hence the continuous function $f^{(k)}(\ell)$) serves as the feedback to the time loop, and above steps are repeated until time $0.2\,T_{\rm res}$. Enroute the values of conserved quantities $\{\mathscr{N}, \mathscr{L}, \mathscr{E}\}$, along with entropy S are recorded. $\mathscr{N}$ is exactly conserved in the scheme of the code. The reason is the conservative form of the time-stepping discrete equation (4.38) and also, the cubic spline interpolation of the cumulative DF array which ensures that bin-areas are not changed while getting the continuous function $f^{(k)}(\ell)$. The other conserved quantities $\mathscr{L}$, $\mathscr{E}$ remain close to their initial values to good precision; see § 4.3. Entropy S increases with time and saturates by the end of the calculation. Dynamical stability of the evolving DF is checked after a few time-steps by solving the integral eigenvalue equation (2.23); details of the method are provided in § 4.2.3.

Now, we elaborate on some of the steps of the above methodology.

4.2.1 Cubic Spline Interpolation of Cumulative DF

In the RR code, these quantities are available from the previous time-step – cumulative DF array $\{F_i\}$ with $i = 0, 1, ..., N$, and the DF values $\{f_0, f_N\}$ at end-points. Cubic spline interpolation gives the following interpolated cumulative DF:

$$F_i(\ell) = a_i + b_i(\ell - \ell_i) + c_i(\ell - \ell_i)^2 + d_i(\ell - \ell_i)^3 \quad \text{for } \ell \in [\ell_i, \ell_{i+1}] \tag{4.41}$$

with $i = 0, 1, .., N - 1$. This is a piece-wise cubic polynomial with $4N$ interpolation coefficients $\{a_i, b_i, c_i, d_i\}$. These are derived in the standard manner from the continuity relations of cumulative DF and its derivatives at the grid points ℓ_i, as given in Appendix E.

The continuous functional form for DF at time t_k, $f^{(k)}(\ell)$ (henceforth k dependence will be dropped for convenience) is the derivative of the interpolated cumulative DF and hence is given by the following piece-wise quadratic polynomial:

$$f_i(\ell) = \frac{\mathrm{d}F_i}{\mathrm{d}\ell} = b_i + 2c_i(\ell - \ell_i) + 3d_i(\ell - \ell_i)^2 \quad \text{for } \ell \in [\ell_i, \ell_{i+1}] \ . \tag{4.42}$$

It is evident from the procedure of the spline interpolation in Appendix E, the cumulative DF $F(\ell)$ and its first two derivatives are continuous (even at the grid points). This implies the continuity of the first derivative of the interpolated DF $\mathrm{d}f(\ell)/\mathrm{d}\ell = \mathrm{d}^2F(\ell)/\mathrm{d}\ell^2$; but $\mathrm{d}^2f(\ell)/\mathrm{d}\ell^2$ is not continuous at the grid points. Still, this methodology is effective in the present context, because analytical expressions (see equation 4.16) do not require the second derivative. The benefit of doing the interpolation for the cumulative DF $F(\ell)$ (instead of the DF $f(\ell)$ itself) is that this preserves the norm to high precision when used in combination with our conservative scheme of the algorithm; see equation (4.38).

Physical quantities in terms of the interpolated function: For evaluation of the current using equation (4.16), we need to calculate the quantities f, $\mathrm{d}f/\mathrm{d}\ell$ and $\mathrm{d}\Omega/\mathrm{d}\ell$ at the resonant points, which generally lie between the grid points. Here we present these quantities in terms of the interpolated function $F(\ell)$ (and/or continuous function $f(\ell)$). Firstly, differentiating the equation (4.42), we have $\mathrm{d}f/\mathrm{d}\ell$ expressed as:

$$\frac{\mathrm{d}f_i(\ell)}{\mathrm{d}\ell} = 2c_i + 6d_i(\ell - \ell_i) \quad \text{for } \ell \in [\ell_i, \ell_{i+1}] \ . \tag{4.43}$$

Equation (4.14) for $\Omega(\ell)$ can be manipulated to the following form:

$$\Omega(\ell, t) = \frac{-2\ell}{1 - \ell^2} \left[1 - F(|\ell|) + F(-|\ell|)\right] \tag{4.44}$$

where the interpolated cumulative DF F is explicitly known; see equation (4.41). Differentiating the above equation, it is straightforward to manipulate the Ω derivative to the following form:

$$\frac{\mathrm{d}\Omega(\ell)}{\mathrm{d}\ell} = \frac{1 + \ell^2}{\ell(1 - \ell^2)}\Omega(\ell) + \frac{2|\ell|}{1 - \ell^2} \left[f(\ell, t) + f(-\ell, t)\right] \tag{4.45}$$

where the continuous model DF f is explicitly known from equation (4.42).

4.2.2 Locating Resonances

Here we explain the detailed steps involved in locating the resonant points having equal apse precession frequency Ω. We limit the domain of investigation to the positive half of the ℓ space. Firstly, the extremum points ℓ_0 of Ω profile are identified. These points divide the half space into monotonic slots of Ω. Then, sets of resonant points $\ell_{\rm r}$'s are located for each grid point ℓ_i, to evaluate the current J_i from equation (4.39).

With the interpolated function $F(\ell)$ available, it is straightforward to calculate the apse precession Ω_i at grid points ℓ_i from equation (4.44). Then we locate the extremum points ℓ_0 of the Ω profile using the scheme, given below. We first look for the grid points ℓ_i which satisfy the condition:

$$(\Omega_i - \Omega_{i-1})(\Omega_{i+1} - \Omega_i) \leq 0\,; \quad i \in \left[\frac{N}{2} + 1, N-1\right]\,. \tag{4.46}$$

Then i is the grid index which locates the turning point of Ω profile on the grid; there can be more than one such points in general. Hence the extremum point ℓ_0 should be located in either of the two grid intervals $[\ell_{i-1},\ell_i]$ or $[\ell_i,\ell_{i+1}]$ and respectively we have the grid index $i_0 = i-1$ or i for the extremum point ℓ_0. We evaluate the derivatives of the precession rate $\Omega' \equiv {\rm d}\Omega/{\rm d}\ell$ at the consecutive grid points ℓ_{i-1}, ℓ_i and ℓ_{i+1} using equation (4.45). If $\Omega'_{i-1}\,\Omega'_i \leq 0$, $i_0 = i-1$ and else if $\Omega'_i\,\Omega'_{i+1} \leq 0$, $i_0 = i$. After knowing the grid-index i_0, we have to locate the extremum point $\ell_0 \in [\ell_{i_0}, \ell_{i_0+1}]$, for which the derivative of the apse precession vanishes. We numerically locate it by employing the bisection method for the condition, $|\Omega'_0| < 10^{-10}$, to be satisfied.

In general, we can have some finite number $m_{\rm s}$ of the extremum points $\ell_0^{(m)}$ with the corresponding precession rates $\Omega_0^{(m)}$ where $m = 1, 2, ...m_{\rm s}$. But, for RR of the initial example DF of equation (4.52), the evolving Ω profile at a time is characterized by a single extremum point in the half-space; see Figure 4.2b. These extrema $\ell_0^{(m)}$ divide the positive half of the ℓ space into $(m_{\rm s}+1)$ slots within which the Ω–profile remains monotonic. These slots are $[\ell_0^{(m)}, \ell_0^{(m+1)}]$ for $m = 0, 1, ..., m_{\rm s}$ where $\ell_0^{(0)} = 0$ and $\ell_0^{(m_{\rm s}+1)} = 1$ are the bounds of the half-space. For a point ℓ_i, the resonant point $\ell_{\rm r}$ is the one satisfying the condition $\Omega(\ell_{\rm r}) = \Omega(\ell_i)$. For a given ℓ_i, there can be at the most a single resonant point in each monotonic slot, except the one containing ℓ_i. So any point can have at the most $m_{\rm s}$ number of resonant points. Firstly it is determined whether or not a given monotonic slot contains any resonant point. A slot $[\ell_0^{(m)}, \ell_0^{(m+1)}]$ will have a resonant point for ℓ_i only if the condition $(\Omega_i - \Omega_0^{(m)})(\Omega_i - \Omega_0^{(m+1)}) < 0$ is satisfied. Then a grid interval $[\ell_j, \ell_{j+1}]$ (within the monotonic slot) contains the resonant point if $(\Omega_i - \Omega_j)(\Omega_i - \Omega_{j+1}) < 0$. Till here, the grid-index j of the interval containing a resonant point $\ell_{\rm r}$ is determined.

Then we need to further pinpoint the resonant point $\ell_{\rm r} \in [\ell_j, \ell_{j+1}]$ so as to evaluate the current J_i. Using equation (4.14) (for positive ℓ) in the resonance condition $\Omega(\ell_{\rm r}) = \Omega_i$, we have:

$$-\frac{2\ell_{\rm r}}{1-{\ell_{\rm r}}^2}\left(1-\int_{-\ell_{\rm r}}^{\ell_{\rm r}} \mathrm{d}\ell' f(\ell')\right) = \Omega_i \,. \tag{4.47}$$

From the definition of cumulative DF $F(\ell)$, the above equation can be expressed in the form:

$$\ell_{\rm r}\left[1+F(-\ell_{\rm r})-F(\ell_{\rm r})\right]+\frac{\Omega_i}{2}(1-{\ell_{\rm r}}^2) = 0 \,. \tag{4.48}$$

Since F is a piece-wise cubic polynomial, the above equation is a quartic polynomial equation in $\ell_{\rm r}$. Using equation (4.41), we have the following expressions for $F(\pm\ell_{\rm r})$ with $\ell_{\rm r} \in [\ell_j, \ell_{j+1}]$ and $-\ell_{\rm r} \in [\ell_{N-j-1} = -\ell_{j+1}, \ell_{N-j} = -\ell_j]$:

$$F(\ell_{\rm r}) = a_j + b_j(\ell_{\rm r}-\ell_j) + c_j(\ell_{\rm r}-\ell_j)^2 + d_j(\ell_{\rm r}-\ell_j)^3 \tag{4.49a}$$

$$F(-\ell_{\rm r}) = a_{N-j-1} + b_{N-j-1}(\ell_{j+1}-\ell_{\rm r}) + c_{N-j-1}(\ell_{j+1}-\ell_{\rm r})^2 + d_{N-j-1}(\ell_{j+1}-\ell_{\rm r})^3 \,. \tag{4.49b}$$

This leads to the final quartic polynomial equation in $\ell_{\rm r}$ given explicitly in equation (F.1) of Appendix F. A general quartic equation can be solved analytically for its four roots. The explicit forms of these roots are provided in equation (F.2). Exactly one out of these four roots satisfies $\ell_{\rm r} \in [\ell_j, \ell_{j+1}]$ and is the required resonant point for ℓ_i. This analytic root-finding is highly favored so as to minimize the numerical errors in the RR code.

4.2.3 Secular Dynamical Stability

The RR code keeps a check on the dynamical stability of the resonantly relaxing system to non-axisymmetric secular modes. Linear secular stability of monoenergetic axisymmetric discs is analyzed in § 2.2.2 of Chapter 2. It is already noted that the axisymmetric modes of an axisymmetric Keplerian disc are neutrally stable (ST16a). The linearly perturbed system has the DF $f(\ell,t)/(2\pi) + \mathrm{Re}\{f_{1m}(\ell,t)\exp\left[\mathrm{i}(mg-\omega_m(t)t)\right]\}$ for a mode corresponding to the azimuthal wavenumber m. Here $\omega_m(t)$, $f(\ell,t)$ and $f_{1m}(\ell,t)$ have a long-term time dependence over the RR timescales $T_{\rm res}$. The eigenvalues $\omega_m(t)$ can be complex in general; its real part signifies the rotational frequency of the m-pattern, and the imaginary part represents the growth rate of the mode. Using the Fourier coefficients of equation (4.13), the linear integral eigenvalue problem for secular stability given in equation (2.23) can be rewritten as:

$$[\omega_m(t) - m\,\Omega(\ell,t)]\,f_{1m}(\ell,t) = -m\,\frac{\partial f(\ell,t)}{\partial \ell}\int_{-1}^{1}\mathrm{d}\ell'\,C_m(\ell,\ell')f_{1m}(\ell',t) \qquad (4.50)$$

where $\Omega(\ell,t)$ evolves over the timescale $T_{\rm res}$.

We discretize the above integral equation over the ℓ-space grid to get the corresponding matrix eigenvalue problem. The ℓ and ℓ' are written as ℓ_i and ℓ_j respectively. We represent the discretized form of eigen-amplitudes $f_{1m}(\ell,t)$ as X_i, where i indicates evaluation at ℓ_i. The long term time-dependence of all the quantities is suppressed in the discretized representation. We represent $C_m(\ell,\ell')$ as C_{ij}, with the suppression of m-dependence in the notation. The ℓ'-integral is discretized using mid-point method considering uniformly spaced grid-points ℓ_j, $j = 1, 2, ..., (N-1)$. Note that the end-points $\ell_0 = -1$ and $\ell_N = +1$ need not be considered as $C_m(\ell,\ell')$ and hence the integrand vanishes at $\ell' = \pm 1$. From equation (4.50), $f_{1m}(\pm 1, t) = 0$ and hence $X_{0,N} = 0$. The final $(N-1)\times(N-1)$ matrix eigenvalue problem is given as:

$$\sum_{j=1}^{N-1} M_{ij}\,X_j \;=\; \omega_m\,X_i \qquad \text{where} \qquad M_{ij} \;=\; m\,(\Omega_j\,\delta_{ij} - \Delta\ell\; f_i'\; C_{ij}) \qquad (4.51)$$

for $i = 1, 2, ..., (N-1)$. The problem is numerically solved using the DGEEV subroutine from LAPACK[1]. The eigenvalues are computed for $m = 1, 2, ..., 100$, with attention paid to their imaginary parts. The initial DF of equation (4.52), evolved by the RR code, remains dynamically stable throughout the evolution, as discussed in § 4.3.

Now the question arises, what if the system goes unstable on the way for some general initial DF? Under such a situation, the unstable state should be evolved by N-Ring simulations (Touma et al., 2009). After witnessing the emergence of the fastest growing linear unstable mode (deducible from the above calculations), the system will further evolve non-linearly towards a secularly stable collisionless equilibrium. The resulting DF from the simulations should be further evolved by the RR kinetic equation; the RR code can be used for axisymmetric DFs.

4.3 RR Code Results

In this section, we present results from the RR code for a sample DF. The discretized grid contains $N = 200$ intervals in ℓ-space with the grid interval $\Delta\ell = (\ell_N - \ell_0)/N =$

[1]Linear Algebra PACKage (a library of Fortran subroutines)

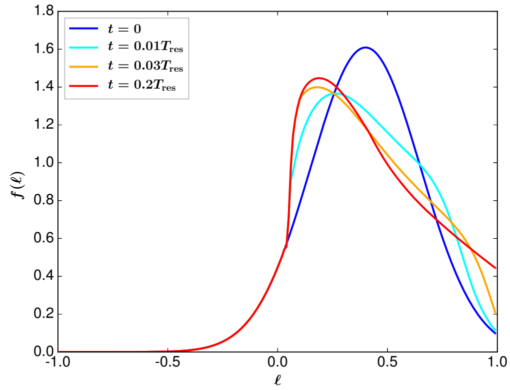

(a) Distribution function $f(\ell)$

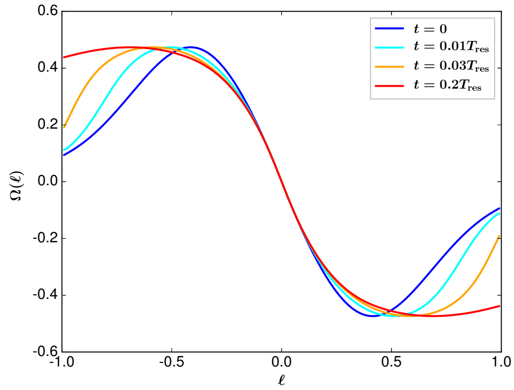

(b) Apse precession rate $\Omega(\ell)$

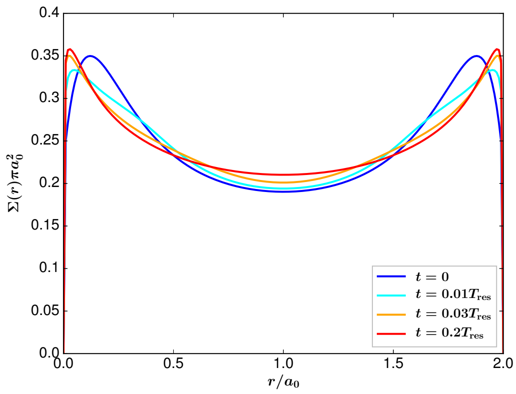

(c) Surface probability density $\Sigma(r)$

Fig. 4.2 RR Code results for a typical Gaussian DF: (a). Distribution function $f(\ell)$, (b). Apse precession $\Omega(\ell)$ (in the units of $T_{\rm sec}{}^{-1}$), (c). Surface density $\Sigma(r)$ profiles, are plotted for the resonantly relaxing disc by the RR code at various intermediate times, including the initial state (in blue) and the final state at $0.2T_{\rm res}$ (in red). The initial Gaussian DF is given by equation (4.52).

$2/N = 0.01$. Since the RR kinetic equation (4.11) has a diffusive term, the time-step $\Delta t = CFL \times \Delta\ell^2$ (in units of $T_{\rm res}$) is chosen for the stability of numerical algorithm (Press et al., 1992). Here we choose $CFL = 10^{-4}$. The RR code is run till $0.2\,T_{\rm res}$. We choose an initial Gaussian DF $f_{\rm in}(\ell)$ explicitly given as:

$$f_{\rm in}(\ell) = A\exp\left(-\frac{(\ell-\ell_0)^2}{2\sigma^2}\right) \tag{4.52}$$

with $A \simeq 1.6$, $\ell_0 = 0.4$ & $\sigma = 0.25$. The DF evolves by the RR code and settles to a *stationary state* by $\sim 0.08\,T_{\rm res}$. The evolving DF profile is shown in the Figure 4.2a at different intermediate times, including the initial and end-states. For the sub-dominant retrograde population ($\ell < 0$), DF seems to remain frozen throughout the evolution. A prograde DF, on the other hand, spreads in ℓ-space towards both higher and lower eccentricities. Mass in near-circular orbits increases with time. Also, the median of the profile (initially at $\ell_0 = 0.4$) shifts gradually towards the high eccentricities. Hence RR heats up the system, resulting in states with apparently higher velocity dispersions. Stars orbiting along the high eccentricity Rings, approach central MBH closely (evident from the evolving surface density profile in Figure 4.2c), and are susceptible to various astrophysical phenomena discussed earlier, like TDEs, EMRIs and/or MBH feeding. The evolving apse precession Ω profiles are shown in the Figure 4.2b. It is intriguing to see that the Ω profiles become more and more flattened with time, especially for the moderate and low eccentricity Rings. High eccentricity Rings keep precessing differentially throughout the evolution, while the remaining Rings for the end-state distribution seem to be co-precessing with a constant apse precession rate, which is very close to the maximum precession rate (corresponding to time $\sim 14\,T_{\rm sec}$) for the initial Ω profile.

We compute the real-space surface probability density $\Sigma(r)$ for the evolving DFs (Figure 4.2a) using equation (G.4) derived in Appendix G. Figure 4.2c shows $\Sigma(r)$ profiles at the corresponding times. The $\Sigma(r)$ profiles are double humped (or horned), which is typical of the monoenergetic discs (see Figure 2.3a for waterbags). As a result of the angular momentum relaxation due to RR, the radial distance between these density humps widens, channeling the mass – inwards closer to the MBH, and also outwards near outer edge of the disc. This characteristic arises due to the increase in the population of the high eccentricity Rings, as a result of RR. Since the near-circular population of Rings also rise in a resonantly relaxing disc, the Σ at mid-radius a_0 of the disc also increases with time.

It is evident from the Figure 4.2 that there is an interval about $\ell = 0$ within which the $f(\ell)$ and $\Omega(\ell)$ profiles do not undergo any change throughout the evolution. This is due to the absence of resonances and hence the currents in this region. This is the region of non-resonance described in § 4.1.1; see Figure 4.1b. Figure 4.2b for the evolving $\Omega(\ell)$ profiles shows that this region keeps expanding with time (as $\Omega(\ell = \pm 1)$ keeps increasing in magnitude). This also shows up in Figure 4.3, where the region of ℓ space with non-zero currents keeps shrinking with time. The decaying magnitudes of the current $J(\ell)$ with time are evident, as the $J(\ell)$ profiles are shown for the evolving DFs of Figure 4.2a. The current magnitudes drop to $\sim 10^{-4}$ for the final state, with the initial state values being of the order ~ 50.

Conserved quantities and entropy: The RR code preserves the conservation of the norm $\mathscr{N}$, normalized angular momentum $\mathscr{L}$ and normalized energy $\mathscr{E}$, introduced in § 4.1.3. In Figure 4.4a, we plot the quantity $\mathscr{N} - 1$ and it turns out to be of the order $\sim 10^{-10}$. This almost exact conservation of $\mathscr{N}$ is due to the conservative scheme and other features of the algorithm, as explained in § 4.2. The angular

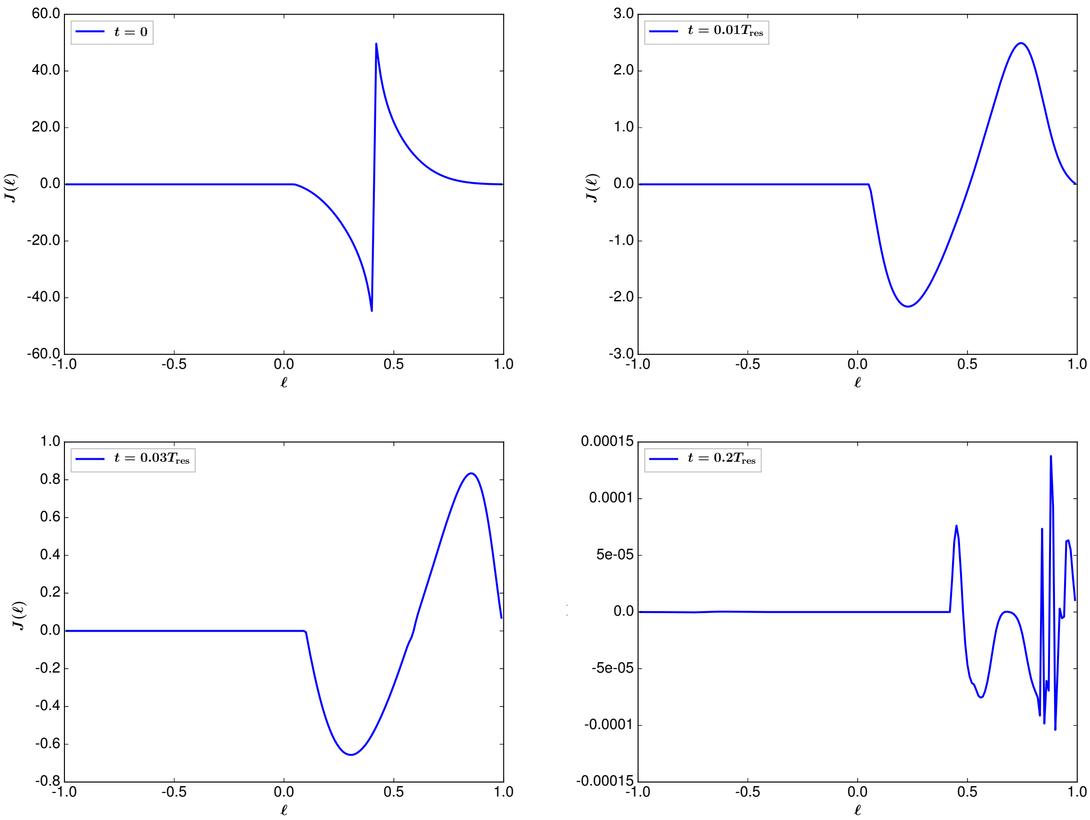

Fig. 4.3 RR evolution of current profiles $J(\ell)$ plotted for the evolving DFs of Figure 4.2a.

momentum $\mathscr{L}$ is conserved till four decimals, with approx. relative error $\leq 10^{-4}$; see Figure 4.4b. The energy $\mathscr{E}$ is conserved till fifth decimal with the approx. relative error of $\sim 10^{-6}$, as evident from Figure 4.4c. From Figure 4.4d, the entropy S is an ever increasing function in relevance to theoretical predictions of ST17, as described in § 4.1.4. Initially, there is a gradual rise in S till $\sim 0.05\, T_{\rm res}$; afterwards the S remains nearly constant signifying the fact that system has reached a stationary state.

Dynamical stability checks: The RR code checks linear dynamical stability of the system throughout the evolution, making use of the scheme described in § 4.2.3. For the chosen initial DF of equation (4.52), the evolving system remains stable to the non-axisymmetric modes with the azimuthal wave-numbers upto $m = 100$ (which is the maximum wave-number explored during this exercise). The stability matrix equation (4.51) is solved for its eigenvalues using LAPACK. It is found that the maximum magnitude of the growth rate (or imaginary part of the eigenvalues) is of the order $\sim 10^{-3}$. Hence the instabilities can possibly grow over times $\sim 1000\, T_{\rm sec}$. As the timescale can be quite comparable to $T_{\rm res} \sim N_\star T_{\rm sec}$, these slowly growing instabilities do not get the enough time to mark a change in the evolution pathway,

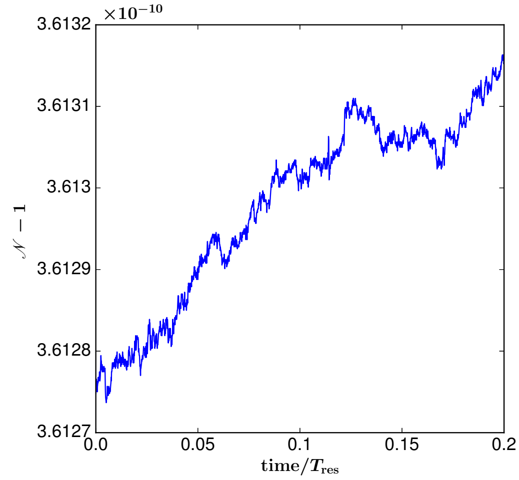

(a) Norm $\mathscr{N}-1$

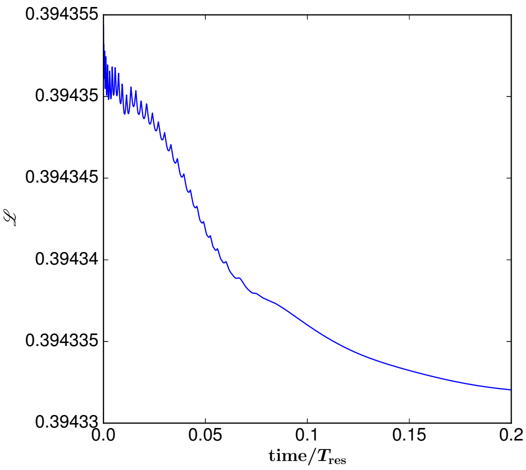

(b) Angular Momentum $\mathscr{L}$

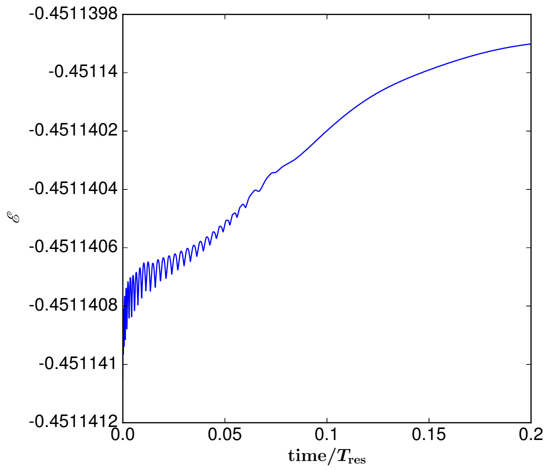

(c) Energy $\mathscr{E}$

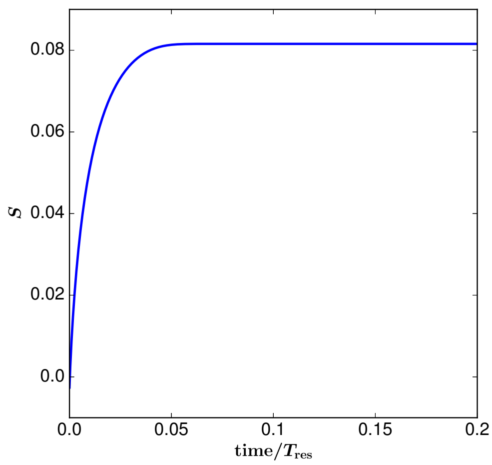

(d) Entropy S

Fig. 4.4 Evolution of the conserved quantities $\{\mathscr{N}, \mathscr{L}, \mathscr{E}\}$ and the entropy S by the RR code.

as in the mean time system evolves to a different state by RR. Hence, the example system is considered to be secularly stable throughout the evolution.

4.3.1 Nature of end states

The end state DF at $t = 0.2\, T_{\rm res}$ (shown in Figure 4.2a) corresponds to the extremely low magnitude of current $J(\ell)$ (fourth panel of Figure 4.3). Stationary state DF $f_{\rm s}(\ell) = A\ \exp\left[\int_{-1}^{\ell} \eta[\Omega_{\rm s}(\ell)]\, {\rm d}\ell\right]$, which are constructed in § 4.1.5, corresponds to the absolute zero currents. For the stationary states, $f_{\rm s}^{-1}{\rm d}f_{\rm s}/{\rm d}\ell = \eta[\Omega_{\rm s}]$ is a single-valued functional of $\Omega(\ell)$.

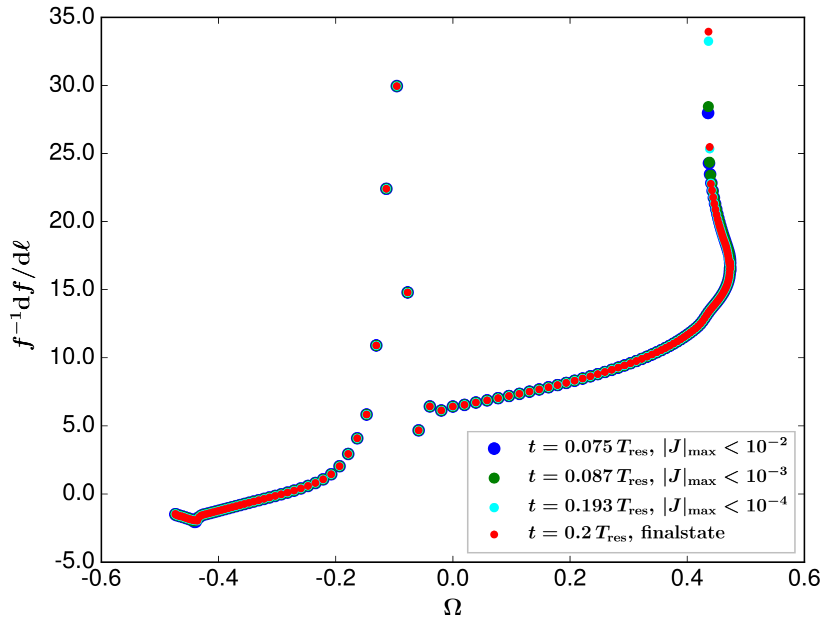

Fig. 4.5 $f^{-1}\mathrm{d}f/\mathrm{d}\ell$ *vs* Ω *profiles* for the states where the current magnitudes have fallen significantly.

In Figure 4.5, we plot $f^{-1}\mathrm{d}f/\mathrm{d}\ell$ vs Ω for the evolving DF for which the maximum current magnitude falls to almost 10^{-2}(at $\sim 0.075\,T_{\mathrm{res}}$), 10^{-3}(at $\sim 0.088\,T_{\mathrm{res}}$), 10^{-4} (at $\sim 0.193\,T_{\mathrm{res}}$), and also for the end state at $0.2\,T_{\mathrm{res}}$. The profiles nearly superpose for these four states, and it can be seen that $f^{-1}\mathrm{d}f/\mathrm{d}\ell$ is a single–valued functional of Ω for most of the range in ℓ space, except the largish positive values of Ω (corresponding to $\ell < 0$) where f itself is very small (see Figure 4.2). Hence, the end states, from the RR code, correspond very closely to the stationary states of the RR kinetic equation (4.11). The analysis serves as a good consistency check for the RR code.

Note that the $f^{-1}\mathrm{d}f/\mathrm{d}\ell$ profile in Figure 4.5 appears to be linear for some parts of ℓ-space. If $f^{-1}\mathrm{d}f/\mathrm{d}\ell$ is a linear polynomial in Ω for the entire ℓ-space, then the stationary state corresponds to a thermal equilibrium of the form $f_{\mathrm{th}}(\ell) = A\exp\left[-\beta\Phi_{\mathrm{th}}(\ell) + \gamma\ell\right]$ (the equation 4.35). Hence, the end state does not correspond to the thermal equilibrium contrary to usual physical expectations. The sharp peak in the figure for $\Omega \sim [-0.2, 0]$, corresponds to the prograde population of Rings lying in the region of non-resonance (see Figure 4.2). This points out that the occurrence of non-thermal end states is possibly related with the non-relaxed DF in this region of zero current.

4.4 Discussion and conclusions

In this chapter, we have presented a study of the implementation of the present version of the RR code. We plan to improve various aspects of the code in the future. *Firstly* we have chosen the simplest time-stepping algorithm employing Euler scheme; see equation (4.38). We will upgrade it to the more sophisticated time-stepping schemes, like `RK4` (Press et al., 1992), that might lead to the better conservation of quantities $\{\mathscr{L}, \mathscr{E}\}$. Still with our very simple scheme, the approx. relative errors for $\mathscr{L}$ and $\mathscr{E}$ are 10^{-4} and 10^{-6} respectively. *Secondly* we will implement adaptive time stepping in the future version of the RR code, for better efficiency. For the present example study, the initial evolution is faster till $0.05\,T_{\mathrm{res}}$; afterwards it is much slower as evident from the entropy S evolution plot of Figure 4.4d. Hence, it is more efficient to choose smaller time-steps initially and longer time-steps for later parts of the evolution, rather than the present uniform time-stepping interval.

In the present example, central MBH is not considered as a sink and hence, the DF $f(\ell, t)$ has a conserved norm throughout the evolution. The resonantly relaxed system has greater population of high-eccentricity Rings, as discussed in § 4.3. If a loss-cone is considered around the MBH, it might lead to the accelerated feeding of the MBH and other astrophysically fascinating events like TDEs and EMRIs. Extensions of the present study can help deducing occurrence rates for such events. Also, it is interesting to see the effects of general relativistic precession on the RR evolution. There have been interesting results from previous simulation studies (Merritt et al., 2011; Bar-Or & Alexander, 2014; Hamers et al., 2014) where relativistic precession turns out to quench RR near MBH (*Schwarzschild barrier*), hampering the inward flow of stellar mass. It would be interesting to see the manifestation of this barrier in the present semi-analytical picture of ST16b.

The end state from the RR evolution turns out to be a stationary state of the form given in equation (4.34), and does not correspond to the expected Boltzmann-type thermal equilibrium of equation (4.35). We suspect that the occurrence of the region of non-resonance deprives a part of the phase space from having currents and evolving by RR. This non-occurrence of resonances in a part of the ℓ-space is responsible for preventing the system to reach the corresponding thermal equilibrium state. This might be a reason for the evolution of the system to the non-thermal stationary states by the RR code. As a check, we plan to construct the thermal equilibrium for given $\mathscr{L}$ and $\mathscr{E}$ (for the present example DF), and compare it with the stationary end state got from the RR code.

It would also be interesting to compare the results of the RR code with N-Ring simulations (Touma et al., 2009). Evolution of the high eccentricity Rings corresponding to the non-resonant region around $\ell = 0$, would be especially interesting to study. In the present semi-analytical approach, DF remains frozen in this region, which keeps expanding with time. The surmised evolution of DF in this region in simulations is important for understanding the underlying physics of RR. It would be quite important to compare the end-states from the RR code and simulations. The RR code end state is dynamically stable; while its thermodynamic stability is yet to be deduced. N-Ring simulations of this end state would provide an ultimate check on the thermal stability and hence, on the physical significance of these stationary states.

The present study of RR evolution of a monoenergetic axisymmetric disc seems to represent a pathological case due to presence of the region of non-resonance about $\ell = 0$. This might be the reason for the non-thermal end states of the RR code. It is important to note that the RR evolution of a monoenergetic disc occurs in one-dimensional ℓ-space, where the $\Omega(\ell, t)$ curve at any time t, can offer a discrete and finite set of resonant points $\ell_{\mathrm{r}j}$ for any point ℓ_i; see the Figure 4.1b. This leads to the region of non-resonance where even a single resonant point is geometrically unavailable. It is apparent that the lower dimensionality of the problem is responsible for non-resonant region. Hence, it is necessary to generalize these studies to axisymmetric Keplerian disc, by lifting the monoenergetic assumption. Resonances take a more generic form in discs composed of stars with a range of semi-major axes. The RR occurs in two-dimensional $(I,\ L)$-space, and $\Omega(I,\ L,\ t)$ is a curved two-dimensional surface, which will allow resonant lines $L_{\mathrm{r}}(I)$ and hence a continuous set of resonant points for any point (I, L). It is likely that every point in the space would manage to avail resonances and DF can resonantly relax throughout the space, leading to the thermal equilibrium end states. Hence, moving to the more general and realistic case of non-monoenergetic axisymmetric discs seems to be important to understand the collisional behaviour of naturally occurring astrophysical Keplerian discs.

The RR kinetic equation (4.3)-(4.4) (as derived by ST17) is based on direct two-Ring interactions and does not take into account collective gravitational encounters (gravitational polarization) among Rings. A natural question that arises is whether the inclusion of polarization effects will modify RR evolution in some fundamental manner. Also, the studies considering collective interactions are more suited for comparisons with N-Ring simulations proposed above. In the next chapter, we take forth this mission and set up the analytical framework to include gravitational polarization for RR of axisymmetric Keplerian discs.

Chapter 5

Resonant Relaxation with Gravitational Polarization

ST17 derived a Fokker-Planck equation for the resonant relaxation (RR) of axisymmetric Keplerian discs. They evaluated the wake function in the passive response approximation (PRA) limit, which corresponds to the neglect of gravitational polarization. This implies that collective gravitational encounters among the constituent Gaussian Rings are not taken into account. In this chapter, we extend the RR theory of ST17 for axisymmetric discs by incorporating polarization. We develop an analytical perturbative scheme to incorporate polarization terms iteratively, formally accounting for all the orders. We recover the PRA current of the zeroth order theory, and derive the leading order polarization current from the first order terms. The different orders of the perturbation theory can be thought of as accounting for the multiplicities of encounters among Rings. The PRA theory is based on two-Ring encounters; the first order polarization theory is based on three-Ring encounters; and the n^{th} order theory on $(n+2)$-Ring encounters.

In § 5.1, we present the general RR kinetic equation of ST16b and the perturbative series solutions of the wake equation as derived by ST17. We specialize to an axisymmetric Keplerian disc in § 5.2, and interpret the physical meaning of the leading order wake-function $W^{(0)}$ in terms of the angular momentum change a Ring accumulates due to two-Ring or direct interactions. The higher order wake $W^{(n)}$, with $n = 1, 2, ...$, is proportional to the angular momentum change a Ring accumulates due to gravitational interactions with the wake $W^{(n-1)}$. Hence the higher order wakes ($W^{(1)}$, $W^{(2)}$ and so on) account for collective interactions among the constituent Gaussian Rings; going to each higher order further improves this accounting. In § 5.2.1, we explicitly derive the Fourier series of the lowest order wake function $W^{(0)}$.

We also derive a recurrence relation for Fourier coefficients, leading to higher order wakes $W^{(n)}$, with $n = 1, 2, ...$ Hence, in principle we have the complete solution of the wake equation in terms of a perturbative expansion. This leads to a general perturbative expansion of the two-Ring correlation function $F^{(2)}_{\rm irr}$ in § 5.3, which further leads to a series expansion of the RR current J in § 5.4. We also derive the RR kinetic equation for an axisymmetric Keplerian disc (including polarization effects). In this series expansion framework, a coefficient depends upon only the lower order coefficients and hence, the theory can be truncated consistently at a certain order. In § 5.4.1, we give expressions for the lowest order currents $J^{(0)}$ (corresponding to PRA) and $J^{(1)}$ (corresponding to the first order polarization). We reduce the RR kinetic equation for truncation at $O(1)$ theory, for which we evaluate currents explicitly. Then, we study the nature of stationary states of this reduced kinetic equation in § 5.5. Finally, we conclude in § 5.6.

5.1 Basic Formalism and Perturbation Theory

We consider a star cluster of mass M composed of $N_\star \gg 1$ Gaussian Rings. The central MBH is of mass $M_\bullet \gg M$ and the system is a Keplerian star cluster with the small parameter $\epsilon = M/M_\bullet$. The formalism of theoretical framework of ST16b was presented in § 1.4.2. The RR kinetic equation (1.19)-(1.20) is reproduced here as:

$$\frac{\partial F}{\partial \tau} + \left[F, H - \frac{\Phi(\mathcal{R},\tau)}{N_\star}\right] = \mathcal{C}[F] = \frac{1}{N_\star}\int \left[\Psi(\mathcal{R},\mathcal{R}'), F^{(2)}_{\rm irr}(\mathcal{R},\mathcal{R}',\tau)\right] {\rm d}\mathcal{R}' \qquad (5.1)$$

where $\mathcal{C}[F]$ is the collision integral. The irreducible part of the two-Ring correlation function $F^{(2)}_{\rm irr}$ can be written in terms of wake function W (as given in equation 1.21):

$$\begin{aligned} F^{(2)}_{\rm irr}(\mathcal{R},\mathcal{R}',\tau) \;&=\; W(\mathcal{R}\,|\,\mathcal{R}',\tau)\,F(\mathcal{R}',\tau) \;+\; W(\mathcal{R}'\,|\,\mathcal{R},\tau)\,F(\mathcal{R},\tau) \\ &\quad + \int W(\mathcal{R}\,|\,\mathcal{R}'',\tau)\,W(\mathcal{R}'\,|\,\mathcal{R}'',\tau)\,F(\mathcal{R}'',\tau)\,{\rm d}\mathcal{R}''\,. \end{aligned} \qquad (5.2)$$

The wake function $W(\mathcal{R}\,|\,\mathcal{R}',\tau)$ represents the linear response of the system at a generic point $\mathcal{R}$ to a discrete Gaussian Ring $\mathcal{R}'$. The *gedanken* experiment (Rostoker, 1964; Gilbert, 1968) leads to the wake equation (1.23), which is rewritten here as:

$$\begin{aligned} &\frac{\partial W}{\partial \tau'} \;+\; [\,W(\mathcal{R}\,|\,\mathcal{R}'(\tau'),\tau')\,,\,H(\mathcal{R},\tau')\,] \;+\; [\,F(\mathcal{R},\tau')\,,\,\Phi^{\rm w}(\mathcal{R},\mathcal{R}'(\tau'),\tau')\,] \\ &\qquad = \;[\,\Phi^{\rm p}(\mathcal{R},\mathcal{R}'(\tau'),\tau')\,,\,F(\mathcal{R},\tau')\,]\,, \qquad \text{for } \tau' \;\le\; \tau. \end{aligned} \qquad (5.3)$$

To follow the RR evolution of the system, the above pde for the wake function is to be simultaneously solved with the kinetic equation (5.1), with the adiabatic turn-on initial condition for the wake function i.e. $W(\mathcal{R}\,|\,\mathcal{R}'(\tau'),\tau') \to 0 \;\text{ as } \tau' \to -\infty\,.$ The wake equation can be solved in perturbative manner of ST17. Perturbative expansion for the wake $W(\mathcal{R}\,|\,\mathcal{R}',\tau)$ of Ring $\mathcal{R}'$:

$$W = W^{(0)} + W^{(1)} + W^{(2)} + ... \tag{5.4}$$

is substituted in the wake equation (5.3) to get the explicit solutions (from equation (26) of ST17):

$$W^{(0)}(\mathcal{R}\,|\,\mathcal{R}',\tau) = \int_{-\infty}^{\tau} \mathrm{d}\tau' \,[\, \Psi(\mathcal{R}(\tau'),\mathcal{R}'(\tau'),\tau') - \Phi(\mathcal{R}(\tau'),\tau')\,,\; F(\mathcal{R}(\tau'),\tau')\,]\;\;, \tag{5.5a}$$

$$W^{(n+1)}(\mathcal{R}|\mathcal{R}',\tau) = \int_{-\infty}^{\tau} \mathrm{d}\tau' \int \mathrm{d}\mathcal{R}''\,[\Psi(\mathcal{R}(\tau'),\mathcal{R}'',\tau'), F(\mathcal{R}(\tau'),\tau')]\, W^{(n)}(\mathcal{R}''|\mathcal{R}'(\tau'),\tau'),$$
$$\text{for } n = 0, 1, 2, \ldots . \tag{5.5b}$$

Here $\mathcal{R}(\tau')$ and $\mathcal{R}'(\tau')$ refer to the collisionless orbits of the Rings for the potential $\Phi(\mathcal{R},\tau)$ for $\tau' \le \tau$; $\mathcal{R} = \mathcal{R}(\tau)$ and $\mathcal{R}' = \mathcal{R}'(\tau)$ denote their phase space positions at $\tau' = \tau$. Here $W^{(0)}$ corresponds to the PRA wake function which does not include polarization effects. The $W^{(1)}$ is the leading order term accounting for polarization; and the higher order wakes add to further corrections. Note that the above equations have the two-Ring interaction potential with the explicit dependence on time given as

$$\Psi(\mathcal{R}(\tau'),\mathcal{R}'(\tau'),\tau') = \exp\,[\lambda\tau']\Psi(\mathcal{R}(\tau'),\mathcal{R}'(\tau'))\,, \quad \lambda \to 0^+\,, \tag{5.6}$$

because the wake function, and hence the interaction among the Rings, vanishes in the distant past $\tau' \to -\infty$. Here λ is a small positive parameter that controls the adiabatic switching on of interactions in the distant past.

The general wake function $W(\mathcal{R}\,|\,\mathcal{R}',\tau)$ satisfies the following two properties.

P1: The total mass contained in the wake of the Ring $\mathcal{R}'$ at any time τ is zero,

$$\int \mathrm{d}\mathcal{R}\; W(\mathcal{R}\,|\,\mathcal{R}',\tau) = 0\,, \tag{5.7}$$

because mutual torquing among Rings just leads to their rearrangement in phase space.

P2: The net wake at $\mathcal{R}$ due to all the Rings in the system vanishes,

$$\int \mathrm{d}\mathcal{R}'\; F(\mathcal{R}',\tau) W(\mathcal{R}\,|\,\mathcal{R}',\tau) = 0\,. \tag{5.8}$$

Henceforth we specialize to the case of an axisymmetric Keplerian stellar disc. In the next section, we evaluate the explicit expressions for the general wake function.

5.2 Wake Function for an Axisymmetric Disc

For a planar system, the Ring space is three-dimensional with $\mathcal{R} \equiv \{I, L, g\}$. An axisymmetric Keplerian disc has a DF of the form $F(I, L, \tau)$, which represents a collisionless (quasi) equilibrium over the secular timescales $T_{\rm sec}$, as we saw in § 2.1.1. The time-dependence of $F(I, L, \tau)$ signifies its collisional evolution over the RR timescales $T_{\rm res}$. The resultant self-gravitational potential $\Phi(I, L, \tau)$ (given by equation 2.7) of the disc evolves over the similar timescale, which is much longer than the apse precessional (secular) timescale $T_{\rm sec}$ of Rings. A wake arises due to interactions among the Rings, which build up over a few times $T_{\rm sec}$. Hence, the $\mathcal{R}(\tau')$ and $\mathcal{R}'(\tau')$ in the equations (5.5) are effectively the Ring orbits in an axisymmetric collisionless equilibrium at τ. These orbits are uniformly and rigidly precessing Gaussian Rings; see the equation (2.8) for the Ring orbits. Hence over timescales $\sim T_{\rm sec}$, the angular momentum L of a Ring is conserved and its apse precesses uniformly with frequency $\Omega(I, L, \tau) = \partial\Phi/\partial L$. Thus $\mathcal{R}(\tau') \equiv \{I, L, g(\tau') = g + \Omega\,(\tau' - \tau)\}$ and $\mathcal{R}'(\tau') \equiv \{I', L', g'(\tau') = g' + \Omega'\,(\tau' - \tau)\}$ where $\Omega \equiv \Omega(I, L, \tau)$ and $\Omega' \equiv \Omega(I', L', \tau)$. Both the Ω and Ω' have time-dependence over the time $T_{\rm res}$. Hence, for the axisymmetric disc, the lowest order or PRA wake function of equation (5.5a) reduces to:

$$W^{(0)}(\mathcal{R}\,|\,\mathcal{R}',\tau) = \frac{\partial F}{\partial L}\int_{-\infty}^{\tau} \mathrm{d}\tau' \frac{\partial}{\partial g}\Psi(I, L, g(\tau'), I', L', g'(\tau'), \tau')\,, \tag{5.9}$$

since the DF $F(I, L, \tau)$ is independent of g and its derivative $\partial F/\partial L$ is pulled out of the time-integral for its slower evolution over the time $T_{\rm res}$. Hence, the PRA wake is proportional to the net angular momentum change of the Ring $\mathcal{R}$ due to torquing by the Ring $\mathcal{R}'$ during the entire history of their interaction. Similarly, the $(n+1)^{\rm th}$ order wake function $W^{(n+1)}$ of equation (5.5b) can be expressed as:

$$\begin{aligned} W^{(n+1)}(\mathcal{R}|\mathcal{R}',\tau) &= \frac{\partial F}{\partial L}\int_{-\infty}^{\tau}\mathrm{d}\tau'\!\int\!\mathrm{d}\mathcal{R}''\frac{\partial}{\partial g}\Psi(I, L, g(\tau'), I'', L'', g'', \tau')W^{(n)}(\mathcal{R}''|\mathcal{R}'(\tau'),\tau') \\ &= \frac{\partial F}{\partial L}\int_{-\infty}^{\tau}\mathrm{d}\tau'\frac{\partial}{\partial g}\Phi^{(n)}_{\rm W}(I, L, g(\tau'), I', L', g'(\tau'), \tau') \end{aligned} \tag{5.10}$$

where the n^{th} order wake potential $\Phi_{\mathrm{W}}^{(n)}(\mathcal{R},\mathcal{R}',\tau)$ of $\mathcal{R}'$ is given as:

$$\Phi_{\mathrm{W}}^{(n)}(\mathcal{R},\mathcal{R}',\tau) = \int \mathrm{d}\mathcal{R}''\; \Psi(I,L,g,I'',L'',g'',\tau) W^{(n)}(\mathcal{R}''\,|\,\mathcal{R}',\tau)\,. \tag{5.11}$$

From the above equations, the $(n+1)^{\mathrm{th}}$ order wake function $W^{(n+1)}$ turns out to be proportional to the angular momentum change of the Ring $\mathcal{R}$ due to its interaction with the n^{th} order wake of $\mathcal{R}'$ throughout their orbital history. Hence, the successive orders of wake functions measure the response of the system to the gravity of the wake of one lower order; PRA wake being a measure of direct interactions among the pairs of Rings. Hence, the higher order wakes are successive iterative corrections taking into account gravitational polarization in more and more complete sense.

Below we check that the properties P1 and P2 (given in the equations (5.7)-(5.8)) of a wake function are satisfied by any general order wake function $W^{(n)}(\mathcal{R}\,|\,\mathcal{R}',\tau)$.

Firstly, we verify the property P1 which states that the net mass in the general order wake $W^{(n)}$ of $\mathcal{R}'$ vanishes. We start with the PRA wake function of equation (5.9),

$$\int \mathrm{d}\mathcal{R}\; W^{(0)}(\mathcal{R}\,|\,\mathcal{R}',\tau) = \int \mathrm{d}I\mathrm{d}L\,\frac{\partial F}{\partial L}\int_{-\infty}^{\tau}\mathrm{d}\tau'\;\oint \mathrm{d}g\,\frac{\partial}{\partial g}\Psi(I,L,g(\tau'),I',L',g'(\tau'),\tau')\,. \tag{5.12}$$

Here the g–integral vanishes straightforwardly and hence, the property P1 is satisfied by the PRA wake. Now, we consider the $(n+1)^{\mathrm{th}}$ order wake of equation (5.10),

$$\begin{aligned}\int \mathrm{d}\mathcal{R}\; W^{(n+1)}(\mathcal{R}\,|\,\mathcal{R}',\tau) = \int \mathrm{d}I\mathrm{d}L\,\frac{\partial F}{\partial L}\int_{-\infty}^{\tau}\mathrm{d}\tau'\int \mathrm{d}\mathcal{R}''\, W^{(n)}(\mathcal{R}''\,|\,\mathcal{R}'(\tau'),\tau')\\ \oint \mathrm{d}g\;\frac{\partial}{\partial g}\Psi(I,L,g(\tau'),I'',L'',g'',\tau')\end{aligned} \tag{5.13}$$

The above integral also vanishes similar to the earlier one.

Now, we verify the property P2 which states that the net general order wake $W^{(n)}$ due to all the Rings vanishes at any general phase space location $\mathcal{R}$. For the PRA wake function of equation (5.9), we have,

$$\begin{aligned}\int \mathrm{d}\mathcal{R}'\; F(\mathcal{R}',\tau)W^{(0)}(\mathcal{R}\,|\,\mathcal{R}',\tau) =\\ \frac{\partial F}{\partial L}\int_{-\infty}^{\tau}\mathrm{d}\tau'\int \mathrm{d}I'\mathrm{d}L'\oint \mathrm{d}g'\,\frac{\partial}{\partial g}\Psi(I,L,g(\tau'),I',L',g'(\tau'))\,.\end{aligned} \tag{5.14}$$

We know that Ψ depends upon $g(\tau') = g + \Omega\,(\tau' - \tau)$ and $g'(\tau') = g' + \Omega'\,(\tau' - \tau)$ as a function of $g(\tau') - g'(\tau') = g - g' + (\Omega - \Omega')(\tau' - \tau)$. Hence we have $\partial\Psi/\partial g = -\partial\Psi/\partial g'$ in the above expression and the resultant g'–integral vanishes trivially.

For the $(n+1)^{\rm th}$ order wake function of the equation (5.10), we have,

$$\int \mathrm{d}\mathcal{R}' F(\mathcal{R}',\tau) W^{(n+1)}(\mathcal{R}\,|\,\mathcal{R}',\tau) = \frac{\partial F}{\partial L}\int_{-\infty}^{\tau}\mathrm{d}\tau' \int \mathrm{d}\mathcal{R}'' \frac{\partial}{\partial g}\Psi(I, L, g(\tau'), I'', L'', g'', \tau') \int \mathrm{d}I'\mathrm{d}L'\mathrm{d}g'\; F(\mathcal{R}',\tau) W^{(n)}(\mathcal{R}''\,|\,\mathcal{R}'(\tau'),\tau')\,. \tag{5.15}$$

Since $F(\mathcal{R}',\tau) = F(I', L', \tau)$ for the axisymmetric system and F evolves slowly as compared to apse precession (or secular) timescales, $F(\mathcal{R}',\tau)$ can be replaced by $F(\mathcal{R}'(\tau'),\tau')$. The above integral depicting the net $(n+1)^{\rm th}$ order wake at $\mathcal{R}$ due to all the Rings in the system:

$$\int \mathrm{d}\mathcal{R}' F(\mathcal{R}',\tau) W^{(n+1)}(\mathcal{R}\,|\,\mathcal{R}',\tau) = \frac{\partial F}{\partial L}\int_{-\infty}^{\tau}\mathrm{d}\tau' \int \mathrm{d}\mathcal{R}'' \frac{\partial}{\partial g}\Psi(I, L, g(\tau'), I'', L'', g'', \tau') \int \mathrm{d}\mathcal{R}'\; F(\mathcal{R}'(\tau'),\tau') W^{(n)}(\mathcal{R}''\,|\,\mathcal{R}'(\tau'),\tau') \tag{5.16}$$

vanishes if the net $n^{\rm th}$ order wake due to all the Rings in the system vanishes at τ'. Since the zeroth order or PRA wake satisfies this property, the general higher order wakes will also behave similarly by mathematical induction. Hence any general order wake satisfies the property P2.

Below we evaluate explicitly the general order wake functions of the equations (5.9)-(5.10), employing the orbital structure of an axisymmetric disc.

5.2.1 Explicit Wake Functions

The reduced expressions for the wake functions in equations (5.9) and (5.10) can be simplified further by incorporating the uniform precession of apses in the axisymmetric disc. Hence, $g(\tau') = g + \Omega\,(\tau' - \tau)$ and $g'(\tau') = g' + \Omega'\,(\tau' - \tau)$, and the PRA wake $W^{(0)}$ of equation (5.9) takes the following form:

$$W^{(0)}(\mathcal{R}|\mathcal{R}',\tau) = \frac{\partial F}{\partial L}\int_{-\infty}^{\tau}\mathrm{d}\tau'\;\frac{\partial}{\partial g}\Psi\left(I, L, g + \Omega\,(\tau' - \tau), I', L', g' + \Omega'\,(\tau' - \tau)\right)\,. \tag{5.17}$$

Using the equation (4.1), the two-Ring interaction potential Ψ of equation (5.6) can be Fourier expanded as:

$$\Psi(\mathcal{R}, \mathcal{R}', \tau') = \exp\left[\lambda\tau'\right] \sum_{m=-\infty}^{+\infty} \widetilde{C}_m(I, L, I', L') \exp\left[\mathrm{i}m(g - g')\right] \tag{5.18}$$

where $\lambda \to 0^+$ for the slow build up of the wake from extremely small magnitudes in the distant past as $\tau' \to -\infty$. Employing the above Fourier series in equation (5.17), we have:

$$W^{(0)}(\mathcal{R}|\mathcal{R}', \tau) = \frac{\partial F}{\partial L} \int_{-\infty}^{\tau} \mathrm{d}\tau' \; \exp\left[\lambda\tau'\right] \sum_{m\neq 0} \mathrm{i}m\widetilde{C}_m \exp\left[\mathrm{i}m\left\{g - g' + (\Omega - \Omega')(\tau' - \tau)\right\}\right]. \tag{5.19}$$

Then, changing the variable of integration to $x = \tau' - \tau$, we get:

$$\begin{aligned} W^{(0)}(\mathcal{R}|\mathcal{R}', \tau) = \exp\left[\lambda\tau\right] \frac{\partial F}{\partial L} \sum_{m\neq 0} \mathrm{i}m\widetilde{C}_m \exp\left[\mathrm{i}m(g - g')\right] \times \\ \int_{-\infty}^{0} \mathrm{d}x \; \exp\left[\left\{\lambda + \mathrm{i}m(\Omega - \Omega')\right\} x\right], \end{aligned} \tag{5.20}$$

and this leads to the following form of the PRA wake function $W^{(0)}$:

$$W^{(0)}(\mathcal{R}\,|\,\mathcal{R}', \tau) = \exp\left[\lambda\tau\right] \frac{\partial F}{\partial L} \sum_{m\neq 0} A_m^{(0)}(I, L, I', L') \exp\left[\mathrm{i}m(g - g')\right] \tag{5.21a}$$

$$A_m^{(0)}(I, L, I', L') = \frac{\mathrm{i}m}{\lambda + \mathrm{i}m(\Omega - \Omega')} \widetilde{C}_m(I, L, I', L') \tag{5.21b}$$

where $A_m^{(0)}$ evolves slowly over the time $\sim T_{\mathrm{res}}$ like Ω and Ω', and its time-dependence is suppressed in the above notation.

The next order wake function $W^{(1)}$ can be expressed in terms of the $W^{(0)}$ of equation (5.21), using the recursive relation given in equation (5.5b) with $n = 0$ as:

$$\begin{aligned} W^{(1)}(\mathcal{R}|\mathcal{R}', \tau) &= \int_{-\infty}^{\tau} \mathrm{d}\tau' \int \mathrm{d}\mathcal{R}'' \; \frac{\partial F}{\partial L} \frac{\partial}{\partial g} \Psi(I, L, g(\tau'), I'', L'', g'', \tau') \\ &\qquad \exp\left[\lambda\tau'\right] \frac{\partial F''}{\partial L''} \sum_{m\neq 0} A_m^{(0)}(I'', L'', I', L') \exp\left[\mathrm{i}m(g'' - g'(\tau'))\right] \\ &= \frac{\partial F}{\partial L} \int_{-\infty}^{\tau} \mathrm{d}\tau' \; \exp\left[2\lambda\tau'\right] \int \mathrm{d}I''\mathrm{d}L'' \frac{\partial F''}{\partial L''} \oint \mathrm{d}g'' \; \sum_{n\neq 0} \mathrm{i}n\widetilde{C}_n(I, L, I'', L'') \\ &\qquad \exp\left[\mathrm{i}n(g(\tau') - g'')\right] \sum_{m\neq 0} A_m^{(0)}(I'', L'', I', L') \exp\left[\mathrm{i}m\left\{g'' - g'(\tau')\right\}\right]. \end{aligned} \tag{5.22}$$

Only the terms with $n = m$ contribute to the g''–integral. Using the explicit forms of $g(\tau')$ and $g'(\tau')$, while changing the variable of integration to $x = \tau' - \tau$, we have:

$$W^{(1)} = 2\pi \frac{\partial F}{\partial L} \exp\left[2\lambda\tau\right] \sum_{m\neq 0} \mathrm{i}m \exp\left[\mathrm{i}m(g-g')\right]$$

$$\int \mathrm{d}I''\mathrm{d}L'' \, \frac{\partial F''}{\partial L''} \widetilde{C}_m(I,L,I'',L'') A_m^{(0)}(I'',L'',I',L') \int_{-\infty}^{0} \mathrm{d}x \;\exp\left[(2\lambda + \mathrm{i}m(\Omega-\Omega'))x\right]. \tag{5.23}$$

Solving the x-integral leads to the final expression:

$$W^{(1)}(\mathcal{R}|\mathcal{R}',\tau) = \exp\left[2\lambda\tau\right] \frac{\partial F}{\partial L} \sum_{m\neq 0} A_m^{(1)}(I,L,I',L') \exp\left[\mathrm{i}m(g-g')\right] \tag{5.24a}$$

$$A_m^{(1)}(I,L,I',L') = \frac{2\pi \mathrm{i}m}{2\lambda + \mathrm{i}m(\Omega-\Omega')} \int \mathrm{d}I''\mathrm{d}L'' \frac{\partial F''}{\partial L''} \widetilde{C}_m(I,L,I'',L'') A_m^{(0)}(I'',L'',I',L'). \tag{5.24b}$$

Following the similar steps and using the recurrence relation of equation (5.5b), we have the general order wake function:

$$W^{(n)}(\mathcal{R}\,|\,\mathcal{R}',\tau) = \exp\left[(n+1)\lambda\tau\right] \frac{\partial F}{\partial L} \sum_{m\neq 0} A_m^{(n)}(I,L,I',L') \exp\left[\mathrm{i}m(g-g')\right] \tag{5.25a}$$

$$A_m^{(n)} = \frac{2\pi \mathrm{i}m}{(n+1)\lambda + \mathrm{i}m(\Omega-\Omega')} \int \mathrm{d}I''\mathrm{d}L'' \, \frac{\partial F''}{\partial L''} \widetilde{C}_m(I,L,I'',L'') A_m^{(n-1)}(I'',L'',I',L'), \quad n = 1,\, 2, \ldots \tag{5.25b}$$

Note that the $n = 1$ corresponds to the expression for $W^{(1)}$ given in equation (5.24). Using equations (5.21) and (5.25) in the series expansion of wake function of equation (5.4), the general wake function can be expressed as:

$$W(\mathcal{R}\,|\,\mathcal{R}',\tau) = \frac{\partial F}{\partial L} \sum_{m\neq 0} A_m(I,L,I',L',\tau) \exp\left[\mathrm{i}m(g-g')\right] \tag{5.26a}$$

$$A_m(I,L,I',L',\tau) = \sum_{n=0}^{\infty} A_m^{(n)}(I,L,I',L') \exp\left[(n+1)\lambda\tau\right]. \tag{5.26b}$$

Since W and all $W^{(n)}$'s are the real valued functions, $A_m^{(n)*} = A_{-m}^{(n)}$ and $A_m^* = A_{-m}$ for all the Ring pairs. Here " * " indicates complex conjugation.

5.3 Correlation Function

The irreducible part of the two-Ring correlation function $F^{(2)}_{\rm irr}$ for an axisymmetric Keplerian disc is evaluated using equation (5.26) in (5.2):

$$
\begin{aligned}
F^{(2)}_{\rm irr} = {} & F'\frac{\partial F}{\partial L}\sum_{m\neq 0} A_m(I,L,I',L',\tau)\exp\left[{\rm i}m(g-g')\right] \\
& + F\frac{\partial F'}{\partial L'}\sum_{m\neq 0} A_m(I',L',I,L,\tau)\exp\left[{\rm i}m(g'-g)\right] + ... \\
& + \frac{\partial F}{\partial L}\frac{\partial F'}{\partial L'}\int {\rm d}I''{\rm d}L''F''\oint {\rm d}g''\Bigg\{\sum_{m\neq 0} A_m(I,L,I'',L'',\tau)\exp\left[{\rm i}m(g-g'')\right] \\
& \times \sum_{n\neq 0} A_n(I',L',I'',L'',\tau)\exp\left[{\rm i}n(g'-g'')\right]\Bigg\}
\end{aligned}
\tag{5.27}
$$

where $F' \equiv F(I',L',\tau)$, $F'' \equiv F(I'',L'',\tau)$. In the g''-integral, only the $n=-m$ terms contribute, and the above expression can be manipulated to:

$$
\begin{aligned}
F^{(2)}_{\rm irr} = {} & \sum_{m\neq 0}\exp\left[{\rm i}m(g-g')\right]\Bigg[F'\frac{\partial F}{\partial L}A_m(I,L,I',L',\tau) + F\frac{\partial F'}{\partial L'}A_{-m}(I',L',I,L,\tau) \\
& + 2\pi\frac{\partial F}{\partial L}\frac{\partial F'}{\partial L'}\int {\rm d}I''{\rm d}L''\; F''A_m(I,L,I'',L'',\tau)A_{-m}(I',L',I'',L'',\tau)\Bigg]\,.
\end{aligned}
\tag{5.28}
$$

Using equation (5.26b) in the above equation, $F^{(2)}_{\rm irr}$ can be ordered as a perturbative series in terms of $\exp\left[\lambda\tau\right]$ (similar to the wake function):

$$
F^{(2)}_{\rm irr}(\mathcal{R},\mathcal{R}',\tau) = \sum_{n=0}^{\infty}\sum_{m\neq 0} B^{(n)}_m(I,L,I',L')\exp\left[{\rm i}m(g-g')\right]\exp\left[(n+1)\lambda\tau\right] \tag{5.29a}
$$

$$
B^{(0)}_m(I,L,I',L') = F'\frac{\partial F}{\partial L}A^{(0)}_m(I,L,I',L') + F\frac{\partial F'}{\partial L'}A^{(0)}_{-m}(I',L',I,L) \tag{5.29b}
$$

$$
\begin{aligned}
B^{(n)}_m(I,L,I',L') = {} & F'\frac{\partial F}{\partial L}A^{(n)}_m(I,L,I',L') + F\frac{\partial F'}{\partial L'}A^{(n)}_{-m}(I',L',I,L) \\
& + 2\pi\frac{\partial F}{\partial L}\frac{\partial F'}{\partial L'}\int {\rm d}I''{\rm d}L''\; F''\sum_{k=0}^{n-1} A^{(k)}_m(I,L,I'',L'')A^{(n-k-1)}_{-m}(I',L',I'',L'')
\end{aligned}
\tag{5.29c}
$$

for $n=1,2,...$ Since $F^{(2)}_{\rm irr}$ is a real-valued function, $B^{(n)*}_m = B^{(n)}_{-m}$. As $F^{(2)}_{\rm irr}$ is symmetric under the interchange of the two Rings, $B^{(n)}_m(I,L,I',L') = B^{(n)}_{-m}(I',L',I,L)$.

5.4 Collision Integral and Current

Now we evaluate the collision integral given in equation (5.1) using (5.29) and (4.1):

$$\mathcal{C}[F] = \frac{1}{N_\star}\sum_{n=0}^{\infty}\exp\left[(n+1)\lambda\tau\right]\int \mathrm{d}I'\mathrm{d}L' \oint \mathrm{d}g' \left[\sum_{m\neq 0} \mathrm{i}m\widetilde{C}_m(I,L,I',L')\exp\left[\mathrm{i}m(g-g')\right]\right.$$

$$\times\sum_{m'\neq 0}\frac{\partial}{\partial L}B^{(n)}_{m'}(I,L,I',L')\exp\left[\mathrm{i}m'(g-g')\right] - \sum_{m=-\infty}^{\infty}\frac{\partial}{\partial L}\widetilde{C}_m(I,L,I',L')\exp\left[\mathrm{i}m(g-g')\right]$$

$$\left.\times\sum_{m'\neq 0}\mathrm{i}m'B^{(n)}_{m'}(I,L,I',L')\exp\left[\mathrm{i}m'(g-g')\right]\right].$$

Only the terms with $m' = -m$ contribute in the g'-integral, and with simple manipulations, we have:

$$\mathcal{C}[F] = \frac{\partial}{\partial L}\sum_{n=0}^{\infty}\exp\left[(n+1)\lambda\tau\right]\left[\frac{2\pi}{N_\star}\int \mathrm{d}I'\mathrm{d}L'\sum_{m\neq 0}\mathrm{i}m\widetilde{C}_m(I,L,I',L')B^{(n)}_{-m}(I,L,I',L')\right].$$

Changing the dummy variable as $m \to -m$ and using the symmetry property of $\widetilde{C}_m$ (from ST16a) being even in m, i.e. $\widetilde{C}_{-m} = \widetilde{C}_m$, we have:

$$\mathcal{C}[F] = -\frac{\partial}{\partial L}\sum_{n=0}^{\infty}\exp\left[(n+1)\lambda\tau\right]\left[\frac{2\pi}{N_\star}\int \mathrm{d}I'\mathrm{d}L'\sum_{m\neq 0}\mathrm{i}m\widetilde{C}_m(I,L,I',L')B^{(n)}_{m}(I,L,I',L')\right]. \tag{5.31}$$

The current $J(I,L,\tau)$ is defined as:

$$\mathcal{C}[F] = -\frac{\partial J}{\partial L}. \tag{5.32}$$

Comparing the equations (5.31) and (5.32), the current can be represented as perturbative series of the form:

$$J(I,L,\tau) = \sum_{n=0}^{\infty}\exp\left[(n+1)\lambda\tau\right]J^{(n)}(I,L,\tau) \tag{5.33a}$$

$$J^{(n)}(I,L,\tau) = \frac{2\pi}{N_\star}\int \mathrm{d}I'\,\mathrm{d}L'\sum_{m\neq 0}\mathrm{i}m\widetilde{C}_m(I,L,I',L')B^{(n)}_{m}(I,L,I',L') \tag{5.33b}$$

where the τ dependence on right side of the equation is suppressed in $B^{(n)}_m$. The above equation can be manipulated to the form:

$$J^{(n)}(I,L,\tau) = \frac{-4\pi}{N_\star}\int \mathrm{d}I'\mathrm{d}L'\sum_{m=1}^{\infty}m\widetilde{C}_m(I,L,I',L')\,\mathrm{Im}\left[B^{(n)}_{m}(I,L,I',L')\right] \tag{5.34}$$

using the symmetry property $B^{(n)}_{-m} = B^{(n)*}_{m}$, as mentioned earlier in the text below the equation (5.29). Here "Im" denotes the imaginary part. Note that the real part of the correlation function coefficient $B^{(n)}_{m}$ does not contribute to the RR evolution of the system.

Using the equation (5.32) in the RR kinetic equation (5.1), we have the following form of the kinetic equation:

$$\frac{\partial F}{\partial \tau} + \left[F, H - \frac{\Phi(\mathcal{R},\tau)}{N_\star} \right] + \frac{\partial J}{\partial L} = 0\,. \tag{5.35}$$

For the above equation to present the RR evolution of the system, the Poisson Bracket term will nearly vanish for the system being a quasi collisionless equilibrium evolving slowly over $T_{\rm res}$ timescales. Hence, we have the following final form of the RR kinetic equation for an axisymmetric disc:

$$\frac{\partial F}{\partial \tau} + \frac{\partial J}{\partial L} = 0\,. \tag{5.36}$$

The above equation is similar to the form of the RR kinetic equation (4.3), with the two DFs related as $F = \widetilde{f}/2\pi$.

5.4.1 Low-order Currents

Here we evaluate the explicit expressions for the first two leading order terms $J^{(0)}$ and $J^{(1)}$ in the current series of equation (5.33a). Employing the equation (5.29b) in equation (5.34) (for $n = 0$), we have the PRA current $J^{(0)}$:

$$\begin{aligned} J^{(0)} = -\frac{4\pi}{N_\star} \int \mathrm{d}I'\,\mathrm{d}L' \sum_{m=1}^{\infty} m\widetilde{C}_m(I,L,I',L') \\ \mathrm{Im}\left[F' \frac{\partial F}{\partial L} A^{(0)}_{m}(I,L,I',L') + F \frac{\partial F'}{\partial L'} A^{(0)}_{-m}(I',L',I,L) \right] \end{aligned} \tag{5.37}$$

where $A^{(0)}_{\pm m}$ is given by equation (5.21). To further simplify the expressions for $A^{(n)}_{m}$ given in equation (5.21) and (5.25), we will frequently use the following result from Plemelj's theorem:

$$\frac{im}{\lambda + im\xi} \to \frac{1}{\xi} + \mathrm{i}\pi \mathrm{sign}(m)\delta(\xi) \tag{5.38}$$

in the limit $\lambda \to 0^+$.

We simplify the equation (5.21) in the desired limit by using the above theorem, to get:

$$A^{(0)}_m(I,L,I',L') = \left[\frac{1}{\Omega-\Omega'} + \mathrm{i}\pi\,\mathrm{sign}(m)\delta(\Omega-\Omega')\right]\widetilde{C}_m(I,L,I',L') \tag{5.39}$$

and hence the final form for the PRA current $J^{(0)}$ of equation (5.37) becomes:

$$J^{(0)} = \frac{2\pi}{N_\star}\int \mathrm{d}I'\mathrm{d}L'\left(2\pi\sum_{m=1}^{\infty} m\widetilde{C}_m(I,L,I',L')^2\right)\delta(\Omega'-\Omega)\left\{F\frac{\partial F'}{\partial L'} - F'\frac{\partial F}{\partial L}\right\} \tag{5.40}$$

which is consistent with the current (equation 4.4 of Chapter 4) evaluated in § 5.2 of ST17; note that a factor of 2π difference comes due to the different normalizations of the DFs as $F = \widetilde{f}/2\pi$. The term in "( )" is the interaction kernel $\widetilde{K}(I,L,I',L')$ of equation (4.5).

Now we evaluate the next higher order current $J^{(1)}$ which incorporates the leading order polarization effects. Using equation (5.29c) with $n=1$ for $B^{(1)}_m$ in (5.34), we have $J^{(1)}$:

$$J^{(1)} = -\frac{4\pi}{N_\star}\int\mathrm{d}I'\mathrm{d}L'\sum_{m=1}^{\infty} m\widetilde{C}_m(I,L,I',L')\mathrm{Im}\Bigg[F'\frac{\partial F}{\partial L}A^{(1)}_m(I,L,I',L') +$$

$$F\frac{\partial F'}{\partial L'}A^{(1)}_{-m}(I',L',I,L) + 2\pi\frac{\partial F}{\partial L}\frac{\partial F'}{\partial L'}\int\mathrm{d}I''\mathrm{d}L''F''A^{(0)}_m(I,L,I'',L'')A^{(0)}_{-m}(I',L',I'',L'')\Bigg]. \tag{5.41}$$

We have $A^{(1)}_m$ from equation (5.24b); the factor $\mathrm{i}m/(2\lambda+\mathrm{i}m(\Omega-\Omega')) \to 1/(\Omega-\Omega') + \mathrm{i}\pi\,\mathrm{sign}(m)\,\delta(\Omega-\Omega')$ using the theorem of equation (5.38). Also, using the reduced form of $A^{(0)}_m$ from equation (5.39), we have:

$$A^{(1)}_m(I,L,I',L') = 2\pi\Bigg[$$

$$\left(\frac{1}{\Omega-\Omega'} + \mathrm{i}\pi\,\mathrm{sign}(m)\delta(\Omega'-\Omega)\right)\int\mathrm{d}I''\mathrm{d}L''\frac{\partial F''}{\partial L''}\frac{\widetilde{C}_m(I,L,I'',L'')\widetilde{C}_m(I',L',I'',L'')}{\Omega''-\Omega'} -$$

$$\left(\pi\delta(\Omega'-\Omega) + \frac{\mathrm{i}\pi\mathrm{sign}(m)}{\Omega'-\Omega}\right)\int\mathrm{d}I''\mathrm{d}L''\frac{\partial F''}{\partial L''}\widetilde{C}_m(I,L,I'',L'')\widetilde{C}_m(I',L',I'',L'')\delta(\Omega''-\Omega')\Bigg]. \tag{5.42}$$

Employing the expressions for $A^{(0)}_{\pm m}$ and $A^{(1)}_{\pm m}$ from equations (5.39) and (5.42) respectively, in equation (5.41) and upon further simplification, we have:

$$J^{(1)} = \frac{4\pi^2}{N_\star}\int \mathrm{d}I'\mathrm{d}L'\mathrm{d}I''\mathrm{d}L''\left(2\pi\sum_{m=1}^{\infty} m\widetilde{C}_m(I,L,I',L')\widetilde{C}_m(I,L,I'',L'')\widetilde{C}_m(I',L',I'',L'')\right)$$
$$\left[\frac{\delta(\Omega'-\Omega)}{\Omega''-\Omega}\frac{\partial F''}{\partial L''}\left\{F\frac{\partial F'}{\partial L'}-F'\frac{\partial F}{\partial L}\right\}+\frac{\delta(\Omega''-\Omega)}{\Omega'-\Omega}\frac{\partial F'}{\partial L'}\left\{F\frac{\partial F''}{\partial L''}-F''\frac{\partial F}{\partial L}\right\}\right.$$
$$\left.+\frac{\delta(\Omega''-\Omega')}{\Omega'-\Omega}\frac{\partial F}{\partial L}\left\{F'\frac{\partial F''}{\partial L''}-F''\frac{\partial F'}{\partial L'}\right\}\right]. \tag{5.43}$$

The last term in the square bracket vanishes as it is anti-symmetric in interchange of the Ring variables $\{I,L\}\longleftrightarrow\{I',L'\}$ which are the dummy variables of integration. Also, note that the second term becomes identical to the first one under the interchange. The final expression for the lowest order polarization current $J^{(1)}$ becomes:

$$J^{(1)} = \frac{4\pi^2}{N_\star}\int \mathrm{d}I'\mathrm{d}L'\mathrm{d}I''\mathrm{d}L''\left(2\pi\sum_{m=1}^{\infty} m\widetilde{C}_m(I,L,I',L')\widetilde{C}_m(I,L,I'',L'')\widetilde{C}_m(I',L',I'',L'')\right)$$
$$\left[\frac{\delta(\Omega'-\Omega)}{\Omega''-\Omega}\frac{\partial F''}{\partial L''}\left\{F\frac{\partial F'}{\partial L'}-F'\frac{\partial F}{\partial L}\right\}+\frac{\delta(\Omega''-\Omega)}{\Omega'-\Omega}\frac{\partial F'}{\partial L'}\left\{F\frac{\partial F''}{\partial L''}-F''\frac{\partial F}{\partial L}\right\}\right]. \tag{5.44}$$

It is evident from the above expression that the current $J^{(1)}$ arises due to pair-wise interactions among three Rings, as the term within "( )" contains coefficients $\widetilde{C}_m$ corresponding to the three Ring coordinates – (I,L), (I',L') and (I'',L''). Both the terms within "[ ]" contain the δ-functions $\delta(\Omega'-\Omega)$ and $\delta(\Omega''-\Omega)$, signifying that only the Rings that have apsidal resonances with $\{I,L\}$ contribute to $J^{(1)}$. This indicates that polarization terms of the current ($J^{(1)}$ and higher order currents) are also driven by strict resonances, like the PRA current $J^{(0)}$. This is true for the next higher order term $J^{(2)}$ as well; but we do not present the rather lengthy calculation here, since it involves the same steps discussed above for $J^{(1)}$.

Now, we present the RR kinetic equation considering the gravitational polarization upto the leading order. Restricting the current series of equation (5.33a) upto the first order implies $J(I,L,\tau)=J^{(0)}(I,L,\tau)+J^{(1)}(I,L,\tau)$ (in the limit of $\lambda\to 0^+$), where the explicit expressions for $J^{(0)}$ and $J^{(1)}$ are given by equations (5.40) and (5.44). For RR evolution of an axisymmetric disc, we need to solve the RR kinetic equation (5.36), which becomes:

$$\frac{\partial F}{\partial \tau} + \frac{\partial J^{(0)}}{\partial L} + \frac{\partial J^{(1)}}{\partial L} = 0\,. \tag{5.45}$$

In the next section, we work out the form of stationary states for which the current $J = J^{(0)} + J^{(1)}$ vanishes at all points in the (I, L)-plane.

5.5 Stationary States and Thermal Equilibria

Similar to the monoenergetic limit of § 4.1.5, a family of stationary states for an axisymmetric Keplerian disc has the DFs $F_{\rm s}(I, L)$ of the following form:

$$F_{\rm s}(I, L) = A(I)\,\exp\left[\int_{-1}^{L} \eta[\Omega_{\rm s}(I, L')]\,{\rm d}L'\right] \tag{5.46}$$

where $A(I)$ is a positive function; $\eta[\Omega_{\rm s}]$ is a single-valued functional of $\Omega_{\rm s}$, the apse precession rate corresponding to the DF $F_{\rm s}(I, L)$. Equations (2.7)-(2.8) give the form of $\Omega_{\rm s}$, which is rewritten below:

$$\Omega_{\rm s}(I, L) = \int {\rm d}I'\,{\rm d}L'\,F_{\rm s}(I, L) \oint \frac{{\rm d}g'}{2\pi}\frac{\partial}{\partial L}\Psi(I, L, g, I', L', g')\,. \tag{5.47}$$

The coupled equations (5.46)-(5.47) form a non-linear integral pde, and its self-consistent solution gives explicit functional form of $F_{\rm s}(I, L)$ in the (I, L)-plane.

Differentiating the equation (5.46) wrt L, we get:

$$\frac{1}{F_{\rm s}(I, L)}\frac{\partial F_{\rm s}(I, L)}{\partial L} = \eta[\Omega_{\rm s}(I, L)]\,. \tag{5.48}$$

Recalling the stability theorem of ST16a for axisymmetric Keplerian discs (also see § 2.1.1), the DFs $F(I, L)$ for which $\partial F/\partial L$ is of the same sign everywhere in its domain of support in the (I, L)-plane, are stable to secular perturbations of all azimuthal wavenumbers m. Therefore, the property of equation (5.48) implies that the stationary states with DFs $F_{\rm s}(I, L)$ are dynamically stable, if $\eta[\Omega_{\rm s}]$ is either always positive or negative for all $\Omega_{\rm s}(I, L)$.

Using equation (5.48) in (5.40), we have the stationary state PRA current $J_{\rm s}^{(0)}$:

$$J_{\rm s}^{(0)} = \frac{2\pi}{N_\star}\int {\rm d}I'{\rm d}L'\left(2\pi\sum_{m=1}^{\infty} m\widetilde{C}_m(I, L, I', L')^2\right)\delta(\Omega'_{\rm s} - \Omega_{\rm s})F_{\rm s}F'_{\rm s}\left\{\eta[\Omega'_{\rm s}] - \eta[\Omega_{\rm s}]\right\} \tag{5.49}$$

which vanishes, because of the presence of both antisymmetric term "{ }" and δ-function.

Similarly, using equation (5.48) in (5.44) for $J^{(1)}$, we have:

$$J_{\mathrm{s}}^{(1)} = \frac{4\pi^2}{N_\star} \int \mathrm{d}I'\mathrm{d}L'\mathrm{d}I''\mathrm{d}L'' \left(2\pi \sum_{m=1}^{\infty} m\widetilde{C}_m(I,L,I',L')\widetilde{C}_m(I,L,I'',L'')\widetilde{C}_m(I',L',I'',L'') \right)$$

$$F_{\mathrm{s}}\, F'_{\mathrm{s}}\, F''_{\mathrm{s}} \left[\frac{\delta(\Omega'_{\mathrm{s}} - \Omega_{\mathrm{s}})}{\Omega''_{\mathrm{s}} - \Omega_{\mathrm{s}}} \eta[\Omega''_{\mathrm{s}}] \left\{ \eta[\Omega'_{\mathrm{s}}] - \eta[\Omega_{\mathrm{s}}] \right\} + \frac{\delta(\Omega''_{\mathrm{s}} - \Omega_{\mathrm{s}})}{\Omega'_{\mathrm{s}} - \Omega_{\mathrm{s}}} \eta[\Omega'_{\mathrm{s}}] \left\{ \eta[\Omega''_{\mathrm{s}}] - \eta[\Omega_{\mathrm{s}}] \right\} \right] \tag{5.50}$$

which vanishes in a similar manner, as $J_{\mathrm{s}}^{(0)}$. Note that the denominators of the form $(\Omega'_{\mathrm{s}} - \Omega_{\mathrm{s}})$ for the two terms within "[ ]" never lead to divergences, because the corresponding Ring $\{I', L'\}$ would not be a resonant one. This is evident since the two terms (and corresponding integrands) are identical under the interchange of dummy variables $\{I', L'\} \longleftrightarrow \{I'', L''\}$.

Hence DFs of the form $F_{\mathrm{s}}(I, L)$ indeed represent the stationary states, for which the leading order current $J = J^{(0)} + J^{(1)}$ vanishes.

Thermal Equilibria: ST17 constructed the Boltzmann-type thermal equilibria for axisymmetric Keplerian discs, having DFs of the form:

$$F_{\mathrm{th}}(I, L) = A(I) \exp\left[-\beta \Phi_{\mathrm{th}}(I, L) + \gamma L\right] \tag{5.51}$$

where $\Phi_{\mathrm{th}}(I, L)$ is given by the integral relation of the equation (2.7). Hence, one has to solve this integral equation to have the explicit form of $F_{\mathrm{th}}(I, L)$. Differentiating the above equation wrt L, we have:

$$\frac{1}{F_{\mathrm{th}}(I, L)} \frac{\partial F_{\mathrm{th}}(I, L)}{\partial L} = -\beta\, \Omega_{\mathrm{th}}(I, L) + \gamma \tag{5.52}$$

where $\Omega_{\mathrm{th}}(I, L) = \partial \Phi_{\mathrm{th}} / \partial L$ is the apse precession profile for the thermal state. It is evident from equations (5.48) and (5.52) that the thermal states with DF F_{th} form a subset of the stationary state DFs F_{s}, for which the η functional is a linear polynomial in Ω_{th}.

The above stationary states F_{s} or thermal equilibria F_{th} might correspond to the end states of the RR kinetic equation (5.45), if they are dynamically and thermally stable.

5.6 Discussion

We have presented an analytical formalism to study the RR evolution of an axisymmetric Keplerian disc, including gravitational polarization effects. The general framework developed upto § 5.4 allows for the inclusion of higher orders of polarization. Starting from the explicit form of the lowest order wake-coefficient $A_m^{(0)}$ given in the equation (5.21b), all the higher order coefficients can be worked out using the recursion relation of the equation (5.25b). Each $A_m^{(n)}(I, L, I', L')$ is a four-dimensional function, and can be calculated in principle by evaluating a two-dimensional integral over the just lower order coefficient $A_m^{(n-1)}(I, L, I', L')$. If we have all the wake-coefficients $A_m^{(n)}$ for $n = 0, 1, 2, ...N$, we can evaluate the correlation function coefficients $B_m^{(n)}(I, L, I', L')$ upto the same order N from the equation (5.29c). Then the imaginary part of $B_m^{(n)}$ for various m, are employed to evaluate the current coefficient $J^{(n)}(I, L, \tau)$ using the equation (5.34). This leads to the current $J = J^{(0)} + J^{(1)} + ... + J^{(N)}$, from the equation (5.33a) in the limit $\lambda \to 0^+$. Finally, employing the $J(I, L, \tau)$ one has to numerically solve the RR kinetic equation (5.36) for some given initial DF $F(I, L, 0)$. This method includes the gravitational polarization till the N^{th} order.

It is relatively simpler to study the RR evolution of the disc, with inclusion of the first order polarization effects. The current $J = J^{(0)} + J^{(1)}$ is explicitly known from equations (5.40) and (5.44). The resulting RR kinetic equation (5.45) can be numerically solved with a generalized RR code. The resultant end states of this evolution are expected to be dynamically and thermally stable, and might be of the form of the stationary states F_{s} of equation (5.46) or the thermal equilibria F_{th} of equation (5.51). As pointed out in § 4.4, we expect a non-monoenergetic axisymmetric disc to have resonant points throughout the (I, L)-plane in general. This would allow the DF to resonantly relax all over the phase space and hence, might lead to the thermal equilibria in the end.

In § 4.4 while studying the RR of a monoenergetic axisymmetric disc, we speculated that the problem of existence of non-resonant region might be resolved, if gravitational polarization is taken into account. The RR kinetic equation (5.45), with the first order polarization, can be reduced to the monoenergetic case as done in § 4.1.1. But, it is evident from the equation (5.44), presenting the explicit form of the leading order polarization current $J^{(1)}$, that it is also driven by apsidal resonances. If there are no resonant points for a phase-space location, the local currents will vanish. But the nature of the apse precession profile of a monoenergetic axisymmetric disc leads to a region (for high eccentricity Rings) devoid of resonances. Hence, the resulting end-states again might be of the form of non-thermal stationary states. Therefore it seems necessary to study RR in the more generic setting of a Keplerian disc composed of stars with a range of semi-major axes.

Chapter 6

Conclusions

In the thesis we have explored some aspects of the gravitational dynamics of nuclear star clusters (NSCs) orbiting massive black holes (MBHs) at the centres of galaxies. Both collisionless and collisional dynamics were considered, based on the formalism of secular theory developed by Sridhar & Touma (2016a,b, 2017). Since the gravitational force on a star is dominated by the Keplerian potential of the MBH (of mass $M_\bullet$), stellar orbits can be approximated as Keplerian elliptical rings (Gaussian Rings) which precess and deform due to the mean gravitational potential of the cluster (of mass $M \ll M_\bullet$), over several secular collisionless timescales $T_{\rm sec} \sim T_{\rm Kep}/\epsilon$; $T_{\rm Kep}$ refers to the Keplerian orbital timescale. Here the mass ratio $\epsilon = M/M_\bullet \ll 1$ is a natural small parameter of the problem. Discrete interactions among the finite number $N_\star \gg 1$ of Gaussian Rings constituting the system become important over still longer collisional times $T_{\rm res} \sim N_\star T_{\rm sec}$. Resonant relaxation (RR) is the collisional phenomenon governing stochastic exchanges of angular momentum between the Rings (Rauch & Tremaine, 1996). Our study of the secular dynamics and physical kinetics of these Keplerian stellar systems was presented in two parts. Part I containing Chapters 2 and 3 covered the secular collisionless dynamics, and Part II containing Chapters 4 and 5 dealt with collisional studies of RR. Here we briefly recall the work presented, and discuss some applications and possible extensions.

Secular Collisionless Instabilities: In Chapter 2, an idealized model of a razor–thin, axisymmetric, Keplerian stellar disc around an MBH was constructed, and non-axisymmetric secular instabilities were studied in the absence of counter-rotation and loss cones. These discs are prograde monoenergetic waterbags, whose phase space distribution functions (DFs) are constant for orbits within a range of eccentricities (e) and zero outside this range. The linear normal modes of waterbags are composed of sinusoidal disturbances of the edges of the DF in phase space. Waterbags which include circular orbits (*polarcaps*) have one stable linear normal mode for each azimuthal wavenumber m. The $m = 1$ mode always has positive pattern speed and, for polarcaps consisting of orbits with $e < 0.9428$, only the $m = 1$ mode has positive pattern speed. Waterbags excluding circular orbits (*bands*) have two linear normal modes for each m, which can be stable or unstable. We derive analytical expressions for the instability condition, pattern speeds, growth rates and normal mode structure. Narrow bands are unstable to modes with a wide range in m. N-Ring simulations confirm linear theory and follow the non-linear evolution of instabilities. Long-time integration suggests that instabilities of different m grow, interact non-linearly and relax collisionlessly to a coarse-grained equilibrium with a wide range of eccentricities.

The above study can be extended to understand the orbital structure of the compact young stellar disc (within 0.5 pc) at the Galactic Centre. The young stars follow quite eccentric orbits with a mean eccentricity ~ 0.3 (Yelda et al., 2014). Collisionless relaxation of the distribution of eccentricities through non-axisymmetric secular instabilities (similar to what we studied for waterbags) is a possible mechanism for eccentricity excitation of the young stellar orbits. The waterbag DF should be extended to more realistic DFs for axisymmetric discs, by (i) lifting the monoenergetic assumption, (ii) including the gravitational potential of the spheroidal old star cluster, (iii) making the problem three dimensional by considering a disc with non-zero thickness, which will also allow for the excitation of vertical motions.

Cusp Deformation: The Galactic Centre NSC is an extended, cuspy distribution of old stars with an effective radius ~ 4 pc. The embedded compact cluster of young stars was probably born in situ in a massive accretion disc around the Galactic Centre MBH. In Chapter 3, we investigated the effect of the growing gravity of the gas disc on the orbits of old stars, using an integrable model of the deformation of a spherical star cluster with anisotropic velocity dispersions. A formula for the perturbed phase space DF was derived using secular, adiabatic linear theory, and the new density and surface density profiles were computed. The cusp undergoes a spheroidal deformation with the flattening increasing strongly at smaller distances from the MBH; the intrinsic axis ratio ~ 0.8 at ~ 0.15 pc. Stellar orbits are deformed such that they spend more time near the disc plane and sample the dense inner parts of the disc; this could result in enhanced stripping of the envelopes of red giant stars, which is thought to be responsible for the cored density profile of old giants within ~ 0.5 pc. The mechanism of spheroidal cusp deformation is a generic dynamical process, and it may be common in galactic nuclei.

Linear theory accounts only for orbits whose apsides circulate. The non-linear theory of adiabatic capture into resonance (Sridhar & Touma, 1996) is needed to understand orbits whose apsides librate. The work can be extended to more general geometries of both the star cluster and the perturbing disc potential. Chatzopoulos et al. (2015) constructed a self-consistent axisymmetric, flattened and rotating DF for the Galactic NSC. Whereas such a DF does not change due to the growth of an axisymmetric gas disc, it can respond to non-axisymmetric geometries corresponding to a warped disc, explored in previous work (Šubr et al., 2009). The deformed cluster would then have more complex geometry, like the triaxial models of the Galactic Centre NSC constructed by Feldmeier-Krause et al. (2017).

Resonant Relaxation: In Chapter 4, we studied the RR evolution of a razor-thin, axisymmetric monoenergetic Keplerian stellar disc by solving the RR kinetic (Fokker-Planck) equation of Sridhar & Touma (2017) in the monoenergetic limit. This integral partial differential equation (pde) was solved by constructing an algorithm "RR code". The RR current density depends on the behavior of the DF, $f(\ell)$, in its entire domain, $\ell \in [-1, 1]$, where ℓ is the normalized angular momentum of a stellar orbit. The RR current is driven by apsidal resonances; for the current at ℓ to be non-zero, there should exist ℓ' such that the corresponding apse precession rates (Ω), satisfy the resonance condition $\Omega(\ell') = \Omega(\ell)$. We employed a "conservative" scheme for the discretization of the integral pde. The cumulative DF was interpolated with a cubic spline, providing a smooth continuation of the DF within the grid and ensuring the conservation of norm upto high precision. The apse precession rate for high eccentricity rings is very small, and completely vanishes when $\ell = 0$. As a result there is in general a region in ℓ-space around $\ell = 0$ where apsidal resonances do not occur. Then local currents vanish and the DF in the region remains frozen. The code conserves total energy and angular momentum of the disc to a good precision. We identified a family of model DFs that are stationary solutions of the RR kinetic equation with zero current density in phase space. The RR code results for a Gaussian initial DF were presented, for which the end state is a dynamically stable non-thermal stationary state. The resonantly relaxed distribution is dynamically hotter, as the median of the DF shifts to high e orbits. This brings some stars closer to the MBH, and can lead to a host of astrophysical events, like tidal disruption of stars, extreme mass ratio inspirals (EMRIs) of compact stellar remnants and MBH feeding of stars.

It would be interesting to compare the RR code end-states with actual thermal equilibrium DFs. N-Ring simulations of these systems are important especially to investigate the surmised evolution in the non-resonant region. We suspect that non-occurrence of resonances inside the non-resonant region about $\ell = 0$ leads to non-thermal end states. This unavailability of resonances is due to the one-dimensional nature of the system (in ℓ-space) being studied. Hence, generalizing the system to axisymmetric discs (without the monoenergetic assumption) might lead to thermal end states.

Gravitational Polarization: In Chapter 5, we generalized the RR theory of Sridhar & Touma (2017) (ST17) for an axisymmetric Keplerian stellar disc, to include gravitational polarization. We developed an analytical perturbative scheme to incorporate polarization terms iteratively, to all orders. The different orders of the perturbation theory may be thought of as accounting for the multiplicities of encounters among the Rings. The PRA theory is based on two-Ring encounters; the first order polarization theory is based on three-Ring encounters; and the n^{th} order theory on $(n+2)$-Ring encounters. We use the perturbative expansion of the wake function (ST17), to explicitly evaluate the lowest order PRA wake, and derive a recurrence relation for deducing higher order wakes. The series form of the wake function is used to derive series expressions for the two-Ring correlation function and RR current. Since the higher order coefficients only depend upon the lower order ones (as given by the recurrence relation), the theory can be consistently truncated at any desired order. We derived the form of the RR kinetic equation for an axisymmetric disc, which implicitly includes polarization in a perturbative manner. Then, we calculated explicitly the lowest order (PRA) current and the first order (leading order polarization) currents, thereby generalizing the RR kinetic equation of ST17 to include the leading order polarization effects. We consider a family of stationary states corresponding to this kinetic equation, and compare them with the thermal equilibrium states derived by ST17.

We need to develop an algorithm (like the RR code) to solve the RR kinetic equation of an axisymmetric Keplerian disc, considering leading order polarization, derived in this chapter. It would be interesting to compare the end states from the code with DFs of the form of stationary state and thermal equilibrium.

Bibliography

Agarwal M., Milosavljević M., 2011, The Astrophysical Journal, 729, 35

Alexander T., 2017, Ann. Rev. Astron. Astrophys., 55, 17

Allen D. A., Hyland A. R., Hillier D. J., 1990, Mon. Not. R. Astron. Soc., 244, 706

Amaro-Seoane P., Chen X., 2014, The Astrophysical Journal Letters, 781, L18

Antonini F., 2013, The Astrophysical Journal, 763, 62

Antonini F., Merritt D., 2013, The Astrophysical Journal Letters, 763, L10

Antonini F., Barausse E., Silk J., 2015, The Astrophysical Journal, 812, 72

Arca-Sedda M., Capuzzo-Dolcetta R., 2014, Mon. Not. R. Astron. Soc., 444, 3738

Bacon R., Emsellem E., Monnet G., Nieto J. L., 1994, Astronomy & Astrophysics, 281, 691

Bacon R., Emsellem E., Combes F., Copin Y., Monnet G., Martin P., 2001, Astronomy & Astrophysics, 371, 409

Bahcall J. N., Wolf R. A., 1976, The Astrophysical Journal, 209, 214

Bar-Or B., Alexander T., 2014, Classical and Quantum Gravity, 31, 244003

Bar-Or B., Alexander T., 2016, The Astrophysical Journal, 820, 129

Bar-Or B., Fouvry J.-B., 2018, The Astrophysical Journal Letters, 860, L23

Bartko H., et al., 2009, The Astrophysical Journal, 697, 1741

Bartko H., et al., 2010, The Astrophysical Journal, 708, 834

Bekki K., 2007, Publications of the Astronomical Society of Australia, 24, 77

Bekki K., Couch W. J., Shioya Y., 2006, The Astrophysical Journal Letters, 642, L133

Bender C. M., Orszag S. A., 1978, Advanced Mathematical Methods for Scientists and Engineers

Bender R., et al., 2005, The Astrophysical Journal, 631, 280

Berk H. L., Nielsen C. E., Roberts K. V., 1970, Physics of Fluids, 13, 980

Binney J., Tremaine S., 2008, Galactic Dynamics: Second Edition. Princeton University Press

Boehle A., et al., 2016, The Astrophysical Journal, 830, 17

Böker T., Laine S., van der Marel R. P., Sarzi M., Rix H.-W., Ho L. C., Shields J. C., 2002, Astronomical Journal, 123, 1389

Böker T., Sarzi M., McLaughlin D. E., van der Marel R. P., Rix H.-W., Ho L. C., Shields J. C., 2004, Astronomical Journal, 127, 105

Borderies N., Goldreich P., Tremaine S., 1983, Astronomical Journal, 88, 1560

Brown C. K., Magorrian J., 2013, Mon. Not. R. Astron. Soc., 431, 80

Buchholz R. M., Schödel R., Eckart A., 2009, Astronomy & Astrophysics, 499, 483

Capuzzo-Dolcetta R., 1993, The Astrophysical Journal, 415, 616

Capuzzo-Dolcetta R., Miocchi P., 2008a, Mon. Not. R. Astron. Soc., 388, L69

Capuzzo-Dolcetta R., Miocchi P., 2008b, The Astrophysical Journal, 681, 1136

Carson D. J., Barth A. J., Seth A. C., den Brok M., Cappellari M., Greene J. E., Ho L. C., Neumayer N., 2015, Astronomical Journal, 149, 170

Chandrasekhar S., 1942, Principles of stellar dynamics

Chandrasekhar S., 1943a, The Astrophysical Journal, 97, 255

Chandrasekhar S., 1943b, The Astrophysical Journal, 97, 263

Chang P., Murray-Clay R., Chiang E., Quataert E., 2007, The Astrophysical Journal, 668, 236

Chatzopoulos S., Fritz T. K., Gerhard O., Gillessen S., Wegg C., Genzel R., Pfuhl O., 2015, Mon. Not. R. Astron. Soc., 447, 948

Christopher M. H., Scoville N. Z., Stolovy S. R., Yun M. S., 2005, The Astrophysical Journal, 622, 346

Cohn H., Kulsrud R. M., 1978, The Astrophysical Journal, 226, 1087

De Lorenzi F., Hartmann M., Debattista V. P., Seth A. C., Gerhard O., 2013, Mon. Not. R. Astron. Soc., 429, 2974

Do T., Ghez A. M., Morris M. R., Lu J. R., Matthews K., Yelda S., Larkin J., 2009, The Astrophysical Journal, 703, 1323

Do T., Lu J. R., Ghez A. M., Morris M. R., Yelda S., Martinez G. D., Wright S. A., Matthews K., 2013, The Astrophysical Journal, 764, 154

Dressler A., Richstone D. O., 1988, The Astrophysical Journal, 324, 701

Dritschel D. G., 1988, Journal of Computational Physics, 79, 477

Eisenhauer F., et al., 2005, The Astrophysical Journal, 628, 246

Etxaluze M., Smith H. A., Tolls V., Stark A. A., González-Alfonso E., 2011, Astronomical Journal, 142, 134

Feldmeier-Krause A., Zhu L., Neumayer N., van de Ven G., de Zeeuw P. T., Schödel R., 2017, Mon. Not. R. Astron. Soc., 466, 4040

Feldmeier A., et al., 2014, Astronomy & Astrophysics, 570, A2

Fouvry J.-B., Pichon C., Chavanis P.-H., 2018, Astronomy & Astrophysics, 609, A38

Fritz T. K., et al., 2016, The Astrophysical Journal, 821, 44

Gallego-Cano E., Schödel R., Dong H., Nogueras-Lara F., Gallego-Calvente A. T., Amaro-Seoane P., Baumgardt H., 2018, Astronomy & Astrophysics, 609, A26

Gammie C. F., 2001, The Astrophysical Journal, 553, 174

Gatley I., Jones T. J., Hyland A. R., Wade R., Geballe T. R., Krisciunas K., 1986, Mon. Not. R. Astron. Soc., 222, 299

Genzel R., et al., 2003, The Astrophysical Journal, 594, 812

Genzel R., Eisenhauer F., Gillessen S., 2010, Reviews of Modern Physics, 82, 3121

Georgiev I. Y., Böker T., 2014, Mon. Not. R. Astron. Soc., 441, 3570

Georgiev I. Y., Böker T., Leigh N., Lützgendorf N., Neumayer N., 2016, Mon. Not. R. Astron. Soc., 457, 2122

Gerhard O. E., Binney J., 1985, Mon. Not. R. Astron. Soc., 216, 467

Ghez A. M., Becklin E., Duchjne G., Hornstein S., Morris M., Salim S., Tanner A., 2003, Astronomische Nachrichten Supplement, 324, 527

Ghez A. M., Salim S., Hornstein S. D., Tanner A., Lu J. R., Morris M., Becklin E. E., Duchêne G., 2005, The Astrophysical Journal, 620, 744

Gilbert I. H., 1968, The Astrophysical Journal, 152, 1043

Gillessen S., Eisenhauer F., Trippe S., Alexander T., Genzel R., Martins F., Ott T., 2009, The Astrophysical Journal, 692, 1075

Gillessen S., et al., 2017, The Astrophysical Journal, 837, 30

Gnedin O. Y., Ostriker J. P., Tremaine S., 2014, The Astrophysical Journal, 785, 71

Goldreich P., Peale S., 1966, Astronomical Journal, 71, 425

Goodman J., 1988, The Astrophysical Journal, 329, 612

Goodman J., Binney J., 1984, Mon. Not. R. Astron. Soc., 207, 511

Gradshteyn I. S., Ryzhik I. M., Jeffrey A., Zwillinger D., 2007, Table of Integrals, Series, and Products

Guesten R., Genzel R., Wright M. C. H., Jaffe D. T., Stutzki J., Harris A. I., 1987, The Astrophysical Journal, 318, 124

Guillard N., Emsellem E., Renaud F., 2016, Mon. Not. R. Astron. Soc., 461, 3620

Gulati M., Saini T. D., Sridhar S., 2012, Mon. Not. R. Astron. Soc., 424, 348

Gültekin K., Richstone D. O., Gebhardt K., Faber S. M., Lauer T. R., Bender R., Kormendy J., Pinkney J., 2011, The Astrophysical Journal, 741, 38

Gürkan M. A., Hopman C., 2007, Mon. Not. R. Astron. Soc., 379, 1083

Hamers A. S., Portegies Zwart S. F., Merritt D., 2014, Mon. Not. R. Astron. Soc., 443, 355

Hamers A. S., Bar-Or B., Petrovich C., Antonini F., 2018, The Astrophysical Journal, 865, 2

Hartmann M., Debattista V. P., Seth A., Cappellari M., Quinn T. R., 2011, Mon. Not. R. Astron. Soc., 418, 2697

Henrard J., 1982, Celestial Mechanics, 27, 3

Hopman C., Alexander T., 2006a, in Schödel R., Bower G. C., Muno M. P., Nayakshin S., Ott T., eds, Journal of Physics Conference Series Vol. 54, Journal of Physics Conference Series. pp 321–327 (arXiv:astro-ph/0605457), doi:10.1088/1742-6596/54/1/051

Hopman C., Alexander T., 2006b, The Astrophysical Journal, 645, 1152

Jacobs V., Sellwood J. A., 2001, The Astrophysical Journal Letters, 555, L25

Jalali M. A., Tremaine S., 2012, Mon. Not. R. Astron. Soc., 421, 2368

Kaur K., Sridhar S., 2018, Mon. Not. R. Astron. Soc., 477, 112

Kaur K., Kazandjian M. V., Sridhar S., Touma J. R., 2018, Mon. Not. R. Astron. Soc., 476, 4104

Kazandjian M. V., Touma J. R., 2013, Mon. Not. R. Astron. Soc., 430, 2732

King I. R., Stanford S. A., Crane P., 1995, Astronomical Journal, 109, 164

Kocsis B., Tremaine S., 2011, Mon. Not. R. Astron. Soc., 412, 187

Kocsis B., Tremaine S., 2015, Mon. Not. R. Astron. Soc., 448, 3265

Kormendy J., 1988, The Astrophysical Journal, 325, 128

Kormendy J., Ho L. C., 2013, Ann. Rev. Astron. Astrophys., 51, 511

Kormendy J., Richstone D., 1995, Ann. Rev. Astron. Astrophys., 33, 581

Krabbe A., Genzel R., Drapatz S., Rotaciuc V., 1991, The Astrophysical Journal Letters, 382, L19

Krolik J. H., 1999, Active galactic nuclei : from the central black hole to the galactic environment

Kupi G., Eilon E., Alexander T., 2010, in Journal of Physics Conference Series. p. 012056, doi:10.1088/1742-6596/228/1/012056

Lauer T. R., et al., 1993, Astronomical Journal, 106, 1436

Lauer T. R., et al., 1996, The Astrophysical Journal Letters, 471, L79

Lauer T. R., Faber S. M., Ajhar E. A., Grillmair C. J., Scowen P. A., 1998, Astronomical Journal, 116, 2263

Lauer T. R., et al., 2005, Astronomical Journal, 129, 2138

Lee E., Goodman J., 1999, Mon. Not. R. Astron. Soc., 308, 984

Levin Y., 2007, Mon. Not. R. Astron. Soc., 374, 515

Levin Y., Beloborodov A. M., 2003, The Astrophysical Journal Letters, 590, L33

Light E. S., Danielson R. E., Schwarzschild M., 1974, The Astrophysical Journal, 194, 257

Lu J. R., Ghez A. M., Hornstein S. D., Morris M. R., Becklin E. E., Matthews K., 2009, The Astrophysical Journal, 690, 1463

Lyubenova M., et al., 2013, Mon. Not. R. Astron. Soc., 431, 3364

Madigan A.-M., Hopman C., Levin Y., 2011, The Astrophysical Journal, 738, 99

Madigan A.-M., Halle A., Moody M., McCourt M., Nixon C., Wernke H., 2018, The Astrophysical Journal, 853, 141

Merritt D., 2013, Dynamics and Evolution of Galactic Nuclei

Merritt D., 2015a, The Astrophysical Journal, 804, 52

Merritt D., 2015b, The Astrophysical Journal, 804, 128

Merritt D., 2015c, The Astrophysical Journal, 810, 2

Merritt D., Valluri M., 1999, in American Astronomical Society Meeting Abstracts #194. p. 893

Merritt D., Vasiliev E., 2011, The Astrophysical Journal, 726, 61

Merritt D., Alexander T., Mikkola S., Will C. M., 2011, Phys. Rev. D, 84, 044024

Misgeld I., Hilker M., 2011, Mon. Not. R. Astron. Soc., 414, 3699

Murray C. D., Dermott S. F., 1999, Solar system dynamics

Nayakshin S., 2006, Mon. Not. R. Astron. Soc., 372, 143

Nayakshin S., Cuadra J., 2005, Astronomy & Astrophysics, 437, 437

Neumayer N., Walcher C. J., 2012, Advances in Astronomy, 2012, 709038

Neumayer N., Walcher C. J., Andersen D., Sánchez S. F., Böker T., Rix H.-W., 2011, Mon. Not. R. Astron. Soc., 413, 1875

Norris M. A., et al., 2014, Mon. Not. R. Astron. Soc., 443, 1151

Paudel S., Lisker T., Kuntschner H., 2011, Mon. Not. R. Astron. Soc., 413, 1764

Paumard T., et al., 2006, The Astrophysical Journal, 643, 1011

Peiris H. V., Tremaine S., 2003, The Astrophysical Journal, 599, 237

Perets H. B., Gualandris A., 2010, The Astrophysical Journal, 719, 220

Plummer H. C., 1960, An introductory treatise on dynamical astronomy

Polyachenko E. V., Polyachenko V. L., Shukhman I. G., 2007, Mon. Not. R. Astron. Soc., 379, 573

Polyachenko E. V., Polyachenko V. L., Shukhman I. G., 2008, Mon. Not. R. Astron. Soc., 386, 1966

Poon M. Y., Merritt D., 2001, The Astrophysical Journal, 549, 192

Press W. H., Teukolsky S. A., Vetterling W. T., Flannery B. P., 1992, Numerical recipes in FORTRAN. The art of scientific computing

Puzia T. H., Sharina M. E., 2008, The Astrophysical Journal, 674, 909

Rauch K. P., Ingalls B., 1996, in American Astronomical Society Meeting Abstracts. p. 1408

Rauch K. P., Tremaine S., 1996, New Astron., 1, 149

Rees M. J., 1984, Ann. Rev. Astron. Astrophys., 22, 471

Requena-Torres M. A., et al., 2012, Astronomy & Astrophysics, 542, L21

Rossa J., van der Marel R. P., Böker T., Gerssen J., Ho L. C., Rix H.-W., Shields J. C., Walcher C.-J., 2006, Astronomical Journal, 132, 1074

Rostoker N., 1964, Physics of Fluids, 7, 491

Salow R. M., Statler T. S., 2001, The Astrophysical Journal Letters, 551, L49

Salow R. M., Statler T. S., 2004, The Astrophysical Journal, 611, 245

Sambhus N., Sridhar S., 2000, The Astrophysical Journal, 542, 143

Sambhus N., Sridhar S., 2002, Astronomy & Astrophysics, 388, 766

Schödel R., Genzel R., Ott T., Eckart A., 2003, Astronomische Nachrichten Supplement, 324, 535

Schödel R., et al., 2007, Astronomy & Astrophysics, 469, 125

Schödel R., Feldmeier A., Kunneriath D., Stolovy S., Neumayer N., Amaro-Seoane P., Nishiyama S., 2014, Astronomy & Astrophysics, 566, A47

Schödel R., Gallego-Cano E., Dong H., Nogueras-Lara F., Gallego-Calvente A. T., Amaro-Seoane P., Baumgardt H., 2018, Astronomy & Astrophysics, 609, A27

Scott N., Graham A. W., 2013, The Astrophysical Journal, 763, 76

Seth A. C., Dalcanton J. J., Hodge P. W., Debattista V. P., 2006, Astronomical Journal, 132, 2539

Sridhar S., Saini T. D., 2010, Mon. Not. R. Astron. Soc., 404, 527

Sridhar S., Touma J., 1996, Mon. Not. R. Astron. Soc., 279, 1263

Sridhar S., Touma J., 1997a, Mon. Not. R. Astron. Soc., 287, L1

Sridhar S., Touma J., 1997b, Mon. Not. R. Astron. Soc., 292, 657

Sridhar S., Touma J., 1999, Mon. Not. R. Astron. Soc., 303, 483

Sridhar S., Touma J. R., 2016a, Mon. Not. R. Astron. Soc., 458, 4129

Sridhar S., Touma J. R., 2016b, Mon. Not. R. Astron. Soc., 458, 4143

Sridhar S., Touma J. R., 2017, Mon. Not. R. Astron. Soc., 465, 1856

Sridhar S., Syer D., Touma J., 1999, in Sellwood J. A., Goodman J., eds, Astronomical Society of the Pacific Conference Series Vol. 160, Astrophysical Discs - an EC Summer School. p. 307

Statler T. S., 1999, The Astrophysical Journal Letters, 524, L87

Stone N. C., Metzger B. D., Haiman Z., 2017, Mon. Not. R. Astron. Soc., 464, 946

Touma J. R., 2002, Mon. Not. R. Astron. Soc., 333, 583

Touma J. R., Sridhar S., 2012, Mon. Not. R. Astron. Soc., 423, 2083

Touma J., Tremaine S., 2014, Journal of Physics A Mathematical General, 47, 292001

Touma J. R., Tremaine S., Kazandjian M. V., 2009, Mon. Not. R. Astron. Soc., 394, 1085

Tremaine S., 1995, Astronomical Journal, 110, 628

Tremaine S., 2001, Astronomical Journal, 121, 1776

Tremaine S., 2005, The Astrophysical Journal, 625, 143

Tremaine S. D., Ostriker J. P., Spitzer Jr. L., 1975, The Astrophysical Journal, 196, 407

Turner M. L., Côté P., Ferrarese L., Jordán A., Blakeslee J. P., Mei S., Peng E. W., West M. J., 2012, The Astrophysical Journal Supplement Series, 203, 5

Walcher C. J., et al., 2005, The Astrophysical Journal, 618, 237

Walcher C. J., Böker T., Charlot S., Ho L. C., Rix H.-W., Rossa J., Shields J. C., van der Marel R. P., 2006, The Astrophysical Journal, 649, 692

Wernke H. N., Madigan A.-M., 2019, arXiv e-prints,

Yelda S., Ghez A. M., Lu J. R., Do T., Meyer L., Morris M. R., Matthews K., 2014, The Astrophysical Journal, 783, 131

Young P., 1980, The Astrophysical Journal, 242, 1232

Yusef-Zadeh F., Stolovy S. R., Burton M., Wardle M., Ashley M. C. B., 2001, The Astrophysical Journal, 560, 749

den Brok M., et al., 2014, Mon. Not. R. Astron. Soc., 445, 2385

Šubr L. ., Schovancová J., Kroupa P., 2009, Astronomy & Astrophysics, 496, 695

van der Marel R. P., Rix H. W., Carter D., Franx M., White S. D. M., de Zeeuw T., 1994, Mon. Not. R. Astron. Soc., 268, 521

Appendix A

Two-Ring Interaction Potential

A.1 Derivation of Log-Interaction Potential

We consider two coplanar Gaussian Rings of equal semi-major axes ($a = a' = a_0$), with eccentricities e and e' and apsidal longitudes g and g'. Let $\hat{\boldsymbol{u}} = (\cos g\,, \sin g)$ and $\hat{\boldsymbol{u}}' = (\cos g'\,, \sin g')$ be unit vectors in the directions of the periapses of the two Rings. Let $\hat{\boldsymbol{v}} = (-\sin g\,, \cos g)$ and $\hat{\boldsymbol{v}}' = (-\sin g'\,, \cos g')$ be unit vectors that are perpendicular to $\hat{\boldsymbol{u}}$ and $\hat{\boldsymbol{u}}'$, respectively. We also define the "eccentricity vectors", $\boldsymbol{e} = e\,\hat{\boldsymbol{u}} = e(\cos g\,, \sin g)$ and $\boldsymbol{e}' = e'\,\hat{\boldsymbol{u}}' = e'(\cos g'\,, \sin g')$. The time–averaged gravitational potential energy between the Rings can be written as:

$$\Psi \;=\; \frac{GM_{\bullet}}{2\pi a_0}\,\psi(\boldsymbol{e}, \boldsymbol{e}')\,, \qquad \psi(\boldsymbol{e}, \boldsymbol{e}') \;=\; -2\pi\left\langle\!\!\left\langle \frac{1}{|\boldsymbol{r} - \boldsymbol{r}'|} \right\rangle\!\!\right\rangle . \tag{A.1}$$

Here $\boldsymbol{r}$ and $\boldsymbol{r}'$ are the (normalised) position vectors, given by

$$\boldsymbol{r} \;=\; \hat{\boldsymbol{u}}(\cos\eta - e) \;+\; \hat{\boldsymbol{v}}\sqrt{1 - e^2}\,\sin\eta\;, \tag{A.2a}$$

$$\boldsymbol{r}' \;=\; \hat{\boldsymbol{u}}'(\cos\eta' - e') \;+\; \hat{\boldsymbol{v}}'\sqrt{1 - e'^2}\,\sin\eta' \tag{A.2b}$$

in terms of the eccentric anomalies η and η'. The above equations are analogous to the form given in equation (1.5). Without loss of generality, we have assumed that the Rings have prograde circulation. The time averages can be written explicitly as:

$$\psi(\boldsymbol{e}, \boldsymbol{e}') \;=\; -2\pi\int_0^{2\pi}\!\!\int_0^{2\pi} \frac{(1 - e\cos\eta)(1 - e'\cos\eta')}{|\boldsymbol{r} - \boldsymbol{r}'|}\,\frac{\mathrm{d}\eta}{2\pi}\,\frac{\mathrm{d}\eta'}{2\pi}\,. \tag{A.3}$$

To obtain the dominant terms of $\psi(\boldsymbol{e}, \boldsymbol{e}')$ for small eccentricities we can make the following two simplifications: (a) we set $(1 - e\cos\eta)(1 - e'\cos\eta') \to 1$; and

(b) in equation (A.2) we drop terms of order (e^2, e'^2) and higher order and write $\boldsymbol{r} \rightarrow \hat{\boldsymbol{\xi}}(\eta+g) - \boldsymbol{e}$ and $\boldsymbol{r}' \rightarrow \hat{\boldsymbol{\xi}}'(\eta'+g') - \boldsymbol{e}'$, where $\hat{\boldsymbol{\xi}}(\eta) = (\cos\eta\,,\sin\eta)$ and $\hat{\boldsymbol{\xi}}'(\eta') = (\cos\eta'\,,\sin\eta')$ are unit vectors. Then

$$\psi(\boldsymbol{e}_0) \;=\; -2\pi\int_0^{2\pi}\!\!\int_0^{2\pi}\frac{1}{\left|\,\hat{\boldsymbol{\xi}}(\eta+g) - \,\hat{\boldsymbol{\xi}}'(\eta'+g') \;-\; \boldsymbol{e}_0\right|}\frac{\mathrm{d}\eta}{2\pi}\frac{\mathrm{d}\eta'}{2\pi} \;\;+\;\ldots\,, \tag{A.4}$$

where $\boldsymbol{e}_0 = \boldsymbol{e} - \boldsymbol{e}'$, and "…" indicate (sub–dominant) terms that vanish in the limit $e \rightarrow 0$ and $e' \rightarrow 0$. The integral has a basic symmetry that can be exploited to simplify it. Under a transformation of variables $\eta \rightarrow \eta + \chi$ and $\eta' \rightarrow \eta' + \chi'$, where χ and χ' are arbitrary real numbers, we get

$$\psi(\boldsymbol{e}_0) \;=\; -2\pi\int_0^{2\pi}\!\!\int_0^{2\pi}\frac{1}{\left|\,\hat{\boldsymbol{\xi}}(\eta+g+\chi) - \,\hat{\boldsymbol{\xi}}'(\eta'+g'+\chi') \;-\; \boldsymbol{e}_0\right|}\frac{\mathrm{d}\eta}{2\pi}\frac{\mathrm{d}\eta'}{2\pi} \;\;+\;\ldots\,. \tag{A.5}$$

It should be noted that, whereas the initial phases of $\hat{\boldsymbol{\xi}}$ and $\hat{\boldsymbol{\xi}}'$ can be arbitrary, $\boldsymbol{e}_0 = (e\cos g - e'\cos g'\,, e\sin g - e'\sin g')$ is unaffected by the transformation of integration variables and is to be regarded as a given and fixed vector. Therefore

$$\psi(\boldsymbol{e}_0) \;=\; -2\pi\left\langle\!\!\left\langle\frac{1}{\left|\,\hat{\boldsymbol{\xi}} - \,\hat{\boldsymbol{\xi}}' \;-\; \boldsymbol{e}_0\right|}\right\rangle\!\!\right\rangle \;\;+\;\ldots\,, \tag{A.6}$$

where $\hat{\boldsymbol{\xi}}$ and $\hat{\boldsymbol{\xi}}'$ are now regarded as the position vectors of two points A and A' which are distributed *independently and uniformly* on the unit circle, and "$\langle\!\langle\;\rangle\!\rangle$" indicates averaging over the distributions of A and A'. Let $\boldsymbol{q} = \hat{\boldsymbol{\xi}} - \hat{\boldsymbol{\xi}}'$ be the directed chord from A' to A, and let $P(\boldsymbol{q})\mathrm{d}^2\boldsymbol{q}$ be the probability that $\boldsymbol{q}$ lies in the area element $\mathrm{d}^2\boldsymbol{q}$. Then

$$\psi(\boldsymbol{e}_0) \;=\; -2\pi\int\frac{P(\boldsymbol{q})\mathrm{d}^2\,\boldsymbol{q}}{|\;\boldsymbol{q} \;-\; \boldsymbol{e}_0\,|} \;\;+\;\ldots\,. \tag{A.7}$$

We can think of $P(\boldsymbol{q})$ as the surface mass density of a razor–thin disc of unit total mass. Then $G\cdot\psi(\boldsymbol{e}_0)/(2\pi)$ is the self–gravitational potential at location $\boldsymbol{e}_0$ in the $\boldsymbol{q}$–plane. Since the end points of the chord, A and A', are independently and uniformly distributed over the unit circle, the distribution of $\boldsymbol{q}$ must be isotropic in its plane. The surface density $P(q)$ being axisymmetric, so is the self–gravitational potential $\psi(e_0)$. There are different ways of relating $\psi(e_0)$ to $P(q)$ given in Binney & Tremaine (2008). We choose equation (2.155) which views the disc as a superposition of flattened spheroids:

$$\psi(e_0) \;=\; -8\pi \int_0^{e_0} \frac{\mathrm{d}\lambda}{\sqrt{e_0^2-\lambda^2}} \int_\lambda^\infty \mathrm{d}q \frac{qP(q)}{\sqrt{q^2-\lambda^2}} \;+\; \ldots\,. \tag{A.8}$$

Since $2\pi qP(q)$ is the probability distribution of chord lengths, a straightforward calculation in plane geometry gives:

$$P(q) \;=\; \begin{cases} (2\pi^2 q)^{-1}\left[1-(q/2)^2\right]^{-1/2} & \text{if } 0<q<2 \\ 0 & \text{otherwise.} \end{cases} \tag{A.9}$$

Substituting equation (A.9) in (A.8) we get:

$$\psi(e_0) \;=\; -\frac{4}{\pi} \int_0^{e_0} \frac{\mathrm{d}\lambda}{\sqrt{e_0^2-\lambda^2}} \int_\lambda^2 \frac{\mathrm{d}q}{\sqrt{(1-(q/2)^2)(q^2-\lambda^2)}} \;+\; \ldots\,. \tag{A.10}$$

The integral over q can be written as a complete elliptic integral of the first kind $\mathcal{K}$ (see equation C.2 for definition) by transforming to a new integration variable θ, where $\sin^2\theta = 4(q^2-a^2)/q^2(4-a^2)$:

$$\psi(e_0) \;=\; -\frac{4}{\pi} \int_0^{e_0} \frac{\mathrm{d}\lambda}{\sqrt{e_0^2-\lambda^2}}\, \mathcal{K}\left(\sqrt{1-(\lambda/2)^2}\right) \;+\; \ldots\,. \tag{A.11}$$

Since $0 \le \lambda < e_0 \ll 1$, we have $\mathcal{K}\left(\sqrt{1-(\lambda/2)^2}\right) = \log(8/\lambda) + O(\lambda^2)$. Then

$$\begin{aligned} \psi(e_0) \;&=\; -\frac{4}{\pi} \int_0^{e_0} \frac{\mathrm{d}\lambda}{\sqrt{e_0^2-\lambda^2}} \log(8/\lambda) \;+\; \ldots \;=\; -2\log(16/e_0) \;+\; \ldots \\ &= -8\log 2 + \log e_0^2 + \ldots \\ &= -8\log 2 + \log|\boldsymbol{e}-\boldsymbol{e}'|^2 + \ldots\,. \end{aligned} \tag{A.12}$$

Substituting equation (A.12) in (A.1), we get:

$$\Psi \;=\; \frac{GM_\bullet}{a_0}\left\{-\frac{4}{\pi}\log 2 \;+\; \frac{1}{2\pi}\log|\boldsymbol{e}-\boldsymbol{e}'|^2\right\} \;+\; \ldots\,. \tag{A.13}$$

We refer to Ψ as two-Ring log interaction potential for planar monoenergetic Rings. Note that this expression should be most accurate for Rings with small eccentricities.

A.2 Interaction Kernels

A.2.1 Interaction Kernel for Log-Potential

The normalised two-Ring log interaction potential from equation (A.12) is:

$$\psi(\ell, \ell', g - g') = -8 \log 2 + \log (\boldsymbol{e} - \boldsymbol{e}')^2 \,. \tag{A.14}$$

The Fourier series for ψ can be written as:

$$\psi(\ell, \ell', g - g') = C_0(\ell, \ell') + \sum_{m \neq 0} C_m(\ell, \ell') \exp\left[im(g - g')\right]. \tag{A.15}$$

Touma & Tremaine (2014) derived the following expressions for Fourier coefficients C_m's (as given in equation (C.2) of the paper):

$$C_0(\ell, \ell') = -8 \log 2 + \log e_>^2 \;\; ; \qquad C_m(\ell, \ell') = -\frac{1}{|m|} \left(\frac{e_<}{e_>}\right)^{|m|} . \tag{A.16}$$

Hence the normalised kernel $K(\ell, \ell')$ becomes:

$$K(\ell, \ell') = 2\pi \sum_{m=1}^{\infty} m C_m^2 = 2\pi \sum_{m=1}^{\infty} \frac{1}{m} \left(\frac{e_<}{e_>}\right)^{2m} = -2\pi \log \left[1 - \left(\frac{e_<}{e_>}\right)^2\right]. \tag{A.17}$$

A.2.2 Softened Interaction Kernel

For computational purposes it is useful to softened the two-Ring potential of equation (A.14). Hence we consider the softened logarithmic potential,

$$\begin{aligned} \psi_{\mathrm{S}}(\ell, \ell', g - g') \;&=\; -8 \log 2 + \log \left(|\boldsymbol{e} - \boldsymbol{e}'|^2 + \delta^2\right) \\ &=\; -8 \log 2 + \log \left(e^2 + e'^2 - 2ee' \cos(g - g') + \delta^2\right) \end{aligned} \tag{A.18}$$

where $0 < \delta \ll 1$ is the softening parameter. Similar to equation (A.15), we write the Fourier series as:

$$\psi_{\mathrm{S}}(\ell, \ell', g - g') = C_0^{\mathrm{S}}(\ell, \ell') + \sum_{m \neq 0} C_m^{\mathrm{S}}(\ell, \ell') \exp\left[im(g - g')\right]. \tag{A.19}$$

The 0^{th} order Fourier coefficient C_0^{S} is:

$$C_0^{\mathrm{S}}(\ell, \ell') \;=\; -8 \log 2 + \log\left[e^2 + e'^2 + \delta^2\right] + \frac{1}{2\pi} \oint \mathrm{d}g \log\left(1 - \Delta \cos g\right) \tag{A.20}$$

where $\Delta = 2ee'/(e^2 + e'^2 + \delta^2)$. The integral in the above expression can be solved using the formula 4.224...12 of Gradshteyn et al. (2007), which gives:

$$\begin{aligned} C_0^{\mathrm{S}}(\ell,\ell') &= -8\log 2 + \log\left(e^2 + e'^2 + \delta^2\right) + \log\left(\frac{1+\sqrt{1-\Delta^2}}{2}\right) \\ &= -8\log 2 + \log\left[\frac{e^2 + e'^2 + \delta^2 + \sqrt{(e^2 - e'^2)^2 + \delta^4 + 2\delta^2(e^2 + e'^2)}}{2}\right]. \end{aligned} \tag{A.21}$$

For $m \neq 0$, we have:

$$\begin{aligned} C_m^{\mathrm{S}}(\ell,\ell') &= \frac{2}{2\pi}\int_0^{\pi} \mathrm{d}g \cos(mg) \log(1 - \Delta\cos g) \\ &= -\frac{2\Delta}{2\pi|m|}\int_0^{\pi} \mathrm{d}g \frac{\sin g \sin(|m|g)}{(1 - \Delta\cos g)}. \end{aligned} \tag{A.22}$$

The integral can be solved using the formula 3.613 ...3 from Gradshteyn et al. (2007), which gives:

$$C_m^{\mathrm{S}}(\ell,\ell') = -\frac{1}{|m|}\left(\frac{1}{\Delta} - \sqrt{\frac{1}{\Delta^2} - 1}\right)^{|m|}. \tag{A.23}$$

Using the explicit form of Δ we have the final expression:

$$C_m^{\mathrm{S}}(\ell,\ell') = -\frac{1}{|m|}\left(\frac{e^2 + e'^2 + \delta^2 - \sqrt{(e^2 - e'^2)^2 + \delta^4 + 2\delta^2(e^2 + e'^2)}}{2ee'}\right)^{|m|}. \tag{A.24}$$

Therefore the softened interaction kernel $K_{\mathrm{S}}(\ell,\ell')$ is:

$$\begin{aligned} K_{\mathrm{S}}(\ell,\ell') &= 2\pi\sum_{m=1}^{\infty} m\left(C_m^{\mathrm{S}}(\ell,\ell')\right)^2 \\ &= 2\pi\sum_{m=1}^{\infty}\frac{1}{m}\left(\frac{e^2 + e'^2 + \delta^2 - \sqrt{(e^2 - e'^2)^2 + \delta^4 + 2\delta^2(e^2 + e'^2)}}{2ee'}\right)^{2m} \\ &= -2\pi\log\left[1 - \left(\frac{e^2 + e'^2 + \delta^2 - \sqrt{(e^2 - e'^2)^2 + \delta^4 + 2\delta^2(e^2 + e'^2)}}{2ee'}\right)^2\right] \end{aligned} \tag{A.25}$$

It can be readily verified that, as the softening parameter $\delta \to 0$, the softened kernel $K_{\mathrm{S}}(\ell,\ell')$ reduces to the original unsoftened log kernel $K(\ell,\ell')$ of equation (A.17).

Appendix B

Surface Density of Waterbags

We consider a monoenergetic axisymmetric Keplerian stellar disc defined by a real-space DF $\hat{f}(\boldsymbol{r}, \boldsymbol{u})$, where $\boldsymbol{r}$ and $\boldsymbol{u}$ are the position and velocity vectors of a star, respectively, in the MBH's rest frame. The surface density function is obtained by integrating the disc DF over velocity space:

$$\Sigma(\boldsymbol{r}) = \int \mathrm{d}\boldsymbol{u}\, \hat{f}(\boldsymbol{r}, \boldsymbol{u})\,. \tag{B.1}$$

For a razor-thin disc, the four dimensional phase volume, $\mathrm{d}\boldsymbol{r}\,\mathrm{d}\boldsymbol{u} = I\mathrm{d}w\,\mathrm{d}I\,\mathrm{d}g\,\mathrm{d}\ell$. Hence the DF of an axisymmetric monoenergetic disc (not necessarily a waterbag) is related to the DF, $f_0(\ell)$, of § 2.2.2, as:

$$\hat{f}(\boldsymbol{r}, \boldsymbol{u}) \;=\; \frac{f_0(\ell)}{4\pi^2 I_0}\,\delta(I - I_0)\,. \tag{B.2}$$

Then

$$\Sigma_0(r) \;=\; \frac{1}{4\pi^2 I_0}\int \mathrm{d}u\,\mathrm{d}\phi\, u\, f_0(\ell)\,\delta(I - I_0)\,, \tag{B.3}$$

where u is the speed, ϕ is the angle between $\boldsymbol{u}$ and $\boldsymbol{r}$, and $I_0 = \sqrt{GM_\bullet a_0}$. Since the discs we consider have only prograde orbits, $\ell > 0$ which implies that $0 \le \phi \le \pi$. We now express the (scaled) Delaunay variables, $\{\ell, I\}$, in terms of $\{u, \phi\}$:

$$I \;=\; \left(\frac{2}{GM_\bullet r} - \frac{u^2}{(GM_\bullet)^2}\right)^{-1/2}\,, \tag{B.4a}$$

$$\ell \;=\; L/I \;=\; I^{-1} r u \sin\phi\,. \tag{B.4b}$$

Hence

$$\delta(I - I_0) \;=\; \frac{\delta(u - u_0)}{|\mathrm{d}I/\mathrm{d}u|_{u_0}} \;=\; \left(\frac{GM_\bullet}{a_0^3}\right)^{1/2} \frac{\delta(u - u_0)}{u_0}\,, \tag{B.5}$$

where

$$u_0(r) \;=\; \begin{cases} \sqrt{GM_\bullet\left(\dfrac{2}{r} - \dfrac{1}{a_0}\right)}\,, & \text{for } r \le 2a_0 \\ 0\,, & \text{for } r > 2a_0 \end{cases} \tag{B.6}$$

is the speed at radius r, of an orbit with semi-major axis a_0. Substituting equation (B.5) in (B.3) and using equations (B.4b) and (B.6), the surface density for a general monoenergetic DF:

$$\Sigma_0(r) \;=\; \frac{1}{4\pi^2 a_0^2}\int \mathrm{d}\phi\, f_0(\ell_0(r)\sin\phi)\;, \tag{B.7}$$

where

$$\ell_0(r) \;=\; \frac{r u_0(r)}{I_0} \;=\; \begin{cases} \sqrt{\dfrac{2r}{a_0} - \dfrac{r^2}{a_0^2}}\,, & \text{for } r \le 2a_0 \\ 0\,, & \text{for } r > 2a_0. \end{cases} \tag{B.8}$$

For the waterbag DF of equation (2.24), $f_0(\ell) = 1/\Delta\ell = 1/(\ell_2 - \ell_1) = \text{constant}$ for $0 \le \ell_1 < \ell_2 \le 1$ and is zero outside this range. This implies that $\Sigma_0(r)$ is non zero only when $|r - a_0| \le a_0 e_1$. Within this range of radii,

$$\Sigma_0(r) \;=\; \frac{1}{4\pi^2 a_0^2 \Delta\ell}\,\Delta\phi(r)\,, \tag{B.9}$$

where $\Delta\phi(r)$ is the range in ϕ for which

$$\frac{\ell_1}{\ell_0(r)} \;\le\; \sin\phi \;\le\; \frac{\ell_2}{\ell_0(r)}\,. \tag{B.10}$$

All we need to do now is to determine $\Delta\phi(r)$. There are two cases to consider:

1. $\ell_2 \le \ell_0(r)$: Using equation (B.8), this condition is equivalent to $|r - a_0| \le a_0 e_2$. Then $\Delta\phi(r) \;=\; 2\,(\phi_2 - \phi_1)$, where $\phi_1(r) = \sin^{-1}\left[\ell_1/\ell_0(r)\right]$ and $\phi_2(r) = \sin^{-1}\left[\ell_2/\ell_0(r)\right]$.

2. $\ell_1 \le \ell_0(r) \le \ell_2$: Using equation (B.8), this condition is equivalent to $a_0 e_2 \le |r - a_0| \le a_0 e_1$. Then $\Delta\phi(r) \;=\; 2\,(\pi/2 - \phi_1)$.

Substituting these expressions for $\Delta\phi(r)$ in equation (B.9), we obtain equation (2.25) for the surface density of an axisymmetric monoenergetic waterbag.

Appendix C

Orbit-Averaged Gas Disc Potential

In order to compute the orbit–averaged disc potential, $\Phi_{\rm d}(I, L, L_z, g, \tau)$ introduced in § 3.2.1, we need the following relations (coming from equation 1.3) between (r, z) and Keplerian orbital elements:

$$r \;=\; a(1 - e\,C_\eta)\,, \qquad \cos\theta \;=\; \frac{z}{r} \;=\; \frac{S_i\left(S_g\,(C_\eta - e) \,+\, C_g\,\sqrt{1-e^2}\,S_\eta\right)}{1 - e\,C_\eta}\,, \tag{C.1}$$

where S and C are shorthand for sine and cosine of the angle given as subscript, and η is the eccentric anomaly. From equation (3.6), we see that the following three averages over the Kepler orbital phase, w, (or mean anomaly) need to be computed: $\langle\, 1/\sqrt{r}\,\rangle$, $\langle\, |\cos\theta|\,/\sqrt{r}\,\rangle$ and $\langle\, \cos^2\theta/\sqrt{r}\,\rangle$. Using $w = (\eta - e\sin\eta)$, all of these can be expressed in terms of the elliptic integrals, given below:

$$\mathcal{F}(\zeta_0, k) \;=\; \int_0^{\zeta_0} {\rm d}\zeta\, \frac{1}{\sqrt{1 - k^2\sin^2\zeta}}\,, \qquad \mathcal{K}(k) \;=\; \int_0^{\frac{\pi}{2}} {\rm d}\zeta\, \frac{1}{\sqrt{1 - k^2\sin^2\zeta}}\,, \tag{C.2}$$

are incomplete and complete elliptic integrals of the first kind, and

$$\mathcal{E}(\zeta_0, k) \;=\; \int_0^{\zeta_0} {\rm d}\zeta\, \sqrt{1 - k^2\sin^2\zeta}\,, \qquad \mathcal{E}(k) \;=\; \int_0^{\frac{\pi}{2}} {\rm d}\zeta\, \sqrt{1 - k^2\sin^2\zeta}\,, \tag{C.3}$$

are incomplete and complete elliptic integrals of the second kind. Then,

$$\left\langle \frac{1}{\sqrt{r}} \right\rangle \;=\; \oint \frac{{\rm d}\eta}{2\pi}\, \frac{(1 - e\cos\eta)}{\sqrt{r}} \;=\; \frac{1}{\pi\sqrt{a}} \int_0^{\pi} {\rm d}\eta\, \sqrt{1 - e\cos\eta} \;=\; \frac{2\sqrt{1+e}}{\pi\sqrt{a}}\,\mathcal{E}(k)\;, \tag{C.4}$$

where $k(e) = \sqrt{2e/(1+e)}$.

The second average is:

$$\left\langle \frac{|\cos\theta|}{\sqrt{r}} \right\rangle \;=\; \oint \frac{\mathrm{d}\eta}{2\,\pi}\,(1-e\cos\eta)\frac{|\cos\theta|}{\sqrt{r}} \;=\; \frac{\sin i}{\sqrt{a}}\int_0^{2\pi}\frac{\mathrm{d}\eta}{2\pi}\frac{|S_g(C_\eta-e)+C_g\sqrt{1-e^2}S_\eta|}{\sqrt{1-e\,C_\eta}}\,. \tag{C.5}$$

Note that $|S_g(C_\eta - e) + C_g\,\sqrt{1-e^2}\,S_\eta| = \sqrt{1-e^2\cos^2 g}\;|\cos(\eta-\eta_0) - \cos\theta_0|$, where

$$\eta_0(e,g) \;=\; \tan^{-1}(\sqrt{1-e^2}\cot g)\,, \qquad\qquad \theta_0(e,g) \;=\; \tan^{-1}\left(\frac{\sqrt{1-e^2}}{e|\sin g|}\right)\,. \tag{C.6}$$

In the angular interval $\eta \in [\eta_0,\,\eta_0+2\,\pi]$, the expression within "| |" changes sign at $\eta = \eta_0 + \theta_0$ and $\eta = 2\pi + \eta_0 - \theta_0$. Rewriting

$$\left\langle \frac{|\cos\theta|}{\sqrt{r}} \right\rangle \;=\; \frac{\sin i}{\sqrt{a}}\left|\,\oint\frac{\mathrm{d}\eta}{2\pi}\frac{S_g(C_\eta-e)\;+\;C_g\sqrt{1-e^2}S_\eta}{\sqrt{1-e\,C_\eta}}\right.$$

$$\left. -\;2\int_{\eta_0+\theta_0}^{2\pi+\eta_0-\theta_0}\frac{\mathrm{d}\eta}{2\pi}\frac{S_g(C_\eta-e)\;+\;C_g\sqrt{1-e^2}S_\eta}{\sqrt{1-e\,C_\eta}}\,\right|\,, \tag{C.7}$$

we obtain

$$\left\langle \frac{|\cos\theta|}{\sqrt{r}} \right\rangle \;=\; \frac{2\sin i}{\pi\sqrt{a}}\,S(e,g)\,, \tag{C.8}$$

where the function

$$S(e,g) \;=\; \frac{\sqrt{1+e}}{e}\,|\sin g|\,\Bigg[-\,\mathcal{E}(k)\;+\;\mathcal{E}(\eta_2,k)\;-\;\mathcal{E}(\eta_1,k)$$

$$+\,(1-e)\left\{\mathcal{K}(k)-\mathcal{F}(\eta_2,k)+\mathcal{F}(\eta_1,k)\right\}\Bigg] + \cos g\,\frac{1-e^2}{e}\left[\frac{1}{\sqrt{1-e\cos g}}\;-\;\frac{1}{\sqrt{1+e\cos g}}\right]. \tag{C.9}$$

Here k is given below equation (C.4), (η_0,θ_0) are defined in equation (C.6), and

$$\eta_1(e,g) \;=\; \frac{\eta_0(e,g)+\theta_0(e,g)-\pi}{2}\,, \qquad\qquad \eta_2(e,g) \;=\; \frac{\eta_0(e,g)-\theta_0(e,g)+\pi}{2}\,. \tag{C.10}$$

The last average is easier to do:

$$\left\langle \frac{\cos^2\theta}{\sqrt{r}} \right\rangle \;=\; \oint \frac{\mathrm{d}\eta}{2\pi}\,(1-e\cos\eta)\frac{\cos^2\theta}{\sqrt{r}} \;=\; \frac{\sin^2 i}{\sqrt{a}}\oint\frac{\mathrm{d}\eta}{2\pi}\frac{\left(S_g(C_\eta-e)+C_g\sqrt{1-e^2}S_\eta\right)^2}{(1-e\,C_\eta)^{\frac{3}{2}}}$$

$$=\; \frac{2\sin^2 i}{\pi\sqrt{a}}\left[\frac{\sqrt{1+e}\,\mathcal{E}(k)}{2}\;-\;T(e)\cos 2g\right] \tag{C.11}$$

where the function

$$T(e) \;=\; \sqrt{1+e}\left[\left(\frac{2}{e^2}-\frac{3}{2}\right)\mathcal{E}(k)-\frac{2}{e^2}(1-e)\mathcal{K}(k)\right]. \qquad \text{(C.12)}$$

Using (C.4), (C.8) and (C.11), the orbit-averaged disc potential is:

$$\Phi_{\rm d} \;=\; \frac{16GM_\bullet}{11\pi r_{\rm c}}\mu(\tau)\sqrt{\frac{r_{\rm d}}{a}}\left[-\frac{297}{100}\sqrt{1+e}\,\mathcal{E}(k) \;+\; \frac{\sin i}{2}\,S(e,g)\right.$$
$$\left. -\;\frac{9}{100}\sin^2 i\left(\frac{\sqrt{1+e}}{2}\mathcal{E}(k)-T(e)\cos 2g\right)\right]. \qquad \text{(C.13)}$$

This expression is used to compute the isocontours shown in Figure 3.2. For dynamical calculations, we found it convenient to approximate the functions, $S(e,g)$ and $T(e)$, by the following polynomials in e^2:

$$T(e) \;\simeq\; a_t e^2 + b_t e^4 + c_t e^6\,, \qquad \text{(C.14)}$$
$$S(e,g) \;\simeq\; \left(1 + a_0 e^2 + b_0 e^4 + c_0 e^6\right) \;-\; \lambda\left(a_t e^2 + b_t e^4 + c_t e^6\right)\cos 2g\,, \qquad \text{(C.15)}$$

where the constants,$(a_t, b_t, c_t, a_0, b_0, c_0, \lambda)$, are given below equation (3.10). This approximation results in a maximum error of $\sim 2\%$ in $\Phi_{\rm d}$, and provides us with the simpler expression of equation (3.10).

Appendix D

Density Deformation of the Cusp

The density perturbation, $\rho_1 = M_c/(2\pi) \int F_1 \, d\boldsymbol{u}$, is defined by a triple-integral over velocities, of the DF perturbation, F_1, of equation (3.16). We use spherical polar coordinates, with $\boldsymbol{u} = (u_r, u_\theta, u_\phi)$. The integrals can be transformed into integrals over E, L and L_z using the following relations:

$$L_z \;=\; r \sin\theta \, u_\phi \, , \qquad L \;=\; r\sqrt{u_\theta^2 + \frac{L_z^2}{r^2 \sin^2\theta}} \, , \qquad E \;=\; \frac{u_r^2}{2} + \frac{L^2}{2r^2} - \frac{GM_\bullet}{r} \, . \quad \text{(D.1)}$$

Then we have:

$$\rho_1(r, \theta) \;=\; \frac{2M_c}{\pi r} \int_{-\frac{GM_\bullet}{r}}^{0} dE \int_0^{L_m} dL \frac{L}{\sqrt{L_m^2 - L^2}} \int_{-L\sin\theta}^{L\sin\theta} dL_z \frac{F_1}{\sqrt{L^2 \, \sin^2\theta - L_z^2}} \, , \quad \text{(D.2)}$$

where $L_m(E, r) = \sqrt{2r^2 E + 2GM_\bullet r}$ is the maximum value of the (magnitude of the) angular momentum that an orbit of energy E can have at distance r.

As $F_1 \propto \cos 2g$, so we first express $\cos g$ in terms of $(\boldsymbol{r}, \boldsymbol{u})$. Since g is the angle between the ascending node and the periapse (see Figure 1.3), we have:

$$\cos g \;=\; \frac{1}{e\sqrt{L^2 - L_z^2}} \left[\left(\frac{L^2}{GM_\bullet} - r \right) (u_r \cos\theta \; - \; u_\theta \sin\theta) \; + \; r u_r \cos\theta \right] . \qquad \text{(D.3)}$$

Then

$$e^2 (L^2 - L_z^2) \cos 2g = \mathscr{E}_1 + \mathscr{E}_2 (L^2 \sin^2\theta - L_z^2) + \text{terms odd in } \boldsymbol{u} \, , \qquad \text{(D.4)}$$

where

$$\mathscr{E}_1 \;=\; L^2\cos^2\theta\left[\frac{2L^2}{(GM_\bullet)^2}\left(E-\frac{L^2}{r^2}+\frac{2GM_\bullet}{r}\right)\;-\;1\right], \tag{D.5}$$

$$\mathscr{E}_2 \;=\; \frac{2}{r^2}\left(\frac{L^2}{GM_\bullet}-r\right)^2\;-\;e^2\,. \tag{D.6}$$

Odd terms in $\boldsymbol{u}$ do not contribute to the $\boldsymbol{u}$-integral, so we can drop them. The integral over L_z gives:

$$\begin{aligned}\mathscr{I}_1 \;&=\; \int_{-L\sin\theta}^{L\sin\theta}\mathrm{d}L_z\frac{F_1}{\sqrt{L^2\sin^2\theta-L_z^2}}\\ &= f_1\left[\frac{\lambda}{2L}\int\mathrm{d}L_z\frac{\mathscr{E}_1+\mathscr{E}_2(L^2\sin^2\theta-L_z^2)}{\sqrt{(L^2\sin^2\theta-L_z^2)(L^2-L_z^2)}}-\frac{9}{100L^2}\int\mathrm{d}L_z\frac{\mathscr{E}_1+\mathscr{E}_2(L^2\sin^2\theta-L_z^2)}{\sqrt{L^2\sin^2\theta-L_z^2}}\right].\end{aligned} \tag{D.7}$$

Although we have not shown it explicitly, the limits of the L_z-integrals in the second line are the same as those in the first line. Here the factor,

$$f_1 \;=\; \frac{2^{\frac{n}{2}}D(\tau)}{(GM_\bullet)^{n+\frac{1}{2}}\sqrt{r_\mathrm{c}}}\,(-E)^{n/2}\,L^{n-2}\left(a_t+b_te^2+c_te^4\right)\,. \tag{D.8}$$

The transformation, $L_z = L\sin\theta\sin\alpha$, simplifies the integrals:

$$\begin{aligned}\mathscr{I}_1 &= f_1\left[\frac{\lambda}{L^2}\int_0^{\frac{\pi}{2}}\mathrm{d}\alpha\frac{\mathscr{E}_1+\mathscr{E}_2L^2\sin^2\theta\cos^2\alpha}{\sqrt{1-\sin^2\theta\sin^2\alpha}}-\frac{18}{100L^2}\int_0^{\frac{\pi}{2}}\mathrm{d}\alpha\left(\mathscr{E}_1+\mathscr{E}_2L^2\sin^2\theta\cos^2\alpha\right)\right]\\ &=\; f_1\left[\lambda\left\{\left(\frac{\mathscr{E}_1}{L^2}-\mathscr{E}_2\cos^2\theta\right)\mathcal{K}(\sin\theta)+\mathscr{E}_2\mathcal{E}(\sin\theta)\right\}\;-\;\frac{9\pi}{100}\left(\frac{\mathscr{E}_1}{L^2}+\frac{\mathscr{E}_2\sin^2\theta}{2}\right)\right]\\ &=\; 2\pi f_1\left[e^2-\frac{2L^2}{(GM_\bullet r)^2}(L_\mathrm{m}^2-L^2)\right]\Theta(\theta)\,,\end{aligned} \tag{D.9}$$

where

$$\Theta(\theta) \;=\; \frac{\lambda}{2\pi}\left[\mathcal{E}(\sin\theta)\;-\;2\cos^2\theta\,\mathcal{K}(\sin\theta)\right]\;-\;\frac{9}{400}(1\;-\;3\cos^2\theta)\,. \tag{D.10}$$

where $\mathcal{K}$ and $\mathcal{E}$ are complete elliptical integrals of first and second kind, as defined in equations (C.2)-(C.3).

The L-integral can be expressed in terms of Beta (B) functions:

$$
\begin{aligned}
\mathscr{I}_2 &= \int_0^{L_\mathrm{m}} \mathrm{d}L \frac{L}{\sqrt{L_\mathrm{m}^2 - L^2}} \mathscr{I}_1 \\
&= \frac{2^{\frac{n}{2}+1}\pi D(\tau)}{(GM_\bullet)^{n+\frac{1}{2}}\sqrt{r_\mathrm{c}}} (-E)^{\frac{n}{2}}\,\Theta(\theta) \int_0^{L_\mathrm{m}} \mathrm{d}L \frac{L^{n-1}}{\sqrt{L_\mathrm{m}^2 - L^2}} (a_t + b_t e^2 + c_t e^4)\left[e^2 - \frac{2L^2(L_\mathrm{m}^2 - L^2)}{(GM_\bullet r)^2}\right] \\
&= \frac{2^{\frac{n}{2}+1}\pi D(\tau)}{(GM_\bullet)^{n+\frac{1}{2}}\sqrt{r_\mathrm{c}}} (-E)^{\frac{n}{2}}\,\Theta(\theta) \left[\frac{L_\mathrm{m}^{n-1}}{2}\left(\lambda_a B_{\left(\frac{n}{2},\frac{1}{2}\right)} + (\lambda_b - \lambda_a)\frac{L_\mathrm{m}^2}{I^2} B_{\left(\frac{n}{2}+1,\frac{1}{2}\right)}\right.\right. \\
&\quad \left. + (\lambda_c - \lambda_b)\frac{L_\mathrm{m}^4}{I^4} B_{\left(\frac{n}{2}+2,\frac{1}{2}\right)} - \lambda_c \frac{L_\mathrm{m}^6}{I^6} B_{\left(\frac{n}{2}+3,\frac{1}{2}\right)}\right) - \frac{L_m^{n+3}}{(GM_\bullet r)^2}\left(\lambda_a B_{\left(\frac{n}{2}+1,\frac{3}{2}\right)}\right. \\
&\quad \left.\left. + \lambda_b \frac{L_\mathrm{m}^2}{I^2} B_{\left(\frac{n}{2}+2,\frac{3}{2}\right)} + \lambda_c \frac{L_\mathrm{m}^4}{I^4} B_{\left(\frac{n}{2}+3,\frac{3}{2}\right)}\right)\right]. \qquad \text{(D.11)}
\end{aligned}
$$

The final step is to evaluate the E-integral, $\rho_1 = (2M_\mathrm{c}/\pi r) \int_{-\frac{GM_\bullet}{r}}^0 \mathrm{d}E\, \mathcal{I}_2$. Substituting the explicit form for L_m given below the equation (D.2), and using $I = GM_\bullet/\sqrt{2(-E)}$, the integrals are once again given in terms of Beta functions. Therefore,

$$
\rho_1(r,\theta,\tau) = \frac{3-\gamma}{4\pi} C_{n,\gamma}(\tau) \frac{M_\mathrm{c}}{{r_\mathrm{c}}^3} \left(\frac{r_\mathrm{c}}{r}\right)^{\frac{5}{2}} \Theta(\theta)\,, \qquad \text{(D.12)}
$$

where

$$
C_{n,\gamma}(\tau) = \frac{16n\,(2-\gamma)\,\mathcal{B}(n,\gamma)}{11\pi\, 2^{\left(\gamma-\frac{1}{2}\right)}\,\alpha_\gamma} \sqrt{\frac{r_\mathrm{d}}{r_\mathrm{c}}}\,\mu(\tau)\,,
$$

$$
\begin{aligned}
\mathcal{B}(n,\gamma) = &\frac{1}{B_{\left(\frac{n}{2}+1,\frac{1}{2}\right)} B_{\left(\frac{2\gamma+n-1}{2},\frac{n+3}{2}\right)}} \left[\lambda_a B_{\left(\frac{n}{2},\frac{1}{2}\right)} B_{\left(\frac{n}{2}+1,\frac{n+1}{2}\right)} + 2^2(\lambda_b - \lambda_a) B_{\left(\frac{n}{2}+1,\frac{1}{2}\right)} B_{\left(\frac{n}{2}+2,\frac{n+3}{2}\right)}\right. \\
&- 2^3\lambda_a B_{\left(\frac{n}{2}+1,\frac{3}{2}\right)} B_{\left(\frac{n}{2}+1,\frac{n+5}{2}\right)} + 2^4(\lambda_c - \lambda_b) B_{\left(\frac{n}{2}+2,\frac{1}{2}\right)} B_{\left(\frac{n}{2}+3,\frac{n+5}{2}\right)} - 2^5\lambda_b B_{\left(\frac{n}{2}+2,\frac{3}{2}\right)} B_{\left(\frac{n}{2}+2,\frac{n+7}{2}\right)} \\
&\left. - 2^6\lambda_c\, B_{\left(\frac{n}{2}+3,\frac{1}{2}\right)}\, B_{\left(\frac{n}{2}+4,\frac{n+7}{2}\right)} - 2^7\lambda_c\, B_{\left(\frac{n}{2}+3,\frac{3}{2}\right)}\, B_{\left(\frac{n}{2}+3,\frac{n+9}{2}\right)}\right],
\end{aligned}
$$

$$
\lambda_a = a_t + b_t + c_t = 0.707106\,, \quad \lambda_b = -(b_t + 2c_t) = -0.915737\,, \qquad \text{(D.13)}
$$

$$
\lambda_c = c_t = 0.703998\,.
$$

Appendix E

Cubic Spline Interpolation

Consider a uniformly spaced grid of $(N+1)$ points ℓ_i, $i = 0, 1, 2, ..., N$, with the interval $\Delta\ell$ between successive points. The cumulative DF values $\{F_i\}$ at these grid points, and its first derivatives at boundaries, F_0' and F_N', are assumed to be given quantities. The interpolating piece-wise cubic polynomial $F(\ell)$, as given in equation (4.41), is rewritten as:

$$F_i(\ell) = a_i + b_i(\ell - \ell_i) + c_i(\ell - \ell_i)^2 + d_i(\ell - \ell_i)^3 \quad \text{for } \ell \in [\ell_i, \ell_{i+1}] \; . \tag{E.1}$$

Hence there are $4N$ unknown interpolation coefficients $\{a_i, b_i, c_i, d_i\}$. These are determined from the conditions of continuity of F and its two lowest order derivatives at the grid points:

$$F_i(\ell_i) = F_{i-1}(\ell_i) = F_i \tag{E.2a}$$

$$F_i'(\ell_i) = F_{i-1}'(\ell_i) \tag{E.2b}$$

$$F_i''(\ell_i) = F_{i-1}''(\ell_i) \tag{E.2c}$$

for $i = 1, 2, ..., (N-1)$; which gives $4(N-1)$ conditions. Here primed functions (F' and F'') represent derivatives wrt ℓ. Including the four given boundary values F_0, F_N, F_0', F_N', there are $4N$ conditions for the same number of unknowns. This defines the complete problem of determination of coefficients for the cubic spline interpolation.

Let $\{F_i'\}$ be the derivative of the interpolated cumulative DF at the grid points ℓ_i; $i = 0, 1, 2, ..., N$. Note that only the boundary values F_0' and F_N' are given, and hence the rest of $(N-1)$ values are unknown. Differentiating the equation (E.1) wrt

ℓ, we have:

$$F_i'(\ell) = b_i + 2\,c_i(\ell - \ell_i) + 3\,d_i(\ell - \ell_i)^2 \quad \text{for } \ell \in [\ell_i, \ell_{i+1}] \ . \tag{E.3}$$

Employing the equations (E.1) and (E.3) at $\ell = \ell_i,\ \ell_{i+1}$, the coefficients $\{a_i, b_i, c_i, d_i\}$ can be expressed in terms of $\{F_i,\ F_{i+1},\ F_i',\ F_{i+1}'\}$, as:

$$a_i = F_i \quad ; \quad b_i = F_i' \ ; \tag{E.4a}$$

$$c_i = \frac{3}{\Delta\ell^2}\,(F_{i+1} - F_i) - \frac{1}{\Delta\ell}\left(2F_i' + F_{i+1}'\right) \ ; \tag{E.4b}$$

$$d_i = \frac{2}{\Delta\ell^3}\,(F_i - F_{i+1}) + \frac{1}{\Delta\ell^2}\left(F_i' + F_{i+1}'\right) \ . \tag{E.4c}$$

So, there are $(N-1)$ unknowns F_i', $i = 1, 2, ..., (N-1)$. These can be worked out using the continuity of the second derivatives F'', given in equation (E.2c). This automatically takes into account the continuity of the function F and its first derivative F'.

Using equations (E.3) and (E.4) in the continuity equation (E.2c), we obtain the following set of $(N-1)$ equations:

$$F_{i-1}' + 4F_i' + F_{i+1}' = \frac{3}{\Delta\ell}\,(F_{i+1} - F_{i-1}) \ , \quad i = 1, 2, ..., (N-1). \tag{E.5}$$

This can be expressed as symmetric tridiagonal matrix linear equation,

$$\begin{bmatrix} 4 & 1 & 0 & ... & 0 & 0 & 0 \\ 1 & 4 & 1 & ... & 0 & 0 & 0 \\ 0 & 1 & 4 & ... & 0 & 0 & 0 \\ \vdots & \vdots & \vdots & & \vdots & \vdots & \vdots \\ 0 & 0 & 0 & ... & 4 & 1 & 0 \\ 0 & 0 & 0 & ... & 1 & 4 & 1 \\ 0 & 0 & 0 & ... & 0 & 1 & 4 \end{bmatrix}_{N-1\times N-1} \begin{bmatrix} F_1' \\ F_2' \\ F_3' \\ \vdots \\ F_{N-3}' \\ F_{N-2}' \\ F_{N-1}' \end{bmatrix}_{N-1\times 1} = \frac{1}{\Delta\ell} \begin{bmatrix} 3\,(F_2 - F_0) - F_0'\Delta\ell \\ 3\,(F_3 - F_1) \\ 3\,(F_4 - F_2) \\ \vdots \\ 3\,(F_{N-2} - F_{N-4}) \\ 3\,(F_{N-1} - F_{N-3}) \\ 3\,(F_N - F_{N-2}) - F_N'\Delta\ell \end{bmatrix}_{N-1\times 1} . \tag{E.6}$$

and solved for the solution $\{F_i'\}$ employing the subroutine DGTSV from LAPACK[1]. Using equations (E.1) and (E.4) along with the solution array $\{F_i'\}$, we get the interpolated cubic polynomial for the cumulative DF $F(\ell)$.

[1]Linear Algebra PACKage, a software package in Fortran.

Appendix F

Quartic Equation for Resonances

In § 4.2.2, we demonstrated that the problem of locating a resonant point in the ℓ-space, reduces to a quartic equation. Here we explicitly present the quartic equation, along with its four roots. Using equation (4.49) in (4.48), we have the quartic polynomial equation for the resonant point ℓ_{r} of the grid-point ℓ_i, explicitly given as:

$$
\begin{aligned}
& a'{\ell_{\mathrm{r}}}^4 + b'{\ell_{\mathrm{r}}}^3 + c'{\ell_{\mathrm{r}}}^2 + d'\ell_{\mathrm{r}} + e' = 0 \\
& \text{where} \\
& a' = -d_j - d_{N-j-1} \\
& b' = -c_j + 3d_j\ell_j + c_{N-j-1} + 3d_{N-j-1}\ell_{j+1} \\
& c' = -\frac{\Omega_i}{2} - b_j + 2c_j\ell_j - 3d_j\ell_j^2 - b_{N-j-1} - 2c_{N-j-1}\ell_{j+1} - 3d_{N-j-1}\ell_{j+1}^2 \\
& d' = 1 - a_j + b_j\ell_j - c_j\ell_j^2 + d_j\ell_j^3 + a_{N-j-1} + b_{N-j-1}\ell_{j+1} \\
& \qquad\qquad + c_{N-j-1}\ell_{j+1}^2 + d_{N-j-1}\ell_{j+1}^3 \\
& e' = \frac{\Omega_i}{2}\ .
\end{aligned}
\tag{F.1}
$$

The quartic equation for ℓ_{r} can be solved to obtain the following four roots:

$$
\begin{aligned}
{\ell_{\mathrm{r}}}^{(1),(2)} &= -\frac{b'}{4a'} - S \pm \frac{1}{2}\sqrt{-4S^2 - 2p + \frac{q}{S}} \\
{\ell_{\mathrm{r}}}^{(3),(4)} &= -\frac{b'}{4a'} + S \pm \frac{1}{2}\sqrt{-4S^2 - 2p - \frac{q}{S}}
\end{aligned}
\tag{F.2}
$$

where:

$$p = \frac{8a'c' - 3b'^2}{8a'^2} \ , \quad q = \frac{b'^3 - 4a'b'c' + 8a'^2 d'}{8a'^3}$$

$$S = \frac{1}{2}\sqrt{-\frac{2p}{3} + \frac{1}{3a'}\left(Q + \frac{\Delta_0}{Q}\right)} \ , \quad Q = \sqrt[3]{\frac{\Delta_1 + \sqrt{\Delta_1^2 - 4\Delta_0^3}}{2}}$$

$$\Delta_0 = c'^2 - 3b'd' + 12a'e' \ , \quad \Delta_1 = 2c'^3 - 9b'c'd' + 27b'^2 e' + 27a'd'^2 - 72a'c'e' \ .$$

Only one of the four roots presented in equation (F.2) lies in the grid-interval $[\ell_j, \ell_{j+1}]$, and is the required resonant point ℓ_r corresponding to the grid-point ℓ_i.

Appendix G

Surface Density of an Axisymmetric Disc

We consider an axisymmetric monoenergetic Keplerian stellar disc given by probability DF $f(\ell)$ at some time t in normalized angular momentum ℓ-space. The expression for surface probability density $\Sigma(r)$ is given by the equations (B.7)-(B.8), which are rewritten here as:

$$\Sigma(r) \;=\; \frac{1}{4\pi^2 a_0^2} \int \mathrm{d}\phi \, f(\ell_0(r)\sin\phi) \;, \tag{G.1}$$

$$\text{where} \qquad \ell_0(r) \;=\; \begin{cases} \sqrt{\dfrac{2r}{a_0} - \dfrac{r^2}{a_0^2}}\,, & \text{for } r \le 2a_0 \\ 0\,, & \text{for } r > 2a_0. \end{cases} \tag{G.2}$$

Since $0 \le \ell_0(r) \le 1$, the argument of f in the integrand, $\ell_0(r)\,\sin\phi \in [-1,1]$. Hence the ϕ-integral is over the complete cycle with $\phi \in [0, 2\pi]$. Separating the integration limits, for which $\sin\phi$ is a monotonic function of ϕ:

$$\Sigma(r) = \frac{1}{4\pi^2 a_0^2}\left[\int_0^{\pi/2} \mathrm{d}\phi f(\ell_0(r)\sin\phi) + \int_{\pi/2}^{3\pi/2} \mathrm{d}\phi f(\ell_0(r)\sin\phi) + \int_{3\pi/2}^{2\pi} \mathrm{d}\phi f(\ell_0(r)\sin\phi)\right] \tag{G.3}$$

and choosing the variable of integration $\ell = \ell_0(r)\sin\phi$, we have the surface density profile:

$$\Sigma(r) \;=\; \frac{1}{2\pi^2 a_0^2} \int_{-\ell_0(r)}^{\ell_0(r)} \mathrm{d}\ell \, \frac{f(\ell)}{\sqrt{\ell_0(r)^2 - \ell^2}} \tag{G.4}$$

for a general monoenergetic axisymmetric Keplerian disc.